

Ultrafast X-ray and Optical Spectroscopy of Binuclear Molecular Complexes

THÈSE N° 4905 (2010)

PRÉSENTÉE LE 10 DÉCEMBRE 2010

À LA FACULTÉ SCIENCES DE BASE
LABORATOIRE DE SPECTROSCOPIE ULTRARAPIDE
PROGRAMME DOCTORAL EN PHOTONIQUE

ÉCOLE POLYTECHNIQUE FÉDÉRALE DE LAUSANNE

POUR L'OBTENTION DU GRADE DE DOCTEUR ÈS SCIENCES

PAR

Renske Marjan VAN DER VEEN

acceptée sur proposition du jury:

Prof. O. Martin, président du jury
Prof. M. Chergui, directeur de thèse
Prof. T. Elsaesser, rapporteur
Prof. N. Schwentner, rapporteur
Prof. H. van den Bergh, rapporteur



ÉCOLE POLYTECHNIQUE
FÉDÉRALE DE LAUSANNE

Suisse
2010

Table of contents

Acknowledgements	vii
Summary	ix
Zusammenfassung	xi
1 The flash of light in chemistry	1
2 Binuclear transition metal complexes	7
2.1 Excited states of transition metal complexes	7
2.2 Square-planar d ⁸ dimers	8
2.3 The [Pt ₂ (P ₂ O ₅ H ₂) ₄] ⁴⁻ molecular complex	10
3 Vibrational wave packets	15
3.1 Introduction	15
3.1.1 Vibrational relaxation in condensed phases	18
3.2 Wave packet simulations	21
3.2.1 Analysis of the ground-state optical absorption spectrum	21
3.2.2 Coherent excitation of vibrational levels	24
3.2.3 Simulations of the time-dependent emission spectrum	25
3.3 Summary	26
4 X-ray absorption theory and data analysis	29
4.1 X-ray interaction with matter	29
4.1.1 Absorption coefficients and cross-sections	30
4.1.2 Absorption edges	31
4.1.3 X-ray relaxation processes	35
4.2 Theory of EXAFS spectroscopy	38
4.2.1 The EXAFS equation	39

4.2.2	Improvements of EXAFS theory	41
4.3	EXAFS data analysis methods	42
4.3.1	Data reduction procedures	42
4.3.2	Structural analysis	45
4.4	Theory of XANES spectroscopy	49
4.4.1	One-electron golden-rule approximation	50
4.4.2	Full multiple scattering	51
4.4.3	Self-consistent field potentials	53
4.4.4	Ab initio calculations of inelastic losses and core-hole screening	54
4.5	The modular structure of the FEFF9 program for XANES analysis	55
4.6	Bayesian fitting approach to XANES analysis	58
4.7	Challenges in calculating XANES spectra	59
4.7.1	XANES calculations of electronically excited molecules in solution	60
4.8	Summary	61
5	Experimental methods	63
5.1	Synchrotron radiation	63
5.1.1	The Swiss Light Source	65
5.2	New flow-capillary setup for air-sensitive samples	67
5.3	Steady-state XAS	68
5.3.1	Ion chamber setup	68
5.3.2	Transmission and fluorescence modes of detection	70
5.4	Time-resolved XAS	74
5.4.1	Experimental setup	75
5.4.2	Data acquisition scheme	77
5.4.3	Pump-probe XAS signals	79
5.4.4	The laser excitation process	81
5.5	Femtosecond pump-probe laser setups	84
5.5.1	Broadband transient absorption setup	84
5.5.2	Polychromatic luminescence up-conversion setup	87
5.6	Synthesis procedure of $(\text{TBA})_4[\text{Pt}_2(\text{P}_2\text{O}_5\text{H}_2)_4]$	89
6	Femtosecond optical spectroscopy	93
6.1	Fluorescence up-conversion results	93
6.2	Broadband transient absorption results	97
6.2.1	Spectro-temporal decomposition	99

6.2.2	Excitation wavelength dependence	105
6.2.3	Solvent effect on the relaxation dynamics	109
6.2.4	Singlet-state vibrational wave packet dynamics	112
6.3	Discussion	116
6.3.1	Vibrational relaxation in the singlet state	116
6.3.2	Vibrational wave packet dynamics	119
6.3.3	Mechanism of intersystem crossing	121
6.4	Summary and conclusions	124
7	Steady-state X-ray absorption spectroscopy	127
7.1	EXAFS structural analysis	127
7.1.1	Data reduction	128
7.1.2	Structural parametrization and fitting	129
7.2	<i>L</i> -edge XANES analysis	136
7.2.1	Self-consistent field calculations	136
7.2.2	<i>Ab initio</i> XANES calculations with improved many-body inelastic parameters	138
7.2.3	Bayesian fitting of the ground-state XANES spectrum	139
7.2.4	Interpretation of the XANES spectrum	143
7.3	Summary and conclusions	148
8	Time-resolved X-ray absorption spectroscopy	149
8.1	Time-resolved XAS results	149
8.1.1	Excited state decay monitored by transient XANES	151
8.2	Estimation of the excitation yield from laser-only experiments	155
8.3	Transient EXAFS analysis	157
8.3.1	A novel data analysis approach for transient EXAFS spectra	157
8.3.2	Model-based fitting of the transient EXAFS spectrum	161
8.3.3	Discussion and conclusions	169
8.4	Time-resolved <i>L</i> -edge XANES analysis	170
8.4.1	Multiple scattering and above-continuum XANES	172
8.4.2	d-DOS and the white-line region	174
8.4.3	XANES signatures of photoproduct formation	177
8.5	Summary and conclusions	178
9	Conclusions and outlook	181

Appendices

A	Input files for FEFF6 EXAFS calculations of PtPOP	187
B	Input file for FEFF9 XANES calculations of PtPOP	189
C	Input file for the Bayesian fitting program applied to PtPOP	191
D	Singular value decomposition, global fit and global analysis	193
E	Character and product tables	197
F	Transient XAS excitation wavelength dependence	199
	Physical constants	201
	Abbreviations	203
	List of Symbols	207
	References	211
	Curriculum Vitae	225

Acknowledgements

First and foremost, I owe my deepest gratitude to my thesis supervisor Professor *Majed Chergui*. His support and encouragement and his deep and vast knowledge in the field of femtochemistry, have guided me coherently through the transition states and intermediates on the complex energy landscape of my PhD work. Majed, thank you for your trust and for all the opportunities you gave me!

I am thankful to the thesis committee members: Professor *Thomas Elsässer*, Professor *Nikolaus Schwentner*, and Professor *Hubert van den Berg* for accepting to evaluate this work, for their recognition and valuable comments during the exam. I would like to thank Professor *Olivier Martin* and *Pierrette Paulou-Vaucher* for providing the excellent scientific framework within the doctoral school of photonics at the EPFL.

I am very grateful to *Esther von Arx* (EPFL), *Monique Grin Celka* (EPFL) and *Charlotte Heer* (PSI) who have patiently taken care of many administrative and organizational issues during my PhD.

I would like to thank the whole X-ray group with which I spent many, many hours of aligning, integrating, plotting and staring at error bars. I really enjoyed the ubiquitous helpfulness, the convivial atmosphere, the nocturnal töggli matches and the champagne celebrations accompanying the beam times. In particular I would like to thank *Chris Milne* for being a great help during the beam times and for introducing me to and supporting me in the MacBook-world. Chris, your good sense of humor and scientific insight made it a great pleasure working with you! Many thanks to my PhD colleagues, *Thai Pham*, *Amal El Nahhas*, *Fred Lima*, *Marco Reinhard* and *Hanne Rittmann-Frank*, for their good fellowship and help during the measurements. Special thanks go to *Christian Bressler* whose catching enthusiasm has catapulted me into the world of ultrafast X-ray science.

The pleasant atmosphere in the Lausanne lab always made it worth the three-hours train trip. I would like to thank in particular *Andrea Cannizzo* and *Frank van Mourik* for the many fruitful discussions and their supervision during the optical measurements. Andrea, grazie mille for your lively company and for introducing me to Mama Mia! Bedankt Frank, for your support and for keeping up the Dutch tradition of being direct. Merci

beaucoup *Gerald Auböck*, *Olivier Bräm*, *Cristina Consani* and *Ahmad Oskouei*, for your assistance in the Cubotron labs.

This thesis would not have been possible without the support of various people at the Swiss Light Source. First I would like to thank *Rafael Abela* for his guidance and for giving me the opportunity to realize my PhD at the Paul Scherrer Institute. The experiments at the microXAS/FEMTO beam line have been made possible due to the excellent support of *Steve Johnson*, *Camelia Borca*, *Daniel Grolimund*, *Paul Beaud* and *Gerhard Ingold*. I am grateful to *Alex Oggenfuss*, *Markus Willimann* and *Beat Meyer* for their support and help with technical problems. Thanks also to *Katja Vorobeva*, *Andrin Caviezel* and *Simon Mariager* for many enjoyable cake- and lunch-time discussions.

I am greatly indebted to *Julia Weinstein* and *Jonathan Best* who provided most of the samples that were measured during my PhD work. Julia, thank you so much for everything! I know that my last-minute large-amount requests were not easy to deal with! I would like to thank Professor *Tony Vlček* for many interesting scientific discussions about the life and times of PtPOP, and Professor *Philip Coppens* for introducing me to the field of time-resolved X-ray crystallography and for his hospitality in Buffalo. Thanks to Professor *John Rehr* for collaborating in the XAS calculations and for hosting me in Seattle.

Finally, this thesis would not be there without the loving care and support from my family. Jor, je bent een fantastische broer, blijf zoals je bent! Mam en pap, jullie liefde, steun en motivatie is onbeschrijfelijk. Dit proefschrift is deels van jullie! Oma, bedankt voor de goede telefoongesprekken. Liefje, Du bist mein eins und alles. Diese Arbeit ist Dir gewidmet.

Summary

In this thesis we followed the synergetic approach of combining ultrafast optical and X-ray spectroscopies to unravel the electronic and geometric structural dynamics of the solvated binuclear transition metal complex $[\text{Pt}_2(\text{P}_2\text{O}_5\text{H}_2)_4]^{4-}$ (**PtPOP**). This molecule belongs to a broader class of d^8-d^8 compounds that are known for their interesting photophysical properties and rich photochemical and photocatalytic reactivity.

Broadband femtosecond fluorescence up-conversion and transient absorption spectroscopy have revealed the ultrafast vibrational-electronic relaxation pathways following excitation into the $^1\text{A}_{2u}$ ($\sigma^*d_{z^2} \rightarrow \sigma p_z$) excited state for different solvents and excitation wavelengths. Both sets of data exhibit clear signatures of vibrational cooling (~ 2 ps) and wave packet oscillations of the Pt-Pt stretch vibration in the $^1\text{A}_{2u}$ state with a period of 224 fs, that decay on a 1-2 ps time scale, and of intersystem crossing into the $^3\text{A}_{2u}$ state within 10-30 ps. The vibrational relaxation and intersystem crossing times exhibit a clear solvent dependence. We also extract from the transient absorption measurements the spectral distribution of the wave packet at given time delays, which reflects the distribution of Pt-Pt bond distances as a function of time, *i.e.* the structural dynamics of the system. We clearly establish the vibrational relaxation and coherence decay processes and we demonstrate that **PtPOP** represents a clear example of an harmonic oscillator that does not comply with the optical Bloch description due to very efficient coherence transfer between vibronic levels. We conclude that a direct Pt-solvent energy dissipation channel accounts for the vibrational cooling in the singlet state. Intersystem crossing from the $^1\text{A}_{2u}$ to the $^3\text{A}_{2u}$ state is induced by spin-vibronic coupling with a higher-lying triplet state and/or (transient) symmetry breaking in the $^1\text{A}_{2u}$ excited state. The particular structure, energetics and symmetry of the molecule play a decisive role in determining the relatively slow rate of intersystem crossing, despite the large spin-orbit coupling strength of the Pt atoms.

Ultrafast **X-ray absorption spectroscopy (XAS)** is a powerful tool to observe electronic and geometric structures of short-lived reaction intermediates. We have measured the photoinduced changes in the Pt L_{III} X-ray absorption spectrum of **PtPOP** with picosecond-

nanosecond resolution. A rigorous analysis of the time-resolved **EXAFS** results allowed us to establish the structure of the lowest triplet ${}^3A_{2u}$ excited state. We found that the Pt atoms contract by as much as $0.31(5)$ Å due to the formation of a new intermetallic bond. In addition, a significant, though minute, elongation of $0.010(6)$ Å of the coordination bonds could be derived from the transient X-ray absorption spectrum for the first time. Using state-of-the-art theoretical **XAS** codes, we were also able to assign photoinduced changes in the **XANES** spectrum, to changes in Pt d-electron density, ligand field splitting and orbital hybridization in the excited state. Spectral changes in the **XANES** multiple-scattering features were used to derive a semi-quantitative value for the Pt-Pt contraction of ~ 0.3 Å, which is in excellent agreement with the time-resolved **EXAFS** results.

Application of ultrafast **XAS** and the data analysis methods to other chemical and biological systems in liquids offers an exciting perspective; in particular, in view of the recent development of intense free electron laser sources delivering ~ 100 fs X-ray pulses, opening new venues in X-ray science that scientists could hitherto only dream of.

Key words: ultrafast spectroscopy, transition metal complexes, time-resolved X-ray absorption spectroscopy, structural dynamics, photocatalysis, wave packet dynamics, synchrotron radiation

Zusammenfassung

In dieser Doktorarbeit untersuchen wir mit Hilfe der Kombination von ultraschnellen spektroskopischen Methoden im optischen und Röntgen Spektralbereich, die elektronische und geometrische Struktur­dynamik des zweikernigen Übergangsmetallkomplexes $[\text{Pt}_2(\text{P}_2\text{O}_5\text{H}_2)_4]^{4-}$ (**PtPOP**) in Lösung. Dieses Molekül gehört der breiteren Klasse von d^8-d^8 Verbindungen an, die sowohl für ihre aussergewöhnlichen photophysikalischen Eigenschaften, wie auch für ihre vielfältigen photochemischen und photokatalytischen Aktivität bekannt sind.

Mittels breitbandiger femtosekunden (fs) Fluoreszenz-Upconversion und transientser Absorptionsspektroskopie haben wir Einblick in die ultraschnellen schwingungs-elektronischen Relaxationsvorgänge, infolge der Anregung in den $^1A_{2u}(\sigma^*d_{z^2} \rightarrow \sigma p_z)$ -Zustand, gewonnen. Beide Datensätze zeigen klare Merkmale der Schwingungsrelaxation und Wellenpaketoszillationen der intermetallischen Bindung im $^1A_{2u}$ -Zustand mit einer Periode von 224 fs, die auf einer Zeitskala von 1-2 ps abklingen. Intersystem-Crossing vom $^1A_{2u}$ -Zustand in den $^3A_{2u}$ -Zustand findet innerhalb von 10-30 ps statt. Die Schwingungsrelaxations- und Intersystem-Crossing-Raten weisen eine klare Lösungsmittelabhängigkeit auf. Zudem entnehmen wir den transienten Absorptionmessungen die Spektralverteilung des Wellenpakets an bestimmten Zeitpunkten, die die Verteilung der Pt-Pt Bindungslängen als Funktion der Zeit reflektiert, und somit die Struktur­dynamik des Moleküls beschreibt. Wir ermitteln die Schwingungsrelaxations- und Kohärenzzerfall-Prozesse und wir zeigen, daß **PtPOP** aufgrund sehr effizienten Kohärenztransfers zwischen den vibronischen Zuständen, die optische Bloch Beschreibung für Schwingungsrelaxation nicht erfüllt. Aus den Daten schliessen wir, daß ein direkter Pt-Lösungsmittel Energiedissipationsweg für die Schwingungskühlung im Singletzustand verantwortlich ist. Intersystem-Crossing wird durch die spin-vibronische Kopplung mit einem höher gelegenen Tripletzustand und/oder (transiente) Symmetriebrechung im $^1A_{2u}$ -Zustand hervorgerufen. Die einzigartige Geometrie, die energetische Struktur, und die Symmetrie des Moleküls bestimmen die relativ langsame Intersystem-Crossing-Rate, trotz der grossen Spin-Bahn-Kopplungskonstante der Pt-Atome.

Ultraschnelle Röntgenabsorptionsspektroskopie ist eine leistungsfähige Methode für die Observation der elektronischen und geometrischen Strukturen von kurzlebigen Reaktionszwischenprodukten. In dieser Doktorarbeit haben wir die lichtinduzierten Änderungen im Pt L_{III} Röntgenabsorptionsspektrum mit piko- und nanosekunden Zeitauflösung erfasst. Eine ausführliche Analyse der Resultate hat es uns ermöglicht die Struktur des energetisch niedrigsten $^3A_{2u}$ -Tripletzustandes zu bestimmen. Eine Verkürzung der intermetallischen Distanz um $0.31(5)$ Å infolge der Bildung einer neuen Pt-Pt Bindung wurde ermittelt. Außerdem konnten wir zum ersten Mal eine statistisch signifikante, wenn auch kleine, Verlängerung um $0.010(6)$ Å der Koordinationsbindungen aus dem zeitaufgelösten Röntgenspektrum ableiten. Mit Hilfe von neuesten theoretischen Berechnungsmodellen konnten wir den Änderungen im Röntgenspektrum, photoinduzierte Variationen in der Pt d-Elektronendichte, in der Ligandenfeldstärke, und in der Oribtalhybridisierung zuweisen.

Die Anwendung der ultraschnellen Röntgenabsorptionsspektroskopie ermöglicht eine aufregende, wissenschaftliche Perspektive für kurzzeitdynamische Strukturstudien an chemischen sowie biologischen Systemen in Lösung. Dies trifft insbesondere angesichts der kürzlich entwickelten Freien-Elektronen-Laser-Quellen (XFEL) mit 100 fs Röntgenpulsen zu, welche Forschungsfelder, von denen Wissenschaftlern bisher nur träumen durften, erschließen werden.

Schlüsselwörter: ultraschnelle Spektroskopie, Übergangsmetallkomplexe, zeitaufgelöste Röntgenabsorptionsspektroskopie, Strukturdynamik, Photokatalyse, Wellenpaketdynamik, Synchrotronstrahlung

Chapter 1

The flash of light in chemistry

Femtochemistry is concerned with the very act of molecular motion, the breaking and formation of chemical bonds occurring with awesome rapidity [1, 2]. Whether in isolation or in any other phase, this ultrafast transformation of chemical bonds is a dynamic process involving the mechanical motion of electrons and atomic nuclei. The speed of nuclear motion is ~ 1 km/second and, hence, to record atomic-scale dynamics over a distance of an Ångström, the average time required is ~ 100 femtoseconds (fs). One of the fundamental problems in chemistry is to understand how these events, which occur in the region of the transition state between reagents and products, determine the entire course of the reaction. For decades, the actual dynamics of this region could not be time-resolved, but chemists developed steady-state spectroscopic, structural, thermodynamic, kinetic and synthetic methodologies for describing the mechanisms behind chemical reactivity.

The introduction of the "flash of light" to chemistry, with microsecond resolution, came in the 1950s with the development of flash photolysis by Norrish and Porter [3]. With the advances made with lasers, the time resolution continually improved over the years, reaching the "picosecond era." As a result, new studies of relaxation processes, energy transfer, and reactions in solutions emerged [4–6]. These developments culminated in the first application of fs lasers in the 1980s to study chemical dynamics on the ultimate time scale of molecular vibrations [7–9]. Since then, the general methodology that is employed to reach the necessary time resolution is based on the so-called *pump-probe scheme*. Just as in the early times of flash photolysis, the reaction is initiated by a short (here, fs) laser *pump pulse*, with typical wavelengths ranging from 200 nm (ultra-violet, UV) to 1200 nm (far infra-red, IR), depending on the process of interest. A subsequent *probe pulse*, clocked at a well-known time delay after the initiating pulse, plays the role of an ultra-high-speed camera to take a snapshot of the evolving molecular system. By changing the mutual delay between the two pulses, a stroboscopic sequence of these snapshots, a "molecular

movie”, can be recorded. The time resolution is determined by the cross-correlation of the intensity profiles of the pump and probe pulses.

Obviously, the dynamic properties one can investigate with this approach depends on the nature of the probe pulse. In ultrafast laser spectroscopy, both pulses lie in the optical (UV-IR) region of the spectrum. Although optical pulses probe valence orbitals, the information from a laser pump-probe experiment is not limited to electronic structure. Atomic-scale *spatial* resolution (typically $\sim 0.05 \text{ \AA}$) can be achieved by a) exploiting the concept of molecular *coherence* in order to localize the nuclei in the initial step of excitation (see Chapter 3) [10–13], and b) correlating the spectroscopic information in the probe signal (the intensity and energy of transitions) with the structure. The latter endeavor, the transformation of spectroscopic observables into bond distances, requires detailed knowledge about the potential energy surfaces of the states involved. While this is clear for small molecules such as I_2 [14, 15], NaI [16] and Na_2 [17–19], and in the case of some elementary chemical reactions such as the dissociation of ICN [8, 20, 21] and HgI_2 [22], it becomes more ambiguous when the system grows in complexity and size. A further degree of complexity is introduced when dealing with the condensed phase, in particular, liquids. In those cases, additional intermolecular (*e.g.* solute-solvent) degrees of freedom come into play (see Section 3.1.1).

In order to overcome these difficulties, various methods have been developed in recent years which are based on the use of high-energy radiation or particles to probe the systems under study [23]. The high energy entails a short wavelength which is used to obtain the desired spatial resolution in a direct fashion, without the necessity of *a priori* knowledge about potential energy surfaces. Probe techniques based on electron diffraction and energy-loss spectroscopy [24–30], X-ray Bragg and powder diffraction [31–39], X-ray diffuse scattering [40–44] and XAS [45–49] have been successfully applied to study the electronic and structural dynamics of a broad range of systems. In most of these cases the system is excited by an ultrashort laser pulse of $\sim 100 \text{ fs}$, while the probe pulse is often longer, determining the time resolution. X-ray pulses routinely obtained from 3rd generation synchrotron sources have a typical pulse length of 50-100 ps, which ”limits” their application to the study of reaction intermediates and excited states with sufficiently long life times. Structural probing of evolving transition states and coherent nuclear motions on the fs/ps time scales, has recently become possible with ultrashort electron pulses [50–52], fs laser plasma sources [39, 53–55], and fs-slicing at synchrotrons [56–61]. However, in these cases the rather low fluxes limit the range of systems that can be investigated, *i.e.* the systems need to exhibit large signals and be sufficiently robust in order to withstand

intense laser pulses for long integration times. In this respect, the latest development of X-ray free electron lasers (X-FELs), as sources of intense ~ 100 fs X-ray pulses, is very promising [62–67].

In this thesis we combine the techniques of ultrafast laser spectroscopy and time-resolved XAS. The latter is especially useful for studying structural chemical dynamics in solution, since it is not limited to ordered samples (in contrast to diffraction techniques), and X-rays have the advantage of a high penetration depth in matter (in contrast to electrons). In addition, the X-ray absorption process locally probes the electronic and geometric structure around the absorbing atom. By changing the X-ray energy, the local environments of different elements in the sample can be probed specifically. This asset of XAS comes to its full bloom in the field of catalysis, where local information about the catalytic site in the working state is of interest [68, 69]. In particular, it has been used as a probe of the morphology and electronic structure of Pt-based catalysts [70–75].

The low-energy (XANES) region of the XAS spectrum is sensitive to chemical bonding of the valence orbitals, *i.e.* orbital occupancies, oxidation state, charge transfer, orbital hybridization, bonding and backbonding contributions *etc.* [76], while the high-energy (EXAFS) region of the spectrum provides direct information about bond distances and coordination numbers. Extending XAS to the ultrafast time domain, allows monitoring these electronic and geometric structural properties in the course of chemical, biochemical and physical transformations. In particular, it opens the doorway to studying photocatalysis [77], *i.e.* the acceleration of a chemical reaction in the presence of a photo-excited catalyst (which is recovered in the photocycle). It should be noted that the expression "time-resolved XAS" also emerged in the field of catalysis and reaction kinetics to denote the *in situ* XAS measurements of active catalysts [78–80]. The time resolution in these experiments is limited to the μs -to- s time scale, without making use of the temporal structure of the X-ray source. In this thesis, time-resolved XAS refers to XAS studies on ultrafast ($< \text{ns}$) time scales using short laser and X-ray pulses to pump and probe the sample, respectively*.

Time-resolved XAS has been applied to a broad range of systems in the fields of biology, chemistry, physics and materials science. For an extensive review we refer to the articles by Bressler and Chergui [45] and Chen [81]. A few important studies should not be left unmentioned in the context of this thesis. First of all it is interesting to note that the very first time-resolved XAS studies were performed on biological systems (Myoglobin [82]) or chemical coordination compounds [83, 84]. Although done with low

*"Ultrafast XAS" or "laser-induced time-resolved (LITR) XAS" are common designations for this field of research.

time resolution (ms- μ s), these pioneering investigations showed the feasibility of the technique and its applicability to dilute molecular systems in solution. With increasing time resolution, more transition metal complexes were studied. Chen and co-workers studied on the ns time scale the transient processes resulting from photodissociation of a Ni-porphyrin system [85], representing the important group of heme-like derivatives. The same group conducted ns-resolved XAS experiments to study the metal-to-ligand charge transfer (MLCT) process in a Cu-phenantroline complex [86]. Both the changes in the structure and the oxidation state (Cu^I to Cu^{II}) could be extracted from the time-resolved XAS spectrum. In the field of photocatalysis and spin cross-over, the class of metal (Ru, Fe, Re) polypyridyl compounds have been investigated extensively [61, 87–92]. The MLCT excited state of the Ru(bpy)₃²⁺ (bpy = bipyridine) complex lies at the origin of many important photocatalytic and solar energy conversion applications [93]. Chergui and co-workers applied time-resolved XAS with \sim 50 ps resolution to determine the excited-state structure and oxidation state change in Ru(bpy)₃²⁺ [90]. It was found that the Ru-ligand distance decreases by \sim 0.03 Å in the charge-separated triplet excited state. Thereafter, the class of Fe polypyridyl-based spin cross-over complexes, in particular the Fe(bpy)₃²⁺ complex, became the focus of ps-resolved XAS studies. All three bpy ligands in the Fe(bpy)₃²⁺ molecule expand in the excited state resulting in very large changes in the XAS spectrum (due to the 6-fold degeneracy of the Fe-N scattering). The excellent data quality lead to an unprecedentedly high precision in the derived structural changes (0.203 ± 0.008 Å for the Fe-N elongation) [94]. Based on the success of these ps measurements, Chergui and co-workers conducted fs-XAS experiments on Fe(bpy)₃²⁺ using the aforementioned fs-slicing technique [61]. With fs resolution they were able to decipher the early relaxation pathways in the spin cross-over process. These measurements, being the first of their kind, pave the way for future XAS studies of ultrafast molecular dynamics with fs time resolution.

While rapid experimental improvements broaden the range of systems and processes that can be studied by time-resolved XAS, developments on the data analysis and theory side are necessary to retrieve precise quantitative chemical information from time-resolved XAS spectra. Different parts of the XAS spectrum require different approaches. Steady-state EXAFS spectra can be routinely analyzed using established methods [68]. For time-resolved EXAFS spectra, a novel data analysis procedure based on fitting the difference spectrum directly in energy space allows to extract photo-induced structural changes with subpicometer resolution [94]. Good-quality data, however, are a prerequisite for such an analysis, which are often difficult to obtain due to the small magnitude of the photo-

induced changes in the EXAFS spectrum. On the other hand, the XANES region close to the absorption edge often exhibits large transient XAS signals. Yet, both the *ab initio* calculation and interpretation of this region have remained challenging tasks, even for the steady-state spectra. Recent developments in theory [95, 96] and fitting [97–99] of XANES spectra have put us one step closer to their quantitative analysis.

Thesis outline

In this thesis we studied the photocatalytic binuclear transition metal complex tetrakis μ -pyrophosphitodiplatinate(II), $[\text{Pt}_2(\text{P}_2\text{O}_5\text{H}_2)_4]^{4-}$ (PtPOP). We applied the synergetic approach of combining ultrafast optical and X-ray spectroscopies to fully map out the electronic and geometric structural dynamics of the photocycle, starting from the earliest events of coherent oscillations (wave packets) and vibrational depopulation, through intersystem crossing and finally, repopulation of the ground state. The steady-state and time-resolved XAS results establish the electronic and geometric structures of the singlet ground and excited triplet states of the complex in solution. The aforementioned recent developments in the data analysis of transient XAS spectra and *ab initio* XAS theory were fully exploited in the analysis of these results. The ultrafast optical results address the structural and relaxation dynamics at ultrashort times, not routinely accessible by X-rays, and delivers insight into the important role of the environment in affecting them.

Details on the photochemical and photophysical properties of binuclear transition metal complexes, and of the diplatinum PtPOP molecule in particular, are given in Chapter 2. Chapters 3 and 4 provide the theoretical framework necessary for the analyses of the steady-state and transient optical and XAS spectra. After a description of the experimental details and the measured signals in Chapter 5, we present the ultrafast optical results in Chapter 6, followed by a detailed study of the steady-state XAS spectrum in Chapter 7, and, finally, the results from the time-resolved XAS experiment in Chapter 8.

The main conclusions are summarized in Chapter 9 and an outlook for the future will be presented.

Chapter 2

Binuclear transition metal complexes

We start this Chapter with a general description of the excited-state properties and dynamics of transition metal complexes, which largely differ from those of organic compounds. In Section 2.2 we focus on the class of binuclear d^8-d^8 complexes, with $d^8 = \text{Pt(II)}$, Ir(I) , Rh(I) . These complexes exhibit unique photophysical and photochemical properties related to intermetallic bonding and the nature of the bridging ligands, making them good candidates for potential photocatalytic applications. Finally, in Section 2.3 the **Pt-POP** complex will be discussed in detail. A brief review of its photochemical reactivity, steady-state spectroscopy and previous (time-resolved) structural studies will be given.

2.1 Excited states of transition metal complexes

The higher energy content of an excited state allows for reactions which are thermodynamically impossible in the ground state [100]. A different electron distribution is responsible for the very different nature, kinetics, and selectivity of excited-state reactions as compared with their ground state counterparts. An accurate description of any photochemical process therefore requires an understanding of the excited-state characteristics of the photoactive molecule. Although most molecular systems absorb light in the optical region of the spectrum, few participate in photochemical reactions. This is largely due to ultrafast nonradiative processes which deactivate the system by emptying the localized electronic and vibrational excited-state energy into a intra- or intermolecular heat bath before it can be used in a more specific way as in a photochemical reaction. The earliest (nonradiative) relaxation events in a photocycle thus determine the branching ratio between reactive and non-reactive relaxation channels, *i.e.* the photochemical quantum yield [100].

An immense amount of theoretical work has gone into developing a quantum mechanical description for a variety of these nonradiative processes [101–107]. Many of the theoretical predictions have been borne out in experiments on organic molecules, which

resulted into the classical picture of energetically and temporally well-separated relaxation steps [108]: **intramolecular vibrational energy redistribution (IVR)** followed by **internal conversion (IC)** to the lowest singlet state, followed by still slower **intersystem crossing (ISC)** to the lowest triplet, which undergoes a chemical reaction, phosphoresces, or just decays nonradiatively to the ground state. However, relaxation of higher excited states of *transition metal complexes* can offer alternatives to this picture [100, 109]. Lowest stable excited states or primary photoproducts of transition metal complexes can be formed extremely rapidly, in subpicosecond processes, and without any discernible intermediate states. The final states of the photocycle are often vibrationally excited, and ultimately, the excess energy is transferred to the solvent bath. Hence, the connection between solvation dynamics and excited-state relaxation also plays an important role, which has been shown for the ultrafast relaxation in a Re-based polypyridyl compound in different solvents [110].

Inorganic studies of these ultrafast relaxation processes have only recently begun to address the photophysical behavior peculiar to transition metal compounds [100, 111]. **IC** and **ISC** rates are different in these systems than in most organic systems. The large spin-orbit coupling relaxes spin selection rules and replaces them with spin-orbit selection rules afforded by the high effective symmetry of these complexes. These new rules allow for the preservation of some state selectivity in nonradiative decay from higher excited states. In addition, unlike most organic systems, inorganic complexes may have low-lying excited states possessing equilibrium geometries greatly distorted from that of the ground state. The consequences of such distortions with intramolecular nonradiative transitions and photochemical reactivity are often poorly understood. Selective spectroscopic probes coupled with appropriate chemical perturbations (*e.g.* in the ligands) can illuminate the significance of excited state distortions regarding inorganic photochemical reactivity.

2.2 Square-planar d^8 dimers

In the above context, binuclear d^8-d^8 platinum(II), rhodium(I) and iridium(I) complexes (bridged by various ligands) have attracted much attention [112–122]. While monomeric d^8 complexes often suffer from short excited-state life times and irreversible oxidation undermining bimolecular and catalytic reactivity, square-planar d^8 dimers have been shown to exhibit rich photochemistry, unique solid state properties, and dramatically different spectroscopic characteristics not present in their parent monomers. The dimers exhibit strong room-temperature luminescence in solution, as well as facile and reversible photo-redox chemistry involving changes in geometry and coordination number [112, 113, 117].

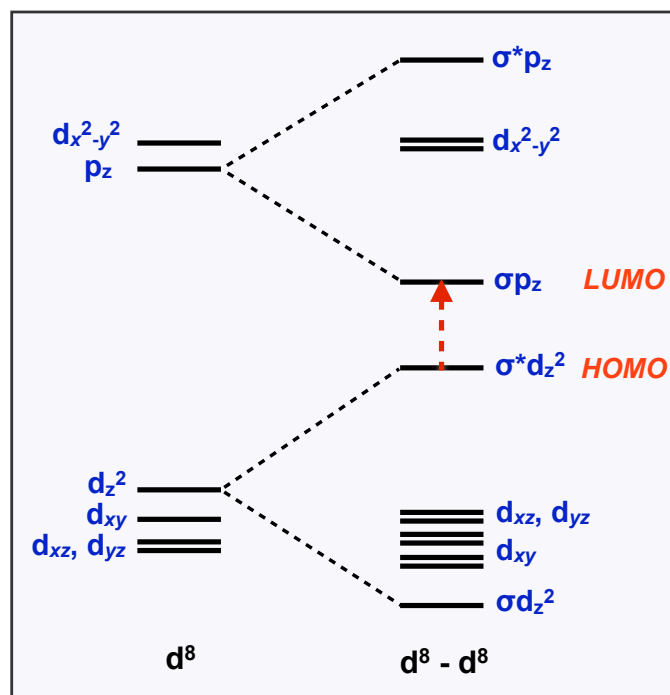


Figure 2.1: Qualitative molecular orbital diagram for d^8-d^8 complexes resulting from the face-to-face interaction of two square-planar d^8 ions. The z -axis is aligned along the metal-metal bond direction. σ and σ^* denote bonding and anti-bonding linear combinations of monomeric d- or p-orbitals, respectively. The d_{xz} , d_{yz} orbitals are split into $\pi(e_u)$ and $\pi^*(e_u)$ levels (for molecular D_{4h} symmetry), but no experimental evidence for such splitting has been found [124]. Similarly, the d_{xy} and $d_{x^2-y^2}$ orbitals should be split into δ and δ^* levels. The arrow denotes the $\sigma^*d_{z^2}(\text{HOMO}) \rightarrow \sigma p_z(\text{LUMO})$ transition resulting in the ${}^{1,3}A_{2u}$ excited states.

Their orbital level ordering can be qualitatively interpreted in terms of two monomeric square-planar complexes interacting with each other face-to-face along the metal-metal bond, as shown in Figure 2.1 [123].

The photochemical reactivity and luminescence of these dimers have been related to the long-lived lowest-lying triplet ${}^3A_{2u}$ state of $\sigma^*d_{z^2} \rightarrow \sigma p_z$ orbital character, which results from HOMO-LUMO excitation into the corresponding singlet ${}^1A_{2u}$ state (see transition in Figures 2.1 and 2.2a)* [112]. The radical-like behavior of these excited states stems from the single-occupancy of the $\sigma^*d_{z^2}$ orbital, which is localized on the metal atoms, pointing out of the molecule. In the electronic ground state, this orbital is doubly occupied. Due to the anti-bonding-to-bonding nature of the excitation, the metal-metal interaction increases in the excited state compared to the ground state. The dimers with rather rigid bridging ligands containing only three members in the bridge (*e.g.* $\text{Rh}_2(\text{b})_4^{2+}$ and

*The state designations are valid for molecules with D_{4h} symmetry. Some complexes have reduced symmetry (D_4) for which the g and u labels are omitted.

$\text{Pt}_2(\text{POP})_4^{4-}$; $\text{b} = 1,3\text{-diisocyanopropane}$, $\text{POP} = \mu\text{-pyrophosphito}$) exhibit pronounced vibronic fine structure to high quantum numbers in the low-temperature $^1,^3\text{A}_{2\text{u}}$ -state absorption and emission spectra [124, 125]; in all cases the main progressing mode is undoubtedly the metal-metal stretch. For binuclear complexes with more flexible ligands this fine structure is absent due to broadening of the vibronic progression, *e.g.* in the case of Rh and Ir 2,5-dimethyldiisocyanohexane and 1,8-diisocyanomenthane complexes [125]. Although the transition energies, bond distances and energies, vibrational frequencies and anharmonicities are different in these complexes, the same qualitative molecular orbital diagram of Figure 2.1 can be used to describe the metal-metal interaction.

Both the strength of the metal-metal interaction and the nature of the bridging ligands were shown to influence the life times of the $^1,^3\text{A}_{2\text{u}}$ states [123]. While the singlet state is short-lived (tens of ps to several ns) allowing only for intramolecular electron transfer with electron acceptors covalently attached to the ligands, the triplet state (several μs) can also react bimolecularly, *e.g.* with oxidants present in the solution. The properties of the ligands and the internuclear interaction have a combined relationship determining the important difference between the monomer and dimer excited-state photophysical properties. In addition, for some of the dimers, other close-lying excited states to the $^1,^3\text{A}_{2\text{u}}$ states have been shown to significantly alter the life times as well [123, 126, 127]. The large effects afforded by small ligand changes in these binuclear complexes demonstrate that the understanding of assignments and geometries of excited states can lead to better synthetic tuning of potential photocatalysts.

2.3 The $[\text{Pt}_2(\text{P}_2\text{O}_5\text{H}_2)_4]^{4-}$ molecular complex

In this thesis, we focus on a specific binuclear transition metal complex: **tetrakis μ -pyrophosphitodiplatinate(II)**, $[\text{Pt}_2(\text{P}_2\text{O}_5\text{H}_2)_4]^{4-}$ (**PtPOP**) (Figure 2.2a), which is one of the most studied molecules in the family of bridged $\text{d}^8\text{-d}^8$ complexes, owing to its versatile photochemistry in solution [116, 117, 128]. The $^3\text{A}_{2\text{u}}$ ($\sigma^*\text{d}_{z^2} \rightarrow \sigma\text{p}_z$) excited state shows a strong green emission whose decay reveals a very long excited-state lifetime, about 10 μs [129]. Besides being a strong photochemical reductant and oxidant, **PtPOP** in its $^3\text{A}_{2\text{u}}$ excited state behaves essentially as a free radical, abstracting H-atoms from isopropanol [112, 128, 130] or organometallic hydrides Ph_3MH , $\text{M} = \text{Si}, \text{Ge}, \text{Sn}$ [131, 132]. The oxidized **PtPOP** H_2 dihydride complex undergoes reductive elimination upon absorption of a second photon, regenerating the original **PtPOP** photocatalyst [133]. The fact that this reaction is reversible, is a direct consequence of the intermetallic bonding characteristics in **PtPOP**. Compared to, for example, the $\text{Rh}_2(\text{b})_4^{2+}$ complex

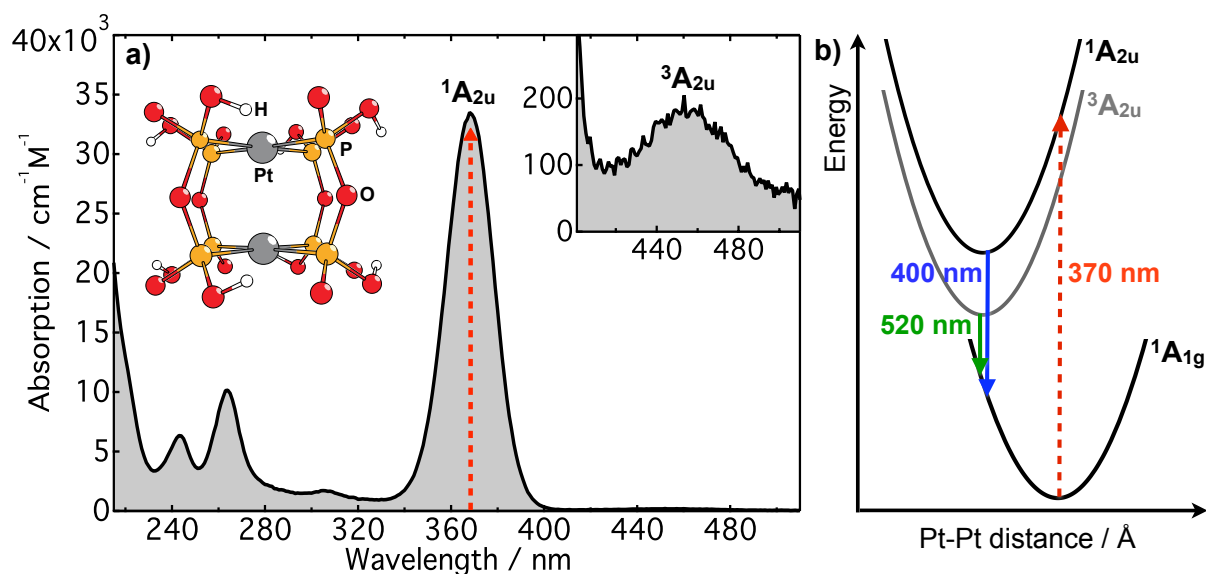


Figure 2.2: a) Molecular structure and absorption spectrum of **PtPOP** (in water). The upper-right inset shows a zoom into the triplet state absorption. The red arrow denotes the $\sigma^*d_{z^2} \rightarrow \sigma p_z$ transition (see Figure 2.1); b) Potential diagram of the lowest-lying states of **PtPOP**. Singlet-state absorption (red), fluorescence (blue) and phosphorescence (green) are indicated by arrows. Note that the $^1A_{2u}$ and $^3A_{2u}$ potentials are vertical, *i.e.* not displaced along the Pt-Pt (or any other) distortion coordinate.

($b = 1,3$ -diisocyanopropane), the metal-metal bond in the ground-state **PtPOP** molecule is much stronger, while the bonds are about equally strong in the $^3(\sigma^*d_{z^2} \rightarrow \sigma p_z)$ excited states [123]. The energy difference from d^8-d^8 to d^7-d^7 dimer may be much less in the platinum system in spite of the "full" metal-metal bond present in the oxidized state. This prevents the photoredox cycle from falling into a thermodynamic trap. An additional example of reversible reactivity is given by the recent study of quasi-one-dimensional halogen bridged chains of **PtPOP** molecules, which have been shown to undergo reversible water-vapor induced switching of the electronic state and physical properties [134].

The **PtPOP** molecule has been the subject of numerous spectroscopic [123, 124, 129, 135–149], theoretical [150–154] and X-ray structural [43, 44, 83, 134, 155–164] investigations. Its steady-state spectroscopy is now well understood. Figure 2.2a shows the **ultra-violet (UV)**-visible absorption spectrum of **PtPOP** in water. The spectrum is characterized by a strong, narrow band around 370 nm due to dipole-allowed absorption into the $^1A_{2u}$ ($\sigma^*d_{z^2} \rightarrow \sigma p_z$) state and a weak band around 460 nm assigned to the corresponding triplet $^3A_{2u}$ state (dipole-forbidden) [124]. Analogues of these bands are not observed in monomeric square-planar Pt(II) complexes. Low-temperature vibronic progressions of these absorption bands and their corresponding fluorescence and phosphorescence spectra

(around 400 nm and 520 nm, respectively; see Figure 2.2b) are dominated by the Pt–Pt stretch vibration with a vibrational frequency of $\sim 150\text{ cm}^{-1}$ for the singlet and triplet absorption bands and $\sim 118\text{ cm}^{-1}$ for the emission bands [129, 137]. Based on the previous section, the higher vibrational frequency in the excited state can be understood as being due to an increased Pt-Pt interaction, *i.e.* a decreased Pt-Pt bond distance. A weak low-frequency (40 cm^{-1}) mode is built onto the vibronic spectra, which has been assigned to a ligand deformation mode, although the possibility that it belongs to a crystal phonon mode could not be fully excluded [137].

The ${}^3A_{2u}$ state is split into two triplet sublevels of E_u and A_{1u} symmetry (D'_{4h} double-group designations) [137, 144]. The degenerate E_u level lies 50 cm^{-1} higher in energy than the A_{1u} level, resulting in a pronounced temperature dependence of the phosphorescence band shape/origin and life time [137, 144, 146]. While emission from the E_u level to the ground state is dipole-allowed (in D'_{4h}), the dipole-forbidden A_{1u} spectrum is understood to obtain intensity completely by vibronic coupling through a nontotally symmetric vibrational mode of e_g symmetry [146]. From the similarities of the band widths, the progression maxima (6-7 quanta from the origin) and vibrational frequencies of the singlet and triplet spectra, it was concluded that the ${}^1A_{2u}$ and ${}^3A_{2u}$ potential surfaces are virtually the same (just shifted vertically in energy) [124], as depicted in Figure 2.2b. The other absorption bands in the UV spectrum are assigned to transitions of $d_{xy}, d_{xz}, d_{yz} \rightarrow \sigma_pz$ (240 nm, 260 nm) and d-d character (310 nm) [124], although the latter could also be a ligand-to-metal charge-transfer transition which have been calculated to occur in the 330 nm region [153].

The mechanism of ISC, *i.e.* the nonradiative relaxation from the ${}^1A_{2u}$ to the ${}^3A_{2u}$ state, in binuclear d^8-d^8 complexes is still a subject of debate [148, 150]. In PtPOP, the formation of the triplet state from the singlet occurs with unity quantum yield [129] on a ps time scale [124, 148]. Direct spin-orbit coupling between these states is, however, symmetry forbidden and no intermediate state is known to lie between the ${}^1A_{2u}$ and ${}^3A_{2u}$ states [150, 153]. A higher-lying ${}^3B_{2u}$ triplet state has been invoked as a thermally activated channel for ISC in both PtPOP [148] and $\text{Rh}_2(\text{b})_4^{2+}$ [126] complexes in order to explain the temperature dependence of the ISC rate.

Many previous studies tried to determine the structural distortions in the ${}^1,{}^3A_{2u}$ excited states of PtPOP. Franck-Condon (FC) analyses of low-temperature excitation and emission spectra [129, 137] and Raman spectroscopy [136, 138, 149] have derived values for the shortening of the Pt–Pt distance in the range 0.175-0.225 Å. These spectroscopic studies all rely on the metal-metal stretch vibrational frequencies in the ground and ex-

cited states to derive the Pt–Pt distortion (the contraction is proportional to the excited state vibrational frequency). X-ray diffraction (XRD) or X-ray absorption spectroscopy (XAS) provide a more direct way of determining the structural changes in the excited state. A stroboscopic XRD study with 33 μs time resolution on helium-cooled crystals of PtPOP derived a shortening of the Pt–Pt bond by 0.28(9) Å [159]. In a different XRD experiment, Ohashi and co-workers derived different values for the Pt contraction in the range 0.23–0.28 Å (depending on the counter ion in the crystalline compound) and a very large Pt–P shortening by 0.49 Å, but the quantitative results depended strongly on the fraction of excited molecules, which could not be derived accurately [158, 160, 161]. A time-resolved XAS study with μs time resolution, based on the Fourier transform of the difference (excited minus unexcited) EXAFS spectrum, reported a shortening of the Pt–P and Pt–O distances in the triplet state [83] but was not sensitive to the Pt–Pt bond itself. The authors therefore used the optically derived Pt–Pt bond length of 2.75 Å in the excited state [129] to derive a large contraction of 0.52 Å along the Pt–Pt axis between both planes containing each four P-atoms, implying unrealistic structure changes within the ligands. Theoretical density functional theory (DFT) calculations of Coppens *et al* [153] predicted a Pt–Pt bond shortening (0.17–0.5 Å) and a slight Pt–P lengthening (0.005–0.05 Å) in the triplet state. The large range of reported values is due to the different functionals used in this calculation. However, all pointed to a Pt–P bond lengthening, which has not previously been observed and is in clear contrast to the EXAFS results of reference [83] and the XRD results of reference [161]. A recent solution-phase X-ray scattering study derived a Pt–Pt contraction of 0.24(6) Å [43]. Therefore, the above review shows that the structural determination of the triplet state of PtPOP is still subject to contradictory claims from theory as well as both optical and X-ray studies.

The present thesis work was performed with the aims of 1) unravelling the initial nonradiative relaxation events in the photocycle of PtPOP (Chapter 6); 2) determining the molecular structure of the $^3A_{2u}$ excited state (Chapter 8). These pieces of information could eventually contribute to the better understanding of the electronic and structural mechanisms that lead to the excellent photocatalytic properties of this diplatinum d^8 – d^8 molecular complex.

Chapter 3

Vibrational wave packets

This Chapter introduces the concept of coherent vibrational motion (wave packets), and the conditions under which it occurs and can be detected. Section 3.1 gives a short overview about previous work done in the field of coherent nuclear motion in molecular systems. It also contains a brief description of vibrational relaxation processes in liquids (Section 3.1.1). Section 3.2 provides the background to simulate the excitation, evolution and emission of a single-mode vibrational wave packet. In Section 3.2.1 we simulate the vibronic progression of the ground-state optical absorption spectrum of PtPOP as a preparative step towards the wave packet calculations described in the last two sections. Section 3.2.2 provides the theoretical background for the coherent excitation of vibrational levels of a single-mode harmonic oscillator applicable to the case of PtPOP. Last, in Section 3.2.3 we describe how to map the wave packet motion by measuring the time-resolved emission spectrum, which will be used to derive the ultrafast structural dynamics in the singlet excited state of PtPOP (Section 6.2.4).

3.1 Introduction

As discussed in Chapter 1, the main interest in chemical dynamics is the process of nuclear rearrangement on reactive potential-energy surfaces. The availability of femtosecond lasers made it possible to perform real-time probing of short-lived molecular complexes that appear at intermediate stages of chemical reactions, constituting the field of "laser femtochemistry" pioneered by Zewail and co-workers [165, 166]. To understand the chemical process in its entirety, one needs to know the nuclear motions during the course of the reaction with sufficient spatial resolution. In this respect, the concept of *vibrational wave packets*, *i.e.* coherent superpositions of vibrational eigenstates, has been proven to be extremely useful [167]. The nuclear wave packets are well localized in space, and their time evolution is a quantum counterpart of the classical particle-like evolution of the system.

The theoretical concept of describing quantum systems using wave packets is fundamental and goes back to the 1920s when Schrödinger pointed out the transition between micro- and macro-mechanics using the superposition of eigenstates [168]. However, it was not until the 1980s [165] that it became possible to create and study such states occurring at the boundary between quantum and classical physics. Since the first observations of coherent vibrational and rotational motion in elementary reactions of small molecules [8, 169, 170], many other cases have been studied using various probe techniques [21, 171, 172] for molecular systems of increasing complexity [173–176] and in different phases of gases, liquids, clusters and solids [177–182].

The benefit of exploiting coherence in monitoring molecular dynamics originates in the use of a short laser pulse to spatially select a significant portion of the ensemble [12]. In the **Franck-Condon (FC)** transition [183] this portion is then transferred to a non-stationary state in the **excited state (ES)** potential (being displaced with respect to the **ground state (GS)** one) after which the molecules start to move in phase, *i.e.* coherently. According to Heisenberg’s uncertainty principle [184], the atomic-scale ($\sim 1 \text{ \AA}$) de Broglie wavelength in the coherent preparation of a quantum system and the uncertainty of probe measurements are both reached on the femtosecond time scale [13]. In molecular systems this implies that only in the limit of short (compared to the vibrational period) excitation pulses and high vibrational quantum numbers, a wave packet might be considered as classical-like, insofar as the probability distribution is well localized following a classical periodic trajectory in time [185]. The large number of eigenstates allows the selection of a single “lobe” of an eigenfunction by means of quantum interference, whereas the high-quantum number requirement renders the selected lobe to have a small spatial extent. This is demonstrated in Figures 3.1 for the harmonic ground and excited state potentials of **PtPOP** (displaced by 0.2 \AA , see later). It is seen that the broader population distribution leads to a more localized wave packet. In addition, the narrow distribution gives rise to a modulated probability distribution corresponding to the node structure of the contained wave functions.

Wave packet states generally exhibit the property that certain expectation values can undergo dynamical evolution. In an anharmonic potential the wave packet eventually disperses so that it is no longer well localized; however, this process may reverse itself leading to a “revival” of the wave packet, as was demonstrated in the case of I_2 [14]. Another example for which the quantum mechanical nature of wave packets emerges, occurs in cases where the excitation pulse length is about 30% of the duration of the vibrational period (the so-called squeezing condition [186, 187]), or if there is a sudden

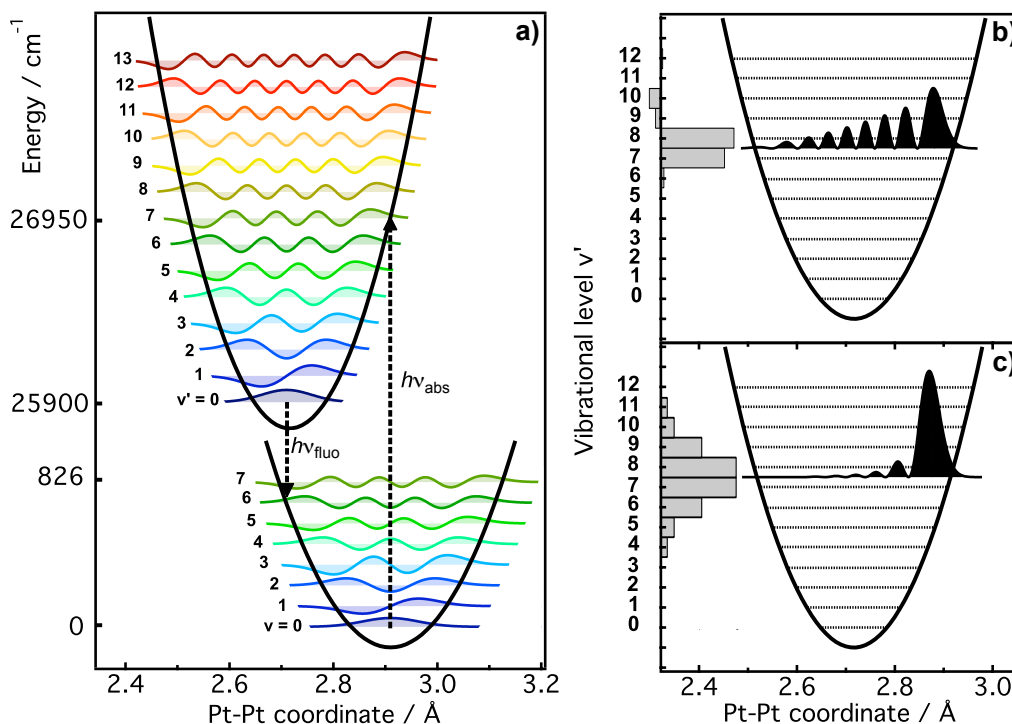


Figure 3.1: a) Harmonic GS and ($^1A_{2u}$) ES potentials for PtPOP. The vibrational wavefunctions are drawn in color and the optical transitions (absorption and fluorescence) are indicated by vertical dashed arrows. The vertical energy axis is not to scale; b) and c) Simulation of the wave packet probability distribution $|X(u,t)|^2$ (see Equation (3.6)) (filled black curves) at $t = 0$ in the excited state potential. The bars along the vertical axis represent the overlap factors C_m for each level given in Equation (3.7). The effect of quantum interference renders the wave packet in c) more localized than in b). b) demonstrates the case for the excitation conditions in the PtPOP TA experiment (370 nm, ~ 100 fs pulse, see also Sections 3.2.2 and 6.2.4).

change in vibrational frequency during the FC transition [185]. These circumstances can cause the wave packet's spatial extent to broaden and refocus during its periodic evolution, *i.e.* the wave packet "breathes", so that at some parts of its trajectory it is quite diffuse [187]. It will be shown in Section 6.2.4 that similar nonclassical signatures were observed in the case of PtPOP.

In order to observe the breathing of the wave packet it is obvious that detection of the particle at a single location is not sufficient. It is the change in the shape of the wave packet at several different times that must be measured. This requires a multicolor probe that samples the wave packet probability distribution simultaneously at many nuclear configurations. In contrast to probing the absorption changes (transient absorption) induced by the wave packet, detection of the fluorescence allows the selection of the wave packet dynamics in only the excited state of the system. At any time while the wave packet

oscillates in the **ES** potential, the molecule might emit a photon and return to the ground state. The wavelength the molecule emits depends on the instantaneous internuclear separation. In fact, the fluorescence wavelength depends on the details of the underlying **GS** and **ES** potential energy surfaces via the spatial **FC** overlap factors connecting them in the probe transition. Therefore, by both time and frequency resolving the emitted radiation, it is possible to map out the wave packet motion along the distortion coordinate, which has been demonstrated for, among other systems, diatomics in the gas phase [14, 19] or embedded in solid-matrix environments [188] and organic molecules in solution [189].

3.1.1 Vibrational relaxation in condensed phases

Much of chemistry and biology deals with reactions in the presence of solvents. The environment is not just a spectator but plays a crucial role in enhancing, driving and selecting the channels of chemical and biochemical reactions. Thus, even the simplest chemical reaction in the gas phase, the unimolecular photodissociation of a molecule in two fragments, becomes a complex phenomenon as the same molecule is embedded in the fluctuating environment of a solvent. Aside from the cage effect, which hinders (totally or partially) the separation of fragments, leading to geminate recombination, more subtle effects occur on bound states, which are due to the interaction of the oscillating molecule with the solvent molecules. When the interaction between solute and solvent is quite strong, the potential energy surfaces for the isolated and solvated molecules may be very different, thereby permitting processes in one case that are not possible in the other. Therefore, a detailed microscopic understanding of solvent-induced vibrational relaxation processes is essential to support the framework of predictive theory of reaction dynamics in solutions.

Vibrational relaxation is a dissipative process that damps the nuclear motion. The principal questions that arise concerning vibrational relaxation in liquids are: How fast is the relaxation process? and What are the primary interactions and pathways? In the gas phase, when a vibrationally excited molecule collides with a ground-state molecule of the same species, there are three possible outcomes [190]: First, the vibrational energy could be transferred to translations or rotations of the encounter molecule, or to different vibrational degrees of freedom of either the excited- or ground-state molecule (*population relaxation*); second, the collision could be vibrationally elastic, with only the phase of the wavefunction changing (*pure dephasing*); or third, the vibrational excitation could be transferred resonantly to the other molecule, giving no net change in vibrational population (*resonant transfer*). In a liquid, population relaxation can involve many-body

interactions rather than simple gas-like bimolecular encounters. The relaxation route is either through **intramolecular vibrational energy redistribution (IVR)** to other modes of lower frequency in the solute, or through **external vibrational relaxation (EVR)** to the solvent. There is also the possibility of solvent-assisted **IVR**, in which the energy couples from one mode of the solute to another through an anharmonic interaction involving a solvent mode. Solvent-induced pure dephasing in a liquid involves the continuous, stochastic, adiabatic fluctuations in the energy levels (and therefore vibrational frequency) of a molecule interacting with its surroundings. In addition, pure dephasing can also be caused by anharmonicity of the intramolecular vibrational modes.

Vibrational relaxation times in liquids can vary over 14 orders of magnitude (from fs to seconds), in large part because of the very different forces that can occur between the solute and solvent molecules. A vast amount of studies on vibrational relaxation in the condensed phase have dealt with small molecules, primarily diatomic and triatomic species [191]. The reason for this is that these simple systems provide the clearest opportunity to evaluate the microscopic details of solute-solvent interactions on vibrational relaxation by minimizing the interference from competing intramolecular pathways such as **IVR**. Diatomics represent the limiting case of an isolated vibrational mode with no opportunity for **IVR**. The only mechanism for energy relaxation is by transferring it to the solvent (as we will show later in Chapter 6, this is also true for the **PtPOP** molecule). One of the most well-studied diatomic molecules is I_2 [192]. Vibrational relaxation times for I_2 range from 50 to 200 ps, depending on the solvent. Polar solutes with low frequency vibrations relax more quickly. For example population decay in HgI (generated by photodissociation of HgI_2) occurs in 2-3 ps [170]. Small molecular anions have large noncompensating charges that are attracted or repelled by the partial charges on the atoms or bonds of the neutral polar solvent molecules, also resulting in faster relaxation [193]. An example is given by diiodide I_2^- , whose relaxation takes 3 ps in water and 4 ps in ethanol in the lower part of the potential [194]. With increasing molecular complexity, the density of vibrational states increases and anharmonic coupling between internal modes provide competing channels for relaxation. If sufficient coupling exist, vibrational energy can be very quickly equilibrated among the many modes of the solute (**IVR**) well before energy transfer to the surrounding solvent can take place through collisions [106]. **IVR** in organic molecules with more than 30 atoms typically occurs in the fs-ps time regime.

Vibrational and electronic relaxation is commonly described by making use of the approximations of the *optical Bloch equations*. For a two-level system, the total *coherence decay rate* in the optical Bloch picture using a statistical treatment of the stochastic,

weakly-coupled solute-solvent interactions, is given by [195]

$$\frac{1}{T_2} = \frac{1}{2} \left(\frac{1}{T_{1a}} + \frac{1}{T_{1b}} \right) + \frac{1}{T_2^*} \quad (3.1)$$

$$\frac{1}{T_2} = \frac{1}{2T_1} + \frac{1}{T_2^*} \quad , \quad (3.2)$$

where the second equation represents the case where the lower level is infinitely long-lived (*e.g.* for the $\mathbf{v} = 1 \rightarrow \mathbf{v} = 0$ transition). Here T_{1a} and T_{1b} are the population life times of vibronic levels a and b and T_2^* is the pure dephasing time. In the second case of Equation (3.2), T_1 is the life time of the upper level and T_2 can never exceed $2T_1$. For the general two-level case, the coherence decay time is limited by

$$T_2 \leq \frac{2T_{1a}T_{1b}}{T_{1a} + T_{1b}} \quad , \quad (3.3)$$

which implies that T_2 cannot exceed T_1 if $T_{1a} = T_{1b} = T_1$. As seen from the Equations (3.1) and (3.2), the optical Bloch picture only incorporates dissipative terms that correspond to transitions between the system levels (population relaxation; T_1 times), and random fluctuations of system energy levels (pure dephasing; T_2^* times).

In many cases, the observation of vibrational wave packets can be related to a slow rate of vibrational energy relaxation, as described by Equations (3.1), (3.2) and (3.3). However, this is not generally valid. Coupling between populations and coherences, as well as transfer of coherences between pairs of levels are neglected on the optical Bloch level. The latter two terms are treated explicitly in the *Redfield approach* of relaxation dynamics [196]. It can be shown using Redfield theory [195], that in certain unusual cases the loss of energy from the system to the environment occurs faster than, or on a similar time scale as, the destruction of phase coherence in the system, *i.e.* $T_1 < T_2$. The origin of this behavior can be seen as being the result of very efficient coherence transfer between levels. This is especially the case for harmonic potentials, which guarantees exact frequency matching between pairs of levels that differ by the same number of quanta. An anharmonic form of the potential would result in frequency mismatches rendering the coherence transfer less effective.

Some confusion exists in the literature about the definitions of the various relaxation processes. In Chapter 6 of this thesis we will adopt the following definitions. Population relaxation denotes the decay of a single vibrational or vibronic state, quantified by the depopulation time T_1 . *Vibrational cooling* is a sequence of depopulation events quantified by the experimentally observable vibrational cooling time τ_E , representing the energy relaxation time of the multilevel system as a whole. The coherence decay time T_2 is the

composite time constant according to Equations (3.1) and (3.2) (in the Bloch picture), that quantifies the rate of coherence loss between two levels. The experimental observable that represents the coherence loss of the system as a whole is called the *coordinate damping time* τ_C . Finally, pure dephasing (T_2^*), as described above, represents the coherence decay channel that does not involve energy transfer / dissipation, which is caused by anharmonicity and elastic solvent-induced shifts in the vibrational frequency. Using Redfield theory, it can be shown that after a short transient time of about one period the population relaxation rates are independent of quantum number and are equal to the rate of energy relaxation of the system as a whole [197]. The experimentally determined times τ_E and τ_C can then be equated to the collective times T_1 and T_2 generalized for a multilevel system [195, 197].

3.2 Wave packet simulations

The following sections provide the necessary framework to simulate the excitation and evolution of a single-mode vibrational wave packet and the time-resolved emission arising from it. Eventually, in Section 6.2.4 this will be used in mapping the wave packet trajectory in the singlet excited state of PtPOP. The descriptions are therefore specific for the case of PtPOP. All calculations have been implemented using MATHEMATICA 7.0 [198].

3.2.1 Analysis of the ground-state optical absorption spectrum

In order to determine which ES vibrational levels are populated by the laser pulse, we need to characterize the vibrational progression in the GS absorption spectrum. From previous low-temperature absorption and emission studies of PtPOP, the ${}^1A_{1g} \rightarrow {}^1A_{2u}$ absorption band is known to be dominated by a progression of the Pt–Pt stretching mode [129, 137]. We therefore simulated the absorption spectrum of PtPOP with a thermally weighted single-mode FC progression under the Born-Oppenheimer (BO) and Condon approximations, according to the equation [199, 200]

$$W(\nu) = A \cdot \nu \cdot \sum_{n=0}^{n_{\max}} \frac{\exp\left(\frac{-E_n^{\text{GS}}}{k_B T}\right)}{Z_{\text{GS}}} \cdot \sum_{m=0}^{m_{\max}} \exp\left(-\frac{1}{2} \left[\frac{\nu - \nu_{00} - m\nu_{\text{ES}} + n\nu_{\text{GS}}}{\Delta\nu_{\text{abs}}}\right]^2\right) |\langle \chi_m^{\text{ES}} | \chi_n^{\text{GS}} \rangle|^2 \quad (3.4)$$

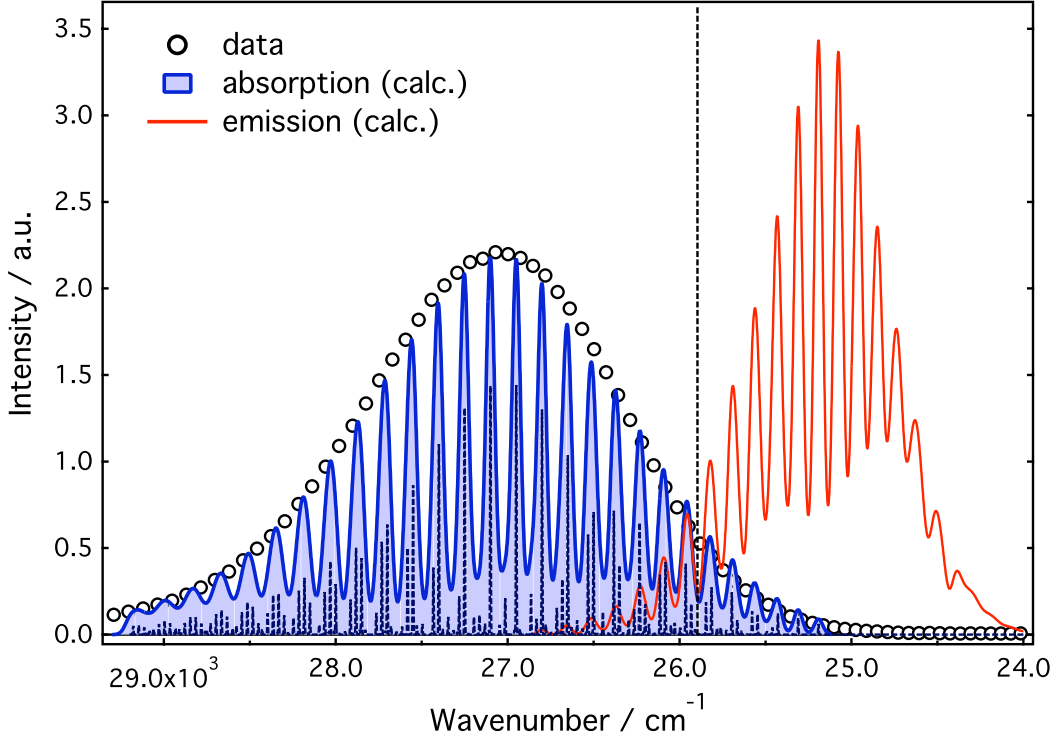


Figure 3.2: Experimental absorption spectrum of PtPOP in ethanol (open circles) and the theoretical simulated spectrum according to Equation (3.4) (solid blue line) for a Huang-Rhys factor of $S = 8.16$ and a line width of $\Delta\nu_{\text{abs}} = 25 \text{ cm}^{-1}$. The corresponding vibrational progression with reduced broadening ($\Delta\nu_{\text{abs}} = 1 \text{ cm}^{-1}$) is indicated by the dashed blue stick spectrum. The location of the 0-0 transition is indicated by the vertical dashed line at 25900 cm^{-1} and the simulated emission spectrum is indicated by the solid red curve.

where n, m are the vibrational quantum numbers for the **GS** and **GS** vibrational levels respectively, A is an arbitrary scaling factor depending on the electronic dipole strength, $E_n^{\text{GS}} = (n + \frac{1}{2}) h\nu_{\text{GS}}$ is the vibrational energy of level n in the **GS**, Z_{GS} is the **GS** vibrational partition function, ν_{00} is the 0-0 transition frequency, ν_{ES} and ν_{GS} are the Pt–Pt vibrational stretch frequencies in the **ES** and **GS** respectively, $\Delta\nu_{\text{abs}}$ represents the inhomogeneous line broadening and $|\langle \chi_m^{\text{ES}} | \chi_m^{\text{GS}} \rangle|^2$ is the **FC** factor for the **GS** vibrational function χ_m^{GS} and the **ES** vibrational function χ_m^{ES} (for an harmonic oscillator, see Figure 3.1a). The steady-state emission spectrum is calculated similarly by summing over the Boltzmann populated states $m = 0 \dots m_{\text{max}}$ in the **ES** (Boltzmann term in Equation (3.4)). The vibrational overlap factors $\langle \chi_m^{\text{ES}} | \chi_m^{\text{GS}} \rangle$ were calculated using the MATHEMATICA program package FRANCK described in reference [201].

The **FC** factors are a function of the Huang-Rhys factor S [202] which contains information about the shape of the potentials (both are harmonic in this case) and their

horizontal displacement along the vibrational coordinate. The Huang-Rhys factor S is defined as [199]

$$S = \frac{1}{2} (\alpha_{\text{ES}} d)^2, \quad \text{with} \quad \alpha_{\text{ES}} = \sqrt{\nu_{\text{ES}} \mu_{\text{vib}} / \hbar}, \quad (3.5)$$

where d is the distortion along the vibrational coordinate and μ_{vib} is the reduced mass of the specific vibrational mode. A , ν_{00} , $\Delta\nu_{\text{abs}}$ and S were taken as fitting parameters, while the vibrational frequencies ν_{ES} and ν_{GS} were fixed to the values 150 cm^{-1} and 118 cm^{-1} respectively (as determined in Section 6.2.1) and the temperature T was set to 298 K (room temperature). **GS** levels up to vibrational quantum number $n_{\text{max}} = 6$ (accounting for 98% of the **GS** population) and **ES** levels up to vibrational quantum number $m_{\text{max}} = 26$ were included in the calculation of the spectrum according to Equation (3.4).

The simulated absorption spectrum is shown in Figure 3.2 together with the simulated fluorescence spectrum centered around 25170 cm^{-1} (397 nm). Vibronic absorptions to the red of the 0-0 transition around 25900 cm^{-1} (386 nm) are due to transitions from higher-lying **GS** levels ($m > 0$) that are significantly populated at room temperature according to the Boltzmann distribution. The Huang-Rhys factor was changed in such a way that both the shape of the absorption spectrum and the Stokes shift between absorption and emission best match the experimental data. The optimum correspondence was achieved for $S = 8.16$. If it is assumed that the vibration only involves the two Pt atoms, the reduced mass μ_{vib} in Equation (3.5) is that of half a Pt atom. Inserting $\nu_{\text{ES}} = 150 \text{ cm}^{-1}$ then results in a value of $d = \pm 0.194 \text{ \AA}$ for the Pt–Pt distortion (we know it is a contraction, *i.e.* $d = -0.194 \text{ \AA}$, see Chapter 8).

No vibronic fine structure is observed experimentally at room temperature. The smooth spectrum could however not be reproduced theoretically by increasing the Gaussian line width for the case of the simple single-mode model that is used here. The missing intensity might be due to vibrational modes with small Huang-Rhys factors (*i.e.* small distortion) that add to the total intensity or an inhomogeneous broadening mechanism. A low frequency mode of 40 cm^{-1} has indeed been observed in low-temperature absorption and emission spectra [137, 140], although it remained ambiguous whether this mode was an intramolecular one or a phonon mode of the crystal lattice. For the sake of the following analysis it is not necessary to include these minor contributions. The spectrum is clearly dominated by the Pt–Pt stretch progression as was found in low-temperature vibronic progression studies. The maximum of the progression occurring around $\mathbf{v}' \simeq 7$ quanta from the origin (see also Figure 3.1a) is in good agreement with these studies [137].

3.2.2 Coherent excitation of vibrational levels

The low vibrational frequency ($\sim 150 \text{ cm}^{-1}$) and the long vibronic progression peaking at $v' \simeq 7$ (370 nm) are good prerequisites for spatial localization of the wave packet (*vide ante*). An excited ensemble with vibrational coherence can be described by [199]

$$X(u, t) = \sum_{m=0}^{m_{\max}} C_m \chi_m^{\text{ES}}(u) e^{-2\pi i(m+\frac{1}{2})\nu_{\text{ES}}t} . \quad (3.6)$$

where k_B and T are the Boltzmann constant and temperature and u represents a dimensionless nuclear coordinate. In the **BO** approximation and in the regime of linear excitation, the coefficients C_m are given by

$$C_m \approx A \cdot \sum_{n=0}^{n_{\max}} \frac{\exp\left(\frac{-E_n^{\text{GS}}}{k_B T}\right)}{Z_{\text{GS}}} \langle \chi_m^{\text{ES}} | \chi_n^{\text{GS}} \rangle I_{m,n} , \quad (3.7)$$

where A is an arbitrary scaling factor depending on the electronic dipole strength. Here $I_{m,n}$ is the spectral overlap of the excitation pulse with the homogeneous absorption band for the vibronic transition from **GS** level n to **ES** level m , calculated as

$$I_{m,n} = \frac{1}{I_{\text{tot}} 2\pi \Delta\nu_{\text{exc}} \Delta\nu_{\text{hom}}} \int_{-\infty}^{\infty} \exp\left(-\frac{1}{2} \left[\frac{\nu - \nu_{\text{exc}}}{\Delta\nu_{\text{exc}}}\right]^2\right) \cdot \exp\left(-\frac{1}{2} \left[\frac{\nu - \nu_{00} - m\nu_{\text{ES}} + n\nu_{\text{GS}}}{\Delta\nu_{\text{hom}}}\right]^2\right) d\nu , \quad (3.8)$$

where I_{tot} is the sum of the integrals of Equation (3.8) for all values $m = (0, 1, 2 \dots m_{\max})$ and $n = (0, 1, 2 \dots n_{\max})$, ν_{exc} is the excitation frequency, $\Delta\nu_{\text{hom}}$ is the homogeneous line width of the vibronic lines and $\Delta\nu_{\text{exc}}$ is the excitation band width.

The pulse length in the experiment is approximately 100 fs (**FWHM** of the Gaussian intensity profile, see Section 5.5.1). Assuming the pulse is Fourier-transform limited, this corresponds to a **FWHM** of 208 cm^{-1} of the *amplitude* profile in frequency space ($\Delta\nu_{\text{exc}} = 90 \text{ cm}^{-1}$ standard deviation). The homogeneous line width of the vibronic transitions depicted in Figure 3.2 is not known *a priori*. Typical natural line widths range from $10\text{-}50 \text{ cm}^{-1}$ (standard deviation), while inhomogeneous widths are hundreds of cm^{-1} . For the calculation of the spectral overlap factors $I_{m,n}$ we choose a homogeneous line width of $\Delta\nu_{\text{hom}} = 25 \text{ cm}^{-1}$, which is similar to the line width of the vibronic peaks in the low-temperature absorption spectrum of the triplet $^3\text{A}_{2u}$ state (20 cm^{-1}) [123, 129].*

*It was found that the coefficients C_m are not very sensitive to the homogeneous line width in the range $5\text{-}80 \text{ cm}^{-1}$.

Changes in the line width as a function of the vibrational quantum number are neglected. For excitation into the ${}^1A_{2u}$ band with a ~ 100 fs (~ 208 cm^{-1} FWHM) pulse centered at 370 nm, a coherent superposition of ~ 3 vibrational levels in the ES is generated. The overlap factors C_m for these excitation conditions are shown in Figure 3.1b.

It is noted that the absolute sign of the distortion matters for the correct description of the coherent superposition. Depending on whether the distortion is positive or negative, the overlap factors $\langle \chi_m^{\text{ES}} | \chi_m^{\text{GS}} \rangle$ flip sign for m, n is odd/even or even/odd, but they retain sign for m, n is odd/odd or even/even. This is clearly seen in Figure 3.1a. In the present study we adopt the convention that a negative distortion means a contraction along the vibrational coordinate (*i.e.* a decreased Pt–Pt bond length).

3.2.3 Simulations of the time-dependent emission spectrum

As the wave packet moves back and forth between the classical turning points of the potential according to Equation (3.6), the molecule can emit a photon. This can occur spontaneously or induced by the probe pulse (stimulated emission). The probability that the molecule will emit at frequency ν depends on the FC factor for a transition between the ES wave packet and the GS vibronic level that lies lower in energy by $h\nu$. Neglecting any decoherence processes or population decay, the time-dependent stimulated emission spectrum can be approximated by

$$F(\nu, t) \approx B \cdot \nu \cdot \sum_{n=0}^{n'_{\max}} \exp\left(-\frac{1}{2} \left[\frac{\nu - \nu_{00} - \nu_{\text{ave}} + n\nu_{\text{GS}}}{\Delta\nu_{\text{em}}} \right]^2\right) \cdot \left| \sum_{m=0}^{m_{\max}} C_m \langle \chi_n^{\text{GS}} | \chi_m^{\text{ES}} \rangle \exp\left(-2\pi i \left(m + \frac{1}{2}\right) \nu_{\text{ES}} t\right) \right|^2 \quad (3.9)$$

with C_m given by Equation (3.7), $\Delta\nu_{\text{em}}$ is the inhomogeneous line width for the emission spectrum, B is an arbitrary scaling factor and ν_{ave} is the average vibrational energy of the wave packet in the ES given by

$$\nu_{\text{ave}} = \frac{\sum_{m=0}^{m_{\max}} C_m^2 \cdot m\nu_{\text{ES}}}{\sum_{m=0}^{m_{\max}} C_m^2} . \quad (3.10)$$

Vibrational levels of the GS up to $n'_{\max} = 26$ were taken into account in the calculation of the emission spectra. The time-smearing effect of the probe pulse is taken into account by convoluting the time-dependent emission of Equation (3.9) with a Gaussian of FWHM

~ 100 fs.

For 370 nm excitation, the average energy of the instantaneously created wave packet is 1130 cm^{-1} which corresponds to an average population level of $m_{\text{ave}} = 7.5$ (see Figure 3.1b). The energy dissipation is simulated by shifting the population distribution to lower average quantum numbers. Of course, not only its average energy but also the coherence of the wave packet is affected during the process of vibrational relaxation. This coherence decay is not taken into account in this qualitative simplified picture.

3.3 Summary

Wave packets are generated by exciting a coherent superposition of several vibrational states. Only at the limit of many states and large quantum numbers, the wave packet is spatially well localized and classical (particle-like) behavior is achieved. In general, however, wave packets exhibit quantum-mechanical signatures, such as revivals and temporal and spatial modulations in their extent. The solvent plays a paramount role in the ultrafast energy and phase relaxation processes of solvated molecules. Energy relaxation can occur either through **IVR** to other modes of lower frequency in the solute, or through **EVR** to the surrounding solvent. Population relaxation and pure dephasing are two possible mechanisms responsible for the overall rate of coherence decay observed in the wave packet dynamics.

The optical absorption spectrum of **PtPOP** is dominated by a vibronic progression in the Pt–Pt stretch vibration. The Boltzmann-populated **GS** levels lead to significant broadening of the absorption spectrum at room temperature. For a mutual displacement of the **GS** and **ES** potentials of $d = -0.194\text{ \AA}$, the shape of the ${}^1A_{2u}$ absorption spectrum and the fluorescence Stokes shift could be satisfactorily simulated with a single-mode vibronic progression. The progression peaks at vibrational quantum number $v' \simeq 7$ which is in good agreement with low-temperature studies. Excitation with a 100 fs pulse at 370 nm (the center of the band) mainly populates vibrational levels $v' = 7$ and 8. The resulting $t = 0$ wave packet has highest probability density in the **FC** region, but it exhibits clear quantum-mechanical signatures such as a significant probability density for shorter bond lengths and quantum interference fringes corresponding to the nodes of the excited-state vibrational wave function. These signatures are due to the finite band width of the excitation pulse and the change in vibrational frequency between the **GS** and **ES** potentials.

The dynamical evolution of the emission spectrum can be used to map the wave packet motion along the vibrational coordinate. The instantaneous emission depends on the internuclear separation, the details of the potential energy surfaces and the FC factors connecting them via the spatial overlap of the wave packet with the vibrational wave functions in the ground state.

Chapter 4

X-ray absorption theory and data analysis

This Chapter provides the necessary theoretical background for the analysis of the X-ray absorption measurements on PtPOP described in Chapters 7 and 8. First, in Section 4.1 we provide a general introduction to the interaction of X-ray radiation with matter, with a focus on X-ray excitation (absorption) and relaxation processes. It is shown that the X-ray absorption spectrum of given compound can be divided into two regions: the low-energy X-ray absorption near-edge structure (XANES) and the high-energy X-ray absorption fine structure (EXAFS). In Section 4.2 we show that the EXAFS spectrum can be used to obtain quantitative structural information and that it is phenomenologically formulated in terms of a few parameters that are calculated by theory or determined in the data analysis. The practical tools necessary to obtain such information from EXAFS are concisely described in Section 4.3. The remainder of the Chapter discusses the XANES spectrum, which is not as yet fully quantitative as EXAFS and requires different physical consideration. The theoretical framework necessary to understand and calculate XANES is provided in Section 4.4. The FEFF9 computer code and the Bayesian fitting program that are used for the XANES calculations in Chapters 7 and 8 are described in Section 4.5 and 4.6, respectively. Finally, in Section 4.7 we discuss the existing challenges in calculating XANES spectra, in particular for (excited) molecules in solution.

4.1 X-ray interaction with matter

X-rays, electromagnetic radiation with energies in the range 120 eV to 120 keV, have been discovered by Röntgen in 1895 [203]. Since then, they have become an invaluable tool to study the structure of matter. Progress in both the theoretical understanding of the interaction of X-rays with matter, and in our knowledge of how to exploit them experimentally, have contributed to the structural elucidation of a vast amount of systems, ranging from simple systems such as small molecules, through to more complex and

celebrated examples, such as DNA and proteins.

X-rays, like any other electromagnetic radiation, can be treated as either a wave or a particle. This wave-particle duality is described by the *Einstein relation*

$$E = h\nu = hc/\lambda_{\text{ph}} \quad , \quad (4.1)$$

where E is the energy of the photon with h being Planck's constant and ν and λ_{ph} are the frequency and the wavelength of the wave. Likewise, electrons possess the wave-particle duality. The wavelength λ_{el} and the momentum p_{el} of an electron are related by the *de Broglie equation*

$$\lambda_{\text{el}} = h/p_{\text{el}} = 2\pi/k_{\text{el}} \quad (4.2)$$

and its kinetic energy is given by

$$E_{\text{el}} = h^2/2m_e\lambda_{\text{el}}^2 \quad , \quad (4.3)$$

with the electron mass m_e .

In general, an X-ray photon can interact with an atom in one of two ways: it can be scattered or it can be absorbed [204]. In scattering, the X-ray photons are deflected from their original direction of propagation, either with (*Compton scattering*) or without (*Rayleigh scattering*) loss of energy, by collision with an electron or an atom. In the X-ray absorption process, the energy of the X-ray photon is used to expel an electron from the atom, leaving the atom ionized. The excess photon energy is transferred as kinetic energy to the electron. The process is called *photoelectric absorption* which was first rigorously described by Einstein in 1905 [205] for which he received the Nobel price in physics in 1921. The remaining of this Chapter describes how this absorption process can be used as a probe of the structure of matter.

4.1.1 Absorption coefficients and cross-sections

Quantitatively, the X-ray absorption is given by the *linear absorption coefficient* μ [68, 206]. By definition, the attenuation of a beam of intensity I_T through an infinitesimal sheet of thickness dz at depth z from the sample surface is given by

$$-dI_T = I_T(z)\mu dz \quad (4.4)$$

which, by integration, leads to the well-known *Lambert-Beer law* [207]:

$$I_T(z) = I_0 e^{-\mu z} \quad (4.5)$$

where I_0 is the incoming intensity (intensity without the sample). If the total sample thickness d is known, the absorption coefficient can thus be derived from the measured intensities, using $\mu = \ln(I_0/I_T)/d$, as described in Section 5.3. The number of absorption events, W , in the thin sheet is proportional to I_T , and to the number of atoms per unit area, $\rho_a dz$, where ρ_a is the atomic number density. The proportionality factor is by definition the *atomic absorption cross-section*, σ_a , so that [204]

$$W = I_T(z) \rho_a dz \sigma_a = I_T(z) \mu dz \quad (4.6)$$

where in the last step Equation (4.4) is used. The linear absorption coefficient and the absorption cross-section are therefore related by

$$\begin{aligned} \mu &= \rho_a \sigma_a = \left(\frac{\rho_m N_A}{A} \right) \sigma_a \\ &= c_{\text{mol}} N_A \sigma_a \end{aligned} \quad (4.7)$$

where N_A , ρ_m , A_m and c_{mol} are Avogadro's number, the mass density, the atomic mass number and the molar concentration, respectively.

The absorption cross-section has a distinct dependence on the photon energy. An example is shown in Figure 4.1 for the element platinum, together with the elastic (Rayleigh) and inelastic (Compton) scattering contributions [208]. The double-logarithmic plot illustrates that the absorption cross-section is approximately proportional to $1/E^3$ below and above the discontinuities. The latter occur at characteristic energies for which the X-ray photon has enough energy to expel an electron from an atomic core level giving rise to a sudden increase of the absorption cross-section. These *absorption edges* lie at the basis of **X-ray absorption spectroscopy (XAS)** which will be discussed in detail in the following.

4.1.2 Absorption edges

According to the *Bohr model* and the *Aufbau principle*, electrons within an atom occupy successive electronic shells with discrete element-specific energies. The shells are classified as *K*, *L*, *M*, *etc*, according to the values of their principal quantum number $n=1, 2, 3, \dots$ respectively. In a pure Coulomb field, each shell has a degeneracy of n^2 and is capable of housing $2n^2$ electrons. Due to interelectron repulsion and coupling between spin and angular momenta, however, the degeneracy is lifted into subshells labelled as $(nl_j)^{2j+1}$, where, n , l and j are the principal, orbital angular momentum, and total angular momentum quantum numbers, respectively, of the single-electron states ($2j + 1$ is the

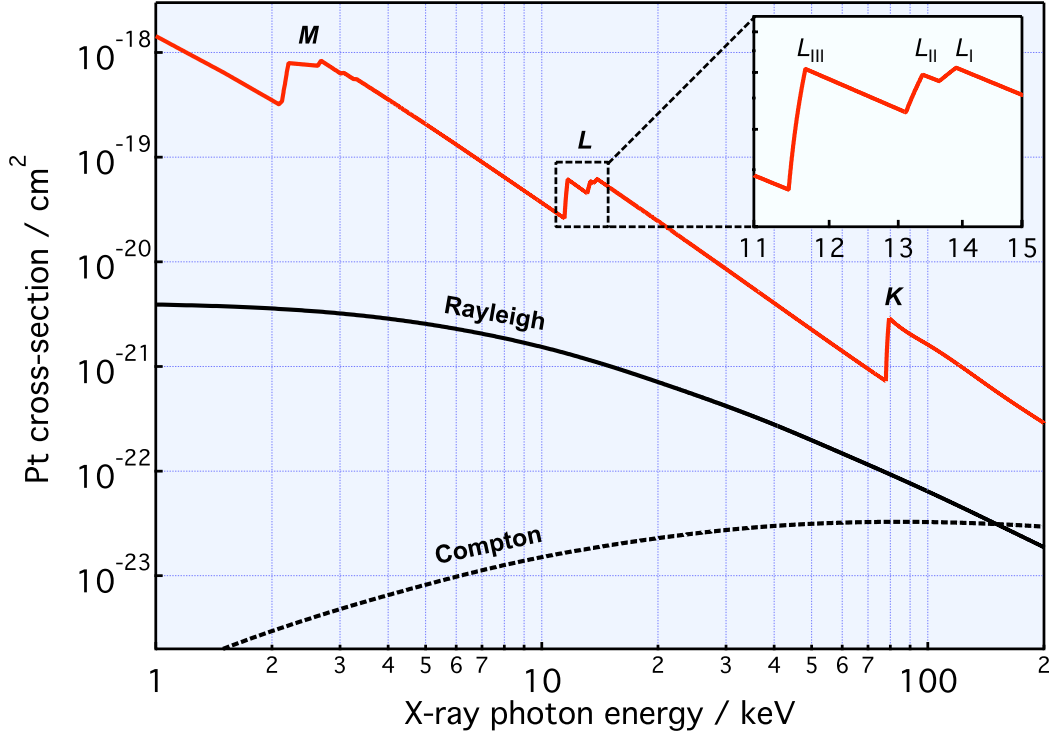


Figure 4.1: X-ray absorption (red) and scattering (black) cross-sections for the element platinum as a function of photon energy (obtained using the XOP program [208]). The inset zooms into the energy region around 12 keV where the L -edges occur. Note that both axes are in logarithmic scales.

multiplicity). In the presence of an external electric or magnetic field, the levels are split further depending on the magnetic, $m = -l, \dots, 0, \dots, l-1, l$, and spin quantum numbers, $s = \pm 1/2$.

An X-ray absorption edge occurs if the photon energy matches the energy necessary to excite an atomic core-level electron in one of the subshells into an unoccupied level above the Fermi energy E_F . The latter can be either a valence orbital (in this case a bound-bound transition occurs) or a (quasi-)continuum level above the IP. In general, the intensity of the quantum-mechanical transition is governed by the transition matrix element $\langle f | \hat{\varepsilon} \cdot \mathbf{r} | i \rangle$ [209], where i is the initial core-level state, f is the final state and $\hat{\varepsilon} \cdot \mathbf{r}$ is the electric dipole operator (see Sections 4.2 and 4.4.1). For the bound-bound transitions the optical dipole selection rules ($\Delta j = 0, \pm 1$, $\Delta m = 0, \pm 1$; ignoring spin) can be applied. It will be shown later in Section 4.4.1 that the intensities of transitions to final continuum states can similarly be interpreted by using the close connection between the absorption cross section and the final-state local l -projected density of states (LDOS).

The nomenclature (Sommerfeld notation) used to label the X-ray absorption edges is

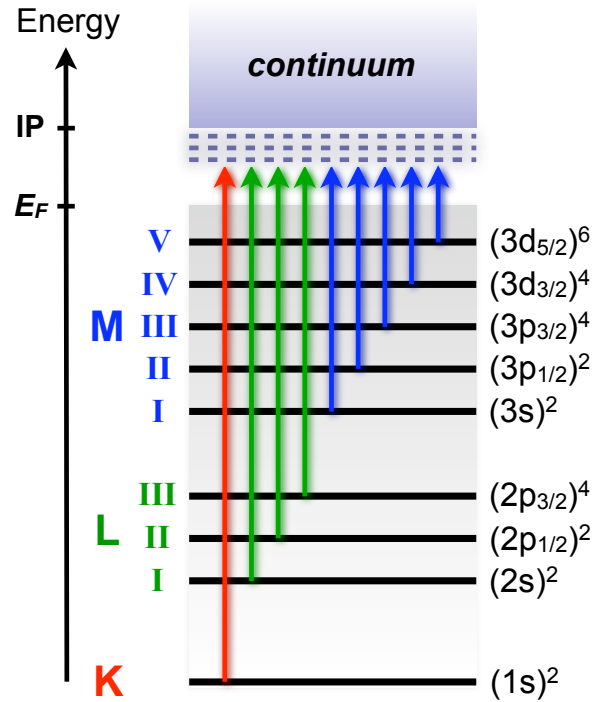


Figure 4.2: Schematics of the atomic energy levels and the nomenclature used to label the X-ray absorption edges of the elements. The electronic shells are labelled as $(nl_j)^{2j+1}$ (see text). The horizontal dashed lines just below the **IP** represent empty valence states. Transitions occur to all empty states above the Fermi level that exhibit appropriate symmetry governed by the dipole selection rules. (Redrawn and adapted from reference [204])

given in Figure 4.2. For example, the L_I , L_{II} and L_{III} edges arise for absorption from the $(2s)^2$, $(2p_{1/2})^2$ and $(2p_{3/2})^4$ subshells, respectively. The energies of the edges (or ionization energies) are unique to the type of atom that absorbs the X-ray, and hence themselves are signatures of the atomic species present in a material. The energy-dependent absorption cross-section for a specific element (*e.g.* Pt shown in Figure 4.1) exhibits the following qualitative trends [204, 206]: (1) The energy difference between the subshells within each shell are always much smaller than that between the different shells; (2) The difference in energy between the successive absorption edges, K , L , M , *etc.*, decreases with increasing principal quantum number n ; (3) The edge jump magnitudes (the ratio between the two cross-section values just below and above the edge) generally decrease in going from low- to high-energy edges, *e.g.* $L_{III} > L_{II} > L_I > K$; (4) With increasing atomic number Z , the absorption edges shift to higher energies and the edge jumps show a decrease (although the overall cross-section scales with Z^4).

X-ray absorption fine structure

The X-ray absorption spectra of atoms in molecules or embedded in the condensed phase display a modulation of the absorption coefficient, typically by a few percent, around and above the absorption edge, which is absent for isolated atoms such as gas-phase rare gas atoms. This fine structure turns out to be a unique signature of a given material: it depends on the detailed atomic structure and electronic and vibrational properties of the material. For this reason **XAS** is a very important probe of materials, as knowledge about local atomic structure is essential in many scientific fields, such as chemistry, biology and material science.

In general, the **XAS** spectrum is divided into two regions differing in the energy of the photoelectron and the information content of the fine structure: the **XANES** region up to ~ 50 eV above the **IP**, and the **EXAFS** region $\gtrsim 50$ eV above the **IP**, as illustrated in Figure 4.3 for a molecular complex in solution (in this case **PtPOP**). The **XANES** region (including the pre-edge region) contains valuable electronic information such as the energetics of hybridization orbitals, the electronic configuration, and the site symmetry. The edge position also contains information about the charge on the absorber. Due to the overlapping contributions of many electronic and structural effects and the approximations

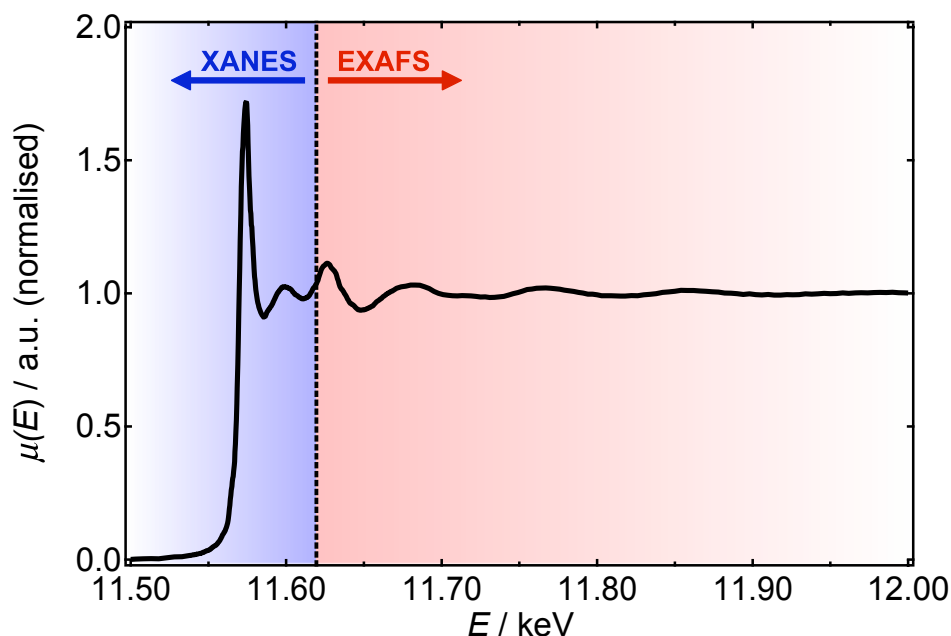


Figure 4.3: **XAS** spectrum of a molecule (**PtPOP**) in solution illustrating the two regions: the low-energy **XANES** region up to ~ 50 eV above the **IP** and the high-energy **EXAFS** region $\gtrsim 50$ eV. The spectrum has been normalized as described in Section 4.3.

necessary for its theoretical description, the XANES spectrum is often only qualitatively (or at most semi-quantitatively) interpretable, as is discussed in Sections 4.4–4.7. The EXAFS spectrum is more directly related to the (geometric) structure around the absorbing atom. Electronic effects play a reduced role making the interpretation of the EXAFS spectrum straight-forward. In Sections 4.2 and 4.3 it will be described how to obtain accurate quantitative structural information from this part of the spectrum.

4.1.3 X-ray relaxation processes

After excitation of the core-level electron in the X-ray absorption process, the excited atom can relax through several mechanisms, giving rise to fluorescence X-rays, Auger electrons, or secondary electrons as shown schematically in Figure 4.4 [76, 204].

Radiative decay

The filling of an inner shell vacancy (core hole) by an outer shell electron produces *X-ray fluorescence* with an energy equal to the energy difference between the two shells (Figure 4.4b). In the case of *K*-shell absorption, transitions from higher-lying *L*, *M*, and *N* shells to the *K*-shell core hole are designated as K_α , K_β and K_γ fluorescence, respectively, where transitions from within one shell are numbered $K_{\alpha 1}$, $K_{\alpha 2}$, $K_{\alpha 3}$, etc. in sequence of decreasing energy. Similarly, L_α and L_β lines correspond to electronic transitions from the *M* and *N* shells to the *L*-shell, respectively. The fluorescent yield, or the radiative probability, ϵ_f is defined as the ratio of emitted X-rays to the number of primary vacancies created. It is a monotonically increasing function of atomic number Z , and it is larger for *K*-line emissions than *L*- or subsequent line emissions. The measured fluorescence intensity I_F is proportional to the incoming intensity I_0 , the fluorescence yield ϵ_f , the absorption coefficient $\mu(E)$ and the fractional solid angle of detection $\Omega/4\pi$, but care should be taken in the case of thick samples for which the different energies of absorption and emission should be taken into account (see Section 5.3).

Non-radiative decay

The other major phenomenon following photoelectric absorption is the *Auger effect* (Figure 4.4c). In this process, the core hole is filled by an electron dropping from a higher shell while the atom simultaneously ejects another electron, usually from the same higher shell [76]. Auger decay is a radiationless process that can be seen as a "one-step two-electron" Coulombic readjustment to the initial core hole. On the other hand, *secondary electron decay* is a two- or multistep many-body radiationless process in which outer-shell

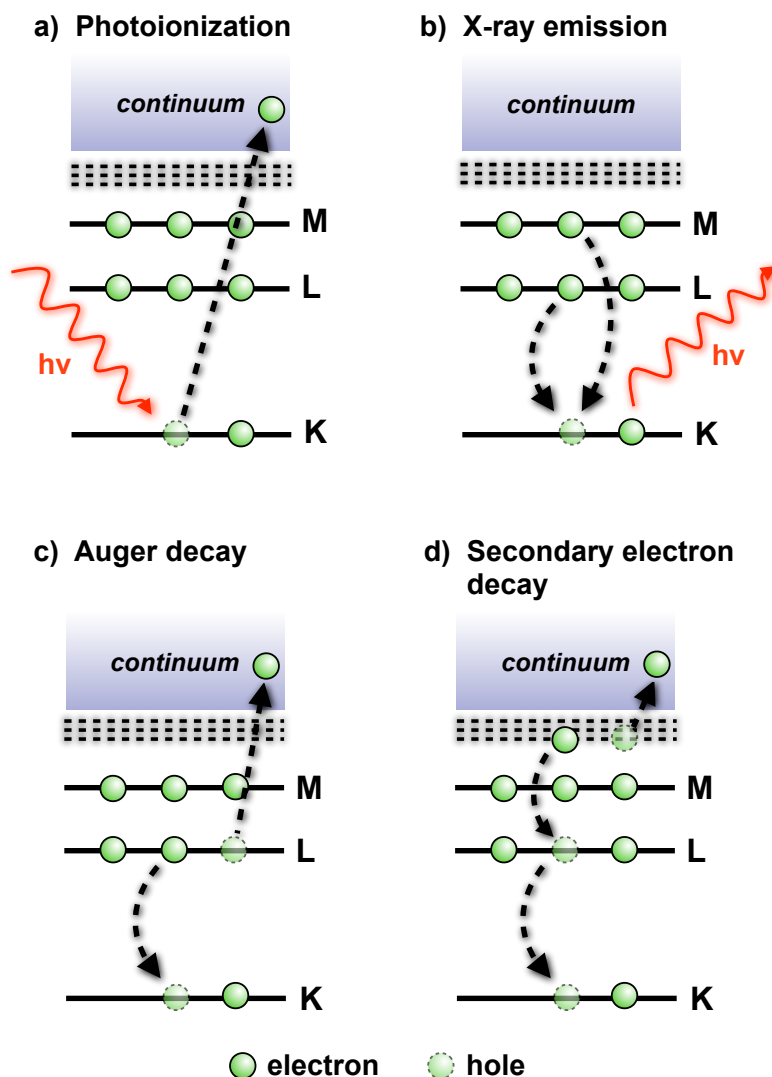


Figure 4.4: Schematic energy level diagrams of atomic excitation and relaxation processes. For clarity only the lowest three levels are indicated. Redrawn and adapted from reference [204].

electrons are ejected by Auger electrons or X-ray fluorescence photons, *e.g.* shake-up and shake-off processes (Figure 4.4d). The total yield of radiationless processes ϵ_n is simply the complement of the fluorescence yield via $\epsilon_n = 1 - \epsilon_f$. The relative yields depend on Z : the heavier the element (the higher Z), the larger the fluorescence yield [210]. Therefore, while Auger decay dominates the relaxation for light elements ($Z = 1 - 10$), heavy elements with $Z > 40$ mainly relax radiatively [206, 210, 211].

Broadening of the spectrum

The above described decay processes lead to a finite life time of the core-hole state. Through the *Heisenberg uncertainty principle*, every state with a finite life time does not

K-shell				L-shell											
abs.	em.			width (eV)	abs.			em.					width (eV)		
K	$K_{\alpha 1}$	$K_{\alpha 2}$	$K_{\beta 1}$	K	L_I	L_{II}	L_{III}	$L_{\alpha 1}$	$L_{\alpha 2}$	$L_{\beta 1}$	$L_{\beta 2}$	$L_{\gamma 1}$	L_I	L_{II}	L_{III}
78.40	66.83	65.11	75.75	49.30	13.88	13.27	11.56	9.44	9.36	11.07	11.25	12.94	9.39	5.86	5.31
	100	58	23					100	11	67	23	13			

Table 4.1: Summary of the X-ray absorption (abs.) and emission (em.) energies (both in keV) and natural line widths for the element Pt [210, 214]. The bottom row shows the relative intensities of the emission lines (an intensity of 100 is assigned to the strongest line in each shell). The $L_{\alpha 1}$, $L_{\alpha 2}$ and $L_{\beta 2}$ lines involve transitions to the L_{III} level, while the $L_{\beta 1}$ and $L_{\gamma 1}$ emissions involve transitions to the L_{II} level.

have a sharp (or delta-function-like) energy level, but is better thought of as having a finite width, *e.g.* a Lorentzian line shape. This life time broadening, or *natural width*, of the XAS spectrum increases with Z , *e.g.* from 1 eV (V, $Z=23$) up to 40 eV (W, $Z=74$) for K -shell absorption, and for the L_{III} -shell from 3.7 eV (Nd, $Z=60$) up to 7.4 eV (U, $Z=92$) [211]. Due to this broadening, the energy resolution of the incident beam needs not be much smaller than the natural line width. These limitations can be overcome by dispersing the X-ray emission and detecting it with a better resolution than the natural line width [212].

The photoelectron loses energy due to inelastic interactions such as plasmon excitations, electron-hole pairs and scattering which destroy the coherence of the photoelectron wave. These losses give the final photoelectron state a finite life time and hence leads to an additional broadening of the absorption spectrum [213]. They can be accounted for phenomenologically by an energy-dependent *electron mean-free path* $\lambda(k_{el})$ (not to be confused with the de Broglie wavelength λ_{el} of Equation (4.2)), typically in the range 5-20 Å, *i.e.* a life time broadening of a few eV. However, a more precise description of inelastic losses is obtained by using a complex, energy-dependent *self-energy* $\Sigma(E)$, which is particularly important for the XANES region as described in Section 4.4.4. The net effect is that XAS can only measure the local (short-range) atomic structure over a range limited by the net life time (or effective mean free path) of the excited photoelectron.

The X-ray absorption and emission energies, relative intensities [210, 214] and natural line widths [211] for platinum are summarized in Table 4.1.

4.2 Theory of EXAFS spectroscopy

X-ray absorption fine structure (EXAFS) refers to the oscillatory variation of the absorption coefficient as a function of photon energy just above ($\gtrsim 50$ eV) an absorption edge. Although the extended fine structure in **XAS** spectra has been known for a long time [215, 216], its structural content was not fully recognized until the work of Stern, Lytle and Sayers in 1971 [217–219].

EXAFS is a final-state quantum-interference effect involving scattering of the outgoing photoelectron from the neighbouring atoms. In a qualitative golden-rule picture, the probability that an X-ray photon will be absorbed by a core electron depends on both the initial $|i\rangle$ and the final states $|f\rangle$ of the electron via the transition matrix element $\langle f|\hat{\varepsilon}\cdot\mathbf{r}|i\rangle$, where $\hat{\varepsilon}\cdot\mathbf{r}$ is the electric dipole operator. The initial state is the localized core level, while the final state is that of the ejected photoelectron represented as an outgoing spherical wave originating from the absorbing atom. This outgoing wave is backscattered by nearby atoms thereby producing an incoming wave at the absorption site. The amplitude of all the reflected waves at the absorbing atom interferes with the outgoing photoelectron wave and hence modulate the matrix element $\langle f|\hat{\varepsilon}\cdot\mathbf{r}|i\rangle$ that controls the strength of the transition (and thus the magnitude of $\mu(E)$). The phase difference between the two components (outgoing and incoming) is approximately $2k_{\text{el}}R$, where R is the distance to the neighbouring atoms and $k_{\text{el}} = 2\pi/\lambda_{\text{el}}$ (Equation (4.2)). Thus λ_{el} decreases with increasing energy, and the modulation in μ arises from the alternating constructive and destructive interference between these components as the photon energy is varied. The amplitude and frequency of the modulation depends on the type, bonding and number of neighbouring atoms and their distances from the absorbing atom, respectively. Inelastic interactions of the photoelectron with the electrons and phonons of the surroundings destroy the coherence of the waves making them unsuitable for interference. This limits the maximum interatomic distance that can contribute to the interference pattern, *i.e.* the **EXAFS** spectrum.

Figure 4.5 pictorially illustrates the process of backscattering from 1st-shell (nearest) and 2nd-shell (next-nearest) neighbouring atoms (with respect to the absorbing atom). If the photoelectron scatters off a neighbouring atom only once (to and fro), this is referred to as *single scattering (SS)*, in contrast to *multiple scattering (MS)* if the wave scatters off twice or multiple times before returning to the absorbing atom.

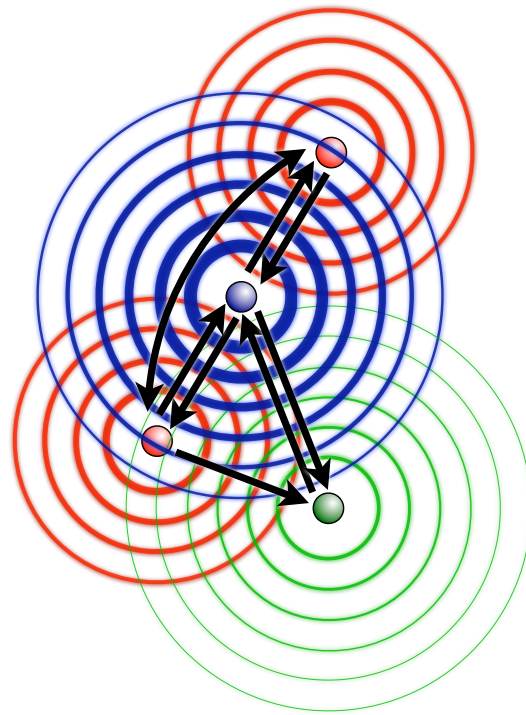


Figure 4.5: Pictorial view of the single- and multiple-scattering pathways of an outgoing photoelectron wave (blue) off 1st-shell (red) and 2nd-shell (green) neighbouring atoms. The strength of the scattered wave is reflected in the line thickness (redrawn and adapted from reference [213]).

4.2.1 The EXAFS equation

The initial development and application of **EXAFS** have been impeded by a great deal of confusion about its correct theoretical description. The question arose as to whether a long-range order theory formulated in terms of Bloch waves [215] or a short-range order theory in terms of scattering from nearby atoms [216, 220] was more appropriate. With the advent of synchrotron X-ray sources in the 1970s, a quantitative comparison between theory and experiment became possible for the first time. Since then it is generally established that the *single-electron short-range-order description* is adequate in most cases to explain the theory of **EXAFS**, although both approaches can be reconciled when appropriate broadening is introduced [213].

Within this picture, **EXAFS** can be phenomenologically described by the so-called *EXAFS equation*. Its derivation can be abundantly found in the literature [68, 204, 206]. Here we prefer to focus on the physical meaning of its various components and how the equation is used to extract structural information from the **XAS** spectrum. The **EXAFS** spectrum is defined phenomenologically as the normalized, oscillatory part of the

absorption coefficient above a given absorption edge, *i.e.*

$$\chi(E) = \frac{\mu(E) - \mu_0(E)}{\mu_0(E)} \quad , \quad (4.8)$$

where $\mu_0(E)$ is the smoothly varying atomic-like background absorption of an "embedded atom" (in the absence of neighbouring scatterers but incorporated in the lattice of neighbouring potentials). In order to relate $\chi(E)$ to structural parameters, we need to make the transformation from (absolute) E -space into (relative) k -space. The kinetic energy of the photoelectron is given by the difference in energy E of the X-ray photon and the energy E_0 necessary to expel the electron from its core level (the IP). By using Equations (4.2) and (4.3), the electron wave vector is expressed as

$$k_{\text{el}} = \sqrt{\frac{2m_e}{\hbar^2}(E - E_0)} \quad , \quad (4.9)$$

which can be used to transform $\chi(E)$ into $\chi(k)$ (from now on, the wave vector subscript referring to the photoelectron is omitted). The latter is given by the EXAFS equation, expressed as a scattering path expansion generalized to include MS pathways [213]:

$$\chi(k) = \sum_{\gamma} \frac{N_{\gamma} S_0^2 |f(k)|}{k R_{\gamma}^2} e^{-2\sigma^2 k^2} e^{-2R_{\gamma}/\lambda_{\text{tot}}(k)} \sin [2kR_{\gamma} + 2\delta_c + \phi(k)] \quad (4.10)$$

with the scattering path index γ , the number of equivalent scattering paths N_{γ} , the half-path distance R_{γ} and the squared Debye-Waller (DW) factor σ^2 . In the case of SS, R_{γ} represents the direct interatomic distance between absorber and scatterer. In addition, $f(k) = |f(k)|e^{i\phi(k)}$ is the complex backscattering amplitude for path γ , δ_c is the central-atom phase shift of the final state, $\lambda_{\text{tot}}(k)$ is the energy-dependent mean free path and S_0^2 is the overall amplitude reduction factor, which was added later to account for many-body (shake-up, shake-off) effects (Section 4.1.3).

In principle, Equation (4.10) contains all of the key elements that a correct theory must entail and it provides a convenient parameterization that allows fitting the local atomic structure around the absorbing atom to the experimental EXAFS data (see Section 4.3). The relation between the oscillatory fine structure and the interatomic distances is clearly reflected by the $\sin(2kR_{\gamma})$ term. The finite life time of the excited state consisting of the photoelectron together with the core hole where it came from is captured by the exponential damping term $e^{-2R_{\gamma}/\lambda_{\text{tot}}(k)}$. The strength of the reflected waves depends on the type and number of the neighbouring atoms via the backscattered amplitude $|f(k)|$. The phase

factors $\phi(k)$ and δ_c reflect the quantum-mechanical nature of the scattering process (the factor of 2 is due to the fact that the photoelectron encounters the potential of the central atom twice). These phases account for the difference between the measured and geometric interatomic distances, which is typically a few tenths of an Å and must be corrected for by using an experimental or theoretical reference [68]. Finally, the damping factor $e^{-2\sigma^2 k^2}$ is partially due to thermal effects causing the atoms to jiggle around their equilibrium atomic positions with a root-mean-square deviation of σ . Thus the contributions of these atoms to the interference will not all be exactly in phase. Effects of static disorder are similar and they give rise to an additional contribution to σ^2 . The Debye-Waller damping term is most pronounced for high energies making it essential for EXAFS, but its energy dependence is often negligible in XANES. In the case of a simple diatomic vibration and scattering along the interatomic axis, the squared DW factor can be expressed as [221]

$$\sigma^2 = \frac{h}{8\pi^2 \mu_{\text{vib}} \nu_{\text{vib}}} \coth\left(\frac{h\nu_{\text{vib}}}{2kT}\right), \quad (4.11)$$

where μ_{vib} is the reduced mass of the vibration, T is the temperature, and ν_{vib} is the frequency of the vibration. As σ^2 increases with T , the fine structure tends to "melt" at high temperatures, confining the spectrum to lower regions of energy.

4.2.2 Improvements of EXAFS theory

The improvements of EXAFS theory since the first formulation of Equation (4.10) can be viewed as successive refinements of the above described key elements [213]. A major improvement has been the accurate treatment of scattering by taking *curved-wave effects* into account. Earlier treatments [222] approximated the photoelectron wave as a plane wave represented by the scattering amplitude $f(k)$. It was shown later by Rehr *et al* [223] that the entire curved-wave theory can be recast as in the standard EXAFS equation, but with an *effective scattering amplitude* $f_{\text{eff}}(k, R)$ replacing $f(k)$ in Equation (4.10)*.

A second major development was the correct description of the amplitudes and phases for MS pathways in the framework of curved-wave theories [213, 223]. MS is known to be essential for the accurate calculations of $\mu(E)$ in most materials. In particular, MS by atoms along a linear path (see Figure 4.5) can exceed the magnitude of SS, which is known as the so-called *focusing* and *shadowing effect* [222]. The additional development of a fast path-generation, -sorting and -filtering algorithm by Zabinsky *et al* [224] (implemented in the FEFF code), made accurate, high-order, MS calculations of EXAFS (and also XANES) in general materials routine.

* $f_{\text{eff}}(k, R)$ gives the name to the XAS program FEFF developed by the same authors [213].

Yet another key development came with the replacement of the phenomenological mean free path term $e^{-2R_\gamma/\lambda_{\text{tot}}(k)}$ by *ab initio* theoretical calculations of inelastic losses based on the complex, energy-dependent self-energy of Hedin and Lundqvist [225], which gives rise to both a real energy shift and a decay. The *Hedin-Lundqvist exchange model* is generally reliable for the EXAFS region, but leads to excessive loss (too much damping) in the XANES regime. Further improvements of the self-energy models for XANES are discussed in Section 4.4.4.

The basic theoretical ingredients used to calculate the amplitudes and phases for EXAFS, such as the muffin-tin scattering potentials and self-consistency, are described in Section 4.4 in the context of XANES spectroscopy.

4.3 EXAFS data analysis methods

On the basis of Equation (4.10) and its key elements described in the previous Section, EXAFS is conceptually simple. However, for many experiments in order to extract information, the most optimal experimental conditions must be realized and a complete theoretical treatment needs to be considered. A thorough theoretical understanding of data analysis is therefore a prerequisite for deriving meaningful structural parameters. The experimental conditions for obtaining distortion-free EXAFS spectra are described in Section 5.3. In the present Section we discuss the analysis of EXAFS data. The procedures are divided into two parts. First is the data processing that reduces the raw data to normalized EXAFS data $\chi(k)$ that can then be interpreted according to the standard theoretical formulations (Equation (4.10)). The various steps of this data reduction are described in Section 4.3.1. Second, the data are analyzed to extract the parameters of interest. This step involves Fourier transforming, filtering, weighting and single- and multiple-shell fitting, as described in Section 4.3.2.

4.3.1 Data reduction procedures

In this Section we present the steps necessary to reduce the raw data ($I_T(E)$, $I_F(E)$ and $I_0(E)$) obtained from the experiment to normalized EXAFS data, $\chi(k)$, suitable for quantitative analysis. The whole data reduction sequence is summarized in Figure 4.6 (the case of transmission is shown, but essentially the same procedures are applied for fluorescence data). The sequence of steps presented is not mandatory and there are different ways to perform the data reduction which can be found in the literature [68, 206]. The steps described in the following are the ones that were performed on the EXAFS data of PtPOP (Section 5.3) using the program ATHENA written by B. Ravel [226].

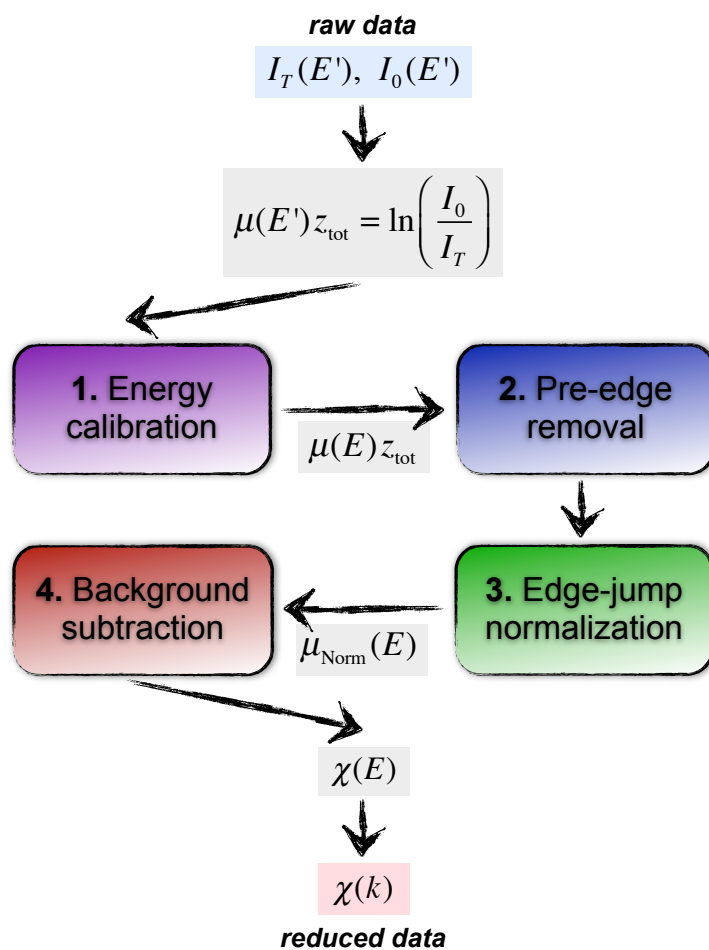


Figure 4.6: Flow chart illustrating the various steps in the data reduction procedure (see text). E' and E are the uncalibrated and calibrated energy axes, respectively. The first step uses Lambert-Beer law of Equation (4.5) and the last step involves a coordinate transformation using Equation (4.9).

1. **Energy calibration:** In principle the EXAFS technique is insensitive to the absolute calibration of the energy, as the edge position E_0 is later optimized in the fit procedure. However, knowledge of the absolute edge position of an element embedded in a compound compared to the pure element, the so-called *chemical shift*, is often useful to extract chemical information about the system. For example, the Pt absorption edges of a sample containing Pt(II) will be shifted to higher energy (by 1-2 eV) compared to a Pt(0) compound, *e.g.* a Pt foil. If the oxidation state of a particular element is not known *a priori*, this can be determined by comparing the edge positions with known compounds. It is therefore common to calibrate the energy axis by measuring the spectrum of a pure material for which the edge positions are tabulated.

2. **Pre-edge background removal:** In analyzing the EXAFS spectrum, we are only interested in the spectrum region after (or just before) the edge jump. The part of the spectrum before the edge jump contains absorption contributions from lower-energy absorption edges, scattering and other processes that are usually not of interest. The slope of the absorption coefficient in the pre-edge region approximately follows a $1/E^3$ dependence (Section 4.1.1), but the exact shape is not known because it can also be influenced by non-linearities in the X-ray flux detection. In order to remove these background contributions one therefore usually fits a linear or quadratic polynomial function to the pre-edge region which is then extrapolated to all energies in the measurement range of the data and subtracted from $\mu(E)$. The pre-edge background removal step is not mandatory, but largely cosmetic and practical, for example in the comparison of edges of different compounds.

3. **Edge-jump normalization:** Normalization is the process of regularizing the experimental data with respect to variations in sample preparation, sample thickness, absorber concentration, detector and amplifier settings *etc.* Normalization is a prerequisite for the comparison with theory; μ and χ computed by FEFF are meant to be compared to normalized data only. The relation between $\mu(E)$ and $\chi(E)$ is given in Equation (4.8) (see also later Equation (4.16)). However, this is usually not the equation that is used to extract χ in data analysis. In practice, one cannot trust the $\mu_0(E)$ function to be sufficiently well behaved that it can be used as a multiplicative factor. In addition, $\mu_0(E)$ is in general neither measurable independently, nor can it be calculated accurately. One therefore commonly avoids functional normalization and instead performs *edge-jump normalization* by dividing by an energy-independent value $\Delta\mu_0(E_0)$, *i.e.* the edge jump. In order to evaluate $\Delta\mu_0(E_0)$, a post-edge polynomial is fitted and extrapolated to E_0 . $\Delta\mu_0(E_0)$ is then the difference between the pre- and post-edge functions at this energy. The E_0 energy is at this stage arbitrary, although it should lie reasonably close to the real IP of the system. The error that is made by normalizing to $\Delta\mu_0(E_0)$ instead of $\mu_0(E)$ is incorporated as an attenuation in $\chi(E)$, which introduces an artificial DW (σ^2) term that adds to whatever thermal or static disorder exists in the data[†].

4. **Background subtraction:** The background subtraction procedure is the final (most important) step in isolating the fine-structure oscillations. In contrast to the normalization step described above, in this case we need to take into account the

[†]The error in the approximation can be accounted for by a small (typically about 10%) correction to the DW factor, which is called the McMaster correction [68]

energy dependence of μ_0 . This complicates matter, as the "real" smoothly varying $\mu_0(E)$ function, the background absorption of a hypothetic free atom embedded in the Coulomb potential of the surrounding atoms, is not known. Various ways to approximate the background function have emerged in the literature [68]. One could, for instance, use the $\mu_0(E)$ calculated from first principles by FEFF (vs. 8 and 9). The ATHENA program uses an iterative background removal scheme (AUTOBK [227]) by making use of Fourier theory and the fact that $\mu_0(E)$ mainly contains low-frequency components. The basic idea of the method is: (a) fit a piece-wise spline to the data (typically using 2-6 spline knots); (b) subtract the spline from the $\mu(E)$ data; (c) Fourier transform the resulting fine structure; (d) analyze the low-frequency components. AUTOBK performs these steps iteratively, *i.e.* it varies the parameters of the spline such that, when the spline is subtracted, what is left has its low-frequency Fourier components minimized below a certain cut-off distance that is smaller than the 1st-shell distance (see next Section). Despite the automation of the iterative procedure, the program offers many ways for the user to affect the outcome of the background removal, such as the spline parameters, the cut-off distance and a k -weight for the Fourier transform [226]. It is however beyond the scope of this work to describe all these parameters. Most important is that one realizes that the background removal is not trivial and extreme care should be taken in order to avoid significant distortions of the χ data.

4.3.2 Structural analysis

The beauty of the formulation of EXAFS according to Equation (4.10) is that a simple Fourier transform (FT) of χ with respect to k gives direct access to the structural parameters of interest (R -space). By definition the Fourier transform performs a spectral analysis of the oscillations contained in $\chi(k)$. Because the fine structure corresponding to different coordination shells oscillates at different frequencies (through the $\sin(2kR_\gamma)$ term in Equation (4.10)), Fourier transformation spectrally isolates these different contributions in the form of an effective radial distribution function. However, the other k -dependent parameters, $f_{\text{eff}}(k)$, $\phi(k)$, $\lambda(k)$ (or $\Sigma(k)$), shift the peaks in R -space away from the real interatomic distances. In fact, the amplitudes and phases for heavy atoms with $Z > 40 - 50$ are complicated (structured) functions of k . In order to extract the structural information from the data, these parameters must therefore be obtained independently either by using experimental or (preferably) theoretical standards [228]. The latter method enables the determination of interatomic distances with an accuracy of ~ 0.02 Å thanks to the tremen-

dous progress made in the *ab initio* computation of inelastic losses, scattering amplitudes and phases [213].

In an ideal case, the peaks in R -space belonging to each shell are sufficiently well separated that they can be analyzed on a shell-by-shell basis. Multiplying the isolated peak by a so-called *windowing function* centered at the peak position in R -space and subsequent inverse Fourier transforming, allows one to obtain the structural parameters of a single shell only. However, this procedure is not generally applicable. Complications arise due to: (1) the finite data range and accompanying truncation effects of the Fourier transform; (2) overlapping scattering peaks in R -space. The former can be reduced by appropriate windowing and weighting methods, while the latter can be overcome by applying multiple-shell fitting procedures.

Windowing and k -weighting

Prior to the forward-FT, the $\chi(k)$ data are multiplied by a rectangular windowing function used to select the data that should be kept for further analysis. First, this allows to eliminate the low- k region ($< 3 \text{ \AA}^{-1}$) which is less reliable due to non-structural XANES effects and insufficient background elimination. Second, the high- k part of the spectrum usually exhibits low signal-to-noise (S/N) ratios, and the windowing function can be used to reduce the noise level by cutting the data before it gets too noisy. However, due to the high frequencies contained within the sharp edges of the window function, truncation effects appear after Fourier transforming. For a purely rectangular windowing function, the untruncated data in R -space is effectively convoluted with a sinc-function (the FT of a rectangle) giving rise to truncation ripples. These ripples can be reduced by smoothing the edges of the window (*i.e.* reducing the higher frequencies), on the expense of slightly broader peaks in R -space. The Hanning function (flattened in the middle) is one such smoothed windowing function [68].

Another type of windowing (or modifying) the data prior to the FT, is weighting the $\chi(k)$ spectrum by a factor k^n , where $n = 1 - 3$. The choice of the power of weighting should be to give a roughly equilibrated amplitude of the weighted data over the range of data to be transformed. Truncation effects are minimized in this way. Because of the different k -dependences of the scattering amplitude for different Z (the lower Z , the faster drops the amplitude with increasing electron energy), the optimal weighting also depends on the mass of the backscatterers. By comparing the Fourier transformed data for differently k -weighted data (*e.g.* k vs. k^3), the Z -dependence of the scattering amplitude can be exploited to identify whether different shells contain high- or low- Z elements. In

addition, simultaneous fitting of differently k -weighted data can help breaking up the interdependencies (correlations) between the fit parameters.

Fitting procedures

The shell-by-shell inverse-FT method can not be generally applied since, in many cases, two or more shells interfere with each other. This interference might not be visible at first sight, as the apparent amplitude where the two peaks are overlapping may be reduced. This often appears as a sharp minimum giving rise to asymmetrical peak shapes. Very large errors may ensue if one tries to separate and back-transform two such shells independently. In such cases it is highly preferable to use a fitting approach for both shells simultaneously. This becomes particularly useful in the case of MS pathways which are often overlapping with SS paths of similar distance.

Multiple-shell fitting procedures using the parameterization Equation (4.10) are nowadays routinely applied in EXAFS analysis. Many fitting programs have emerged: IFEFFIT [229], ARTEMIS (GUI based on IFEFFIT) [226], GNXAS [230], WINXAS [231], EXCURVE [232] *etc.* The following description is valid for the ARTEMIS program and IFEFFIT (both based on the FEFF code), which have been used for the analysis of the steady-state and time-resolved EXAFS data of PtPOP. The IFEFFIT functionality can also be exploited using the program DEMETER developed by B. Ravel [233], which is essentially a Perl programming tool for creating IFEFFIT applications, providing a flexible, user-defined framework for EXAFS fitting. This tool is potentially very useful for the analysis of time-resolved (transient) EXAFS data, as described in Section 8.3.

Generally for each scattering path γ , the parameters N_γ , $f_{\text{eff}}(k)$, $\phi(k)$, $\lambda(k)$, σ_γ , R_γ , S_0^2 and E_0 must be optimized or entered as input data. If the type of atoms surrounding the absorbing atom are known, N_γ is fixed by the input structure. Typically, E_0 and $S_0^2 \simeq 0.9$ (the energy-dependence is neglected) are taken as global fitting parameters, *i.e.* they are optimized for all scattering paths simultaneously, while the structural parameters R_γ and σ_γ are optimized for each path individually (in fact $\Delta R_\gamma = R_\gamma - R_\gamma^0$ is optimized, see below). In some cases, paths involving different atom types need different E_0 values. The other parameters are calculated from first principles using FEFF (embedded in ARTEMIS). The fitting program needs to be supplied with an input structure in the form of (x, y, z) -coordinates and atom types. This input model should be reasonably close to the real structure. The scattering paths are then sorted according to their initial half-path distance R_γ^0 and they can be selected for inclusion in the fit based on their overall scattering amplitude.

Fitting can be either done in k -space or R -space, with no conceptual difference between the two methods. The latter is usually preferred due to the close connection with the scattering path formalism and the avoidance of systematic errors caused by the inverse FT. The IFEFFIT program performs the fit by minimizing the *chi-square function* [234]

$$\chi^2 = \frac{N_{\text{indp}}}{N_{\text{pts}} \epsilon^2} \sum_i^{N_{\text{pts}}} \{ [\text{Re}(\tilde{\chi}_{\text{data}} - \tilde{\chi}_{\text{theo}})]^2 + [\text{Im}(\tilde{\chi}_{\text{data}} - \tilde{\chi}_{\text{theo}})]^2 \} \quad , \quad (4.12)$$

where $\tilde{\chi}_{\text{data}}$ and $\tilde{\chi}_{\text{theo}}$ are the complex Fourier transforms of the experimental and theoretical $\chi(k)$ signals, respectively.[‡] N_{pts} is the number of points in the fitting range of the data and ϵ represents the measurement uncertainty which is calculated automatically from the high- R region and is assumed to be the same for every data point. Finally, N_{indp} is the number of independent data points in the measurement which is a measure of the information content of the data. Although the points of $\mu(E)$ are all independent measurements of absorption, they are not independent measurements of the atomic distribution function, which is what we are interested in when analyzing data. In IFEFFIT, EXAFS data are treated as a bandwidth limited signal processing problem and the bandwidth is a function [235] of the Fourier transform range multiplied by the fitting range. Specifically, from basic information theory, the number of independent measurements in a spectrum is given by

$$N_{\text{indp}} = \frac{2\Delta k \Delta R}{\pi} + 1 \quad . \quad (4.13)$$

Using Bayesian methods, it can be shown [236] that the true information content of an EXAFS signal is 2/3 or less of the value from Equation (4.13). The number of fitting parameters should therefore never exceed the value 2/3 N_{indp} in order for the fitted values to be meaningful. Consequently, the number of scattering paths that are included in the fit can not be too high. This imposes a particular problem in the case of strongly overlapping scattering paths: the data range might not be large enough, *i.e.* the information content is not high enough, to extract structural information for each path individually. In the case of MS paths it is sometimes possible to express the distance parameter ΔR_{MS} in terms of SS path parameters ΔR_{SS} and bond angle changes. Furthermore, in order to reduce the number of fit parameter one could incorporate external data, such as DW factors or S_0^2 values obtained from EXAFS analyses on similar compounds.

χ^2 of Equation (4.12) is the primary figure-of-merit to characterize the goodness of the

[‡]The figure-of-merit χ^2 should not be confused with the fine structure function $\chi(k; E)$ or the figure-of-merit in XANES analysis χ_{Bayes}^2 (Section 4.6). In the following, the context should be clear enough that such confusion is not possible.

fit. There is a related figure-of-merit called *reduced chi-square*, denoted χ_ν^2 . This is equal to χ^2/ν , where $\nu = N_{\text{indp}} - N_{\text{par}}$ is the number of degrees of freedom in the fit (where N_{par} is the number of parameters in the fit). χ^2 and χ_ν^2 are useful for comparing the quality of different fits. The basic rule is that the fit with the lowest χ_ν^2 is the best. This comparison works even if two fits have different number of parameters. The criterion for assessing if a particular variable is useful in the fit is that χ_ν^2 will be lowered for useful variables. If adding a variable causes χ^2 to decrease but χ_ν^2 to increase, the fit is not improved. In the case that the errors are dominated by random fluctuations in the data (given by ϵ), a good fit should have $\chi_\nu^2 \sim 1$. However, in practice with good-quality data, this is rarely the case; usually χ_ν^2 is found to be more like 10 or 100. The most likely reasons for larger χ_ν^2 values are [234]: 1) the FEFF model is not a good representation of the data; 2) ϵ is a poor estimate of the measurement uncertainty of the data; or 3) the fit R -range does not reflect the paths specified in the fit. In most cases (good-quality data with evenly distributed noise), FEFF is poor enough that it will not match the data to within the measurement uncertainty. It should therefore always be kept in mind that theory is often a limiting factor in extracting quantitative information, not the data quality. This is certainly the case for the XANES spectrum, which will be discussed in the following Sections.

While χ_ν^2 is useful in comparing fits with different parameters, it is not clear whether a large value of χ_ν^2 is due to theoretical errors or whether the fit is truly bad. To provide an absolute measure of the goodness of a fit, the so-called \mathcal{R} -factor is useful. This number is directly proportional to χ^2 , and gives a sum-of-squares measure of the fractional misfit [234]. For good fits to carefully measured data on concentrated samples $\mathcal{R} \lesssim 0.02$ and $\chi_\nu^2 > 10$ are common. Such fits are clearly quite good, as the theory and data agree within a percent. But since the misfit is much larger than the random fluctuations in the measured data (typically < 0.01), we return to the conclusion that systematic (theoretical) errors dominate such fits.

For information on the method of calculating parameter uncertainties and correlations in FEFFIT, is referred to reference [234].

4.4 Theory of XANES spectroscopy

The XANES region of the XAS spectrum extending from below the IP to about 50 eV above an absorption edge is composed of many contributions of both structural and electronic nature. In contrast to the EXAFS region, for which accurate quantitative results are generally routine (see previous Sections), both the calculation and interpretation of XANES have remained challenging tasks. The complications arise from the low kinetic

energy of the photoelectron in this region resulting in large scattering amplitudes (and consequently multiple scattering events) and the necessity to adequately describe many-body effects. In addition, the photoelectron's energy is comparable to the fine details of the Coulomb potential which renders the **XANES** spectrum very sensitive to inaccuracies of the simplified model that is chosen to represent the atomic potentials. With the development of an efficient self-consistent, relativistic and full multiple scattering code (FEFF) by Rehr and coworkers [237], the theoretical errors in **XANES** calculations are largely reduced making a (semi-)quantitative interpretation of the spectral features possible. This is achieved in particular by the efficient many-pole representation of the system's dielectric function in order to account for intrinsic and extrinsic inelastic losses of the photoelectron [238] and the possibility to use full potentials instead of the simplified **muffin-tin (MT)** approximation [95].

In this Section the theory of **XANES** spectroscopy is described on the basis of the FEFF9 full multiple scattering code that has been applied to the case of **PtPOP** (see Chapters 7 and 8). Some of the theoretical ingredients described in this Section (*e.g.* Greens' function formalism and **MT** potentials) are also used in the theoretical treatment of **EXAFS**, implemented in earlier versions of FEFF (FEFF6, see previous Section).

4.4.1 One-electron golden-rule approximation

In general, **XAS**, in the single electron and dipole approximations, probes the probability of a dipole-mediated transition of a deep core electron $|i\rangle$ of the absorbing atom into some unoccupied state $|f\rangle$ above the Fermi level E_F . The measured X-ray absorption cross section $\mu(E)$ is described by *Fermi's golden rule* [209, 239]

$$\mu(E) \propto \sum_{f}^{E_f > E_F} |\langle f | \hat{\epsilon} \cdot \mathbf{r} | i \rangle|^2 \delta(E - E_f) \quad (4.14)$$

where $\hat{\epsilon} \cdot \mathbf{r}$ is the dipole operator of the incoming light and the sum is over all energies above the Fermi level. There are two general strategies for solving this equation in order to calculate the **XAS** spectrum [237, 240]. The first implies accurately expressing the deep core state $|i\rangle$ and final states $|f\rangle$ in terms of wave functions and then explicitly evaluating the sum of Equation (4.14). This is essentially the approach adopted by molecular orbital theories, but it is limited by the accurate description of the final state. This limitation is avoided by the second strategy adopted by FEFF9 for which Equation (4.14) is rewritten using a single-particle *Green's function* operator $G = [E - H]^{-1}$, where H is the effective one-electron Hamiltonian and E is the photoelectron energy, according to

$$\mu(E) \propto -\frac{2}{\pi} \int_{E_F}^{\infty} dE' \operatorname{Im} \langle i | \hat{\varepsilon} \cdot \mathbf{r}' G(\mathbf{r}', \mathbf{r}, E') \hat{\varepsilon} \cdot \mathbf{r} | i \rangle \frac{\Gamma_{\text{tot}}}{\pi[(E - E')^2 + \Gamma_{\text{tot}}^2]} \quad (4.15)$$

where Γ_{tot} is determined by the combined sum of the core-hole life time (Section 4.1.3) and experimental resolution [237]. The use of the Green's function formalism as a tool to avoid the explicit representation of final states is the basis of MS theory which originates in the 70s [241–243], originally developed for the EXAFS region.

The close connection between XAS and electronic structure is indicated by the similarity between the contribution μ_{li} to the XAS from a given site i and orbital angular momentum l and the electronic l -projected density of states (LDOS) ρ_{li} at site i [237],

$$\begin{aligned} \mu_{li}(E) &= \mu_{li}^{0'}(E)[1 + \chi'_{li}(E)] \\ \rho_{li}(E) &= \rho_{li}^0(E)[1 + \chi_{li}(E)] \end{aligned} \quad (4.16)$$

where $\mu_{li}^{0'}(E)$ and $\rho_{li}^0(E)$ are the smoothly varying atomic background contributions and χ_{li} is the fine structure or XAFS spectrum [237] (equivalent to μ_0 and χ of Section 4.2, Equation (4.8)). The density of states (DOS) is however usually calculated for the ground state without core hole, whereas the presence of a core hole (indicated by a prime in Equation (4.16)) and the inclusion of inelastic losses (via a self-energy) are very important in a XAS calculation. Indeed, the relation between XAS and DOS is mathematically given by the fact that the spatial and energy dependence of the electron DOS can be directly expressed in terms of the imaginary part of the same Green's function operator as is used in Equation (4.15) to calculate $\mu(E)$ [237].

FEFF9 is based on several key developments that increase the accuracy of the calculation compared to previous codes and which offer the possibility to interpret XANES either in terms of local electronic structure or within a XAFS-like scattering picture [237]: (1) the use of full multiple-scattering (FMS) cluster calculations of both XAS and DOS; (2) the use of self-consistent field (SCF) potentials (both of these developments are based on Green's function calculations); (3) *ab initio* calculations of many-body intrinsic and extrinsic inelastic losses of the photoelectron. These developments are described in the following.

4.4.2 Full multiple scattering

The one-particle Green's-function operator $G = [E - H]^{-1}$, with $H = H_0 + V_{\text{int}} + \delta V$ (H_0 is the free-electron Hamiltonian, V_{int} is a flat interstitial potential and δV are scattering

sites representing the ions in the material; *vide infra*), can be expressed in a propagator series by the *Dyson equation* $G = G^0 + G^0 T G^0$, where $G^0 = [E - H_0]^{-1}$ is the free-electron propagator, and $T = V + V G T$ is the full, atomic scattering matrix which can be expressed in single-site scattering matrices t by $T = t + t G^0 t + t G^0 t G^0 t + \dots$ [224]. By inserting the atomic scattering matrix expansion into the Dyson equation, one recognizes G as a Taylor expansion [237, 240]:

$$G = G^0 + G^0 t G^0 + G^0 t G^0 t G^0 + \dots \quad (4.17)$$

$$G = (1 - G^0 t)^{-1} G^0 \quad (4.18)$$

Physically spoken, G describes all possible ways that the photoelectron can scatter from one or more of the surrounding atoms before the core hole is refilled. G^0 describes how the photoelectron propagates between two sites and t describes how the photoelectron scatters from a particular atom. The terms of different order in Equation (4.17) then describe the different orders of scattering, *i.e.* $G^0 t G^0$ describes all single-scattering processes, the $G^0 t G^0 t G^0$ term includes all scattering paths that involve two surrounding atoms (for example the **MS** path denoted in Figure 4.5), *etc.*, under the constraints that one site is never scattered off twice and the photoelectron always returns to the absorbing atom. The first term G^0 in Equation (4.17) is related to the atomic-like background functions $\mu_{i_i}^0(E)$ and $\rho_{i_i}^0(E)$ in Equation (4.16), while the scattering terms $G^0 t G^0 + G^0 t G^0 t G^0 + \dots$ represent the fine structure functions χ_{i_i} . It is noted that the background function is not equivalent to the $\mu(E)$ of a hypothetical gas-phase atom, but it rather represents the absorption from a free atom *embedded* in the potential of the surrounding atoms.

Due to the low kinetic energy of the photoelectron in the **XANES** region, the scattering amplitudes are large and consequently the electron can propagate far while scattering off many atoms. In this case, the truncated path expansion of Equation (4.17) is not accurate enough and one has to consider higher order processes. Equation (4.17) summed up to infinity results in the exact representation of G shown in Equation (4.18) (via the definition of a Taylor expansion), which obviously contains all orders of scattering. Explicitly inverting the matrix $(1 - G^0 t)$ and multiplying by G^0 in order to calculate G is called the **FMS** technique which is appropriate for **XANES** calculations. This in contrast to the **EXAFS** region, for which an adequately truncated path expansion usually suffices.

The **FMS** calculation is usually performed on a subset, or cluster, of atoms surrounding the absorbing atom. The number of atoms included in the cluster as well as the number of angular momentum and magnetic quantum numbers required for each atom, determine

the size of the matrices G^0 and t and thus the required computation time. The maximum angular momentum l_{\max} that must be considered for convergence is given by the so-called *centrifugal barrier* $l_{\max} \simeq kR_{\text{MT}}$, where k is the photoelectron's wavenumber and R_{MT} is the **MT** radius (*vide infra*). These considerations impose limits on the cluster size and the region of the spectrum that can be accurately described by **FMS**. Practically, the cluster size is naturally limited due to the finite life time (or mean free path λ_{tot}) of the photoelectron which can typically sample only up to 10-20 Å around the absorbing atom. Because the complete calculation is performed in the (complex) energy plane (real space instead of k -space), the **FMS** calculation is not limited to bulk periodic systems. Aperiodic or disordered systems such as molecules in solution are treated on equal footing. For small solvated complexes the **FMS** cluster size would include simply every atom in the molecule.

4.4.3 Self-consistent field potentials

A **FEFF9** calculation starts with the **SCF** loop which is used to compute the electron density and scattering potential within the real-space **MS** framework [237]. The self-consistency allows to redistribute charge in the system in such a way that charge is transferred between atoms based on their chemical electron affinity (*i.e.*, oxidation state). In addition, the **SCF** calculation provides an accurate *ab initio* estimation of the Fermi energy, which is essential for the correct representation of the intensity of "white lines" (strong absorption features just above the Fermi level).

The **SCF** loop is initialized by the construction of a so-called muffin tin (**MT**) potential as an approximation to the real (full) potential. The **MT** potential is obtained by placing the free atoms at the positions specified by the input data. In this scheme, all atoms are treated as spheres and the radii of the spheres are decreased up to a certain level determined by the Norman criterion as described in reference [244], with excess charge placed into the flat interstitial region (V_{MT} , see Figure 4.7). The resulting shape, resembling a mold in which muffins are baked, gives the name to this potential type. In the next step of the **SCF** loop, the relativistic Dirac equation is solved for the above **MT** potentials to obtain photoelectron scattering amplitudes and phases. These quantities are used in turn to construct the Green's function given in Equations (4.17) and (4.18). As we have noted before, the Green function is related to the **DOS** via

$$\rho(\mathbf{r}, E) = -\frac{2}{\pi} \text{Im}[G(\mathbf{r}, \mathbf{r}, E)] \quad (4.19)$$

After spherical averaging, the space integration of $\rho(r, E)$ yields $\rho(E)$, the **DOS**. The

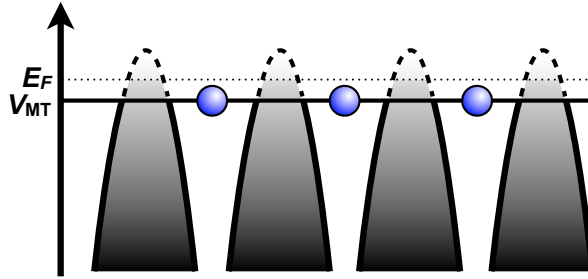


Figure 4.7: Schematic drawing of a one-dimensional **MT** potential. The solid horizontal line denotes the flat interstitial potential truncating the true shape of the potential (dashed line). The dotted line shows the Fermi level. (redrawn and adapted from reference [213])

Fermi level E_F is found iteratively by energy integration of the **DOS** until the total charge corresponds to the total number of electrons in the system. The energy integration of $\rho(r, E)$ in the complex plane up to E_F then gives the new total electron density $\rho(r)$, which is in turn used to calculate new scattering potentials and these steps are iterated to self-consistency [237, 240]. In parallel, the loop calculates a *local* Fermi energy and **DOS** at each atom position, where instead of the charge of each nucleus, the varying energy and space integrated density within the Norman sphere is used as an upper boundary for integration. In this way, charge is allowed to shuffle between Norman spheres until, if self-consistency is reached, the two densities with and without charge transfer are equal (the same for the Fermi energies) [237]. Usually 10 to 20 iterations are necessary to reach a precision in E_F of a fraction of an eV. The calculated charge transfer values are usually an order of magnitude smaller than the formal oxidation states of the ions.

After the **SCF** loop is finished, an energy-dependent self-energy $\Sigma(E)$ is added to the potential which accounts for the inelastic losses that the photoelectron experiences in the potential field of the surrounding atoms (described in the next Section).

4.4.4 Ab initio calculations of inelastic losses and core-hole screening

Many current theoretical efforts are directed towards the accurate *ab initio* calculation and modeling of intrinsic and extrinsic inelastic losses (see also Section 4.1.3). *Extrinsic* processes correspond to the inelastic scattering of the outgoing photoelectron, while *intrinsic* processes involve the relaxation and the excitation of the passive electrons due to the creation of the core hole [245]. Extrinsic losses are usually approximated using a single plasmon pole model for the photoelectron's self-energy $\Sigma(E)$ in the **Hedin-Lundqvist (HL)** framework [238]. This model is too "lossy" around the plasmon pole resonance energy, giving rise to an energy-dependent shift (via $\text{Re}\{\Sigma(E)\}$) and broadening (via $\text{Im}\{\Sigma(E)\}$) of the spectra. Intrinsic many-body effects (shake-up, shake-down) are often included

only phenomenologically by an energy independent multiplicative factor $S_0^2 \sim 1$, whereas in reality these processes affect the amplitudes differently across the spectrum.

The FEFF9 code [95] offers the possibility of calculating many-body intrinsic and extrinsic inelastic losses from first principles. System-dependent self-energies and mean-free paths, as well as intrinsic losses due to multielectron excitations (S_0^2), are calculated from the dielectric response of the system [95], which is provided as an input to the program. Instead of a single plasmon pole (HL) model, a system-specific multi-pole model is used to represent the loss spectrum given by the imaginary part of the inverse dielectric function [238]. The multi-pole model results in a smoothly varying loss spectrum that represents a more realistic self-energy at low energies compared to the single-pole model. As a consequence, via $\text{Re}\{\Sigma(E)\}$, the energy positions of the MS features show better agreement with experiment. As the positions of the features are directly related to the geometric structure of the chemical system (Natoli's rule [246]), their correct *ab initio* calculation is an important prerequisite to extract quantitative structural information from the XANES spectrum.

Of equal importance as the accurate calculation of inelastic parameters is the application of the correct screening model. Core-hole screening (*i.e.* the redistribution of valence electrons after the creation of the core hole partially filling up the hole) affects charge counts and charge transfer as well as the position of the Fermi energy. The accurate computation of the latter is especially important to correctly reproduce white-line intensities at *L*-edges. In the case of PtPOP (Chapter 7) we consider two models of core-hole screening, SCF screening and random-phase approximation (RPA) screening [247], as well as the case without core-hole screening using the ground-state potentials.

4.5 The modular structure of the FEFF9 program for XANES analysis

The FEFF program has a modular structure allowing the user to run certain parts of the calculation separately from others [248]. The input to the program is contained in a single file, the `feff.inp` file, which contains necessary and optional control cards as well as the input structure in the form of x, y, z -coordinates. The different modules are controlled by the CONTROL card followed by a 1 (on) or 0 (off) for each module. The PRINT card specifies at which stage of the calculation the intermediate output files are written out.

Below follows a short description of the modules and the most important control cards

that are used for **XANES** calculations of molecules.[§] The complete `feff.inp` file that is used for the FEFF9 **XANES** calculations of **PtPOP** is given in Appendix B.

- **Module 0:** RDINP - Read input

Reads the `feff.inp` file, makes appropriate operations on the data, and writes the resulting information into several output files, which contain formatted data needed for all following modules. In case the `EGRID` card is given (followed by a file `grid.inp` containing the relative energies), the program recognizes the specified energy grid that is used later in the calculation to generate the **XAS** spectrum at user-defined energy positions.

- **Module 1:** POT - Generate scattering potentials

This can be considered as the most important module. The `POTENTIALS` card contains the list of atom types which are uniquely labeled followed by the l_{\max} values for the **SCF** and **FMS** calculations to limit the angular momentum basis set. Heavy elements, *e.g.* Pt, generally require $l_{\max} = 3$ and $l_{\max} = 4$ for the **SCF** and **FMS** calculations respectively, while lighter elements only need $l_{\max} = 1$ or 2. The **MT** potential is created according to the positions of the atoms as specified in the `ATOMS` list.

The control card `SCF rfms1 lfms1` tells the program to calculate the potentials self-consistently by successively calculating the density of states, electron density and Fermi level at each stage within a small cluster and then iterating. The first argument specifies the radius of the cluster for **FMS** calculations within the **SCF** loop. The second argument specifies whether the system is a molecule (1) or a solid (0).

The `EXCHANGE ixc vr0 vi0` card is used to control the exchange correlation potential (self-energy) of the photoelectron which is used to calculate $\mu_0(E)$ and $\chi'(E)$ (see Equation (4.16)). The first argument `ixc` is used to specify which correlation potential is used (default is the **HL** potential, but this is overwritten by the presence of the `PLASMON` card). The calculated potential can be corrected by adding a constant shift to the Fermi level given by the second argument `vr0` and to a pure imaginary "optical" potential (*i.e.* a uniform decay) given by the third argument `vi0`.

The `NOHOLE` card will cause FEFF to calculate potentials and phase shifts as if there

[§]This is not meant to be a complete description of how to setup a FEFF calculation (for this see reference [248])

is no core-hole, *i.e.* it simulates the effect of complete core-hole screening. For d-DOS and L_{II} or L_{III} absorption calculations, NOHOLE often gives better agreement for white-line intensities than the default core-hole calculation (see later for the case of PtPOP).

- **Module 2: LDOS** - Calculate the l -projected density of states
The LDOS `emin emax eimag` card tells the program to calculate the local l -projected density of states over the energy range `emin` to `emax` in steps of `eimag`. The LDOS calculation uses the output from the POT module.
- **Module 3: XSPH** - Calculate cross-section and phase shifts
Within this module the scattering phase shifts are calculated. The XANES card is used if a XANES calculation is desired.
- **Module 4: FMS** - Calculate full multiple scattering for XANES
This module carries out a FMS XANES calculation for a cluster centered on the absorbing atom if the FMS `rfms` card appears in the input file. Thus all MS paths within this cluster are summed to infinite order by matrix inversion (Equation (4.18)). `rfms` specifies the cluster radius for FMS calculations, typically 6 Å. FMS loses accuracy beyond $k = l_{\max}/R_{\text{MT}}$, *i.e.* 3 to 4 Å⁻¹.
- **Module 5: PATHS** - Path enumeration
This module is not of particular importance for XANES calculations, because usually the FMS cluster can be chosen of appropriate size so that the path list is complete, *i.e.* the calculation has converged with respect to the cluster size. In specific cases a path expansion can be used for important MS paths outside the cluster.
- **Module 6: GENFMT** - Calculate scattering amplitudes and other XAFS parameters
For each path the code calculates the effective scattering amplitude ($f_{\text{eff}}(k, R)$, from which FEFF gets its name) and the total scattering phase shift along with other XAFS parameters using the scattering matrix algorithm of Rehr and Albers [223].
- **Module 7: FF2CHI** - Calculate specified X-ray spectrum
This module constructs the XAS spectrum $\chi(E)$ (`chi.dat`) or $\mu(E)$ (`xmu.dat`) using the XAFS parameters calculated in Module 6. If the S02CONV card is given, the single-particle XAS files are convoluted with a many-body spectral function (derived from the system-specific dielectric response) to include many-body effects in the spectra via an energy-dependent amplitude factor S_0^2 .

4.6 Bayesian fitting approach to XANES analysis

The goal of XAS analysis is to extract quantitative information about the local structure, vibrational amplitudes, coordination numbers *etc.* As described in Section 4.3, this has become common routine for EXAFS analysis using standard least-squares fitting algorithms (*e.g.* FEFFIT). The least-squares fitting routine has also been applied to the XANES region using the MXAN package [98, 249]. However, there are several problems with the least-squares approach [97]: (1) It is not obvious *a priori* which and how many fitting parameters should be included in the procedure; (2) The effects of systematic errors both in theory and experiment are not easily taken into account; (3) Large correlations between fitting parameters might occur, leading to large error bars without the imposition of constraints.

An alternative method based on the Bayes-Turchin approach has been developed by Rehr *et al* [97] in order to address the above difficulties in fitting XANES spectra. This approach has been successfully applied to the model-independent analysis of the EXAFS spectrum of bulk metals [250]. Extending it to the XANES region is important, *e.g.* in the analysis of biostructures such as metalloproteins, as this part of the spectrum exhibits high signal-to-noise ratios. The Bayes-Turchin method has several advantages over traditional data-analysis procedures [97]. First, there is no restriction on the size of the model parameter space by making use of Bayes' theorem. Even for many input parameters, a stable set of linear equations is obtained by imposing restraints based on *a priori* estimates of the parameter values and their errors. In addition, the method naturally divides the parameter space into important and irrelevant subsets. Only the former are affected by the fit, while the latter stay at their *a priori* estimate values. Because a simple analytical structural parameterization such as given by the EXAFS equation (4.10) can not be formulated for the XANES region (in the FMS framework, see Section 4.4.1), fitting structural parameters from XANES requires full MS calculations for every new parameter value. Fast parallel computing algorithms are necessary to achieve this, which have been developed for FEFF [251].

As discussed in Section 4.4.1, MS theory permits a natural analysis of X-ray absorption μ in terms of an atomic background μ_0 and fine structure χ through the relation $\mu = \mu_0(1 + \chi)$. In order to correct in an *ad hoc* manner for theoretical errors such that a quantitative structural analysis of the MS signal χ is possible, the FEFF9 Bayesian fitting program can be applied to μ_0 separately. The atomic background is fitted according to the Bayesian smoothing spline method [252] in which a correction $\delta\mu^0(E)$ is added to an *a priori* background absorption obtained from FEFF, *i.e.* with a small set of spline

parameters $\delta\mu_1^0, \delta\mu_2^0, \dots, \delta\mu_T^0$, where T is typically 3–5. The spline parameters are placed on an exponential, linear or user-defined grid and optimized in a fitting procedure in order to minimize the discrepancy between the theoretical $\mu = [\mu^0(E) + \delta\mu^0(E)][1 + \chi(E)]$ and experimental XANES spectra. In order to avoid correlations with structural parameters (affecting the fine structure χ), one should not use too many spline parameters, *i.e.* the fitted μ_0 should be a smooth, non-oscillating function. The fitting program can also be used to optimize structural and electronic parameters such as the x, y, z -coordinates of the atoms (according to a certain distortion model), the squared DW factor σ^2 (one factor for the whole XANES region) and the Fermi energy E_F [97, 253].

The Bayesian fitting program takes advantage of *a priori* estimates of the model parameters \vec{x} and their uncertainties which are provided in the input file (`ifeffit.inp`). The optimization in parameter space is achieved by minimization of the function [97]

$$\chi_{\text{Bayes}}^2 = \sum_i^{\text{all data points}} \left[\frac{\mu(\vec{x})_i^{\text{theo}} - \mu_i^{\text{exp}}}{\Delta\mu_i} \right]^2 + \vec{x} \mathbf{A} \vec{x} \quad , \quad (4.20)$$

where $\Delta\mu_i$ denotes the experimental error at each data point i and \mathbf{A} is the inverse cross-correlation matrix containing the *a priori* uncertainties (diagonal) and correlations (off-diagonal). A typical (annotated) input file for the XANES fitting program is given in Appendix D. It is used in Section 7.2 to optimize the atomic background, the overall energy shift E_0 , the Fermi energy E_F , the overall DW factor σ^2 and the Pt–ligand distance for PtPOP. The commands and notations are similar to the ones used in the FEFFIT program.

4.7 Challenges in calculating XANES spectra

The goal in the development of a computer code such as FEFF is to reduce the number of *ad hoc* parameters that are necessary for good agreement between theory and experiment [254]. The present version 9.03 of FEFF is *ab initio*, *i.e.* the parameters are calculated from first principles and the only input from the user is the list of atomic coordinates and, if desired, the dielectric function of the system. However, at this stage, the theoretical errors are often too large for a quantitative (fitting) analysis of the experimental data using, for example, the fitting program described above. The calculation of SCF potentials instead of overlapped MT potentials has been a tremendous improvement, also in the accuracy of the calculation of the Fermi level, typically with a precision of 1 eV. The remaining theoretical difficulties that limit the accuracy of the calculation are the following:

- Non-MT effects play a large role for energies just above the IP because in this

region the energy of the photoelectron become comparable to the fine deviations of the interstitial **MT** potentials compared to the real (full) potential (see Figure 4.7). The **MT** approximation is not inherent to the real-space **MS** technique. Extension to full potentials is possible, although mathematically challenging, because it is much more convenient to work with spherical symmetry. Version 9 of FEFF can deal with full potentials that are provided to the program [95]. However, these calculations are not routine and convergence might fail for specific systems.

- Inaccuracies in the calculation of the energy-dependent self-energy $\Sigma(E)$ have similar impact on the spectrum as non-**MT** effects. The generally used **HL** correlation potential is based on the single plasmon pole model, *i.e.* the losses are "turned on" after the photoelectron's energy exceeds a certain plasmon resonance. As discussed above, this model is too lossy around the plasmon pole resonance energy, resulting in inaccurate peak positions and too much damping in the spectrum. Version 9 of FEFF offers the possibility to incorporate more realistic self-energies that are externally calculated from the system-specific dielectric function [238]. However, due to the complex nature of many-body inelastic effects, an accurate theoretical representation remains challenging.
- A better description of particle-hole interactions (corrections to the final-state rule) is necessary.
- The **LDOS** is broadened due to the finite cluster size, core-hole lifetime and non-**MT** effects. Therefore, the **LDOS** calculated by FEFF does not exhibit the high level of detail as for example the **DOS** calculated by band structure methods.

4.7.1 XANES calculations of electronically excited molecules in solution

Besides the difficulties described above, there are several challenges to deal with specifically in calculating **XANES** spectra of excited molecules in solution:

1. Solution phase. For small molecules in solution outer-sphere effects can play a role. The flat **MT** potential outside the molecule is a bad approximation for solvated molecules, as the real potential outside the molecule increases. This leads to a broadening of the unoccupied molecular orbitals above E_F and a less accurate calculation of the **IP** due to a too low interstitial energy.
2. Changes in the electron occupancy in the **excited state (ES)**. There is presently no way to enforce the electron occupancy of the excited state while still taking into ac-

count charge transfer within the **SCF** framework. This is related to the full potential problem mentioned above: the **MT** potentials do not exhibit the level of detail that is necessary to differentiate between ground and excited state configurations. In some cases the different e -occupancy in the **ES** can be simulated by shifting the Fermi energy to lower values (by using the real part of the **HL** self-energy controlled via the **EXCHANGE** card), but in more complicated cases, at L -edges for instance, where the **ES** e -configuration invokes different d-state occupancies than in the ground state, the **MS MT** approach is expected to fail for energies just above the **IP**.

3. Open systems. The spherical averaging around each atom is not well justified for systems with a cavity-like structure. This might play a role in **PtPOP**, as the four bridging ligands form a cage with open space between the two Pt atoms.

4.8 Summary

X-rays are either scattered or absorbed by matter. The latter process can be used as a valuable probe of the structure of matter, constituting the field of **XAS**. The X-ray absorption spectrum of a particular element embedded in a chemical system is characterized by a steadily decaying absorption coefficient intermittently interrupted by sudden jumps at characteristic energies known as X-ray absorption edges. These edges usually show a superimposed modulation of the absorption coefficient. This fine structure contains a wealth of information. In general, the X-ray absorption spectrum is divided into two regions: the **XANES** spectrum consisting of the low-energy fine structure up to ~ 50 eV above the **IP**, and the **EXAFS** spectrum which corresponds to the high-energy $\gtrsim 50$ eV region.

EXAFS can be seen as being the result of quantum-mechanical interference between the outgoing photoelectron wave (generated after X-ray absorption) and incoming waves scattered off the surrounding atoms. Quantitative information is readily extracted by means of the phenomenological **EXAFS** equation for the fine-structure function $\chi(E) = \mu(E) - \mu_0(E)/\Delta\mu_0(E_0)$. *Ab initio* calculations are used to obtain the inelastic losses experienced by the photoelectron, as well as backscattering amplitudes and phases. The other parameters contained in the **EXAFS** equation can be fitted to the experimental data. Structural information is directly obtained by Fourier transforming the **EXAFS** signal $\chi(k)$ and applying fitting procedures to optimize the structural parameters (interatomic distances, **DW** factors) for many single- and multiple-scattering pathways simultaneously.

The **XANES** region is less straight-forward to analyze compared to the **EXAFS** spectrum. This is due to the low kinetic energy of the photoelectron in this region resulting in large scattering amplitudes (and consequently multiple scattering events) and the necessity to adequately describe intrinsic and extrinsic inelastic losses. The low kinetic energy also makes the spectrum very sensitive to the details of the atomic potentials. Nevertheless, progress is made in the calculation of **XANES** spectra so that (semi-)quantitative information can be extracted from **XANES**. The theoretical code used to calculate **XANES** spectra in the present study is the FEFF9 code. The theoretical framework behind FEFF is based on the real-space Green's function approach for which explicit calculation of final states is avoided by expressing the Fermi Golden rule in terms of a single-particle Green's function in the presence of an appropriately screened core-hole ("final state rule"). **XANES** can be interpreted either in terms of local electronic structure or within a XAFS-like scattering picture. This is possible due to two theoretical key ingredients in FEFF: (1) the implementation of full multiple-scattering cluster calculations of both **XAS** and the density of states, and (2) the use of self-consistent field potentials. In addition, an efficient system-specific many-pole representation of the photoelectron's self-energy provides a more realistic representation of inelastic losses resulting in better agreement between experimental and theoretical peak positions and amplitudes in the **XANES** region.

Chapter 5

Experimental methods

This Chapter provides the experimental details of the measurements performed in this thesis. The X-ray absorption experiments were conducted at the Swiss Light Source, which is introduced in Section 5.1. In Section 5.2 we describe a flow-capillary sample holder that was designed for the time-resolved XAS experiments. The steady-state XAS setup and the signals for the two modes of XAS detection (transmission and fluorescence) are given in Section 5.3. In Section 5.4 we describe in detail the time-resolved XAS setup, the experimental pump-probe XAS signals and the difficulties in describing the laser excitation process and deriving the fraction of excited molecules.

5.1 Synchrotron radiation

In the early days after the discovery of X-ray radiation, the applicability and accuracy of X-ray methods was mainly limited by the brilliance* of the source. Starting off with low-flux conventional X-ray tubes and rotating anode sources in the first half of the 20th century, it was realized in the 1970s that the synchrotron radiation emitted from charged particles circulating in storage rings was potentially a much more intense and versatile source of X-rays. The further development of early storage rings has culminated to date in the so-called 3rd-generation synchrotron sources, which are a factor of approximately 10^{12} times brighter than the early lab-based sources. Since then, synchrotron radiation has become an indispensable tool in X-ray science, encompassing the research fields of structural biology, material science, chemical analysis, nanotechnology, condensed matter physics and many more. With the recent development of X-ray free electron lasers, the source brilliance can be further increased by orders of magnitudes, opening yet new doorways to unraveling the structure of matter and its ultrafast dynamics.

Figure 5.1 shows a schematic drawing of a typical beam line (experimental area) at

*Brilliance is defined as Photons/s/(mrad)²/(mm² source area)/(0.1% energy bandwidth).

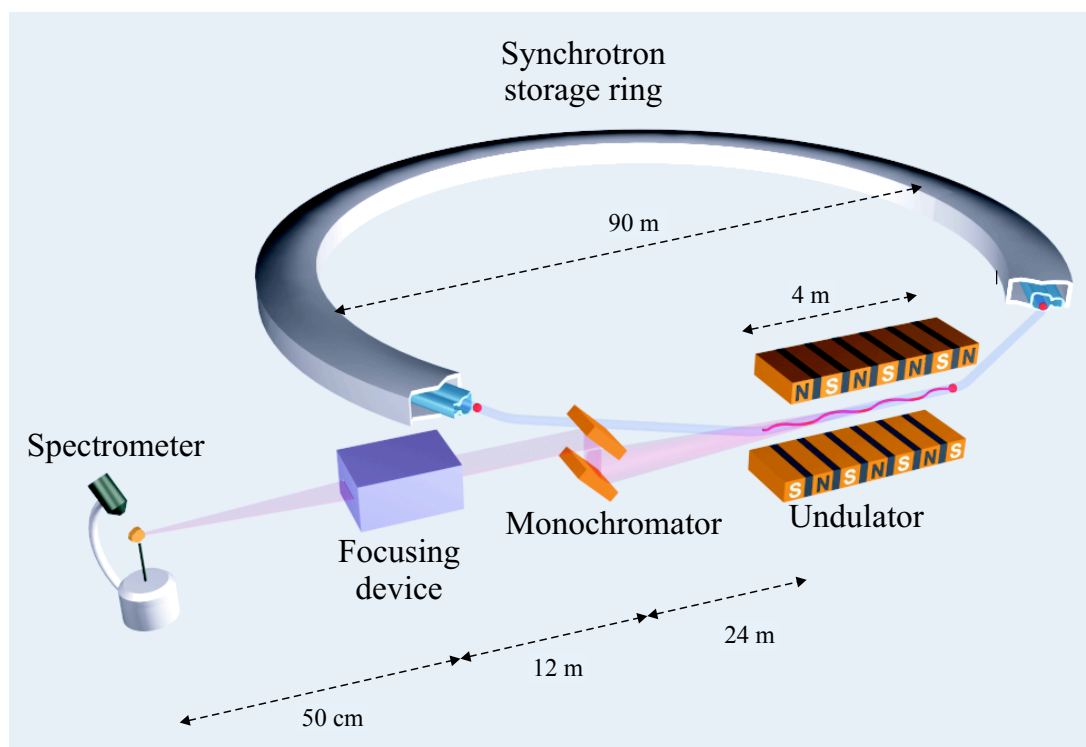


Figure 5.1: Schematic drawing of the key components of a typical beam line at a 3rd-generation synchrotron X-ray source. The distances are typical for the microXAS beam line at the SLS. The magnetic north (N) and south (S) poles of an undulator force the electrons to follow an oscillating path. This makes the electrons to emit synchrotron light, ranging from the infrared to hard X-rays. Taken and modified from Als-Nielsen and McMorrow [204].

a 3rd-generation synchrotron source [204]. Bunches of electrons circulate in the vacuum tube of the storage ring at nearly the speed of light. X-rays are produced by two main components in the ring lattice: 1) *bend magnets* needed to keep the electrons in a closed orbit, and 2) *insertion devices* situated in the straight sections of the storage ring. The latter are subdivided in *wigglers* and *undulators*. In these devices, magnetic fields perpendicular to the horizontal orbit plane force the electrons to follow a bent or oscillating path rather than a straight line. This change in the direction of the velocity (*i.e.* acceleration) causes the electrons to emit electromagnetic radiation (light). The energy of the emitted radiation covers a wide spectral range extending from the far infrared to the hard X-ray region ($<1 \text{ \AA}$). A specific energy (in this thesis, hard X-rays of $\sim 12 \text{ keV}$) is selected by passing the X-ray beam through a monochromator with a typical energy resolution of $\Delta E/E = 1.4 \cdot 10^{-4}$ (Si(111) crystals) and the divergence of the beam is adjusted by using mirrors and slits (see Figure 5.1).

5.1.1 The Swiss Light Source

The XAS experiments in this thesis were performed at the microXAS/FEMTO beam line [255] at the SLS [256, 257], part of the Paul Scherrer Institute in Switzerland. The SLS is a 3rd-generation synchrotron based on a storage ring with an electron reference energy of 2.4 GeV. The ring has a circumference of 288 m, corresponding to an electron round-trip time of 960 ns. In total 18 beam lines are operational using radiation ranging from infrared, to ultra-violet (UV), up to hard X-rays with an energy of 45 keV. The SLS is one of the world-leading sources as regards electron beam emittance, stability and beam brilliance.

Due to Coulomb interactions within the electron beam (*Touschek scattering*), individual electrons can be ejected far enough from their orbit that they are lost on the walls of the accelerator vacuum vessel. This gradual loss of particles determines the beam life time, and it means that the storage ring must be periodically injected with a new complement of particles. At the SLS this re-injection of electrons, called "top-up", is done every 2-4 minutes, keeping the total beam current at 401 ± 0.9 mA. In addition, the electrons lose energy due to the emission of radiation induced by bend magnets and insertion devices (about 500 keV each turn). In order to compensate for this loss, energy is transferred to the electrons by means of radiofrequency (RF) cavities. In the SLS storage ring four RF cavities with a frequency of 500 MHz are installed. In the following it will be shown that the RF cavities are responsible for the pulsed bunch structure of the electron beam, which we use to obtain the time resolution in our laser pump - X-ray probe experiments.

Filling pattern

The low-energy microwaves in the RF cavities cause the electrons in the electron beam to speed up or slow down at the point where the two intersect. When the microwave is near its crest (peak power) as it intersects the beam, it makes the electrons in that part of the beam at that moment speed up, just as a surfer speeds up when he catches a wave. When the microwave is near its trough as it meets the beam, the electrons in that part of the beam at that moment slow down. The result is an electron beam that is broken into pulses that have the same frequency as the low-energy microwaves, *i.e.* 500 MHz, corresponding to a bunch spacing of 2 ns. At maximum 480 of these bunches can circulate at the same time within a round-trip period of 960 ns. However, in usual operation mode not all buckets are filled. A typical *filling pattern* at the SLS is shown in Figure 5.2. The isolated electron bunch situated in the gap of the *multibunch* (MB) pulse train, is called the *camshaft* (CS) pulse, which has a current of 3-4 mA (during the

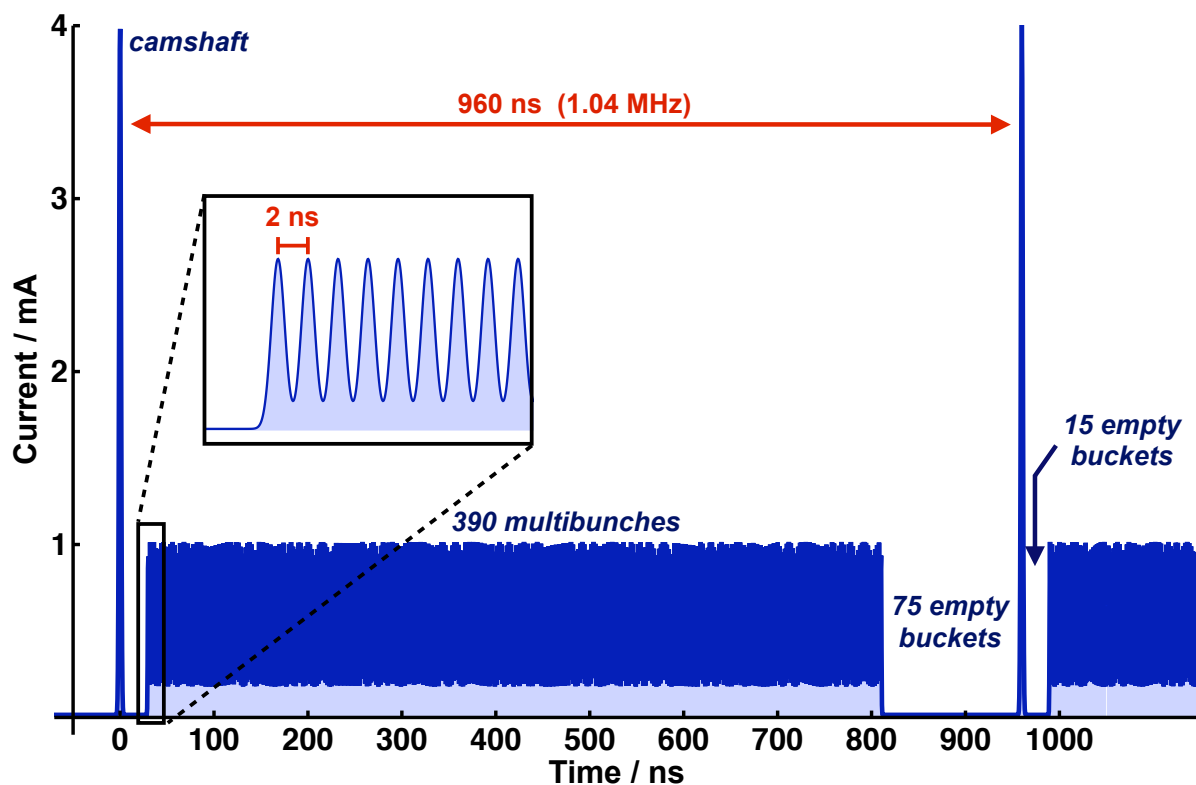


Figure 5.2: Electron-bunch filling pattern (simulated) at the **SLS** during normal user operation. The round-trip time is 960 ns corresponding to a repetition rate of 1.04 MHz. The inset shows a zoom into the first 9 electron bunches of the multibunch pulse train (total 390 bunches), each having a current of ~ 1 mA. The camshaft pulse contains 4 mA (sometimes only 3 mA). The 2 ns multibunch spacing corresponds to the **RF** repetition rate of 500 MHz.

experiments of this thesis 3 mA). The longitudinal spatial extent (~ 2 cm) of this electron bunch is directly related to the temporal length of the X-ray pulse (~ 65 ps **FWHM**) that is produced as it travels through the insertion device. The **CS** X-ray pulse contains a flux of about 4000-10000 photons/pulse, depending on the camshaft current, the X-ray energy and the optics configuration of the beam line. The full flux is on the order of 10^{12} photons/s per 0.014% energy bandwidth for 401 mA filling current.

It is noted that two other modes of operation at the **SLS** allow to obtain X-ray pulses shorter than 65 ps: 1) low- α mode [258], and 2) femto-slicing [259, 260]. In the *low- α mode*, the magnet optics and electron beam current are adjusted such that the electron bunches are much more concentrated, thus producing shorter pulses of X-rays. At present, ~ 25 ps (**FWHM**) is obtained in this mode of operation. A drawback is the low current necessary to avoid space-charge effects lengthening the bunches, making this mode unpractical for users not exploiting the temporal bunch structure, as well as to perform photon-hungry time-resolved experiments. The *femto-slicing technique*, on the other hand, works without

changing the beam optics and current. It is based on the interaction between a short, intense laser pulse and the camshaft electron bunch within an insertion device (the *modulator*). The electron energy is modulated by the laser beam on the time scale of the laser pulse duration (~ 50 fs). The energy modulation is converted into a spatial separation by a dispersive element, after which the electron beam traverses through the second insertion device (the *radiator*) to generate X-ray radiation. The femtosecond portion of the X-ray beam is separated from the unmodulated (core) background by adjusting slits. In this way, X-ray pulses of ~ 120 fs can be obtained. This technique has been successfully applied in the study of ultrafast processes in condensed matter, *e.g.* coherent phonons in crystals [57, 60, 261] and structural dynamics of molecules in solution [61]. However, the low photon flux makes these experiments very challenging and not generally applicable to any (chemical) system of interest.

In Section 5.4.2 is described how the inherent bunch structure of the **SLS** is exploited in the time-resolved **XAS** experiments of this thesis.

5.2 New flow-capillary setup for air-sensitive samples

Refreshing the sample rapidly in the time-resolved **XAS** experiment is important to avoid sample degradation. Ideally the sample is flown at a rate high enough to ensure a fresh spot for each new laser pulse. Our conventional setup uses an open flow-jet from a slit in a Sapphire nozzle in combination with a gear pump. Because the system is exposed to the air (or Helium atmosphere in the sample chamber), the solution is saturated with air. This would impose a problem in the **PtPOP** experiment, as the triplet excited state of **PtPOP** is readily oxidized by O_2 molecules dissolved in the solution. In order to keep the total O_2 concentration as low as possible, a closed-loop flow-capillary setup was designed. This setup is also ideal in cases the solvent is volatile.

The capillaries (*Hilgenberg GmbH*) are made out of quartz glass with a wall thickness in the range 10-20 μm in the measurement area (around 2 cm). The path length in the measurement area varies between ~ 200 μm and several mm. For the smaller diameters, the path length is more difficult to control during the manufacturing process. For these capillaries, the path length can be determined by measuring the edge jump magnitude of a reference solution with known concentration (see Section 5.3.2). Path lengths smaller than 200 μm are technically difficult to manufacture and transport. The capillaries with a total length of 60-100 mm, depending on the inner diameter, are mounted between two pieces of solid aluminum and glued at the interface using normal epoxy glue. The flexible tubing (*PharMed BPT*) is directly attached to the capillary exits (the capillary

enters the tubing about 5 mm). In order to secure the connection between the tubing and the capillary, two short pieces of heat-shrink tubing are used. The holder consists of a removable frame positioned by two precision pins. The frame can be easily exchanged for a frame with a pinhole (for spatial overlap) and put back in the same position afterwards.

It should be noted that the round shape of the capillary acts as a lens focusing the laser beam. Using the lensmaker's equation [262] one can derive that an incoming collimated beam with a diameter of 200 μm is focused to ~ 100 μm at the back surface of the capillary with a diameter of 500 μm (using the index of refraction $n = 1.36$ for ethanol). The excitation profile through the capillary is therefore not uniform. In addition, with a converging incoming beam, care should be taken that the focus does not lie exactly at the back-surface of the capillary. The stability of the capillaries was tested for a laser beam at 400 nm (1 kHz) focused on a capillary filled with **dimethylformamide (DMF)** (not flowing). Under these conditions, the damage threshold was found to lie in the range 0.3-0.6 J/cm².

In using the flow-capillary setup a complication arises due to sample aggregation at the inner wall of the capillary at the spot where the laser and X-rays hit the sample. Depending on the sample, this aggregation can be caused by either the laser or the X-rays, or both. It is seen as an increase in the total amount of fluoresced X-rays. To reduce the aggregation, one can move the capillary vertically to a new spot. By looping through a few spots on the capillary, while changing the position after each scan, the aggregation in the time-resolved **XAS** experiment on **PtPOP** could be widely suppressed.

5.3 Steady-state XAS

The measurement (and analysis) of good-quality undistorted **XAFS** (**XANES** and **EXAFS**) spectra is a challenging research field on itself [68]. Comparison to theory requires stringent attention to systematic errors that can occur in the experiment. In this Section we describe the experimental method that was used to measure the steady-state **XAS** spectra of Chapter 7. After a technical description of the setup in Section 5.3.1, in Section 5.3.2 we describe the two modes of detection in a **XAS** experiment (transmission vs. fluorescence).

5.3.1 Ion chamber setup

The experimental setup for the steady-state **XAS** experiments is sketched in Figure 5.3. Two ion chambers (*Oxford-Danfysik*) filled with 0.9 – 1.1 bar of He gas were used as I_0 and transmission (I_T) detectors (path length 30 cm, 25 μm Kapton windows). The low

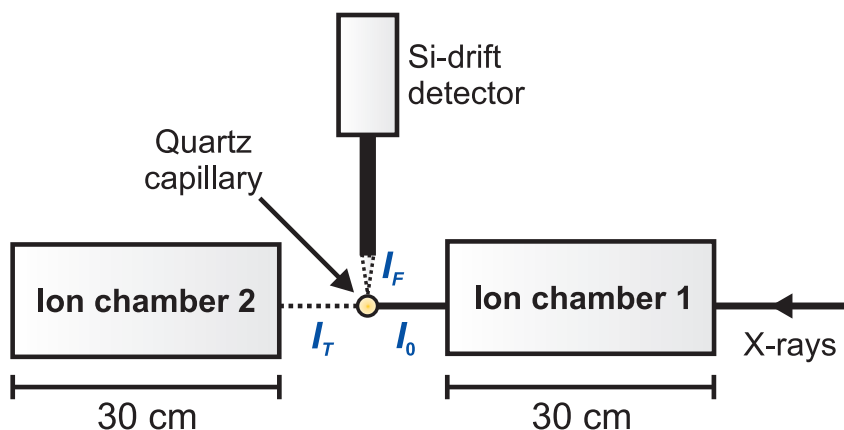


Figure 5.3: Sketch (top-view) of the ion-chamber setup at the microXAS beam line used to measure the steady-state spectra of Chapter 7.

current from each ion chamber was amplified by a current amplifier (*Femto* DLPCA-200). A single-element silicon drift detector (*Ketek* AXAS-SDD10-138500, 10 mm²) with an energy resolution of 150 eV was used for fluorescence detection (I_F). The fluorescence detector was placed at an angle normal to the incoming X-ray beam in order to minimize elastic scattering (for X-rays polarized in the horizontal plane). By setting appropriate regions of interest in the energy-resolved spectrum, one can reduce the background noise by excluding the peaks caused by fluorescence and scattering from air. The position of the *Ketek* fluorescence detector was optimized so that the total number of counts did not exceed 100000/s. The sample was contained in a quartz capillary (*Hilgenberg GmbH*) with 10 μm thick walls and a path length of 2 mm mounted on an xy -stage. The center of the capillary was found by scanning it horizontally and finding the middle of the absorption profile. The X-ray beam size was 300(H) \times 700(V) μm^2 (unfocused, slitted horizontally) and the X-ray energy was calibrated by measuring a Pt reference foil. The data was taken at a rate of 5 cycles per second, where one cycle is composed of 190 ms integration and 10 ms of waiting time. The gain of the amplifiers was adjusted so that the voltage was as close as possible to 10 V (without exceeding it). The integration time per data point was set to 1 s and in total two scans were averaged to give the data in Chapter 7.

The highest **signal-to-noise (S/N)** ratio in a steady-state **XAS** experiment is reached for $\sim 10\%$ absorption in the first (I_0) ion chamber and maximum absorption in the second (I_T) ion chamber [263]. These conditions can be reached by choosing an appropriate mixture of gases (Ar, N₂, He) for both detectors. At undulator beam lines at 3rd generation synchrotrons, however, intensities (flux per unit area) are generally very high and care has to be taken not to saturate the detector. In order to stay in the linear operation regime of the ion chambers, the current should not exceed 100 nA. The number of absorbed photons

N_{ph} in the ion chamber is given by the relation [264]

$$N_{\text{ph}}[\text{ph/s}] = \frac{C[\text{A}] \cdot E_{\text{I}}[\text{eV}/e^-]}{E[\text{eV}] \cdot e[\text{C}]} \quad , \quad (5.1)$$

where C is the measured current, E_{I} is the ionization energy of the gas in the ion chamber and e is the elementary charge (the units are given between square brackets). Using this equation for an energy of 11.5 keV and a typical gas ionization energy of $E_{\text{I}} = 20$ eV, a current of 100 nA corresponds to an absorbed flux of $\sim 1 \cdot 10^9$ ph/s. For typical incoming fluxes of $\sim 10^{12}$ ph/s, this corresponds to only 0.1% absorption. Heavy gases such as Ar and N_2 at ambient pressure and for a path length of 30 cm, absorb 88% and 8% of the incoming flux respectively [265]. These gases would therefore clearly saturate the detector. Instead, for the present experiment the ion chambers were filled with 1 bar He gas which absorbs about 0.1% of the incoming X-ray flux.

Prior to the measurements it should be checked that the detectors behave linear for the range of fluxes and energies during the experiment. While this is usually easily achieved for ion chambers, the linearity of solid-state fluorescence detectors should be carefully checked. In case the fluorescence detector is non-linear, while the I_0 monitor is linear, the **XAFS** amplitudes in the spectrum $\mu \propto I_F/I_0$ are distorted.

5.3.2 Transmission and fluorescence modes of detection

XAFS spectra can be measured in transmission or fluorescence mode (Auger or secondary electron yield are not discussed here). In general, the optimum conditions for either mode of detection are not fulfilled simultaneously. While transmission is experimentally the easiest method of measuring **XAFS** spectra of concentrated samples, X-ray fluorescence detection usually results in higher sensitivity, in particular in the case of dilute samples. The following Sections provide a short description of **XAFS** signals obtained for the two detection modes and their accompanying experimental difficulties.

XAFS measured in transmission mode

In Section 4.1.1 we have seen that the transmitted intensity I_T of a beam of incident intensity I_0 through a slab of material with uniform thickness d is given by Lambert-Beer law $I_T = I_0 e^{-\mu d}$ (Equation (4.5)). The X-ray absorption spectrum $A(E)$, measured by detecting the transmitted and incoming intensities as a function of the X-ray energy E ,

is then defined as

$$\begin{aligned}
 A(E) &= \ln \left(\frac{I_0(E)}{I_T(E)} \right) \\
 &= \mu(E) \cdot d \\
 &= \sigma_a(E) \cdot c_{\text{mol}} N_A d \quad ,
 \end{aligned}
 \tag{5.2}$$

where the expression for μ of Equation (4.7) was used in the last step. In fact, the measured value of $\mu(E) \cdot d$ is the absorption of everything between the two detectors (*e.g.* ion chambers), including air, entrance and exit windows, *etc.* Furthermore, the sensitivities of the ion chambers decrease with increasing X-ray energy. A number of extraneous factors thus multiply the ratio $I_0(E)/I_T(E)$ in Equation 5.2. When the logarithm is taken, these multiplicative factors are transformed into a slowly varying additive background, which is easily and unambiguously subtracted out in the early stages of data analysis. This in contrast to fluorescence signals, as shown in the next Section.

The sample thickness d or concentration c_{mol} can be derived from Equation (5.2) by using the measured change in absorption across the edge ΔA^{edge} and the corresponding calculated change in atomic absorption cross section $\Delta \sigma_a^{\text{edge}}$ for the absorbing element (*e.g.* using the XOP program [208]). ΔA^{edge} is determined by subtracting the $A(E)$ values just after and before the sudden increase in absorption around the ionization potential E_0 . The post-edge value should be chosen such that it does not correspond to a maximum or minimum of the absorption fine structure χ (resulting from multiple scattering or bound-bound transitions in the XANES spectrum), but rather lies on an imaginary smoothly varying background function μ_0 (see Chapter 4).

For optimum transmission detection (highest S/N ratio), one should adjust the sample thickness and/or solute concentration so that $\mu^{\text{solute}} d \approx 2.2$ (10.9% transmission)[†] [45, 68]. Including the background absorption of the matrix or solvent, always decreases the total transmission below this value, but this only decreases the overall S/N ratio and not the optimum solute concentration value for a given thickness. Higher concentrations instead of thicker samples is therefore generally better. Care should be taken that the sample is uniform on a scale determined by the absorption length $1/\mu$ of the material (particles should be smaller than this value). In the case of liquid samples, this is usually not a problem. Solid samples, however, should have a uniform thickness and be free of "pinholes", *i.e.* parts of the sample where the transmission is locally increased. Thickness

[†]This value can be derived by calculating the S/N ratio assuming shot-noise limited detection and finding its extreme value with respect to μd .

effects can severely distort both **XANES** and **EXAFS** regions of the spectra [68, 266].

In order to compare spectra among each other as well as with theoretical spectra, the dependence on the sample thickness d in the expression for $A(E)$ needs to be removed. Normalization is achieved by dividing the measured $A(E)$ spectrum by the edge-jump magnitude ΔA^{edge} , according to

$$\begin{aligned} A^{\text{norm}}(E) &= \frac{A(E)}{\Delta A^{\text{edge}}} \\ &= \frac{\mu(E)}{\Delta\mu_0(E_0)} \end{aligned} \quad (5.3)$$

The resulting normalized absorption spectrum $A^{\text{norm}}(E)$ has an edge-jump of unity and can be directly compared to the theoretically calculated absorption spectra given by the second line in Equation (5.3). In addition to this edge-jump normalization, cosmetic pre- and post-edge correction procedures are commonly applied for reasons of comparison, as described in Section 4.3.1.

XAFS measured in fluorescence mode

Earlier we have noted that for **XAFS** measured in fluorescence mode $\mu(E) \propto I_F/I_0$. In contrast to the transmission mode, spurious multiplicative factors in either I_0 or I_F result in altered **EXAFS** amplitude functions. Such effects do not cancel out even if the two detectors are identical. This makes the fluorescence mode of measuring **XAFS** particularly prone to systematic errors. It is noted that we consider here X-ray fluorescence excitation spectra, *i.e.* the integrated intensity of all possible fluorescence channels $I_F(E)$ is detected as a function of incoming photon energy E . Alternatively, the fluorescence can be dispersed after the sample and specific fluorescence channels can be detected [212, 267–269].

The relation $\mu(E) \propto I_F/I_0$ is slightly oversimplified. The probability of fluorescence is indeed proportional to the absorption probability, but the fluorescence intensity that we measure has to travel back through the sample to get to the detector. Since all matter attenuates X-rays, the fluorescence intensity, and therefore the **XAFS** oscillations, can be damped due to the *self-absorption* effect. In the worst case, for a thick sample of a pure element, the **XAFS** oscillations simply change the penetration depth into the sample, but essentially all the X-rays are absorbed by the sample. Since the fluorescence escape depth is usually longer than the penetration depth, all absorbed X-rays cause fluoresced X-rays reaching the detector, but the **XAFS** oscillations are severely damped.

More correctly, the measured fluorescence intensity is described by [68, 266]

$$I_F(E) = I_0(E) \frac{\epsilon_f \Omega}{4\pi} \frac{\mu_\chi(E) \{1 - e^{-[\mu_{\text{tot}}(E)/\sin\theta + \mu_{\text{tot}}(E_f)/\sin\phi]d}\}}{\mu_{\text{tot}}(E)/\sin\theta + \mu_{\text{tot}}(E_f)/\sin\phi} \quad (5.4)$$

where θ and ϕ are the incident (I_0) and outgoing (I_F) angles with respect to the sample surface, respectively, ϵ_f is the fluorescence yield, Ω is the solid angle of detection, E_f is the energy of the fluorescent X-ray, $\mu_\chi(E)$ is the absorption from the element of interest, and $\mu_{\text{tot}}(E)$ is the total absorption in the sample: $\mu_{\text{tot}}(E) = \mu_\chi(E) + \mu_{\text{other}}(E)$. For the present case of a round sample holder (capillary), we approximate $\theta = \phi = 90^\circ$ [‡], and the dependence on the angles in Equation (5.4) vanishes, resulting in

$$I_F(E) = I_0(E) \frac{\epsilon_f \Omega}{4\pi} \frac{\mu_\chi(E) \{1 - e^{-[\mu_{\text{tot}}(E) + \mu_{\text{tot}}(E_f)]d}\}}{\mu_{\text{tot}}(E) + \mu_{\text{tot}}(E_f)} \quad (5.5)$$

This equation has two interesting limits which are the best cases for XAFS measurements in fluorescence mode [68, 266]: (1) the *thin sample limit* for which $[\mu_{\text{tot}}(E) + \mu_{\text{tot}}(E_f)]d < 1$, and (2) the *thick, dilute sample limit* for which $[\mu_{\text{tot}}(E) + \mu_{\text{tot}}(E_f)]d \gg 1$ and $\mu_\chi(E) < \mu_{\text{other}}(E)$.

For the thin sample limit, the exponential term can be expanded in a Taylor series, and by keeping the first two terms, this results in

$$I_F(E) = I_0(E) \frac{\epsilon_f \Omega}{4\pi} \mu_\chi(E) d \quad (5.6)$$

In the thick, dilute sample limit, the exponential term goes to zero, so that

$$I_F(E) = I_0(E) \frac{\epsilon_f \Omega}{4\pi} \frac{\mu_\chi(E)}{\mu_{\text{tot}}(E) + \mu_{\text{tot}}(E_f)} \quad (5.7)$$

Because $\mu_\chi(E) < \mu_{\text{other}}(E)$, we can ignore the energy dependence of μ_{tot} and derive $I_F(E) \propto I_0(E) \mu_\chi(E)$. For relatively thick and concentrated samples, for which $\mu_\chi(E) \sim \mu_{\text{other}}(E)$, we can not ignore the energy dependence of $\mu_{\text{tot}}(E)$, representing the case of self-absorption. In the worst case, if $\mu_\chi(E) \approx \mu_{\text{tot}}(E)$, the XAFS oscillations will be totally lost, as discussed above.

We now calculate the values of $\mu_{\text{tot}}(E) d$ and $\mu_{\text{tot}}(E_f) d$ for the case of a 18 mM solution of **tetrabutyl ammonium (TBA)₄PtPOP** in ethanol, and test in which regime the steady-

[‡]The exact calculation of the fluorescence intensity for a round sample holder requires solving the integral $\int_{-r}^r \exp[-\mu_{\text{tot}}(E)x - \mu_{\text{tot}}(E_f)\sqrt{r^2 - x^2}] dx$, where r is the radius of the capillary.

state measurements of Chapter 7 were performed. For $E = 11.7$ keV, $E_f = 9.44$ keV (energy of the dominant $L_{\alpha 1}$ emission, see Table 4.1) and $d = 2$ mm (capillary thickness), we calculate a total absorption of $[\mu_{\text{tot}}(E) + \mu_{\text{tot}}(E_f)]d = 1.48$, using the atomic cross sections from reference [208]. A concentration of 17.1 M for bulk ethanol was used, neglecting the relatively small solute concentration. Because neither of the two limits are fulfilled, self-absorption effects are expected to distort the XAFS oscillations in the fluorescence spectra. For this reason, the steady-state data used for the analysis in Chapter 7 were measured in transmission mode. For the time-resolved XAS measurements of Chapter 7, both the sample concentration (10 mM) and sample thickness (500 μm) were smaller, resulting in $[\mu_{\text{tot}}(E) + \mu_{\text{tot}}(E_f)]d = 0.3$, for which we can assume the thin sample limit.

For comparison, one needs to remove the sample thickness and geometry dependent factors $\Omega/4\pi d$ by means of normalization. The normalized fluorescence spectrum F^{norm} is given by

$$F^{\text{norm}}(E) = \frac{I_F(E)}{I_0(E) \Delta I_F^{\text{edge}}} \quad (5.8)$$

where ΔI_F^{edge} is the edge jump of the spectrum $I_F(E)/I_0(E)$. After pre- and post-edge background subtraction to remove absorption, fluorescence and scatter contributions from everything except the element of interest, the normalized spectra $A^{\text{norm}}(E)$ and $F^{\text{norm}}(E)$ can be directly compared to each other.

5.4 Time-resolved XAS

A typical approach for recording molecular dynamics is based on the *pump-probe scheme*. Absorption of a first pulse of light (the pump pulse) brings the molecule from the ground-state potential to the excited-state potential. A second pulse of light (the probe pulse) interrogates the excited ensemble at a certain time delay after the pump pulse. By scanning the delay between the two pulses, time-dependent information about the system is obtained, where the time resolution is determined by the convolution of the pump and probe pulse profiles. In the present thesis, the first pulse of light is a ~ 100 fs laser pulse, while the probe pulse is either another short laser pulse (see Section 5.5) or an X-ray pulse of ~ 65 ps that is used to measure the XAS spectrum of the sample as a function of delay time. The latter technique is the subject of this Section.

The experimental setup used to record the data of Chapter 7 is described in Section 5.4.1. The data acquisition strategy to obtain pump-probe XAS signals is given in Section 5.4.2. The raw signals from the data acquisition need to be normalized in order to compare spectra measured in transmission and fluorescence modes, and theoretical spec-

tra. This normalization is described in Section 5.4.3. Finally, in Section 5.4.4 we discuss the process of laser excitation and the difficulties arising from the mismatch between laser and X-ray absorption cross sections.

5.4.1 Experimental setup

Figure 5.4 shows a schematic drawing of the time-resolved XAS setup that was used to obtain the data of Chapter 8. The experimental chamber containing the sample, translation motors and detectors is not shown for clarity.

X-ray beam path

Monochromatic X-rays of ~ 11.5 keV ($\Delta E \simeq 1.6$ eV) are focused in the horizontal plane by an upstream mirror (not shown) so that the intermediate focus lies before the downstream slits. The X-rays are focused a second time in both directions by two *Kirkpatrick-Baez* (KB) mirrors to a spot of dimensions $160(\text{H}) \times 100(\text{V}) \mu\text{m}^2$ at the sample position, as determined by scanning a pinhole with $25 \mu\text{m}$ diameter through the X-ray beam and measuring the transmitted intensity. The horizontal beam profile was Gaussian (representing the image of the intermediate focus), whereas the vertical profile was rectangular due to clipping the beam with the slits before the KB mirrors. The beam intensity was reduced by a factor of two by an optical chopper rotating at 2 kHz synchronized to the laser reference frequency. A very good contrast between blocked and unblocked beams was achieved. The phase of the chopped signal was adjusted by slightly translating and/or twisting the chopper, so that the integration gates (see below) lie in the 1-ms gap of the transmitted X-ray beam. The reason for inserting the chopper is twofold: 1) the rate of sample damage is lowered by reducing the average X-ray flux; 2) the avalanche photodiode (APD) used to measure the transmitted flux behaves non-linearly if the full flux impinges on the diode. Despite the factor-two reduction by the chopper, the transmitted flux through the sample was still too high. In order to work in a linear detector regime, the beam was attenuated by several foils of aluminum in front of the transmission detector (after the sample). However, as this also reduces the flux of the X-rays containing the time-resolved signal, it would be better to use a chopper with a much shorter opening time, *e.g.* by reducing the size of the openings in the blades of the optical chopper. An X-ray chopper working at a kHz repetition rate with a time window just large enough to pass the camshaft X-ray pulse has been developed at the SLS [270]. Its operation, however, is not yet as practical.

The incoming beam intensity I_0 was monitored by a thin ($0.5 \mu\text{m}$) Zn foil positioned

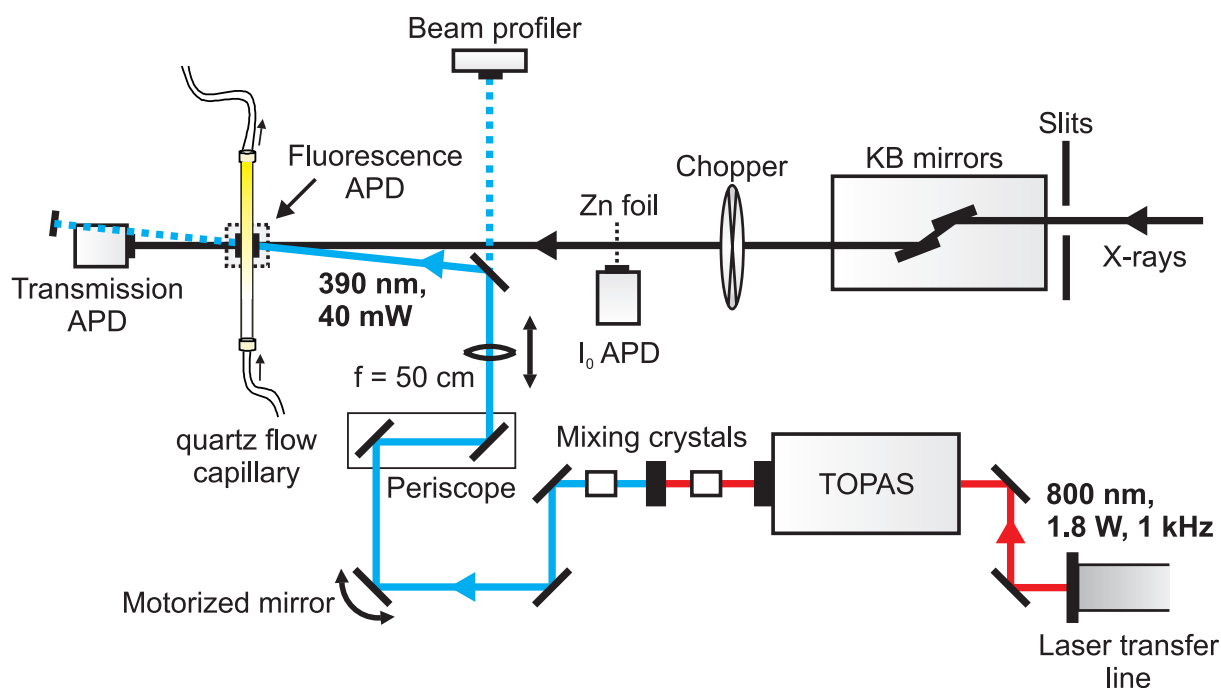


Figure 5.4: Sketch of the time-resolved XAS setup in the X-ray hutch of the micro-XAS/FEMTO beam line at the SLS. The components are described in the text.

perpendicular to the beam. The scattered and fluoresced X-rays (resulting from the Zn K -shell core hole at 9.66 keV), are detected by an APD placed below the foil. The holder for the foil was designed in such a way that the solid angle of detection was as high as possible. The X-ray fluorescence from the sample was detected by two APD detectors positioned perpendicular to the beam in order to minimize scatter (the X-rays are polarized in the horizontal plane). The solid angle Ω was maximized by placing the detectors as close as possible to the sample (~ 5 mm). The transmission APD was placed at tens of cm behind the sample. The full X-ray flux measured with a silicon diode at the sample position was $\sim 10^{12}$ photons/s.

Laser beam path

The laser itself is physically located in a dedicated laser hutch beside the X-ray and control hutches of the beam line. The ~ 2 W, 800 nm laser beam from the 1 kHz Ti:Sapphire regenerative amplifier system (*Positive Light*) is guided through an evacuated transfer tube with a total length of ~ 30 m into the X-ray hutch. The laser beam is consequently aligned into a traveling-wave optical parametric amplifier of superfluorescence (TOPAS) (*Light Conversion Ltd.*). The 780 nm output of the TOPAS is doubled by a β -BaB₂O₄ (BBO) crystal resulting in ~ 50 mW of 390 nm light at 1 kHz (~ 40 mW at the sample).

Two sets of coated mirrors after the **TOPAS** and **BBO** are used to remove the fundamental wavelengths (800 nm for the first stage, 780 nm for the second stage). The laser beam is guided into the experimental chamber via a motorized mirror and a periscope mirror assembly that is used to increase the beam height to the level of the X-ray beam (~ 50 cm from the table surface). The motorized mirror is used for the spatial overlap of laser and X-ray beams through a pinhole at the sample position. The laser is focused by a lens with a focal length of 50 cm to a spot of $\sim 300(\text{H}) \times 200(\text{V}) \mu\text{m}^2$. The angle between laser and X-ray beams is about 5° . The laser beam was imaged on a beam profiler that detects leakage from the last mirror before the sample. The distance between the profiler and the mirror was adjusted to be the same as the distance between the last mirror and the sample. In this way, a 1:1 image of the beam at the sample position is obtained. This allows to monitor the beam stability and to detect any deviations from the position for which the laser and X-ray beams overlap. Appropriate mirror coatings were used for the respective wavelengths.

Temporal overlap of the X-ray **CS** pulse (see next Section) and the laser pulse is achieved by placing a fast photodiode at the position of the sample where the two beams overlap. The beams are attenuated adequately to avoid saturation of the diode. The intensities are recorded with a GHz oscilloscope. The relative delay of the laser is adjusted by the oscillator phase shifter such that the rising slopes of the two pulses temporally overlap. The precision of determining time overlap by this method is approximately 200 ps. A more precise overlap is obtained by measuring the rise of the pump-probe signal itself.

Sample environment

The $(\text{TBA})_4[\text{Pt}_2(\text{P}_2\text{O}_5\text{H}_2)_4]$ sample (10 mM, in ethanol) was contained in a quartz flow-capillary (see Section 5.2) with a path length of 500 μm . A peristaltic pump was used to flow the sample at a speed of approximately 30 ml per minute. Within the same loop, a 10 μm flow-cuvette was used for *in situ* monitoring the oxidation of the sample. The latter is visible as a decrease in intensity of the main absorption band around 370 nm belonging to the absorption of the $^1\text{A}_{2\text{u}}$ state. An oxidation threshold of $\sim 10\%$ was used as a limit to refresh the sample.

5.4.2 Data acquisition scheme

We have seen in Section 5.1.1 that the X-rays originating from the synchrotron exhibit a specific bunch structure, depicted in Figure 5.2, which we exploit in our laser pump - X-ray probe **XAS** experiments in order to obtain the necessary time resolution.

The measured signals from each APD detector are amplified and consequently used as an input for several *boxcar integrators* (*Stanford Research Systems* SR250). The latter allow gated detection and averaging of selected parts of the incoming signal with repetition rates up to 20 kHz. The width of the integration window (*gate*) may vary between 2 ns and 15 μs and its delay, relative to the internal or external trigger signal, can be adjusted manually. In our case, the boxcar integrators are triggered externally with a "6-kHz" signal indicating the delay times at which the incoming signal should be detected (see Figure 5.5). Beside the X-ray signal, two zero signals are recorded (*clearing zero* and *real zero*), which are used to discharge the capacitors in the boxcar before the next X-ray pulse is measured. In addition, one of them (the real zero) is subtracted from the integrated X-ray signal in order to correct for background drifts. The boxcar trigger signal is derived from a "universal" 2 kHz trigger synchronized to the laser oscillator frequency, which is, in turn, synchronized to the 500 MHz RF frequency of the synchrotron (Section 5.1.1). In this way, the X-ray bunches, laser pulses and data acquisition are mutually in phase, and their relative delays can be controlled by the user. The boxcar output is supplied to the data acquisition card, together with two marker signals used to differentiate between 1) X-ray and zero signals, and 2) pumped (laser excited) and unpumped (ground state) X-ray signals. The data acquisition software averages together a minimum of 1000 "shots" (1s) and saves it to a file, where each shot represents the measurement of one pumped and one unpumped X-ray pulse. In addition to the raw pumped and unpumped channels, the

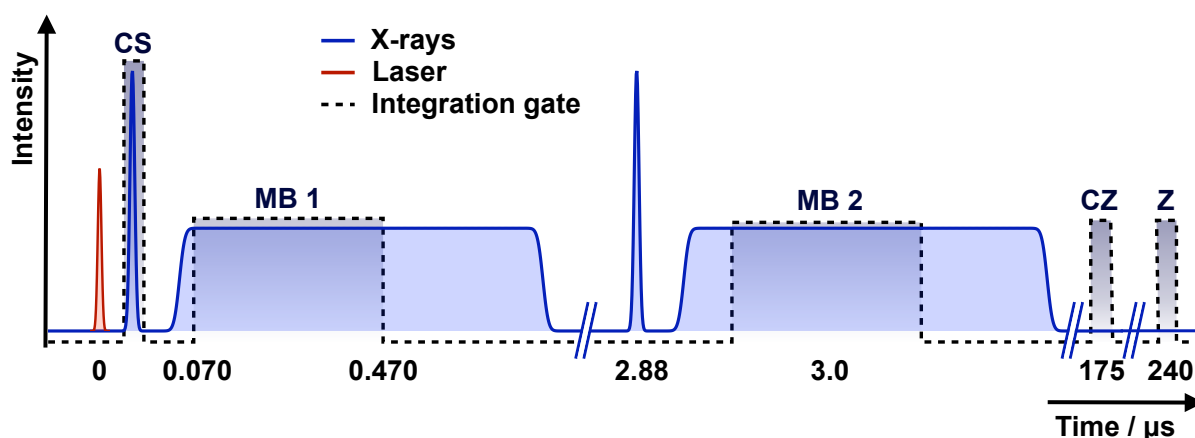


Figure 5.5: Schematic drawing of the filling pattern (blue, see also Figure 5.2) with one of the integration gate configurations during the time-resolved XAS experiment. The laser pulse that is used for excitation is also shown in red. CS = camshaft; MB = multibunch; CZ = clearing zero; Z = zero. The CS gate is set for both fluorescence APD detectors, while the MB 1 and MB 2 gates belong to two different APD detectors. The CZ and Z gates fall in the time window for which the X-rays are blocked by the chopper.

difference signal (pumped minus unpumped) is calculated on a shot-by-shot basis (1 kHz) and averaged. The standard errors of the averages are also provided to the user.

In the time-resolved XAS experiment of this thesis, the signals from the I_0 , transmission and two fluorescence APD detectors are, after amplification, supplied to in total 6 boxcar integrators. For each fluorescence signal, two boxcars were used with gates set to integrate the CS X-ray pulse right after the laser pulse (gate width ~ 10 ns) and a chunk of the MB pulse train (variable gate width). The gates for the transmission and I_0 signals were set for the CS pulse only. The relative delays of the MB gates were changed in the course of the experiment, which allowed us to take snapshots at various delay times up to ~ 100 μ s. We also shifted the laser pulse to a delay just before the start of the MB pulse train, in order to set a sequence of 50-ns wide gates starting from approximately time zero (the precision in setting a gate is several ns). One of the gate configurations during the experiment is shown in Figure 5.5.

It is noted that the statistics of this experiment is limited by the total amount of integrated X-ray flux. The latter, in turn, is limited by the repetition rate (2 kHz) of the data acquisition, which is twice the repetition rate of the laser. A laser that works at higher repetition rates thus allows to measure data with the same S/N ratio in shorter time. In addition, it opens the door of measuring (biological) low-concentration samples that generally suffer from very poor S/N ratios if the 1-kHz setup is used. The recent implementation of pump-probe XAS at high repetition rates using a MHz laser oscillator has resulted in transient XANES spectra of 2-3 mM samples of aqueous Myoglobin with excellent S/N ratio. Drawbacks of using MHz lasers are the rather low peak power (~ 6 μ J per pulse at 532 nm) which must be compensated by tight focusing, and the consequently rapid laser-induced sample degradation.

5.4.3 Pump-probe XAS signals

In Section 5.3.2 we derived the expressions for the steady-state XAS signals for transmission (Equation (5.2)) and fluorescence (Equation (5.6)) detection. In the time-resolved XAS measurement we measure the difference between pumped (laser-excited) and unpumped (ground-state) XAS spectra in both modes of detection. In transmission mode this means that the *transient XAS spectrum* is given by

$$\begin{aligned}\Delta A(E, t) &= A^{\text{pu}}(E, t) - A^{\text{up}}(E) \\ &= \ln \left(\frac{I_T^{\text{up}}(E)}{I_T^{\text{pu}}(E, t)} \right) ,\end{aligned}\tag{5.9}$$

where $I_T^{\text{pu}}(E, t)$ is the transmitted flux in the presence of the laser pump pulse (this signal is time dependent due to the excited-state decay), and $I_T^{\text{up}}(E)$ is the transmitted flux for the unpumped sample. In cases where the laser-induced changes in I_T are small, one can approximate

$$\Delta A(E, t) \simeq \frac{I_T^{\text{pu}}(E, t) - I_T^{\text{up}}(E)}{I_T^{\text{up}}(E)} .\tag{5.10}$$

This expression is useful to increase the sensitivity, because it allows to use the averaged difference signals $I_T^{\text{pu}} - I_T^{\text{up}}$ that are calculated shot-by-shot (*i.e.* every ms) so that "slow" systematic drifts in the background are not contributing to the signal. This in contrast to Equation (5.9) in which the averaged I_T signals must be taken. For calculating the errors of the signals in Equations (5.9) and (5.10), one should propagate the standard errors of the individual channels I_T^{pu} , I_T^{up} and $I_T^{\text{pu}} - I_T^{\text{up}}$ as provided by the data acquisition.

The pumped sample contains a mixture of excited molecules and molecules that are still in the ground state. In order to relate the measured transient XAS spectrum to the theoretically calculated absorption coefficients for the ground and excited states, we need to introduce the excitation yield $f(t)$, *i.e.* the fraction of excited molecules in the sample volume that is probed by the X-rays. Using Equation (5.2), the transient spectrum is given by

$$\begin{aligned}\Delta A(E, t) &= f(t) \cdot [\mu^{\text{ES}}(E) - \mu^{\text{GS}}(E)] \cdot d \\ &= f(t) \cdot \Delta\mu(E) \cdot d ,\end{aligned}\tag{5.11}$$

where $\mu_{\text{ES}}(E)$ and $\mu_{\text{GS}}(E)$ are the XAS spectra of the excited state and ground state structures, respectively. In order to eliminate the dependence on the sample thickness d , an edge-jump normalization is performed according to

$$\begin{aligned}\Delta A^{\text{norm}}(t, E) &= \frac{\Delta A(E, t)}{\Delta A^{\text{edge}}} \\ &= \frac{f(t) \cdot \Delta\mu(E)}{\Delta\mu_0(E_0)} ,\end{aligned}\tag{5.12}$$

where ΔA^{edge} is the edge-jump magnitude of the experimental steady-state $A^{\text{up}}(E)$ spectrum and $\Delta\mu(E)/\Delta\mu_0(E_0)$ represents the transient spectrum as it is calculated by theo-

retical codes (E_0 is the ionization energy, see Section 4.3.1). Note that $f(t)$ in Equation (5.11) assumes only one excited species, but the expression can be easily generalized for the case of several reaction products co-existing in the solution [94].

In analogy to Equation (5.9), one can define the transient fluorescence spectrum as

$$\begin{aligned}\Delta I_F(t, E) &= \frac{I_F^{\text{pu}}(E, t) - I_F^{\text{up}}(E)}{I_0(E)} \\ &= \epsilon_f \cdot \Omega \cdot f(t) \cdot \Delta\mu(E) \cdot d \quad ,\end{aligned}\tag{5.13}$$

where $I_F^{\text{pu}}(E, t)$ is the fluorescence intensity from the pumped sample and $I_F^{\text{up}}(E)$ is the fluorescence from the unpumped sample. In the second step of (5.13), the expression for fluorescence in the thin-sample limit, Equation (5.6), was used. The normalized signal is obtained by dividing by the edge jump, according to

$$\begin{aligned}\Delta I_F^{\text{norm}}(t, E) &= \frac{\Delta I_F(t, E)}{\Delta I_F^{\text{edge}}} \\ &= \frac{f(t) \cdot \Delta\mu(E)}{\Delta\mu_0(E_0)} \quad ,\end{aligned}\tag{5.14}$$

where ΔI_F^{edge} is the edge-jump magnitude of the steady-state fluorescence spectrum $I_F^{\text{up}}(E)/I_0(E)$. Comparing Equations (5.12) and (5.14) it is seen that, after correct normalization to the incoming intensity and the edge jump, the transient fluorescence signal $\Delta I_F^{\text{norm}}(t, E)$ can be directly compared to the transient absorption signal $\Delta A^{\text{norm}}(t, E)$ resulting from the transmission intensities. Furthermore, the experimental normalized transient spectra can be compared to the theoretical transient spectrum $\Delta\mu(E)/\Delta\mu_0(E_0)$, provided the excitation yield $f(t)$ is known.

5.4.4 The laser excitation process

One of the main challenges in pump-probe XAS is related to the orders of magnitude mismatch between absorption cross sections for UV-visible photons and X-ray photons. In addition, the two sources of pump and probe photons are very different with respect to their pulse intensities. These issues pose stringent boundary conditions on the sample design in order to guarantee a feasible experiment.

If we neglect the excitation process for the moment (assuming 100% excitation), an X-ray transmission experiment is optimized in terms of S/N if the total sample transmission approximates 10.9% (see Section 5.3.2). This can be reached by adjusting either the

solute concentration c_{mol} (including the X-ray absorbing element) or the sample thickness d (see Equation (5.2)). As increasing the latter also increases the background absorption from the solvent, usually maximizing c_{mol} while minimizing d until $\mu d \simeq 2.2$ (10.9% transmission), optimizes the S/N ratio. Practical limits for c_{mol} are posed by the maximum solute solubility and aggregation effects occurring at high concentrations. In the case of liquid samples, d is determined by the thickness of the free flowing jet, flow capillary or flow cell. Practical thicknesses are in the range 100-500 μm . Due to these limits, the transmission is often higher than 10.9%, but the closer the transmission reaches this value, the better.

Realistically, excitation yields lie in the range 3-30% and they depend in a complicated manner on many parameters, including the sample concentration, the optical absorption cross section, the excitation volume and the number of laser photons available for excitation. The latter is limited by the laser power which lies, for commercial 1 kHz Ti:Sapphire amplifier systems, in the range 0.5-3 mJ per pulse at 800 nm, which is reduced to 0.02-0.5 mJ if shorter wavelengths are derived by frequency doubling or mixing. The number of photons per pulse thus spans the range $2 \cdot 10^{13}$ (250 nm, 20 μJ) - $1.2 \cdot 10^{16}$ (800 nm, 3 mJ). For a given pumped sample volume (depending on the spot size and the sample thickness), this sets an upper limit to the optimum sample concentration, because there is no sense in having more molecules in the pumped volume than laser photons in the excitation pulse (excess unexcited molecules would just contribute to the background, deteriorating the S/N ratio). In general we can state, as long as we are in the linear excitation regime, it is always preferable to increase the excitation power for a certain laser repetition rate.

For one-photon (linear) absorption processes, the excitation yield averaged over the sample thickness d can be estimated by using Lambert-Beer law, resulting in

$$f = \frac{N_{\text{ph}}}{F d c_{\text{mol}} N_A} (1 - 10^{-\varepsilon_{\lambda} c_{\text{mol}} d}) \quad , \quad (5.15)$$

where N_{ph} is the number of laser photons in the excitation pulse, F is the pump area and ε_{λ} is the optical molar absorptivity (in $\text{M}^{-1}\text{cm}^{-1}$) at the excitation wavelength. If we insert the conditions at which the time-resolved XAS experiment of this thesis has been performed (40 $\mu\text{J}/\text{pulse}$ at 390 nm ($N_{\text{ph}} = 9.8 \cdot 10^{13}$), $\varepsilon_{\lambda=390 \text{ nm}} = 4000 \text{ M}^{-1}\text{cm}^{-1}$, $d = 500 \mu\text{m}$, $c_{\text{mol}} = 10 \text{ mM}$, $F = 200 \times 300 \mu\text{m}^2$), we obtain $f = 54\%$, clearly an unrealistically high value. In fact, it is shown in Section 8.2 by means of optical measurements that f is approximately 10%. Equation (5.15) is obviously not a realistic description of the dependence of f on the various experimental parameters. Although according to the value of $\varepsilon_{\lambda} c_{\text{mol}} d = 2$ almost all the laser photons are absorbed by the sample, apparently not

every absorbed photon leads to an excited PtPOP molecule. As a possible reason for this, absorption by the solvent molecules and/or counter-ions might play a role.

Qualitatively, Equation (5.15) prescribes that f is higher for higher values of $\varepsilon_\lambda c_{\text{mol}} d$. This implies that all laser photons should be absorbed after the total path length d , so that the value of $10^{-\varepsilon_\lambda c_{\text{mol}} d}$ approaches zero, which is achieved for optical density (OD) values larger than 3. With $c_{\text{mol}} d$ fixed to the optimum values with respect to the X-ray transmission (see above), ideally we would maximize ε_λ to achieve this. This is only possible in cases where a variable-wavelength laser (*e.g.* a TOPAS) is used. Often, the wavelength, and thus ε_λ , are set by the fundamental or doubled laser wavelength (800 nm and 400 nm in the Ti:Sapphire case). In the case of PtPOP we were able to tune ε_λ between 100 and 35000 M⁻¹cm⁻¹ by scanning the TOPAS output wavelength over the absorption band centered around 370 nm (see Figure 2.2). However, care should be taken in doing this. The laser penetration depth strongly depends on ε_λ in the OD > 3 regime. For short penetration depths, the local excitation yield might be quite high, but the effective excitation yield probed by the X-rays (penetrating the entire sample) is much lower in such cases. The S/N of the transient signal would therefore decrease. Ideally, one adjusts ε_λ in order to obtain a homogeneous excitation profile for the entire X-ray probe volume, while at the same time all laser photons are absorbed, *i.e.* $\varepsilon_\lambda c_{\text{mol}} d \simeq 2 \text{ OD}$. Homogeneous excitation also has the advantages of a smaller probability of non-linear excitation processes (*e.g.* two-photon absorption) and less aggregation at the walls of the flow capillary/cell.

The conditions for the time-resolved XAS experiment on PtPOP were chosen with the goal of optimizing the S/N ratio according to the above considerations: a) the path length $d = 500 \mu\text{m}$ was the shortest possible, limited by the technical difficulties in making smaller capillaries; b) the sample concentration $c_{\text{mol}} = 10 \text{ mM}$ is determined by the maximum laser power (40 $\mu\text{J}/\text{pulse}$) from the TOPAS at 390 nm (the number of molecules was matched to the number of laser photons per pulse); c) the laser spot size is determined by the damage threshold of the capillary (see Section 5.2); d) the excitation wavelength is chosen in order to ensure a uniform penetration through the entire sample (OD of ~ 2). Based on the above arguments, one would expect a decrease in signal magnitude for an increased value of ε_λ , while the other conditions remain the same. For excitation at 370 nm, for example, $\varepsilon_{\lambda=370 \text{ nm}} = 34000 \text{ M}^{-1}\text{cm}^{-1}$ and the laser penetration depth (1% cut-off level) is only 60 μm . The X-rays therefore see only 60 μm of excited sample on a background of the remaining 440 μm of unexcited (ground-state) sample, seemingly an unfavorable condition. However, it turned out that the signal for 370 nm excitation is in fact a factor

of 2-3 higher compared to excitation at 390 nm, as seen in Appendix F. This is another indication that the relationship for f as given in Equation (5.15) is not generally valid. The reason for these discrepancies are not fully clear at present. More systematic studies are needed in order to better understand the factors influencing the excitation yield under realistic conditions of the pump-probe XAS experiment. In any case, from the above it is clear that we can not rely on theoretical models for calculating f . In the ideal case, f is determined by laser-only pump-probe experiments, but it is seen in Section 8.2 that this is not always possible with sufficient accuracy. In the latter case, f must be derived from the transient XAS signal itself, which is done for the case of PtPOP as described in Section 8.3.

5.5 Femtosecond pump-probe laser setups

This Section provides the technical background of the ultrafast laser pump-probe measurements performed in this thesis. Section 5.5.1 describes the conditions of the transient absorption experiments belonging to the data presented in Chapter 6 and Section 8.2. The technical details of the time-resolved emission experiments of Section 6.1 are given in Section 5.5.2.

5.5.1 Broadband transient absorption setup

The transient absorption (TA) experiments were performed using the femtosecond laser system at the SLS. The setup is based on 100 MHz Kerr-lens mode-locked Ti:Sapphire oscillator (*Femtolasers*) pumped by a 5 W, 532 nm, continuous-wave (CW) Verdi V5 laser (*Coherent*). The oscillator delivers 20 fs, ~ 4 nJ seed pulses directed into the 1 kHz Ti:Sapphire regenerative amplifier system (*Positive Light*) pumped by a 10 W, 532 nm, CW Verdi V10 laser. The amplifier provides ~ 90 fs, ~ 1.8 mJ pulses centered at ~ 795 nm ($\Delta\lambda \simeq 5$ nm). A band-pass filter (BPF) ($\Delta\lambda = 12$ nm) between the oscillator and amplifier reduces the band width of the seed pulse allowing to reach short pulse lengths after the compressor. The central wavelength of this filter could be used to slightly tune the output wavelength of the amplifier. The pulse length was minimized by looking at the auto-correlation signal while slightly moving the compressor grating. This laser system was also used for the time-resolved XAS measurements described in Section 5.4.2 and Chapter 8.

The pump-probe setup is depicted in Figure 5.6. A 20/80% beam splitter (BS) divides the 795 nm amplifier output into a high-power pump branch and a low-power probe branch. The excitation beam was obtained from a TOPAS (*Light Conversion Ltd.*) in

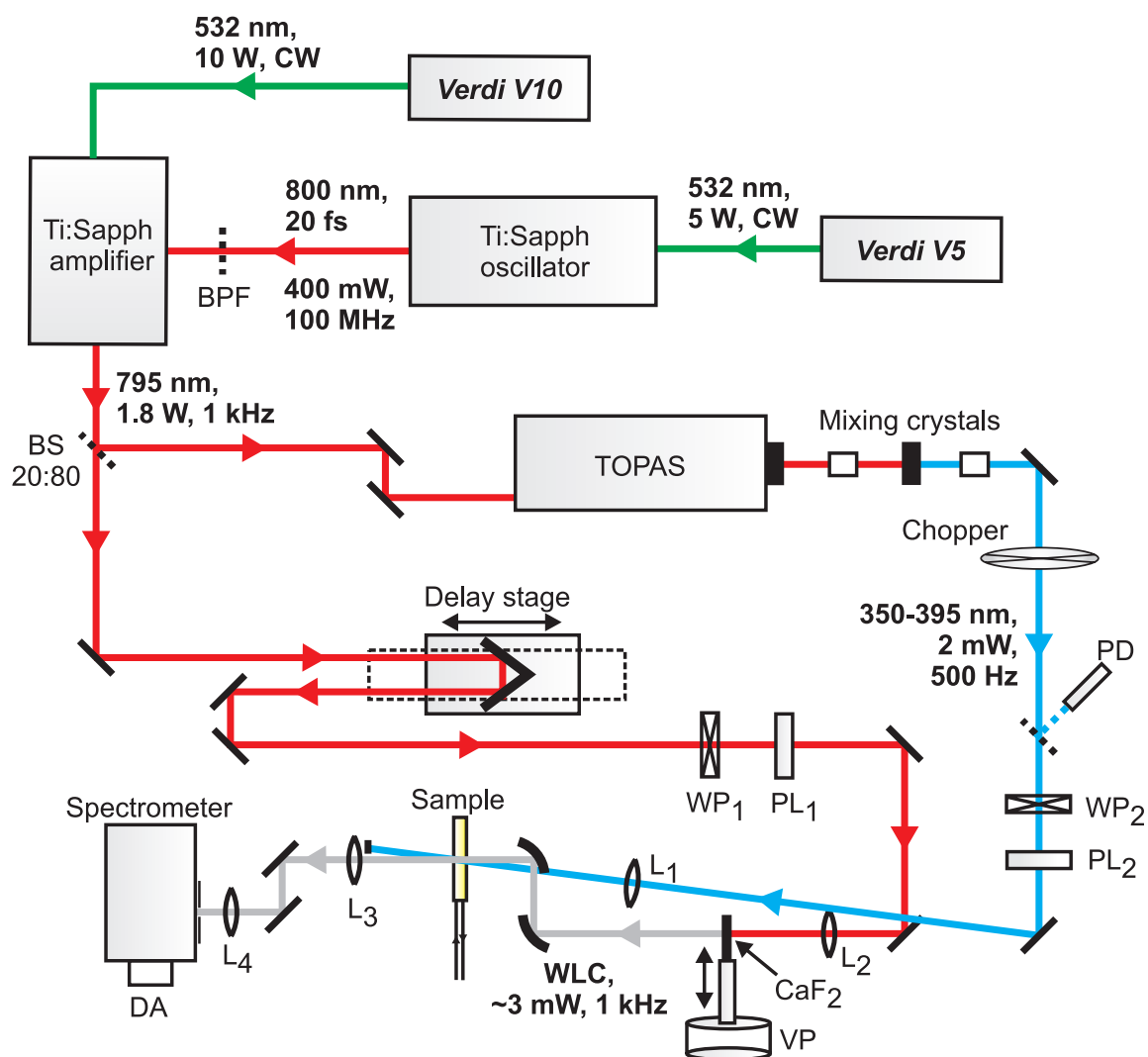


Figure 5.6: Sketch of the pump-probe setup implemented at the *SLS*. The abbreviations are given in the text and in the Abbreviations section.

the wavelength region 350-390 nm. The output pulse length is approximately 90 fs. A **white-light continuum (WLC)** probe beam (330-800 nm) was generated by focusing a small part of the fundamental output into a 2 mm thick CaF_2 window which was oscillating at a frequency of ~ 2 Hz using a **vibrating plate (VP)** (*PASCO scientific*). The vibrating was necessary to prevent the crystal from damaging. The **WLC** was focused on the sample using refractive optics (90° off-axis parabolic Al mirrors) in order to avoid dispersion. The pump and probe beam diameters were fixed to $130 \mu\text{m}$ and $55 \mu\text{m}$, respectively. In the optical **TA** measurements of Chapter 6, a typical excitation power is 2 mW at 500 Hz (varying between 1 and 3 mW for various measurements), while the measurements in preparation of the time-resolved **XAS** experiment (Section 8.2) were performed using the

full range of the TOPAS output (up to ~ 50 mW). The power of the excitation beam was adjusted using a combination of a wave plate (WP) and a polarizer (PL). This was also used to set the relative pump and probe electric-field polarization vectors to the magic angle (54.7°) in order to exclude kinetic signals resulting from rotational diffusion [199]. The overlap of the pump and probe beams was achieved by optimizing the transient signal of the laser dye DCM [271]. The pump beam was chopped at the repetition rate of 500 Hz, whereas the probe beam was detected at the nominal frequency of the laser (1 kHz). A small fraction of the pump beam is deflected by a thin quartz coverslip to a photo-diode (PD) (*Pascher Instruments*) in order to correct for the pump pulse intensity. The probe pulse is delayed with respect to the pump pulse using a motorized delay stage (max. delay ~ 1.5 ns). For the optical measurements of Chapter 6, the sample is contained in a 0.2 mm-thick flow cell with 1 mm thick quartz windows flown fast enough to refresh it after each pair of pump and probe laser pulses. The measurements performed to estimate the excitation yield in the time-resolved XAS experiment (Section 8.2) were done using the flow-capillary setup described in Section 5.2. After the sample, the probe beam was re-collimated and focused on the entrance slit of a grating monochromator (*Acton SpectraPro 2300i*) coupled with a 512 pixel diode array (DA). The energy calibration of the monochromator was measured and corrected using an Hg/Ar pen ray lamp. A monochromator grating of 150 lines/mm (500 nm blaze) was used in order to cover a broad spectral range between 330-680 nm. All mirrors in the probe branch were either gold mirrors or broadband dielectric mirrors for the range 750-1300 nm. The pump branch consisted of mirrors that are coated for the UV spectral region 350-420 nm. The white-light detection branch is setup with UV-enhanced Al mirrors and uncoated lenses.

The data acquisition system (*Pascher Instruments*) uses the trigger from the laser system to detect the dispersed probe pulses at a 1 kHz repetition rate and the pump intensity at a 500 Hz repetition rate. Before the measurement the pump intensity is measured and assigned a scaling factor of 1.0. During the experiment the pump intensity for every single measurement is compared to this average and the signal is scaled up or down depending on whether the measurement is lower or higher than the initial value. Adjacent pairs of pumped and unpumped spectra for each laser shot are measured and after subtraction the TA spectra for each pair of pulses are obtained. The TA signals are expressed in OD units, where ΔOD represents the change in optical density. A total of 500 (1 s) of such pair measurements are averaged together and saved. Repeated measurements for each delay line position are averaged together using the software (*FS version 5.6.4.9, Pascher Instruments*).

The **group velocity dispersion (GVD)** of the **WLC** beam was measured in neat solvent exploiting the **cross-phase modulation (CPM)** [272] signals around time zero. The latter can also be used to determine the **instrumental response function (IRF)** (pump-probe cross-correlation) of the system resulting in a **FWHM** value of ~ 130 fs.

5.5.2 Polychromatic luminescence up-conversion setup

In luminescence (fluorescence) up-conversion, the time-dependent emission from the excited sample is focused on a non-linear crystal together with a short pulse called the gate pulse. According to the phase-matching conditions, the non-linear process **sum-frequency generation (SFG)** takes place in the crystal. The resulting up-converted signal after the crystal has a frequency that is the sum (or difference) of the frequencies of the fluorescence and gate beams. By changing the delay of the gate pulse with respect to the excitation pulse, one can map out the time-dependent fluorescence signal. In a simple picture, the **IRF**, that characterizes the time resolution of the technique, is given by the convolution of the excitation and the gate pulse width. For laser pulses of ~ 50 fs this gives an **IRF** of below 100 fs. The up-converted fluorescence signal is filtered in order to remove pure excitation and gate frequencies and their up-converted companions. Consequently, the signal is dispersed in a spectrometer and sensitively detected with a back-illuminated cooled **charge-coupled device (CCD)** camera. The bandwidth of the signal at one angle of the non-linear crystal is ~ 10 nm. By rotating the crystal for each time delay, one can record the whole spectrum within short time. Repeating this for many different time delays, one finally obtains a **two-dimensional (2D)** wavelength-time plot.

Figure 5.7 shows a sketch of the fluorescence up-conversion setup that was used during the measurements on **PtPOP**, which are presented in Section 6.1. In the following we describe the purpose and characteristics of the different elements of this setup. For a more detailed description of the setup, including theoretical considerations for improved up-conversion efficiency, is referred to reference [273]. The 220 kHz amplified laser system delivers ~ 50 fs pulses with an energy of about $4 \mu\text{J}$ per pulse at 800 nm. The absorption spectrum of **PtPOP** peaks around 370 nm, while almost no absorption is left around 400 nm. Therefore it was necessary to generate an excitation wavelength below 800 nm from which wavelengths < 400 nm can be generated by **single-harmonic generation (SHG)** in a **BBO** crystal. For this purpose a $2 \mu\text{m}$ nitrocellulose pellicle was placed within the amplifier cavity with an inclination of about 45° and the repetition rate of the amplifier was reduced to 75 kHz to prevent the pellicle from burning. This resulted in an output wavelength of about 760 nm.

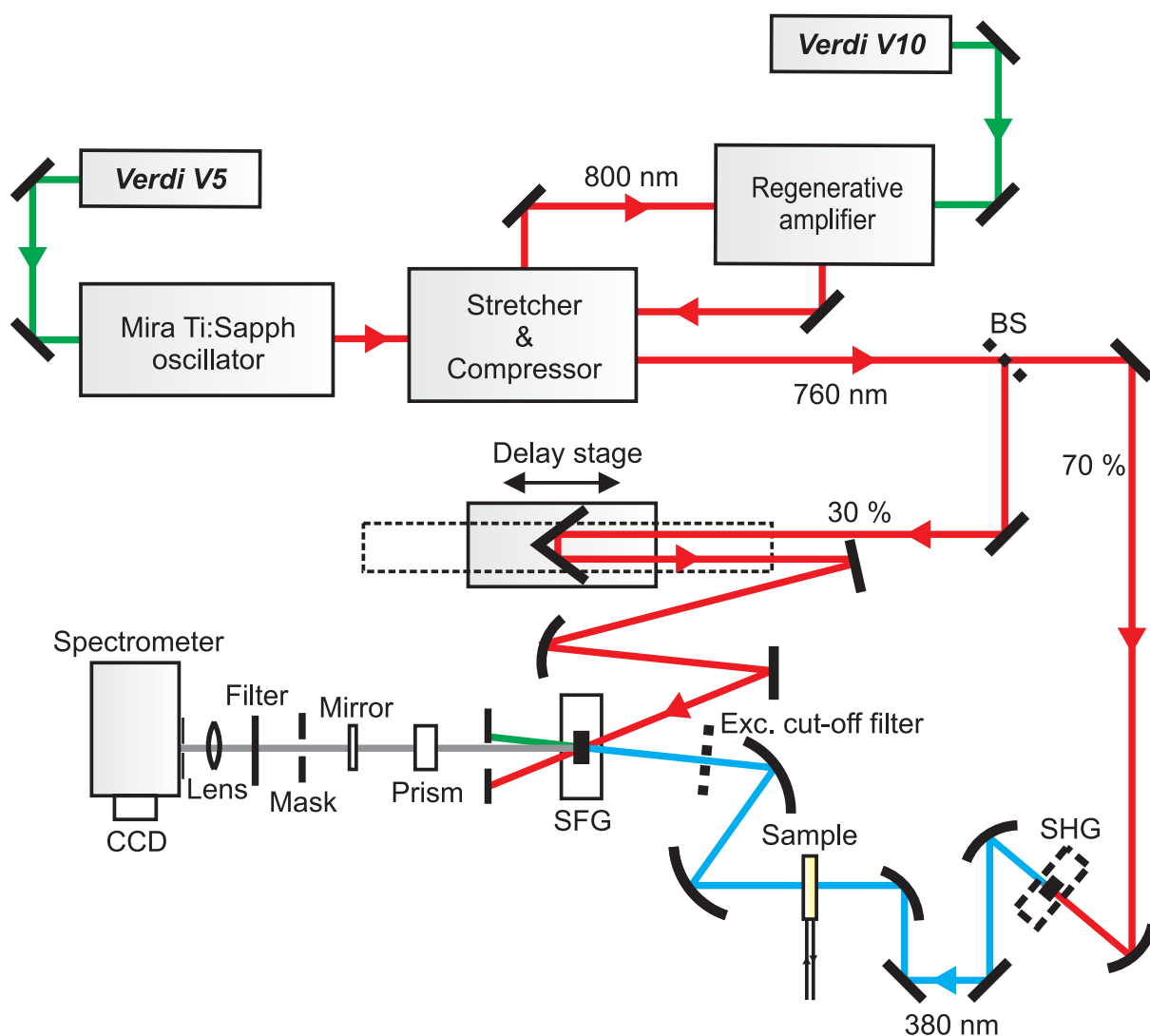


Figure 5.7: Sketch of the polychromatic fluorescence up-conversion setup. A nitrocellulose pellicle within the cavity of the amplifier detunes the output wavelength to 760 nm. The excitation cut-off filter was removed during the experiment.

Both the oscillator and the amplifier are pumped by solid-state diode-pumped frequency-doubled Ni:Vanadate lasers (*Verdi, Coherent*) providing a 532 nm output of 5 and 10 W respectively. The 760 nm beam had a power of ~ 130 mW after the compressor and is split into two branches in the ratio 30/70%. The 70% beam was used to generate 2-3 mW of excitation light with a wavelength of 380 nm by frequency doubling in a BBO crystal. The autocorrelation of the gate pulse was ~ 190 fs, which corresponds to a pulse length of ~ 130 fs. The excitation pulses after frequency doubling are expected to be shorter than this, because of the quadratic power dependence of the SHG. The 30% 760 nm beam is used for gating. The time delay is changed by moving a retroreflector on a motorized

translation stage. In order to avoid **GVD**, only refractive optics are used for focussing. The fluorescence is collected over a large solid angle by an off-axis parabolic mirror. Just before the non-linear crystal, the excitation light is usually removed from the fluorescence signal by an excitation cut-off filter in combination with a mask of 1×1 mm that blocks the direct excitation beam. Because the excitation at 380 nm lies very close to and partially overlaps with the fluorescence spectrum, the excitation cut-off filter was removed in the course of the experiment. Removal of the excitation cut-off filter also resulted in a smaller **GVD**. However, pre- and post-pulses were visible in the spectral region close to 380 nm rendering the detection <400 nm still difficult. The focused fluorescence and gate beams are overlapped in the non-linear crystal where the **SFG** takes place. The direct unconverted beams are blocked by a mask just after the crystal. The remaining up-converted excitation and the up-converted gate beams are reduced by combination of a prism, a mask and a filter (*Schott UG11*). The up-converted fluorescence signal is focused on the slits of the spectrometer. For each time delay one records an entire fluorescence spectrum by rotating the non-linear crystal. In the present experiments, the integration time per spectrum at one time delay was 20 s. The sample is flown through a closed quartz cell with a path length of 500 μm driven by a gear pump. The flow speed was about 21 ml/s. The spot size of the excitation beam in the sample was ~ 30 μm . A strongly fluorescing dye (**DCM** in ethanol) was placed in the sample position for alignment purposes. The fluorescence from the dye was overlapped with the gate beam by placing a pinhole at the position of the non-linear crystal.

5.6 Synthesis procedure of $(\text{TBA})_4[\text{Pt}_2(\text{P}_2\text{O}_5\text{H}_2)_4]$

In this Section a detailed description of the synthesis procedure of $(\text{TBA})_4\text{PtPOP}$ is given [274].

First step: Synthesis of K_4PtPOP

It is recommended to finish this part in one day and to start early in the morning as the day may be long if one scales up the reaction. One should try to work as much as possible under dark conditions. If not new, the phosphonic acid has to be dried under vacuum overnight prior to the synthesis.

1. Put about 100 ml distilled water, constantly under argon bubbling, in a 50 mL erlenmeyer (the exact amount is not very important, this is mostly a source of degazed water for recrystallization).

2. In a 100 ml three-neck round bottom flask, 10 ml of distilled water is degazed by bubbling argon while heating at 70 °C for half an hour. One neck is for argon, the main neck is for the condenser, and the last one is for adding reactants (use a stopper when not adding reactants). It is important to use a much larger flask compared to the amount of water for easier evaporation of water at a later stage.
3. K_2PtCl_4 (2 grams) is added by portion and the mixture is further heated for 5 min. Then, with a pasteur pipette, a small amount of the solution is taken to check if all platinum is solubilized (it is ought to be a red clear solution). If it is still a suspension, add 1 ml of the degazed water from the erlenmeyer and heat further for 5 min. Continue until a clear red solution is obtained.
4. Add by portion 7.3 grams of phosphonic acid $\text{P}(\text{OH})_3$ over 10 minutes.
5. Heat at 95-100 °C for 3 hours, always under argon and protected from light. A clear yellow solution should be obtained (can be checked with a pasteur pipette). If the solution is still reddish, heat further. In case it precipitates, add degazed water and heat further.
6. While still heating at 95-100 °C, stop with bubbling argon and replace the argon arrival with a stopper. Then, replace the condenser with a stopcock connected to a water pump. Run water pump while heating until a yellow solid is obtained.
7. During that time, degaze 500 ml of methanol and 500 ml of acetone in an erlenmeyer.
8. As soon as the yellow solid is obtained, add 50 ml of degazed methanol and use a spatula to obtain a suspension. Pour the suspension in an empty 500 ml erlenmeyer constantly under argon. Repeat this with 50 ml of fresh degazed methanol until almost no solid remains in the round bottom flask. Finish with degazed methanol until a total of 250 ml is reached. Add 250 ml acetone. Filter on a fritted glass (porosity 4) and wash with methanol and acetone. Dry for about an hour. A green luminescent, pale yellow solid should be obtained. At that moment, it might look pale orange solid, which is not a problem. If needed, one can stop at that stage and continue the other day.
9. While the compound is drying, prepare 50 ml of degazed water, 500 ml of degazed methanol and 500 ml of degazed acetone.
10. Put the dried solid in a 1 liter erlenmeyer and use a very small amount of degazed water to rinse the fritted glass to avoid big losses. Dissolve the solid in a minimum

of degazed water. It takes a while to dissolve, sonication may help. However, the compound is very soluble in water, it is just slow to dissolve. Therefore, one should not add too much water too quickly. Pour water at a rate of 1/2 ml every time. At maximum 5 ml should be added, but a smaller amount (3-4 ml) is better.

11. Add 250 ml degazed methanol, shake the solution. Then add 250 mL acetone and shake again. Filter on a fritted glass (porosity 4) and wash with the remaining methanol and acetone. Dry overnight. About 1.7 gram of a pale yellow solid should be obtained.

2 g per batch is found to be the most practical scale. A larger scale makes precipitation hard because a large amount of solvent is needed and filtration become long. It should still be fine on a 3-4 grams scale, but on a 10 g scale, the yield drops dramatically. This is mostly because good precipitation is difficult to achieve (3 liters of methanol and 3 liters of acetone should be used, in a 6 liters erlenmeyer). On a 10 g scale, one can obtain about 5 grams K_4PtPOP .

Second step: cation exchange

It is important to work under dark conditions for this step.

1. Dissolve ~ 1 g K_4PtPOP in 15-20 ml degazed water.
2. Under stirring, add tetrabutyl ammonium chloride (TBACl) by portion until green crystals appear (about 3-4 grams TBACl per 1 gram K_4PtPOP). Store the solution with the crystals in the fridge for 1-2 hours. Also store some degazed acetone in the freezer and degazed water in the fridge. Prepare a degazed diethyl ether solution.
3. Filter the precipitation on fritted glass (porosity 4), wash with cold degazed water (only once with about 20 ml), wash with very cold methanol (twice with about 10-15 ml each) and wash with degazed diethyl ether (300 ml totally).
4. Dry under vacuum.
5. About 1.5 grams of the strongly green luminescent, yellow solid is obtained.

Chapter 6

Femtosecond optical spectroscopy

This Chapter presents the results of the femtosecond optical measurements on **PtPOP**. The polychromatic **fluorescence up-conversion (FU)** results are presented in Section 6.1. They identify the ultrafast relaxation processes of vibrational cooling and wave packet dynamics in the $^1A_{2u}$ state, which are corroborated and complemented by the broadband **transient absorption (TA)** results, given in Section 6.2. We have investigated the excited-state relaxation dynamics for different excitation wavelengths within the $^1A_{1g} \rightarrow ^1A_{2u}$ absorption band around 370 nm (Section 6.2.2) and for **PtPOP** dissolved in a broad range of solvents (Section 6.2.3). A **singular value decomposition (SVD)**, **global fit (GF)** and **global analysis (GA)** of the **TA** data (see also Appendix D), based on a simple two-state relaxation model, have been used to quantify and compare all relaxation components (Section 6.2.1). Section 6.2.4 describes the results of numerical wave packet simulations based on dynamical **Franck-Condon (FC)** overlaps which are used to model the quantum-mechanical spectral signatures in the time-resolved stimulated emission spectrum. Finally, in Section 6.3 we discuss the mechanisms of vibrational cooling in the $^1A_{2u}$ state and intersystem crossing. The latter process is rather slow in **PtPOP** which is correlated with the large energy gap between the lowest-lying $^1A_{2u}$ and $^3A_{2u}$ states and other singlet and triplet states. Section 6.4 summarizes and concludes this Chapter.

The results presented in this Chapter are in part published in reference [275].

6.1 Fluorescence up-conversion results

Figure 6.1a shows a typical **two-dimensional (2D)** time-wavelength plot of the time-resolved fluorescence spectrum obtained upon excitation of aqueous **PtPOP** at 380 nm. Due to excessive scatter from the excitation beam, only the red part >400 nm of the fluorescence band could be detected (see Section 5.5.2). Cuts at fixed emission wavelength provide kinetic traces, shown in Figure 6.1b. The emission in the 400 nm region is due to

fluorescence from the initially excited ${}^1A_{2u}$ state [148]. At least two kinetic components are contained in the data and the initial emission intensity shows clear modulations (see insets) on the time scale of hundreds of fs due to vibrational coherences (wave packets, see Chapter 3) in the ${}^1A_{2u}$ state potential.

Kinetic traces at 4-5 fixed wavelengths for PtPOP dissolved in water (Figure 6.1b) and ethanol (Figure 6.2a) were globally fitted to the following function:

$$\begin{aligned}
 f_{\text{FU}}(t) = & A_2 \cdot \text{ExpErf}[B, t_0, \tau_2, t] \cdots \\
 & + A_3 \cdot \text{ExpErf}[B, t_0, \tau_3, t] \cdots \\
 & + e^{(t-t_0)/\tau_C} \cdot A_4 \cdot \cos \left[\frac{2\pi \cdot t}{T_{\text{ES}}} + \phi \right] \cdot \text{ExpErf}[B, t_0, \tau \rightarrow \infty, t]
 \end{aligned} \tag{6.1}$$

with $\text{ExpErf}[B, t_0, \tau_i, t]$ defined in Equation (D.3) (the ErfExp function results from convoluting an exponential with a Gaussian). B in Equation (6.1) is the **full-width-half-maximum (FWHM)** of the Gaussian **intrumental response function (IRF)**, t_0 is the wavelength dependent time zero and τ_i is the time constant of the i^{th} one-exponential decay with amplitude A_i (time in which the signal decays to $1/e$ of its initial value). The global **IRF** parameter B was fixed to 190 fs as obtained from the autocorrelation of the gate pulse (see Section 5.5.2). The τ_2 and τ_3 time constants (both global parameters) in Equation (6.1) represent the kinetic decay components (with amplitudes A_2 and A_3 , respectively). The third term in Equation (6.1) represents the oscillatory dynamics with period T_{ES} , coordinate damping time τ_C^* (both global parameters), phase ϕ and amplitude A_4 (both local parameters).

The fitted kinetic time constants are summarized in Table 6.1. The long decay component (τ_3) can be identified as the rate of **intersystem crossing (ISC)**, while the short

*The coordinate damping time τ_C is equal the coherence decay time T_2 for a multilevel system, as discussed in Section 3.1.1.

solvent	τ_2 / ps	τ_C / ps	τ_3 / ps	T_{ES} / fs
water	1.5(0.2)	1.6(0.3)	15.4(0.3)	225(1)
ethanol	2.0(0.2)	2.3(0.2)	28.9(0.4)	224(1)

Table 6.1: Fitted relaxation time constants (uncertainties in brackets) for PtPOP in water and ethanol obtained from a **GF** analysis of the time-resolved **FU** data (excitation at 380 nm). τ_2 is the vibrational cooling time, τ_C is the coordinate damping time, τ_3 is the intersystem crossing time and T_{ES} is the coherent oscillation period in the excited state potential.

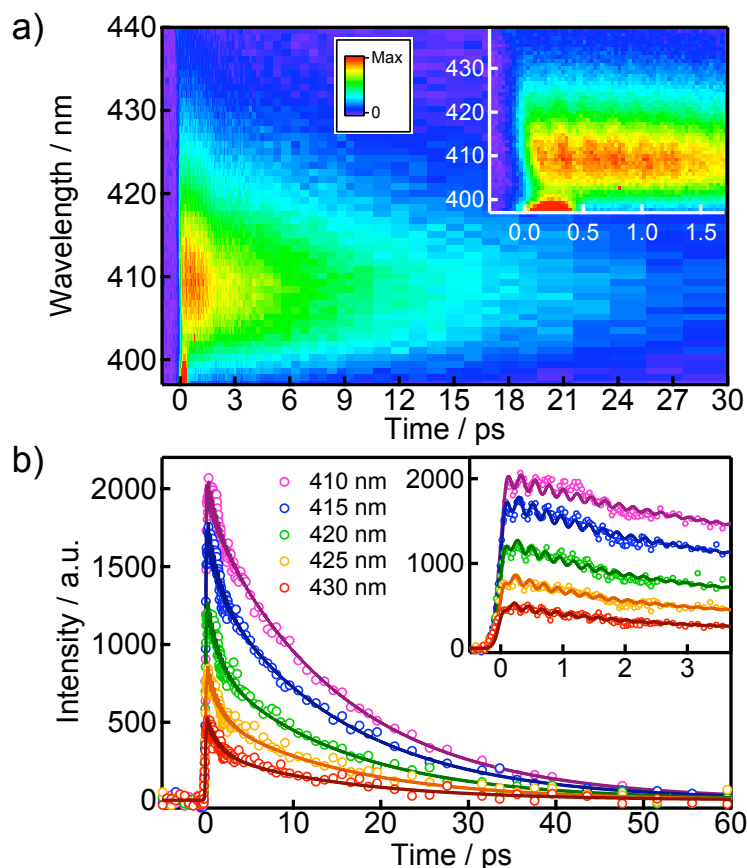


Figure 6.1: Time-resolved fluorescence data for PtPOP in water excited with a ~ 120 fs laser pulse at 380 nm; a) 2D time-wavelength plot of time-resolved fluorescence spectra. The inset shows a zoom into the initial 1.7 ps time window; b) Fluorescence time traces (open circles) at various wavelengths (same data as in a), together with their fit functions using a GF model (solid lines, see text). The inset shows a zoom into the initial 3.7 ps time window. The weak modulation during the first 3 ps is due to a slow fluctuation in the laser power.

one (τ_2), manifested as a narrowing of the emission band, is attributed to vibrational cooling in the singlet $^1A_{2u}$ state. The wave packet period of $T_{ES} = 224$ fs (149 cm^{-1}) is in good agreement with the vibrational wavenumber of 150 cm^{-1} for the Pt–Pt stretch in the excited $^1A_{2u}$ state obtained by steady-state absorption spectroscopy [129, 137]. Interestingly, both the rate of vibrational cooling and ISC exhibit a pronounced solvent dependence.

The data in ethanol have been measured without the excitation cut-off filter (see Section 5.5.2) so that kinetic traces at wavelengths < 400 nm could be recorded, shown in Figure 6.2b. Excessive scatter from the excitation beam at 380 nm leads to a large artefact around t_0 for traces at 396 and 399 nm. Furthermore, the trace at 396 nm contains an artefact caused by a post-pulse of the gate beam. It is seen in Figure 6.2b that the

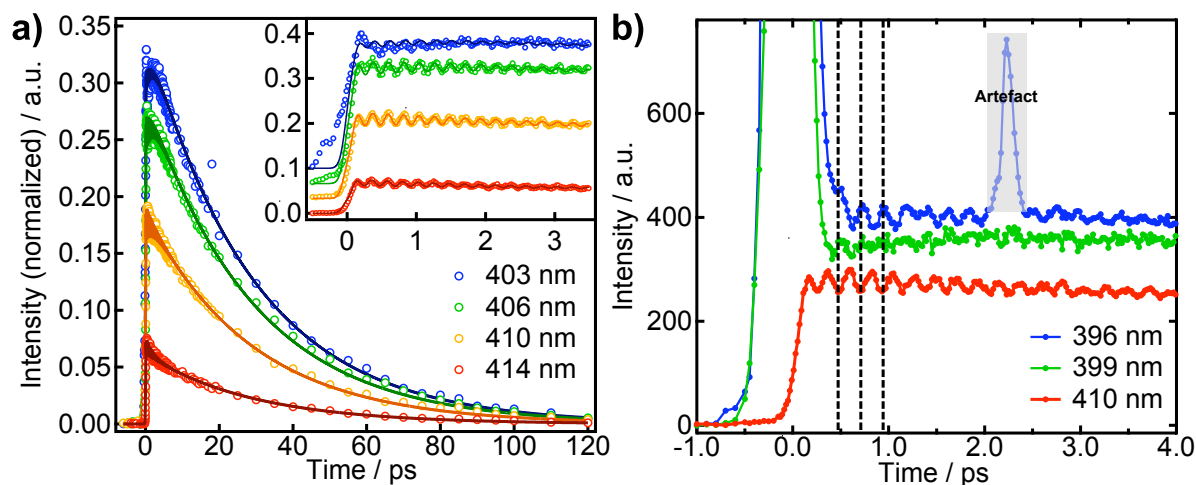


Figure 6.2: Time-resolved fluorescence data for PtPOP in ethanol excited with a ~ 120 fs laser pulse at 380 nm; a) Fluorescence time traces (open circles) at various wavelengths, together with their fit functions using a GF model (solid lines, see text). The inset shows a zoom into the initial 3.7 ps time window (traces are offset vertically for clarity). The traces are normalized to the detection band width (~ 4 nm) and the fluorescence band intensity at the corresponding wavelengths; b) Fluorescence time traces (dots) at three different wavelengths. The vertical dashed lines facilitate to see the π phase shift for traces at either side of the emission band. The peaks around t_0 and 2.25 ps (396 nm trace) are artefacts due to the excitation beam.

modulations exhibit a phase shift of approximately $\Delta\phi = \pi$ between the red and blue sides of the fluorescence band centered around 400 nm.

The FU results are complemented by detailed transient absorption (TA) studies for several excitation wavelengths in a broader range of solvents, described in the following sections.

Summary

The FU results establish the ISC from the $^1A_{2u}$ state to the $^3A_{2u}$ state on the time scales of 15 ps (in water) and 30 ps (in ethanol), vibrational cooling on the time scales of 1.5 ps (in water) and 2 ps (in ethanol), and coherent vibrations along the Pt–Pt bond with a period of ~ 224 fs and a coordinate damping time of ~ 2 ps. The pronounced solvent effect on the rates of vibrational relaxation and ISC are remarkable and will be discussed in detail later (Section 6.3).

6.2 Broadband transient absorption results

Figure 6.3a shows a representative set of time-wavelength TA data measured upon excitation at 370 nm into the $^1A_{2u}$ ($d\sigma^* \rightarrow p\sigma$) band of PtPOP in ethylene glycol.[†] All data have been corrected for group velocity dispersion (GVD) as described in Section 5.5.1.

In Figure 6.3, the spectra are characterized by four features: two excited state absorption (ESA) bands (positive change in optical density, but plotted against the negative ordinate axis), ground state bleach (GSB) (the dip at 370 nm is a pump artefact) and stimulated emission (SE) (both negative change in optical density, but plotted against the positive ordinate axis). The latter two overlap in the region 370-400 nm. The GSB does not decay on the longest time scale of our experiment (1.6 ns), suggesting that the final state is the triplet $^3A_{2u}$ state with a life time of several μs [129]. Based on the FU results of Section 6.1 (Figure 6.1a), the SE band around 400 nm is due to the singlet $^1A_{2u}$ state. The ESA bands around 335 nm (ESA_1) and 460 nm (ESA_2) are present at all time delays, but seem to red-shift on the time scale of several ps to tens of ps. The evolution is more pronounced for ESA_2 than for ESA_1 . Their large intensity indicate they belong to allowed transitions from the $^1A_{2u}$ (at early times) and $^3A_{2u}$ (at late times) excited states

[†]TA units are expressed as the optical density (OD), see Section 5.5.1.

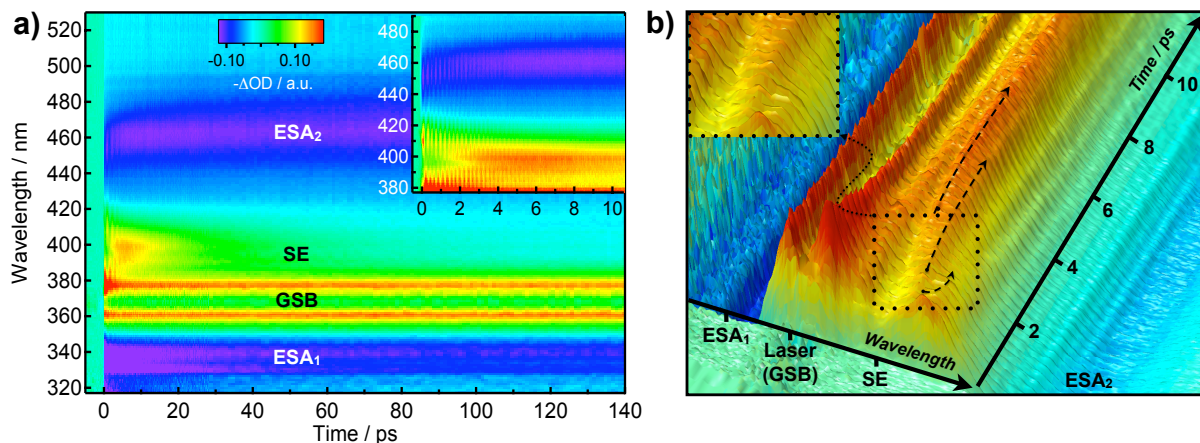


Figure 6.3: TA spectra for PtPOP in ethylene glycol excited with a ~ 100 fs laser pulse at 370 nm; a) 2D time-wavelength plot of TA data. The inset shows a zoom into the initial 10 ps; b) 3D time-wavelength- ΔOD plot zoomed into the region of the SE band which partially overlaps with the GSB in the region < 400 nm (same data as in a). One recognizes periodic intensity modulations and a spectral fine structure in the long-wavelength lobe of the SE band indicated by dashed arrows and magnified in the upper-left inset. The "hole" in the GSB band is a pump artefact. ESA = excited state absorption, GSB = ground state bleach, SE = stimulated emission.

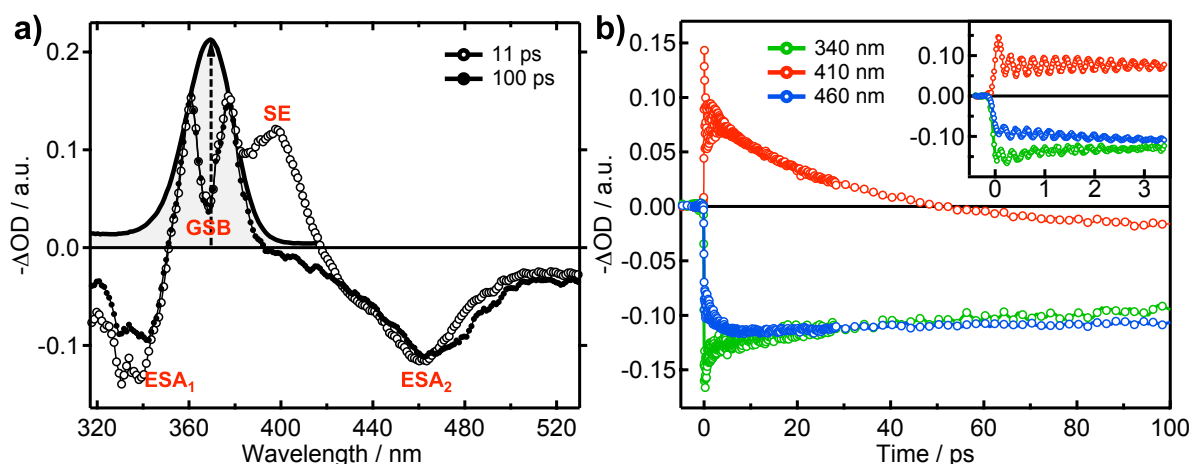


Figure 6.4: a) Representative TA spectra at 11 ps (open circles) and 100 ps (closed circles) after excitation at 370 nm into the $^1A_{2u}$ absorption band (dashed vertical arrow), together with a static absorption spectrum (black curve). The dip around 370 nm in the TA spectra is a pump artefact; b) Time traces at fixed wavelengths. The upper-right inset zooms into the initial 3.5 ps time window. ΔOD is the change in optical density (pumped - unpumped).

(vide infra). Figure 6.3b shows a 3D zoom into the region of the SE band. Just as the fluorescence band (Figure 6.1a), the SE spectrum differs from the steady-state emission fluorescence spectrum [117] indicating vibrationally "hot" (unrelaxed) emission that is not governed by Boltzmann statistics. A close inspection of the spectra in Figure 6.3b reveals a spectral substructure that initially decays in the very red wing while it increases closer to the center of the band around 400 nm. The central "hole" at early times is filled up on a time scale of ~ 2 ps. This fine structure is analyzed in detail in Section 6.2.4.

Cuts at fixed time delays deliver the corresponding transient spectra, which are shown in Figure 6.4a. The ESA around 335 nm could be assigned to the $A_{2u} \rightarrow A_{1g}$ ($\sigma d_{z^2} \rightarrow \sigma^* d_{z^2}$) transition based on the calculated $\sigma d_{z^2} - \sigma^* d_{z^2}$ splitting of ~ 4 eV (see Section 7.2.4 and reference [153]). The ESA around 460 nm may belong to the transitions from the A_{2u} singlet and triplet states to $^1,^3E_g$ states that can be described by the electronic configuration $(5d_{xz}, 5d_{yz})^7(6p\sigma)^1$ (the d_{xz}, d_{yz} manifold splits into $\pi(e_u)$ and $\pi^*(e_g)$ levels for a d^8-d^8 complex [124], see also Figure 2.1). The $A_{2u} \rightarrow E_g$ transition is dipole-allowed in D_{4h} point group symmetry, as seen from the character and product tables in Appendix E.

Additional information is contained in the kinetic traces, which for three characteristic wavelengths (340 nm, 410 nm and 460 nm) are shown in Figure 6.4b. They reveal dynamics on the time scales of hundreds of fs (modulations), a few ps and tens of ps, which can be, based on the above FU results, related to wave packet dynamics, vibrational cooling (in the $^1A_{2u}$ state) and ISC from the $^1A_{2u}$ state to the $^3A_{2u}$ state, respectively.

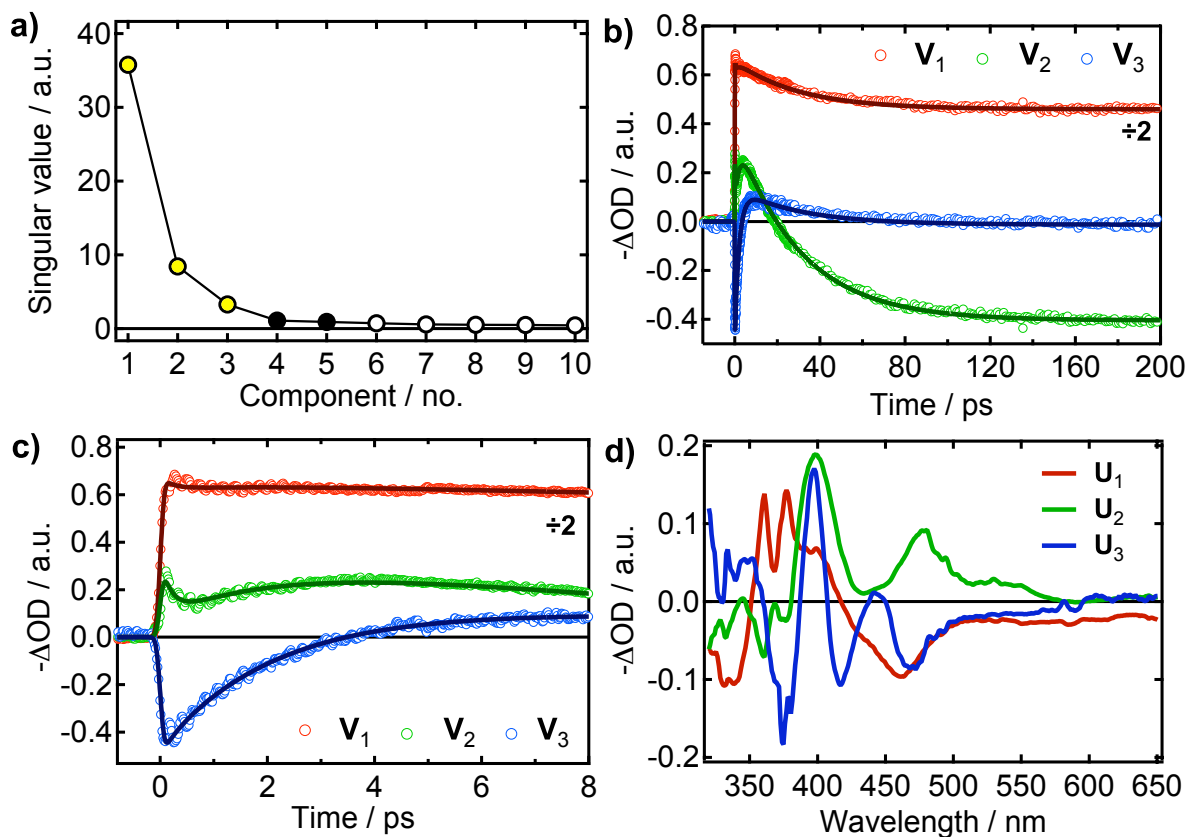


Figure 6.5: Results of the SVD-GF analysis of the ΔA data matrix of PtPOP in ethylene glycol excited at 370 nm. a) Singular values ordered from large to small. The components that are retained for analysis are indicated by yellow (kinetics) and black (wave packets, see Figure 6.7) dots; b) and c) The first three kinetic basis vectors $V_{1,2,3}$ scaled by their respective singular values and their fits according to Equation (6.2). The V_1 trace is scaled down for clarity; d) the first three basis spectra $U_{1,2,3}$.

The detailed analysis presented in the following sections allows us to quantify the time scales of these processes for various excitation wavelengths. In order to gain further insight into the mechanism of the relaxation processes, we have measured TA spectra for samples of PtPOP dissolved in water, ethanol and dimethylformamide (DMF). In addition, we will analyze the evolving spectral fine structure of the SE band seen in Figure 6.3b which is identified as resulting from vibrational cooling and quantum mechanical interference in the vibrational coherent superposition state.

6.2.1 Spectro-temporal decomposition

In order to quantify and assign the kinetic and spectral components, we performed a SVD analysis (see Appendix D) on the 2D data matrix. The 2-variable (λ, t) ΔA data

matrix was decomposed according to Equation (D.1). The five components with the largest singular values $s_{i=1-5}$ were retained for further analysis (see Figure 6.5), the other components mainly represent the stochastic noise of the measurement. Kinetic basis vectors \mathbf{V}_1 , \mathbf{V}_2 and \mathbf{V}_3 weighted by their respective singular vectors (s_1 , s_2 and s_3) were globally fitted to a kinetic two-state model involving the lowest singlet and triplet A_{2u} states only, according to the equation

$$\begin{aligned}
 f_{\text{kin}}(t) = & A_1 \cdot \text{ExpErf}[B, t_0, \tau_1, t] \cdots \\
 & + A_2 \cdot \text{ExpErf}[B, t_0, \tau_2, t] \cdots \\
 & + A_3 \cdot \text{ExpErf}[B, t_0, \tau_3, t] \cdots \\
 & + A_4 \cdot (\text{ExpErf}[B, t_0, \tau_4 = 10 \mu\text{s}, t] - \text{ExpErf}[B, t_0, \tau_3, t])
 \end{aligned} \tag{6.2}$$

where $\text{ExpErf}[B, t_0, \tau, t]$ is defined in Equation (D.3) (the other parameters are defined for Equation (6.1)). Two independent exponential decay components (time constants τ_1 and τ_2) describe the vibrational energy relaxation within the initially excited $^1A_{2u}$ state, while the relaxation from the $^1A_{2u}$ to the $^3A_{2u}$ excited state (*i.e.* ISC) is modeled by an exponential decay and rise with a single time constant (τ_3) but with different amplitudes (A_3 and A_4 , respectively). The A_4 term in Equation (6.2) represents the arrival in the $^3A_{2u}$ state and its subsequent decay with a time constant of $\tau_4 = 10 \mu\text{s}$ (not detectable on the maximum time scale of the experiment). The GSB feature in the spectrum is not explicitly included in the present model, but it appears naturally from the SVD as a spectral region with identical decay and rise amplitudes (see Figure 6.6).

The results from the SVD-GF analysis on the GVD- and background-corrected $\Delta\mathbf{A}$ data matrix for PtPOP in ethylene glycol excited at 370 nm are shown in Figure 6.5. It is seen that the fit of the three largest kinetic basis vectors (Figures 6.5b and 6.5c) to the kinetic model of Equation (6.2) is satisfactory over the entire time range. The following three time constants were obtained: $\tau_1 = 260 \pm 20$ fs, $\tau_2 = 2.14 \pm 0.02$ ps and $\tau_3 = 30.3 \pm 0.2$ ps. The 30.3 ps decay is in good agreement with the long decay component in the FU data belonging to ISC from the $^1A_{2u}$ state to the $^3A_{2u}$ state, while the fast 260 fs[‡] and 2.1 ps (~ 2 ps in FU) decays represent vibrational depopulation and cooling in the singlet state. The IRF parameter B was fitted to ~ 130 fs, which is in good agreement with values obtained from measurements of the coherent cross-phase modulation (CPM)

[‡]It is noted that it was not necessary to include this component in the fit model of the FU data. Due to the limited FU data quality and the small spectral range of detection, the observation of this fluorescent component could have been obscured.

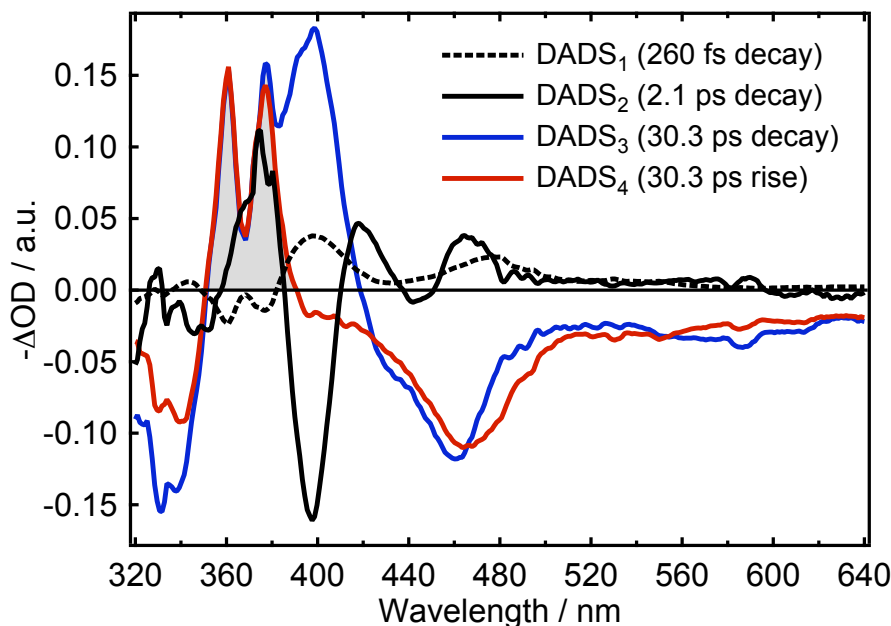


Figure 6.6: Decay-associated difference spectra (DADS) extracted from the TA data after SVD-GF analysis using Equation (6.2). The greyed out area indicates the GSB region, where the dip around 370 nm is a pump artefact.

effects in the pure solvent and in a thin quartz cover slip (see Section 5.5.1).

Figure 6.6 shows the decay associated difference spectra (DADS) reflecting the relative spectral contributions of each time component according to Equation (D.4). DADS_3 associated with the departure from the $^1\text{A}_{2u}$ state exhibits the characteristic SE band around 400 nm, which is absent in the DADS_4 spectrum belonging to the $^3\text{A}_{2u}$ state. The ESA centered at 460 nm (ESA_2) is slightly shifted and broadened in the $^3\text{A}_{2u}$ state compared to the $^1\text{A}_{2u}$ state, but overall the ESA spectra of the two states look very similar. DADS_2 reflects the vibrational cooling in the $^1\text{A}_{2u}$ state. Its decay with a time constant of 2.1 ps causes a narrowing of the singlet state SE band (also seen in Figure 6.1a) and a red shift of the ESA_2 absorption. The amplitude of the τ_1 component is small, but its inclusion in the kinetic model has been found to considerably improve the fit of the short-time dynamics in the SVD kinetic basis vectors. This component is longer than the CPM artefact around time zero (see Section 5.5.1).

After having quantified the kinetic decay components, we now turn to the analysis of the vibrational coherences which are mainly contained in the kinetic basis vectors \mathbf{V}_4 and \mathbf{V}_5 (Figure 6.7a). These components can therefore be used to accurately determine the characteristic time constants of the wave packet dynamics, independent from the kinetic processes as analyzed above. The vectors were linearly combined according to

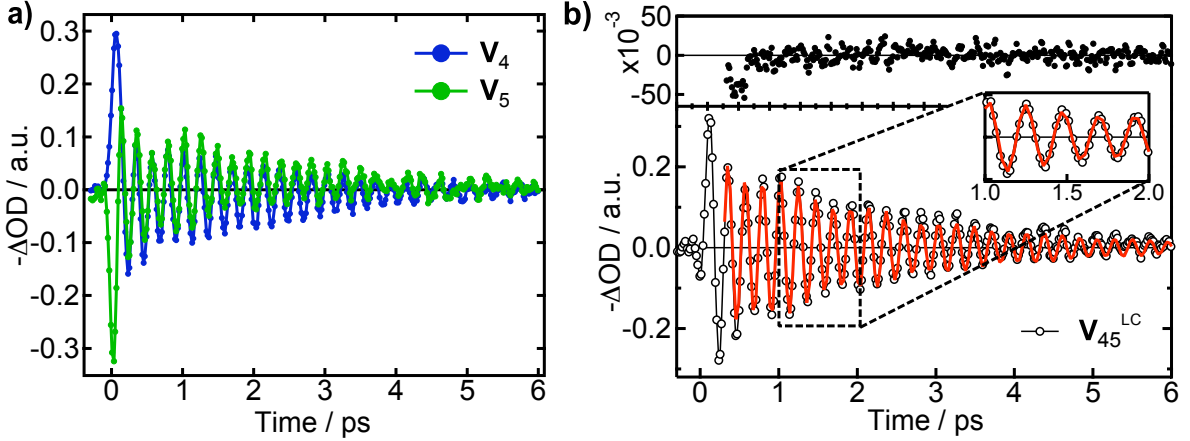


Figure 6.7: a) Kinetic basis vectors \mathbf{V}_4 and \mathbf{V}_5 from the SVD analysis; b) Linear combination $\mathbf{V}_{45}^{\text{LC}}$ of kinetic basis vectors \mathbf{V}_4 and \mathbf{V}_5 from the SVD (open black circles), together with the fit to an exponentially damped superposition of two cosine functions with different periods (red curve; Equation (6.3)). Fit results: $T_{\text{ES}} = 224$ fs, $T_{\text{GS}} = 281$ fs, $\tau_C = 2.1$ ps. The inset shows a zoom into the time window 1-2 ps. The black dots on the top of the graph are the fit residuals.

$\mathbf{V}_{45}^{\text{LC}} = (s_4\mathbf{V}_4 + s_5\mathbf{V}_5)/(s_4 + s_5)$, with singular values s_4 and s_5 (see Appendix D). The resulting oscillatory trace shown in Figure 6.7b was fitted to a superposition of two cosine functions with different amplitudes (A_1 , A_2), phases (ϕ_1 , ϕ_2) and periods (T_{ES} , T_{GS}), multiplied by an exponential decay function with time constant τ_C representing the coordinate damping time of the wave packet dynamics, according to

$$f_{\text{osc}}(t) = e^{-(t-t_0)/\tau_C} \cdot \left(A_1 \cdot \cos \left[\frac{2\pi \cdot t}{T_{\text{ES}}} + \phi_1 \right] + A_2 \cdot \cos \left[\frac{2\pi \cdot t}{T_{\text{GS}}} + \phi_2 \right] \right). \quad (6.3)$$

An excellent fit is achieved for $T_{\text{ES}} = 224.0 \pm 0.1$ fs, $T_{\text{GS}} = 281 \pm 1$ fs and $\tau_C = 2.16 \pm 0.05$ ps (the fit region started around 300 fs to avoid the coherent CPM artefact around time zero). The $T_{\text{ES}} = 224$ fs component is identified as the Pt–Pt stretch vibration in the ${}^1\text{A}_{2\text{u}}$ excited state and is in very good agreement with the FU data (Table 6.1). The superimposed 280 fs oscillation, causing the ps beat pattern in Figure 6.7b, is due to coherent vibrational Pt–Pt stretch oscillations in the ground state (GS) potential that are excited via a resonant impulsive stimulated Raman scattering (RISRS) process [185]. The wavenumber of this component (119 cm^{-1}) is in good agreement with values from the literature [136, 137, 149]. It is noted that the coherent modulations strikingly persist for more than 5.5 ps after excitation (~ 25 oscillations, resulting in the very high precision of 0.1 fs in the fitted oscillation period T_{ES}). Furthermore, the excited state (ES) coherent oscillations are exceptionally harmonic and the coherence decay can be perfectly fit by a purely exponential function.

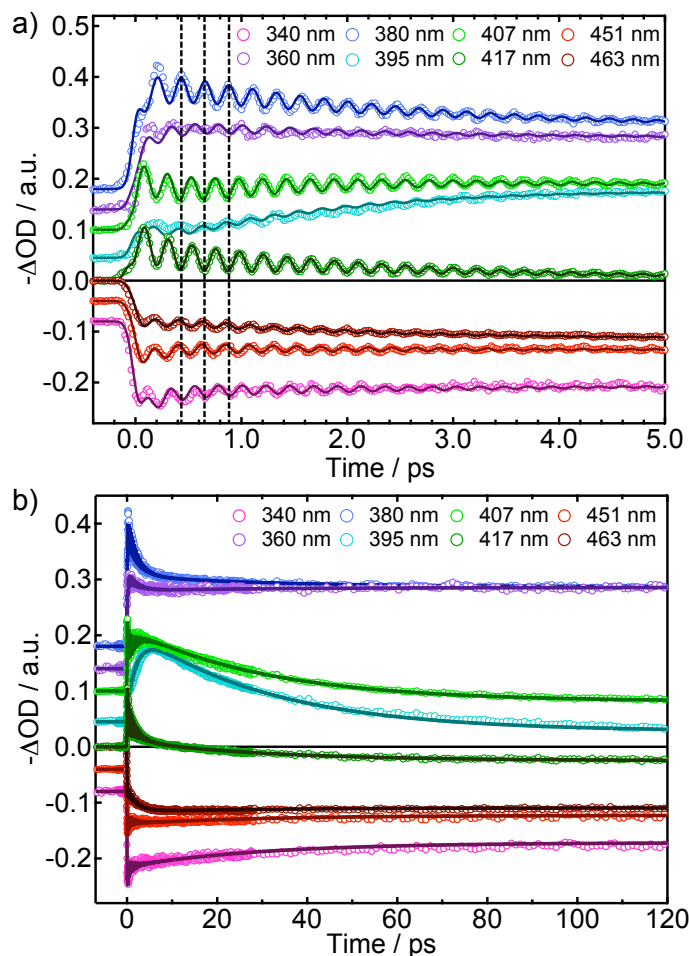


Figure 6.8: Kinetic traces at fixed wavelength, together with their fit functions using a **GA** model **PtPOP** in ethylene glycol excited at 370 nm. a) Short time range. The vertical dashed lines facilitate the observation of the phase shift of π between the oscillations at the red and blue sides of the **SE** band (e.g. 407 nm and 380 nm). b) Long time range. The traces have been offset vertically for clarity.

Global analysis

In addition to the **SVD-GF** analysis, we performed a **global analysis (GA)** of the transient absorption spectra without prior decomposition of the data. The **GA** was performed on a representative set of time traces at fixed wavelengths (total 8 traces) from the "raw" (λ, t) $\Delta\mathbf{A}$ data matrix. The choice of the wavelengths is supported by the fact that they cover the most relevant spectral regions where significant **TA** changes are observed, *i.e.* the **ESA** bands at 330 nm and 460 nm and the regions of the **SE** and **GSB** spectra around 360-420 nm, described in Figure 6.3. The traces were globally fitted to the equation

$$\begin{aligned}
f_{\text{GA}}(t) = & A_1 \cdot \text{ExpErf}[B, t_0, \tau_1, t] \cdots \\
& + A_2 \cdot \text{ExpErf}[B, t_0, \tau_2, t] \cdots \\
& + A_3 \cdot \text{ExpErf}[B, t_0, \tau_3, t] \cdots \\
& + A_4 \cdot (\text{ExpErf}[B, t_0, \tau_4 = 10 \mu\text{s}, t] - \text{ExpErf}[B, t_0, \tau_3, t]) \cdots \\
& + e^{(t-t_0)/\tau_C} \cdot A_5 \cdot \cos \left[\frac{2\pi \cdot t}{T_{\text{ES}}} + \phi \right] \cdot \text{ExpErf}[B, t_0, \tau \rightarrow \infty, t] \quad (6.4)
\end{aligned}$$

with ExpErf as defined in Equation D.3 (the other parameter definitions are given for Equations (6.2) and (6.3)). The amplitudes A_i and phase ϕ were fitted on a local basis (trace by trace), while B , t_0 , τ_i , τ_C and T_{ES} were taken as global parameters. Only one oscillatory component T_{ES} reflecting the coherent oscillations in the excited state potential was included in the fit function. The ground state wave packet oscillations were not included because they are very weak and only present in a small region of the spectrum (namely the GSB region around 370 nm). The following values were obtained from the fit: $\tau_1 = 0.04 \pm 0.03$ ps, $\tau_2 = 2.37 \pm 0.02$ ps, $\tau_3 = 30.5 \pm 0.2$ ps, $\tau_C = 1.93 \pm 0.04$ ps, $T_{\text{ES}} = 224.4 \pm 0.1$ fs. The GA fit result presented in Figure 6.8 shows a good match with the experimental traces over the whole spectro-temporal range. Except for the τ_1 time constant, the values obtained from the GA fit are in satisfactory agreement with the values from both the SVD-GF (Section 6.2.1) and the FU (Table 6.1) analyses. The time constant τ_1 could not be determined accurately by means of GA due to its small amplitude and the limited amount of data included in the fitting. However, as shown above, the noise suppression in the SVD-GF made it possible to determine this component with higher accuracy and precision ($\tau_1 = 260 \pm 20$ fs).

Summary

The TA spectrum of PtPOP is characterized by two ESA bands around 335 nm and 460 nm that shift slightly to the red in tens of ps, along with the decay of a SE band around 400 nm, and a GSB that stays up to the longest time scales studied. We identify the ESA bands as being due to transitions originating from the lowest $^1,^3A_{2u}$ states and the SE band as fluorescence from the initially excited $^1A_{2u}$ state. SVD-GF and GA analyses of the TA data, based on a simple two-state relaxation model, have been applied in order to quantify all relaxation components. For PtPOP in ethylene glycol excited at 370 nm, the following relaxation time scales were obtained: $\tau_1 \simeq 260$ fs, $\tau_2 \simeq 2.1$ ps (vibrational cooling), $\tau_3 \simeq 30$ ps (ISC), $T_{\text{ES}} \simeq 224.0$ fs, $T_{\text{GS}} \simeq 281$ fs (excited- and ground-state wave

packets, respectively) and $\tau_C \simeq 2.1$ ps (excited-state coherence decay). The TA results are in good agreement with the FU analysis (Section 6.1).

6.2.2 Excitation wavelength dependence

Transient absorption data sets were measured for different excitation wavelengths (355 nm, 360 nm, 370 nm and 380 nm) within the $^1A_{2u}$ -state absorption band. Both the SVD-GF and GA methods were applied in order to compare the time constants for the different excitation wavelengths. For all excitation wavelengths, the first 3 singular components after SVD contain most of the kinetics, while the fourth and fifth largest amplitude vectors contain the wave packet oscillations. The GF results (using Equation (6.2)) for the first three kinetic basis vectors are shown in Figure 6.9 and the obtained parameter values are given in Table 6.2. The value of τ_1 was fixed to 0.2 ps for the sake of comparison. Due to its small magnitude, it could not be accurately determined for the off-resonance excitation wavelength data sets ($\neq 370$ nm) which suffer from high noise levels. In addition, the amplitude of the τ_1 component was set to zero for kinetic vectors \mathbf{V}_1 and \mathbf{V}_3 because of its very small contribution to these two vectors (the τ_1 component is mainly contained in \mathbf{V}_2). The fitting results show that there is a pronounced effect on the time constant of vibrational cooling, τ_2 (see also Figure 6.10a), whereas the time constant of ISC, τ_3 , is, within the measurement uncertainty, insensitive to the excitation wavelength. It is also noted that the vibrational cooling times do not change linearly with the different amounts of total energy that are dissipated for the various wavelengths. Whereas ~ 2270 cm^{-1} is dissipated in 2.56 ps for 355 nm excitation, only 415 cm^{-1} is dissipated in 1.46 ps for excitation at 380 nm (the 0–0 transition is around 25900 cm^{-1} , see Section 3.2.1). Vibrational cooling thus gets slower, the lower the average vibrational energy in the excited state.

The corresponding DADS are given in Figure 6.11. Overall, the DADS look very similar for the different excitation wavelengths. However, a significant difference is seen for the DADS belonging to the τ_2 decay component which represents the narrowing of the SE

	355 nm	360 nm	370 nm	380 nm
τ_2/ps	2.56 ± 0.03	2.43 ± 0.03	2.13 ± 0.02	1.46 ± 0.04
τ_3/ps	31.3 ± 0.4	29.9 ± 0.3	30.5 ± 0.2	29.5 ± 0.2

Table 6.2: Results from the SVD-GF analysis for different excitation wavelengths. τ_2 is the vibrational cooling time and τ_3 is the intersystem crossing time. τ_1 was fixed to 0.2 ps.

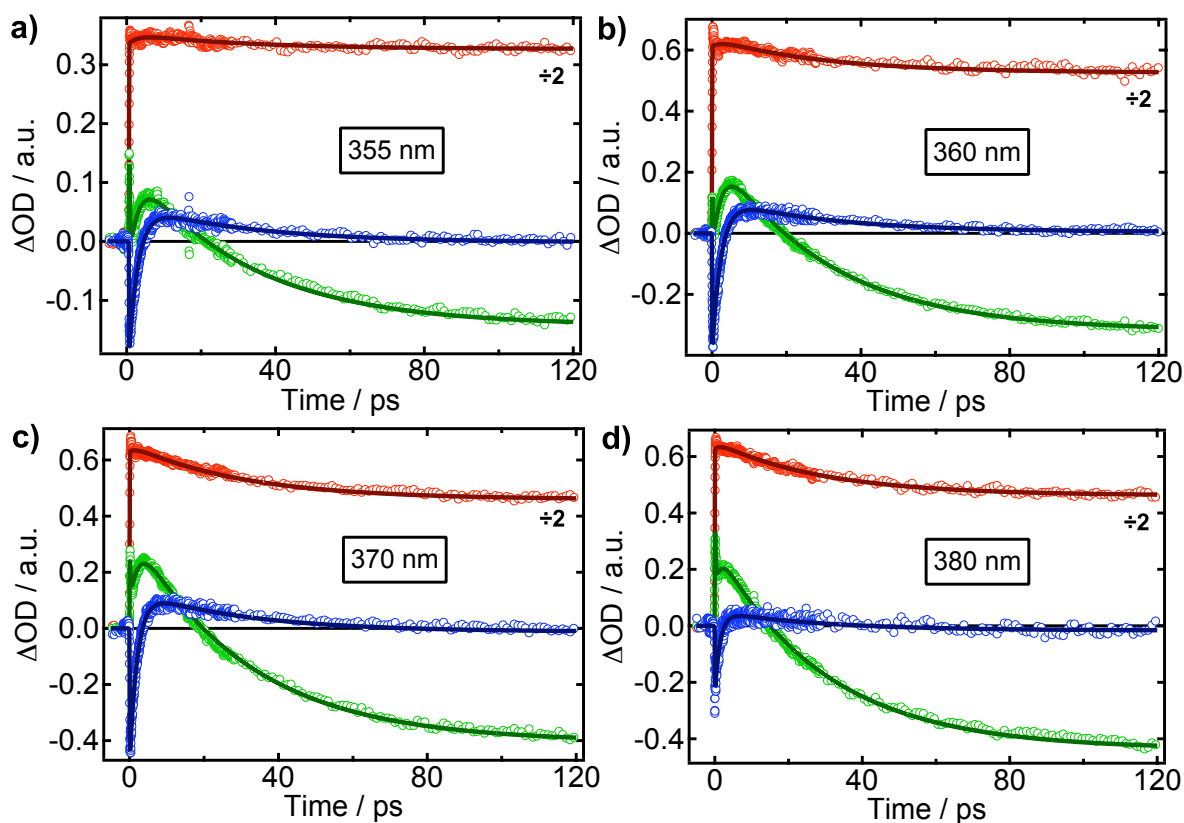


Figure 6.9: Kinetic basis vectors \mathbf{V}_1 (red circles), \mathbf{V}_2 (green circles) and \mathbf{V}_3 (blue circles) from the SVD analysis and their corresponding global fit functions (solid lines) for, a) excitation at 355 nm; b) excitation at 360 nm; c) excitation at 370 nm; d) excitation at 380 nm. τ_1 was fixed to 0.2 ps in all cases. The corresponding fitting parameters are given in Table 6.2. \mathbf{V}_1 is scaled down for clarity.

band: the smaller the excitation wavelength (the higher the excitation energy), the wider is the SE band at time zero. Enlarged views of the broadband TA spectra in the region of the SE band are shown in 6.10b for excitation at 360 nm, 370 nm and 380 nm. The band shows pronounced differences as a function of excitation wavelength. In particular, the width of the band at early times almost linearly decreases upon lowering the excitation energy (*i.e.* increasing the excitation wavelength), while the emission intensity at time zero increases correspondingly. This effect is discussed later in detail in Section 6.2.4. Figure 6.10c shows the Fourier-transformed linear combination of SVD vectors \mathbf{V}_4 and \mathbf{V}_5 for two different excitation wavelengths. For the off-resonance excitation (360 nm), the amplitude of ground state wave packets significantly increased, as expected for the RISRS process [276].

We also performed GA on the data sets for different excitation wavelengths (total

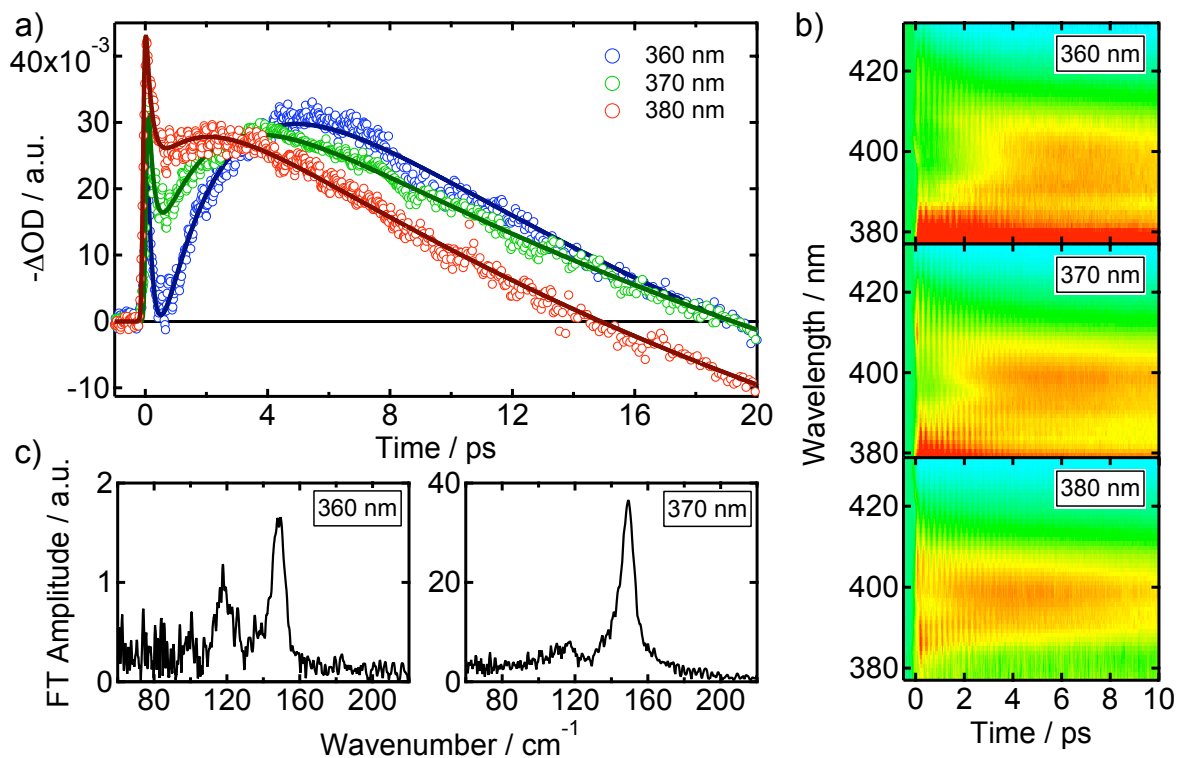


Figure 6.10: a) Kinetic basis vectors \mathbf{V}_2 for different excitation wavelengths (open circles) and their corresponding global fit functions (solid lines). The differences are due to the different time constants of vibrational cooling (τ_2) manifested as the increase in intensity in the first several ps; b) Enlarged view of the 2D plots of TA spectra in the region of the SE band for excitation at 360 nm, 370 nm and 380 nm (red = negative, blue = positive); c) Fourier-transform of the linearly-combined kinetic basis vectors that contain wave packet oscillations for excitation at 360 nm (left-hand) and 370 nm (right-hand).

8 traces, see Figure 6.8) using the fit function of Equation (6.4). The fitted parameter values are given in Table 6.3. Despite the small discrepancies between the parameter values resulting from the two methods SVD-GF (Table 6.2) and GA (Table 6.3), they are

	360 nm	370 nm	380 nm
τ_2 / ps	2.55 ± 0.05	2.19 ± 0.02	1.68 ± 0.05
τ_3 / ps	29.5 ± 0.4	30.3 ± 0.2	28.8 ± 0.2
τ_C / ps	1.91 ± 0.14	1.91 ± 0.04	1.66 ± 0.07
T_{ES} / fs	225.1 ± 0.3	224.7 ± 0.1	223.8 ± 0.2

Table 6.3: Fitted parameters from GA for different excitation wavelengths. τ_2 is the vibrational cooling time, τ_C is the coordinate damping time, τ_3 is the intersystem crossing time and T_{ES} is the coherent oscillation period in the excited state potential. τ_1 was fixed to 0.2 ps.

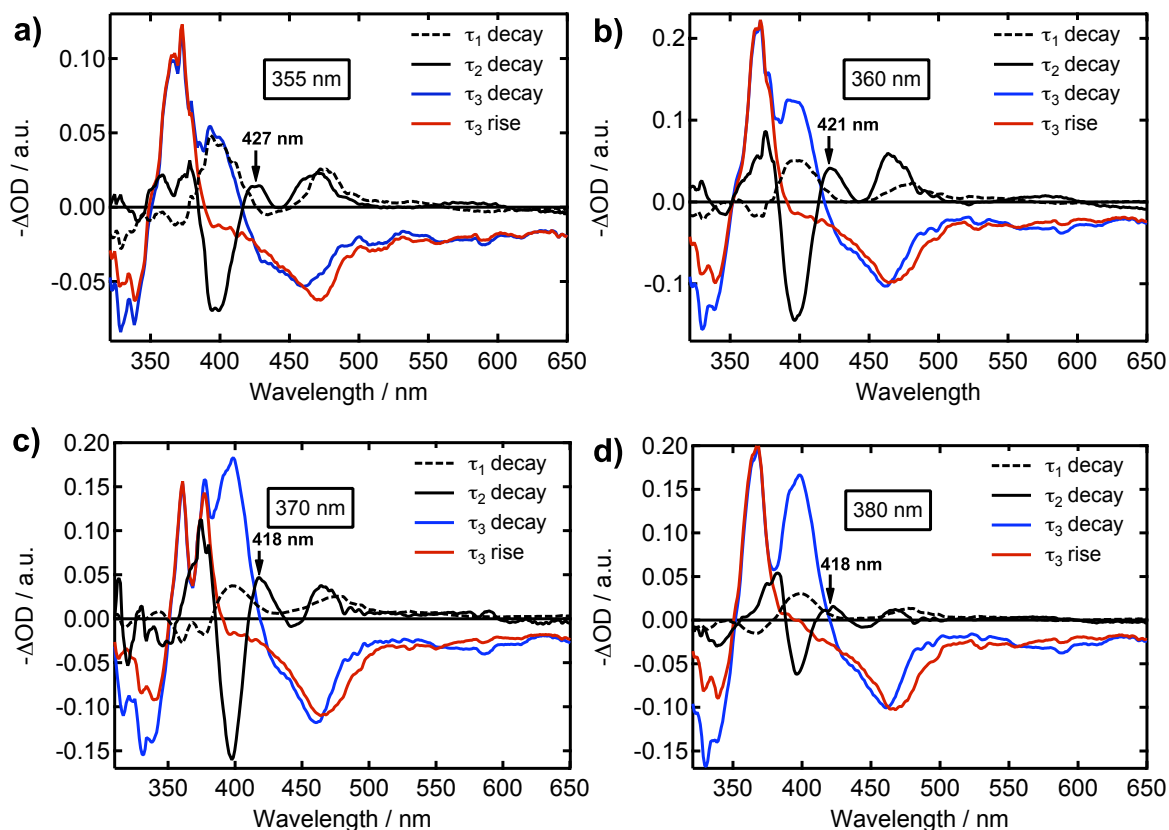


Figure 6.11: Decay-associated difference spectra (DADS) for different excitation wavelengths. a) Excitation at 355 nm; b) Excitation at 360 nm; c) Excitation at 370 nm; d) Excitation at 380 nm. The arrows indicate the position of the right lobe of the τ_2 DADS which represents the narrowing of the stimulated emission band.

considered to be in satisfactory agreement given the reduced amount of data included in the GA, the simplicity of the kinetic model that is used for fitting and the fact that SVD is, in principle, not meant for data sets that contain spectral evolution. From Table 6.3 one could argue that there is a small (statistically significant) effect of the excitation wavelength on the ES wave packet oscillation period T_{ES} . A small effect might also be visible in the Fourier-transformed linear combination of SVD vectors \mathbf{V}_4 and \mathbf{V}_5 for different excitation wavelengths, shown in Figure 6.12. Physically, a longer oscillation period for higher excitation energies results from anharmonicity of the potential energy surface towards longer Pt–Pt bond lengths. The differences are, however, on the order of a wavenumber between 360 nm and 380 nm excitation, which is in any case extremely small given the large energy difference of 1460 cm^{-1} for the two excitation wavelengths. This evidences that the $^1A_{2u}$ state potential of PtPOP is largely harmonic.

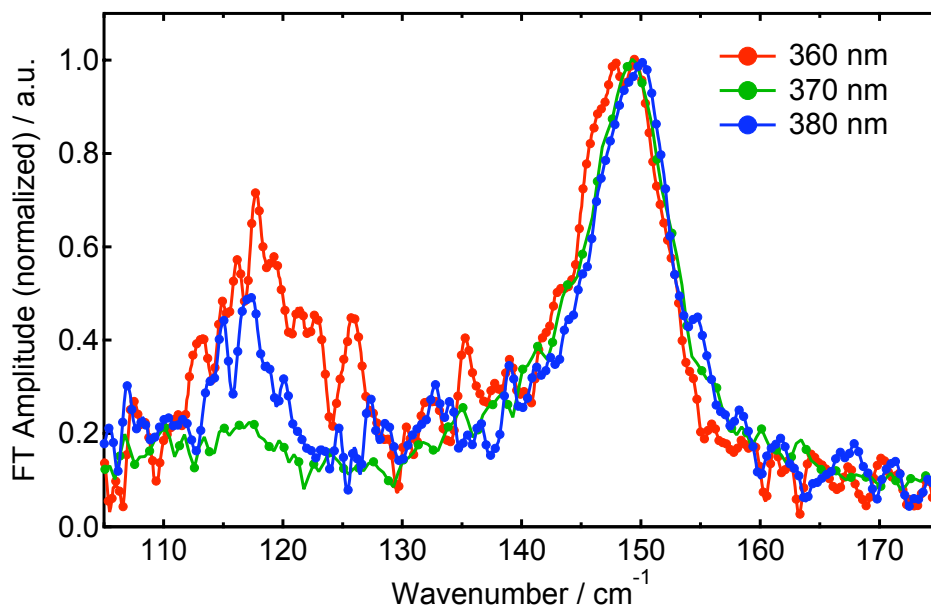


Figure 6.12: Fourier-transform of the linearly combined SVD vectors \mathbf{V}_4 and \mathbf{V}_5 for different excitation wavelengths, normalized to the maximum around 149 cm^{-1} .

6.2.3 Solvent effect on the relaxation dynamics

Figure 6.13 shows the **SVD-GF** results using Equation 6.2 for four different solvents: ethylene glycol, ethanol, water and **DMF** (excitation at 370 nm). In the fits, the **IRF** parameter B was fixed to 0.13 ps and, as before, amplitude A_1 (τ_1 component) was set to zero for kinetic amplitude vectors \mathbf{V}_1 and \mathbf{V}_3 because of its negligible contribution to these vectors. The **SVD** of the **TA** data set in **DMF** delivered four main kinetic

solvent	τ_1 / fs		τ_2 / ps		τ_C / ps		τ_3 / ps		T_{ES} / fs
	TA		TA	FU	TA	FU	TA	FU	TA
eth. glyc.	260(20)		2.14(0.02)	-	1.93(0.04)	-	30.3(0.2)	-	224.0(0.1)
ethanol	280(70)		2.11(0.03)	2.0(0.2)	2.30(0.08)	2.3(0.4)	25.6(0.2)	28.9(0.4)	223.8(0.1)
water	210(40)		1.31(0.04)	1.5(0.2)	1.76(0.08)	1.5(0.5)	13.7(0.2)	15.4(0.3)	224.5(0.1)
DMF	45(5)		1.69(0.04)	-	1.75(0.08)	-	11.0(0.1)	-	222.8(0.1)

Table 6.4: Comparison of relaxation time constants (uncertainties in brackets) for **PtPOP** in four different solvents obtained from the analysis of the transient absorption (TA) data (excitation at 370 nm) and the time-resolved fluorescence up-conversion (FU) data (excitation at 380 nm). τ_1 and τ_2 are vibrational relaxation times, τ_C is the coordinate damping time, τ_3 is the intersystem crossing time and T_{ES} is the coherent oscillation period in the excited state potential. The coherence decay constants τ_C were obtained from a **GA** on a set of representative kinetic traces.

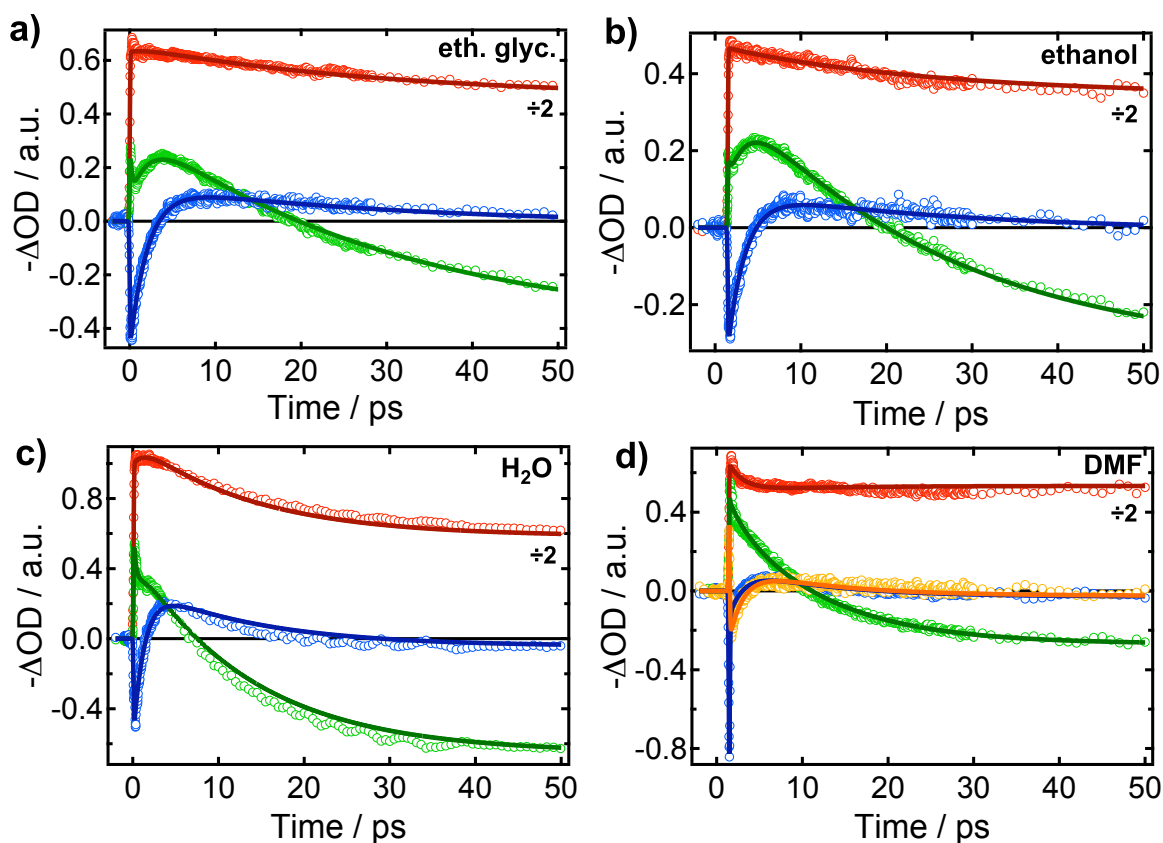


Figure 6.13: Kinetic amplitude vectors \mathbf{V}_1 (red circles), \mathbf{V}_2 (green circles), \mathbf{V}_3 (blue circles) and \mathbf{V}_4 (orange circles) from the **SVD** analysis and their corresponding global fit functions (solid lines) for, a) ethylene glycol; b) ethanol; c) water; d) **DMF**. The corresponding fitting parameters are given in Table 6.4. \mathbf{V}_1 is scaled down for clarity.

basis vectors (instead of three for the other solvents), which have all been globally fitted. The corresponding fit parameter values are given in Table 6.4, together with the time constants obtained from the **FU** data (excitation at 380 nm). In general, the **TA** and **FU** fitting results are in satisfactory agreement given the relatively large uncertainty in the fluorescence data and the different excitation wavelengths in the two experiments. Both the vibrational cooling (τ_2) and the **ISC** (τ_3) times show a pronounced dependence on the solvent following a similar decreasing trend: ethylene glycol > ethanol > water \gtrsim **DMF**. Especially, **ISC** rate changes by almost a factor of 3 between ethylene glycol and **DMF**. For all solvents, the loss of vibrational coherence occurs on the same time scale as vibrational cooling.

Figure 6.14 shows the kinetic **TA** traces at 410 nm for the four different solvents and their fit functions using the time constants given in Table 6.4. Vibrational cooling is seen as a slight increase of the stimulated emission within the first few ps, after which the **SE**

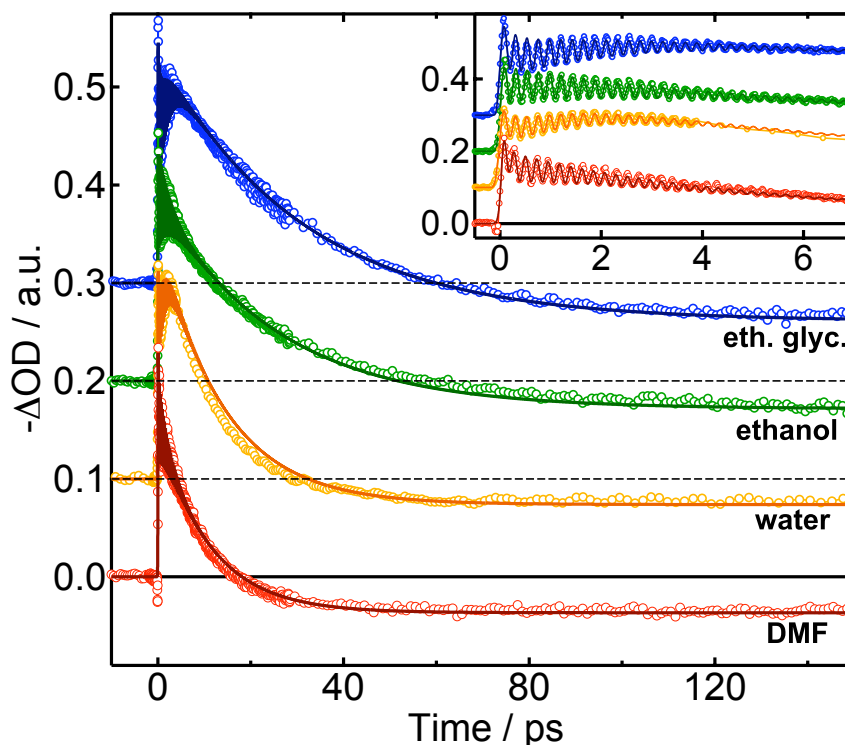


Figure 6.14: Kinetic TA traces at 410 nm for four different solvents and their fit functions. The upper-right inset shows the initial 7 ps time window. Note the different crossing points of the traces with the time axis pointing to the pronounced solvent effect on the rate of ISC.

intensity decays due to ISC. A satisfactory agreement between the experimental data and the fit is obtained for all traces, except for the data in water, which seem to require an additional kinetic component. The TA spectra at 150 ps after excitation are overlapped in Figure 6.15 for the four different solvents (note that the ESA is now along the positive vertical axis for clarity). Both the intensity and the position of the ESA band differs between the solvents.

Summary

Broadband TA measurements have been performed for different excitation wavelengths and in four different solvents (water, ethanol, ethylene glycol, DMF). The time of vibrational cooling in the $^1A_{2u}$ state (τ_2) increases, the higher the excitation energy (the shorter the wavelength), while the width of the t_0 SE band scales with the excitation energy. The solvent affects both the rates of vibrational cooling and ISC (τ_3). A SVD-GF analysis was applied to extract and compare the time constants resulting in the following trend for both τ_2 and τ_3 : ethylene glycol > ethanol > water \gtrsim DMF.

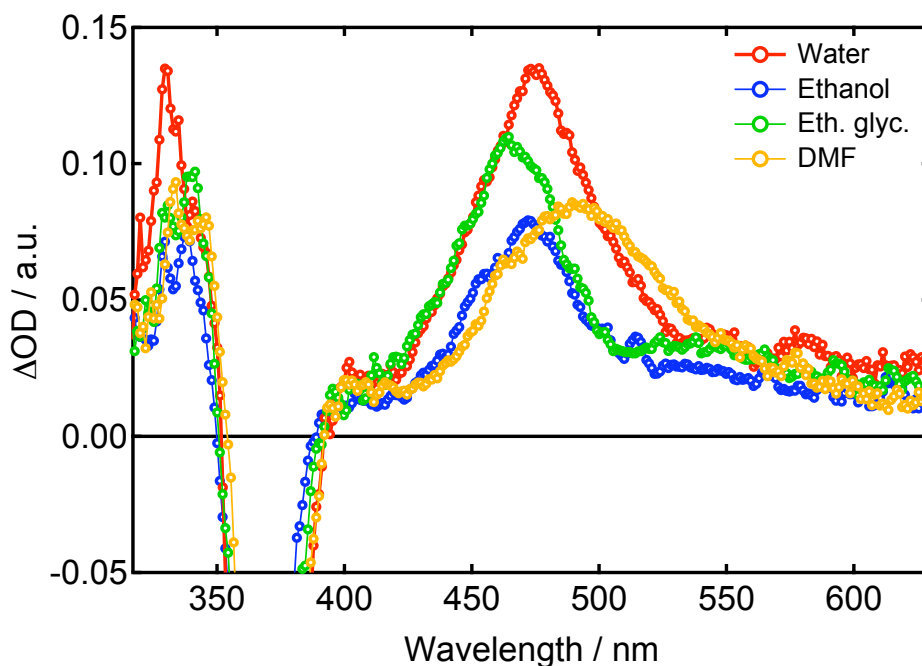


Figure 6.15: Comparison of the TA spectra at 150 ps time delay in four different solvents (ESA = positive, GSB = negative).

6.2.4 Singlet-state vibrational wave packet dynamics

Cuts at fixed time delays of the multicolour SE signal provide snapshots of the spectral distribution of the wave packet, as shown in Figure 6.16a. This is to our knowledge the first example where the distribution of the wave packet is spectrally visualised between the turning points of the potential on which it evolves. Given that the emission wavelengths are directly related to the difference potentials at specific internuclear distances, the upper axis in Figure 6.16a is obtained by mapping the energy difference between the displaced ${}^1A_{2u}$ and ${}^1A_{1g}$ potential curves (*i.e.* the emission energy) on the Pt–Pt bond length axis, as shown in Figure 6.17. In fact, as described in Section 3.2.3, the SE intensity is directly related to the wave packet probability density $|X(u, t)|^2$ via the dynamical Franck-Condon (FC) factors connecting the ground and excited states (see Equation (3.9)). By spectrally resolving the SE spectrum we thus mapped out the spatial distribution of the wave packet along the full Pt–Pt distortion coordinate ranging from 2.91 Å (ground state Pt–Pt bond length) to ~ 2.55 Å (at the ES far turning point). In Figure 6.16a, we see that after half an oscillation the distribution is peaked at the outer turning point, while at a full oscillation period (220 fs) it is peaked at the inner turning point. At an intermediate time (165 fs) corresponding to 3/4 period, the distribution is nearly uniform over the whole range of distances. This is confirmed by numerical simulations of the characteristic time-

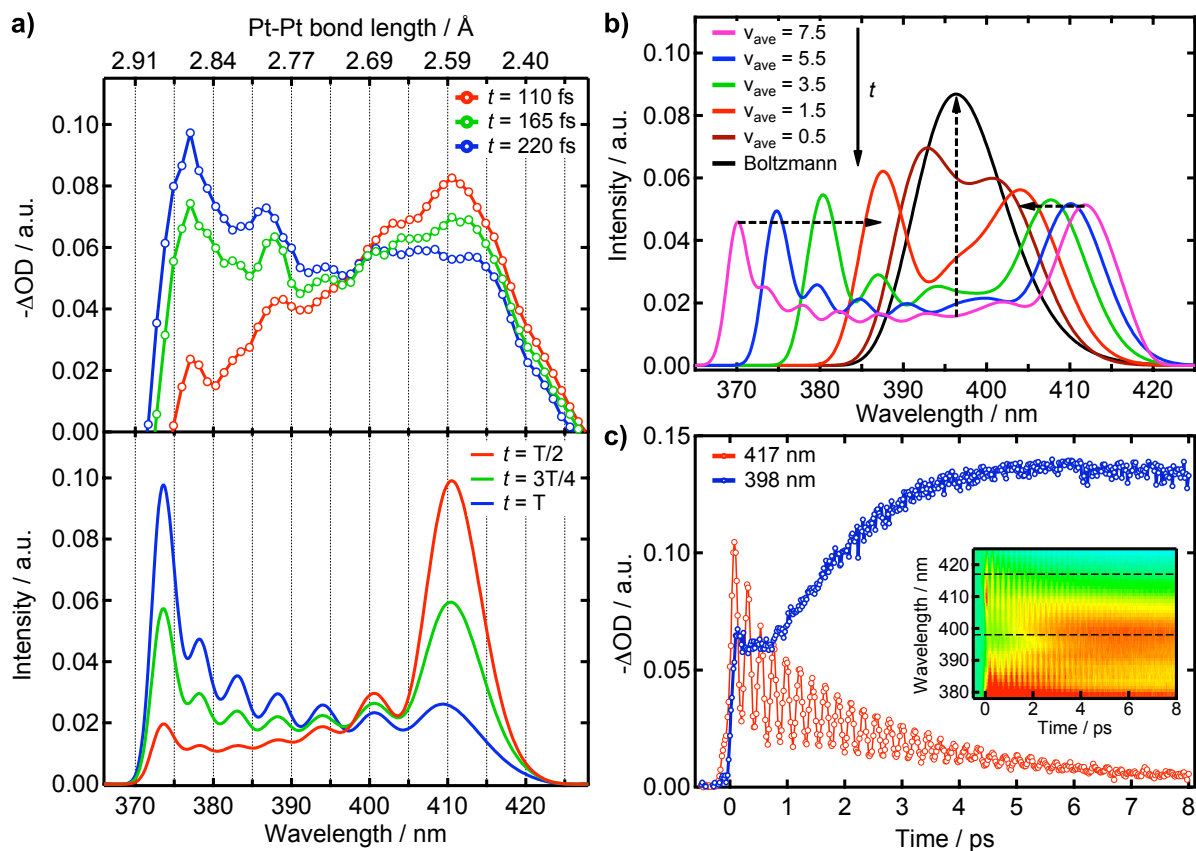


Figure 6.16: a) Top: experimental SE spectra at different delay times (PtPOP in ethylene glycol, excitation at 370 nm). The scaled static absorption spectrum was subtracted to correct for the partially overlapping GSB leading to missing intensity between 370-375 nm. Bottom: simulated SE spectra (see text) for different time delays expressed as a function of the vibrational period $T_{ES} = 220$ fs for an average vibrational quantum number of 6. The vertical grid lines facilitate the observation of the quantum interference fringes; b) Theoretical SE spectra for times at which the wave packet passes the middle of the potential for different average wave packet energies. The dashed arrows indicate the trends that are also observed experimentally; c) Experimental time traces at fixed wavelengths (open circles). The inset shows the corresponding cuts through the 2D plot (dashed lines).

resolved shapes of the SE band centered around 400 nm shown, where we assume that the ES distortion and the vibration involve only the Pt–Pt atoms (no ligand contribution) and we used the ground and excited vibrational frequencies derived in this study (Sections 6.1 and 6.2.1). The shape of the fluorescence spectrum and its Stokes shift are then determined by the zero-phonon energy and the difference in equilibrium Pt–Pt bond length. These two parameters were “fitted” to 25900 cm^{-1} (386 nm) and 0.194 Å , respectively. The qualitatively best agreement between experimental and theoretical SE spectra is shown in Figure 6.16a for different delay times (the scaled static absorption spectrum

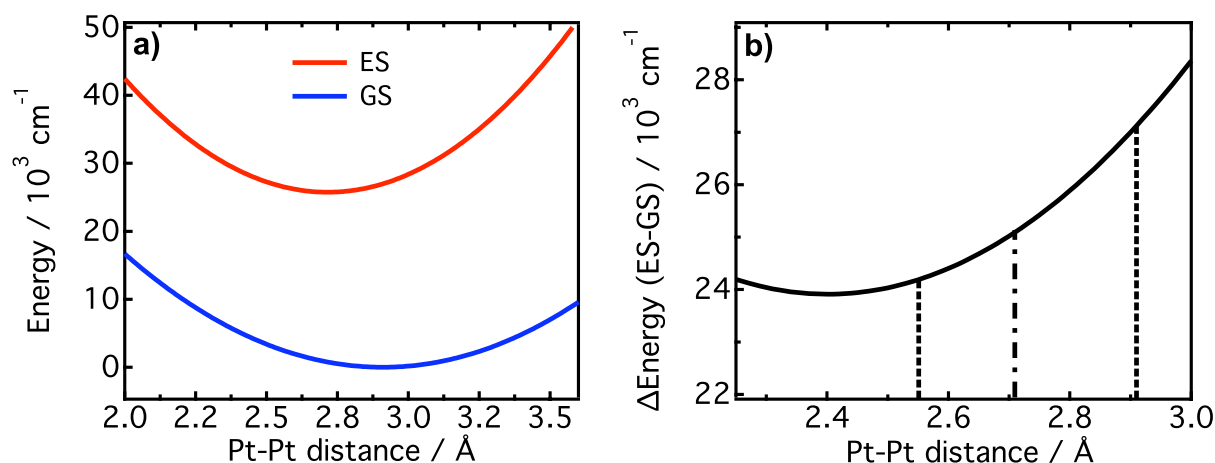


Figure 6.17: a) Calculated potential curves of the excited state (ES) and ground state (GS) for a zero-phonon energy of 25900 cm⁻¹, an ES Pt–Pt contraction of 0.194 Å and the vibrational frequencies of 149 cm⁻¹ (ES) and 119 cm⁻¹ (GS). The energy axis is relative to the bottom of the GS potential. b) Difference potential (ES – GS) yielding the emission energies. The vertical lines demonstrate the wave packet turning-points and the ES equilibrium bond length around 2.7 Å.

was subtracted from the experimental SE data to correct for the partially overlapping GSB).

In Section 3.2.2 it has been shown that the laser pulse centered at 370 nm excites only ~ 3 vibrational levels in the $^1A_{2u}$ excited state. Due to this rather small spectral excitation width and the difference in vibrational frequency between the ground state and the excited state, the extent of the wave packet undergoes a broadening for $t = T_{ES}/4$ and $t = 3T_{ES}/4$ and rephasing at the classical turning points for $t = T_{ES}/2$ and $t = T_{ES}$. This behaviour of the wave packet, called "breathing", is well documented in the literature [167, 186, 187] and it has been described in detail in Chapter 3 of this thesis. The wave packet "breathing" is clearly demonstrated by the probability distributions $|X(u, t)|^2$ (Equation (3.6) modulus squared) at $t = 0, 55$ and 110 fs, shown in Figure 6.18. Here u describes a dimensionless distortion coordinate. The abscissa in Figure 6.18 is obtained by setting $u = \sqrt{\omega_{ES} \cdot \mu / \hbar} (x - d_{ES})$, with x the Pt–Pt distance and d_{ES} the excited state bond distance.[§] The novelty in this study lies in the broadband detection which allowed us to spectrally resolve the fine-structured quantum interference fringes corresponding to the nodes of the ES vibrational wave function of Figure 6.18, *e.g.* occurring at ca. 410 nm, 403 nm, 395 nm, 387 nm and 377 nm during the first oscillation period, shown in Figure 6.16a[¶]. This nodal structure changes as a function of average wavepacket energy. We

[§] $\omega_{ES} = 149$ cm⁻¹, $d_{ES} = 2.71$ Å and $\mu_{vib} = 195/2$ a.u. (half the mass of a Pt atom).

[¶]The very blue side of the experimental spectra is obscured by the insufficient GSB subtraction

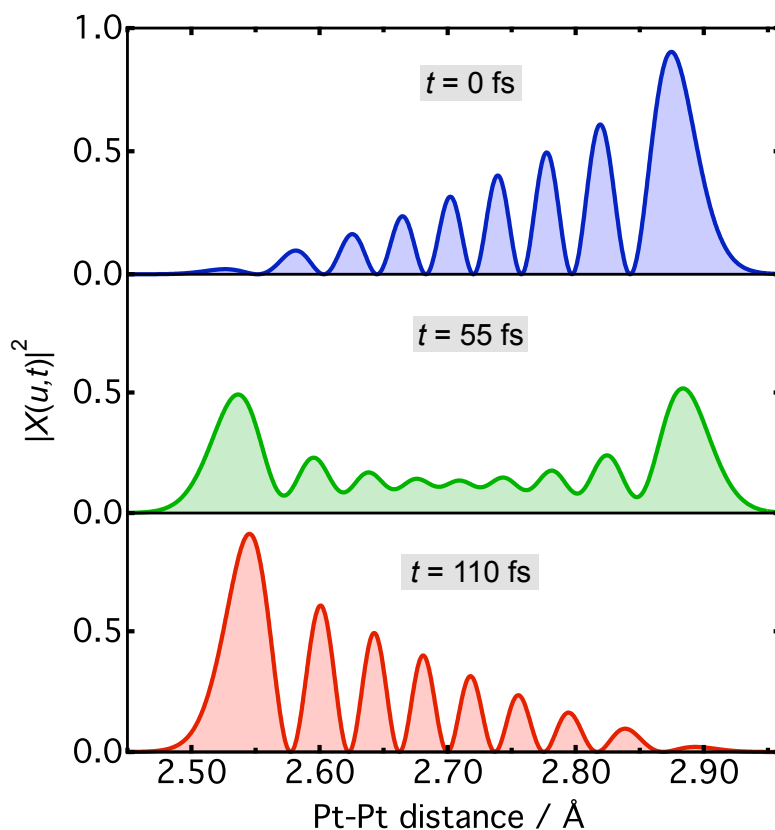


Figure 6.18: Calculated wave packet probability distributions $|X(u,t)|^2$ (Equation (3.6) modulus squared) at different times during the oscillation period. The average wave packet vibrational quantum number is 7.5 here. Note the nodes in the vibrational wavefunctions which are spectrally resolved in the SE band shown in Figure 6.16a.

believe that we are able to observe these fringes due to the fact that the depopulation time (see below) is longer than the vibrational period. The structure is therefore not blurred by fast depopulation to the next level for which the nodal structure looks slightly different. Wavepacket studies are commonly conducted by taking time traces at fixed wavelengths. To our knowledge this is the first time such quantum interference fringes are resolved spectrally by means of multicolor fs spectroscopy.

The PtPOP molecule thus appears as an ideal harmonic oscillator for the study of environment effects on the vibrational cooling. Figure 6.16b shows the simulation of the SE spectrum at the times the wave packet passes the middle of the potential for different average vibrational quantum numbers (see Equation (3.10)). Immediately after excitation at 370 nm, the wave packet has an average energy corresponding to ~ 7.5 vibrational quanta (*i.e.* $\nu_{\text{ave}} = 7.5 \cdot 150 \text{ cm}^{-1}$), relative to the bottom of the potential ($\mathbf{v} = 0$). This means that the FC transition at 370 nm mainly populates vibrational levels

with $\bar{v} = 7$ and $\bar{v} = 8$ (see Figure 3.1a and Section 3.2.2). The process of vibrational cooling is simulated by shifting the wave packet population distribution to lower average vibrational levels. Coherence decay is not included in this simple model, the simulations should therefore only be interpreted qualitatively. The best match between data and the simulated spectra in Figure 6.16a was obtained for an average vibrational quantum number of $\bar{v}_{\text{ave}} = 6$. From Figure 6.16b it is seen that the energy dissipation results in a narrowing of the spectrum accompanied by an increase of the intensity in the middle of the band, which matches the behavior observed in Figure 6.3b and Figure 6.6 (DADS₂). Finally, the system relaxes toward an equilibrium in which the relative probabilities of being in various states are given by the Maxwell-Boltzmann distribution, whose spectrum is also shown in Figure 6.16b. Energy dissipation causes the intensity to decrease monotonically in the wings of the spectrum, while increasing in the middle of the band non-exponentially as a function of the average energy (almost no increase until $\bar{v}_{\text{ave}} = 3.5$, large increase from $\bar{v}_{\text{ave}} = 3.5$ to $\bar{v}_{\text{ave}} = 0.5$). This behavior is also observed experimentally, as shown in Figure 6.16c. The time trace at 398 nm exhibits a plateau during the first ps before it gradually starts to increase, while the trace at 417 nm decays monotonically. Due to this non-exponential behavior, it should be kept in mind that the exponential kinetic model for vibrational relaxation employed in the fitting analyses is a simplification of the real dynamics.

6.3 Discussion

6.3.1 Vibrational relaxation in the singlet state

The above results have shown that there are two kinetics components associated with vibrational energy relaxation in the $^1A_{2u}$ excited state. The first component, $\tau_1 \simeq 260$ fs, is slightly longer than the roundtrip time of an oscillation in the singlet state. The best agreement between experimental and calculated SE spectra during the first oscillation period after excitation (shown in Figure 6.16a) was achieved for an average vibrational quantum number of 6, while excitation populates vibrational levels 7 and 8 at $t = 0$. The 260 fs decay component thus involves the dissipation of 1-2 vibrational quanta. This fast population decay component can have different origins. First, it could correspond to the short transient time for which the population relaxation rates of the different levels are not yet fully in phase [197]. In contrast to the decay of the system as a whole, the population decay of individual levels is generally non-exponential. In reference [195] it is shown that the decay of the highest levels exhibits a fast component comparable to the period of the vibration, similar to the present case. Second, the fast component shows

resemblance to the case of wave packet dynamics of excited diatomic halogen molecules in rare gas matrices. Schwentner, Apkarian and co-workers [182, 277] showed that the impulsive bond elongation in the upper (dissociative) part of the potential resulted in a large dissipation of energy (up to 10 quanta of the intramolecular vibration frequency) due to interaction of the halogen atoms with the matrix cage atoms. The coherence was preserved in this process due to the hard collision of the molecule with the matrix cage in a short interaction time. In the PtPOP case, the bond length impulsively shortens. There is less possibility to interact with the solvent for the contracted configuration. However, one could imagine an increased solute-solvent interaction for the first elongation event (after $T_{\text{ES}}/2$) with a net transfer of energy to the solvent upon elongation, leaving the Pt atoms vibrating with a reduced amplitude and energy, but in a coherent (wave packet) fashion. Compared to the elongation event at the dissociation limit for dihalogens, the energy dissipated is much more modest here, because the elongation is not of large amplitude and it stays confined within the "cage" of the bridging ligands.

The second slower kinetics component, $\tau_2 \simeq 2$ ps, associated with vibrational cooling, is very sensitive to both the excitation wavelength and the solvent (Table 6.4). Because we are dealing with a multilevel system of a single vibrational mode, the depopulation time can be directly derived from the experimentally determined vibrational cooling time under the assumption that the depopulation rate is independent of the vibrational quantum number ν [197]. After the aforementioned short transient time, we assume that the depopulation rate is constant for all subsequent vibronic levels until the population reaches the bottom of the potential. The depopulation time is derived by dividing the cooling time $\tau_2 \simeq 2$ ps (corresponding to the time in which the energy is dissipated to $1/e = 36\%$ of the initial value, *i.e.* from $\nu \simeq 6$ to $\nu \simeq 2$) by the number of vibrational quanta that are dissipated, *i.e.* $\Delta\nu \simeq 4$. This results in the relatively short depopulation time of ~ 500 fs, which raises the question of how the energy is dissipated and to where?

For large molecules one generally distinguishes two main channels of vibrational energy dissipation (see Section 3.1.1), which usually follow each other in sequence: (1) intramolecular vibrational energy redistribution (IVR) with transfer of energy from the FC-active mode to "dark" vibrational modes of lower energy [106] and, (2) external vibrational relaxation (EVR) during which the excess vibrational energy is dissipated into the solvent [191]. In organic molecules of appreciable size (>30 atoms), IVR is typically very fast (< 100 fs) due to the large density of vibrational states and high-frequency modes that exhibit anharmonicity already for low vibrational quantum numbers [278–280]. In the case of PtPOP, however, no vibrational modes of lower energy than the FC-active

Pt–Pt stretch mode (150 cm^{-1}) have been reported [136, 152]. A 40 cm^{-1} side band was superimposed on the Pt–Pt vibronic progression in low-temperature single-crystal spectroscopic studies, but the assignment of this feature as being due to an intramolecular FC-active mode or a phonon mode of the crystal lattice was ambiguous [137, 140]. Given the large mass of the Pt atoms and the fact that the Pt–ligand coordination bonds are the weakest in the molecule, we can confidently say that the Pt–Pt stretch is indeed the lowest-frequency mode in PtPOP. IVR is thus excluded in PtPOP and, consequently, vibrational energy dissipation mainly occurs directly to the solvent.

One can imagine two possible types of solute-solvent interactions mediating the energy flow: (1) interaction between the solvent and the Pt atoms along the open axial coordination sites which should be enhanced in the $^1,^3A_{2u}(d\sigma^* \rightarrow p\sigma)$ excited states due to their radical character and, (2) interaction of the negatively charged ligand P–O–H/P–O groups with polar moieties (*e.g.* O–H groups) of the solvent molecules. For the above reasons, the first mechanism involving a direct Pt–solvent interaction is expected to play a major role in the vibrational relaxation. The Pt–Pt stretch energy of 150 cm^{-1} lies in the spectral region dominated by translational and librational modes of the solvent (and solute) molecules [281], thus providing resonance modes in the solvent. However, in addition to providing resonance modes, a mechanism is necessary to couple the molecular oscillator to the bath of solvent modes.

The vibrational decay rates (Table 6.4) can be divided into two groups: ethanol and ethylene glycol with $\tau_2 > 2\text{ ps}$, water and DMF with $\tau_2 < 1.5\text{ ps}$. The question is what microscopic mechanism lies behind this solvent effect, *i.e.* what determines the ability of the solvent to accept the vibrational energy from the excited Pt–Pt mode? At this stage, in the absence of a detailed microscopic model, we can relate the observed trend to specific solvent properties. One such property is the solvent polarity which follows the decreasing trend in vibrational relaxation rates: water > DMF > ethylene glycol > ethanol. In addition, the ability of the solvent to interact with the Pt atoms could play a role in energy transfer. Indeed, the $^3A_{2u}$ state of PtPOP has been shown to abstract hydrogen atoms from H-atom donors [117], *e.g.* in the photocatalytic conversion of isopropanol into acetone. One can then imagine an interaction of the hydrogen atoms in the solvent (O–H in water, ethanol and ethylene glycol; C–H in DMF) with the Pt atoms. In this respect, water and DMF might be better candidates than alcohols, in that they exhibit a larger number of hydrogen atoms that can participate in the Pt–H interaction (the methyl hydrogens in DMF have been shown to be better donors than the formyl one [282]). Last, the bulkiness of the solvent molecules and the possibility to interact with the polar ligand phosphite

groups can play a role in the strength of the coupling. It should be noted that the nature of the solute-solvent interaction is likely to be a transient rather than a static solvent coordination. The latter would lead to a pronounced solvatochromic shift of the steady-state absorption and emission spectra which is not observed experimentally [124]. The differences in the vibrational cooling rate as a function of the excitation wavelength are attributed to the different amounts of excess vibrational energy that have to be dissipated to the solvent. Because the Pt–solvent interaction can only occur along the Pt–Pt axis (at maximum two solvent molecules coordinate at a certain time at either side of the molecule), a saturation behavior might arise for large vibrational energies leading to an increased relaxation time for higher excitation energies, in complete accordance with the results in this study. This in analogy with catalytic chemical reactions for which a zero-order rate law arises due to saturation of the catalyst (in contrast to a first-order reaction whose reaction rate scales with the reactant concentration) [283]. The saturation effect of vibrational cooling emphasizes that the solvent does not just act as an infinite sink for excess energy, but it actually interacts with the solute in a specific way that the energy can be channeled only via a limited number of solute-solvent modes.

6.3.2 Vibrational wave packet dynamics

Remarkable in the process of vibrational relaxation in PtPOP is the exceptional harmonicity of the coherent Pt–Pt oscillation. Even for the highest excitation wavelengths, the wave packet oscillation frequency hardly deviates from that for excitation into the bottom of the potential, pointing to a deep harmonic ${}^1A_{2u}$ potential energy surface over a range of more than 2000 cm^{-1} (ca. 14 vibrational levels). In contrast to common electronic excitations that populate empty anti-bonding molecular orbitals often leading to pronounced anharmonicity in the excited state potential, the $A_{1g} \rightarrow A_{2u}$ ($d\sigma^* \rightarrow p\sigma$) excitation in bimetallic complexes involves the formation of a new metal-metal bond in the excited state and thus a steeper vibrational potential compared to the ground state (see Figure 6.17a). Despite the rather large Pt–Pt contraction of $0.2\text{--}0.3\text{ \AA}$, the rigid, constraining P–O–P bridging ligands in PtPOP provide a force constant that is independent of the Pt–Pt displacement giving rise to the highly harmonic vibrational dynamics. This in contrast to the flexible bridging ligands in the bimetallic complex $\text{Rh}_2(\text{dimen})_4^{2+}$ (dimen = 1,8-diisocyanomenthane) for which the excited state potential surface has been proposed to be extremely anharmonic due to significant torsional ligand deformations [120].

The coherence persists for a remarkable long time of $\tau_C \simeq 2\text{ ps}$, much longer than the depopulation time of $\sim 500\text{ fs}$ of the individual levels. This indicates that the mech-

anism for depopulation decay in PtPOP does not conform to the optical Bloch picture (Section 3.1.1); on the microscopic level, energy dissipation to the solvent occurs such that the coherence is preserved to a large extent. We believe that this unconventional coherence decay behavior in PtPOP is due to the exceptional harmonicity of the Pt-Pt oscillator, and the fact that it is not entirely exposed to the surroundings, so that solute-solvent interaction can only occur along specific coordinates, most probably the Pt-Pt one. The harmonicity guarantees frequency matching between the vibronic levels resulting in very efficient coherence transfer [195]. The cage-like structure of the molecule protects the oscillator from the stochastically fluctuating solvent, reducing pure dephasing. This behavior shows close resemblance to the vibrational relaxation of dihalogens in rare gas matrices [181, 284]. In those cases, transfer of coherence by collisional interaction of the oscillator with the matrix also provided an unusual relation between T_1 and T_2 , with a coherence decay time T_2 longer than the population relaxation time T_1 [284].

It should be noted that the wave packet simulations performed in this study showed the best correspondence with the experiment for a Pt-Pt contraction of ~ 0.2 Å. This is in satisfying agreement with previous (low-temperature) optical measurements (0.175-0.225 Å) [129, 137, 146, 149], but it is slightly shorter than values for the contraction obtained from time-resolved X-ray diffraction (0.28(9) Å [159] and 0.23-0.28 Å [158, 160, 161]), X-ray scattering (0.24(6) Å) [43] and our X-ray absorption spectroscopy measurements (0.31(5) Å) (see Section 8.3). Although the uncertainties of all derived values are rather large, there seems to be systematic discrepancy between the values derived by optical and X-ray methods. There could be various reasons for this. First, the optical analyses, as in the present study, are often done assuming that only one distortion mode (namely Pt-Pt) occurs during the relaxation. This might seem a good approximation in PtPOP, but the inclusion of small additional distortions, *e.g.* along Pt-ligand, could change the derived value for the Pt-Pt contraction. Second, in the above discussion we argue that a Pt-solvent interaction is likely to occur in the excited state. The X-ray diffraction measurements were done with crystalline samples; therefore care should be taken in a comparison with the solution work. The X-ray absorption measurements were performed in solution, but solvent molecules close to the axial Pt coordination sites were not included in the modeling of the signal. For the solution-phase X-ray scattering measurements the static solute-solvent cross-terms were included in the signal modeling, but their photoinduced changes, *e.g.* an increased Pt-solvent interaction in the excited state, are not taken into account. Third, as will be discussed in Chapter 8, the discrepancy might be caused by the structural parameterization model used to calculate the X-ray absorption fine structure (EXAFS)

spectra limiting the sensitivity to the distortions in the excited state.

6.3.3 Mechanism of intersystem crossing

The $^1A_{2u}$ absorption of **PtPOP** has a molar extinction coefficient of $33500 \text{ M}^{-1}\text{cm}^{-1}$ [129]. In contrast, natural and synthetic organic pigments exhibit absorption bands with extinction coefficients that are often in excess of $200000 \text{ M}^{-1}\text{cm}^{-1}$, corresponding to fully allowed dipole transitions [285]. One of the reason for this lower singlet absorption lies in the very large spin-orbit (**spin-orbit (SO)**) coupling constant of 5d (Pt^{II}) electrons (4000 cm^{-1}) [286], which mixes singlet and triplet states, also leading to a weak absorption for the latter. The same can be found in Fe- and Ru-trisbipyridine complexes [278, 279]. In spite of this large **SO** coupling, the rate of **ISC** in **PtPOP** is rather slow (tens of ps), while for other molecules such as Fe, Ru, Os and Re polypyridine complexes [278, 279, 287–290], Cr acetylacetonates [109] and Fe porphyrins [291] the **ISC** times are $< 200 \text{ fs}$ typically, even though the metal atoms in these complexes have smaller or comparable **SO** coupling constants as Pt. On the other hand, **ISC** in mono-Pt(II) acetylides has been shown to occur on ultrafast ($< 100 \text{ fs}$) time scales [292]. The above indicates that the **ISC** rate in metal complexes is not just governed by the **SO** coupling strengths of the atoms. This was striking in the case of halogenated Re-carbonyl complexes, for which the **ISC** rate was found to decrease in the sequence Cl-Br-I [290]. Instead, other factors (structure, energetics, symmetry *etc.*) contribute to tuning the **ISC** rate in transition metal complexes.

In the case of dimeric d^8-d^8 complexes, the metal-metal interaction largely stabilizes the $^1,^3A_{2u}$ ($\sigma^*d_{z^2} \rightarrow \sigma p_z$) states compared to the corresponding $d_z \rightarrow p_z$ states in monomeric complexes (see Figure 2.1). As a consequence, the $^1,^3A_{2u}$ states in **PtPOP** are the lowest-lying singlet and triplet states. Furthermore, there is a large energy gap between the $^1,^3A_{2u}$ states and higher-lying singlet and triplet states. This energetic isolation of the $^1,^3A_{2u}$ states makes them electronically (except for the spin flip) and geometrically almost identical which is corroborated by the similarity of steady-state absorption and emission spectra at low-temperature [124] and, as shown here, their very similar **ESA** spectra (see Figure 6.6). The **FC** overlap factors between the singlet and triplet state potential curves are therefore very small (the curves are parallel), and a direct **SO** interaction between $^1A_{2u}$ and $^3A_{2u}$ is symmetry forbidden (in D_{4h} , see Tables E.1 and E.2). Furthermore, they are separated by a large energy gap. This is different to other metal complexes with ultrafast **ISC** rates, which often exhibit close-by singlet and triplet states [278, 290]. The question remains, however, what is in fact the mechanism of **ISC**?

In answering this question we have to take into account the following experimental

findings: a) The overall dynamics of our broadband **TA** spectra can be satisfactorily fitted with a two-state model involving direct interconversion from the $^1A_{2u}$ state to the $^3A_{2u}$ state (Figures 6.6 and 6.8). There is no evidence for the population of a third excited state; b) The wave packet dynamics are extremely harmonic with a rather long coherence decay time pointing to a largely unperturbed singlet-state potential (Figure 6.7). Therefore, coupling does not occur along the Pt–Pt coordinate and we can exclude strong coupling between the Pt–Pt coordinate and other modes; c) The **ISC** rate is strongly solvent-dependent (Table 6.4); d) The **ISC** rate follows an Arrhenius-type dependence, as shown by Milder and Brunschwig [148]. They found that **ISC** takes place via two channels: a temperature-independent and temperature-dependent one which are the dominating channels at low and high temperatures, respectively. At room temperature the latter is ~ 18 faster than the temperature-independent channel. Because our measurements were performed at room temperature, in the following we only discuss this regime of **ISC**.

The above results can be reconciled within various models of **ISC** listed below:

(1) **ISC** takes place through a mechanism of **SO**-vibronic coupling according to

$$\langle \phi_a | h_{so} | \phi_b \rangle \langle \phi_b | \partial / \partial Q_i | \phi_c \rangle \quad , \quad (6.5)$$

where ϕ_a corresponds to the $^1A_{2u}$ state which **SO** couples with the perturbing state ϕ_b [104]. The latter in turn vibronically couples with state ϕ_c corresponding to the $^3A_{2u}$ state through a vibrational mode Q_i . As the perturbing state that lies relatively close in energy to the $^1A_{2u}$ state, we propose the 3E_u state resulting from **ligand-to-metal charge transfer (LMCT)** $p_{x,y}(P) \rightarrow 6p_z(Pt)$ excitation which has been located by **density functional theory (DFT)** calculations [153]. This in contrast to the **metal-centered (MC)** $^3E_u(d_{xz,yz} \rightarrow p_z)$ state proposed by Shimizu *et al* [150] which lies much higher in energy. According to the symmetry selection rules, in order for the rate of **ISC** to be finite the direct symmetry products of each of the two terms in Equation (6.5) should contain the totally symmetric representation A_{1g} [293]. In the D_{4h} point group (Table E.1) this means that **SO** coupling between $^1A_{2u}$ and 3E_u is symmetry-allowed and modes of e_g symmetry can vibronically couple the $^3A_{2u}$ and 3E_u states. Within this picture, the solvent effect could be explained by a solvent-dependent stabilization energy of the 3E_u state (the $^1A_{2u} - ^3E_u$ energy gap enters in the denominator of the rate expression), or by the solvent's ability to bridge the energy gap between the vibronic states (ensuring energy conservation during the deactivation). The temperature dependence could enter via the Boltzmann-averaged **FC** factors, *i.e.* **ISC** becomes faster the more vibrational levels are populated thermally.

(2) **ISC** is induced by symmetry lowering in the excited state. Low-temperature phosphorescence measurements have indicated D_{4h} molecular symmetry in the ${}^3A_{2u}$ state [146] for which direct **SO** interaction between ${}^1A_{2u}$ and ${}^3A_{2u}$ state is symmetry forbidden (see character tables in Appendix E). A transiently induced symmetry lowering, *e.g.* towards D_4 symmetry, would make such an interaction allowed. The symmetry breaking could be induced by the solvent interacting with the radical Pt $\sigma^*d_{z^2}$ orbital at the open axial coordination sites (the solvent-induced change in angular momentum is accompanied by a spin flip of the electron residing in the $\sigma^*d_{z^2}$ orbital). Alternatively, the D_{4h} structure could be in equilibrium with a conformation of lower symmetry lying slightly higher in energy for which **ISC** is enhanced. This model would rationalize both the experimentally observed solvent and temperature effects; the former through the solvent-dependent stabilization energies of the lower-symmetry conformation, the latter via a thermal activation barrier between the two conformations. Indeed, isomeric structures of different symmetry and energy have been calculated for **PtPOP** [152]. The isomeric conformers differ in the hydrogen bonding motif (eclipsed vs. staggered) and Pt–P–O–P dihedral angle; the highest-symmetry (eclipsed) structure lies 0.8 kcal/mol lower in energy than the lower-symmetry (staggered) one.

(3) **ISC** occurs via the thermal population of a higher-lying triplet state. This mechanism has been proposed by Milder and Brunschwig [148]. They invoke a ligand-field ${}^3B_{2u}(d\sigma^* \rightarrow d_{x^2-y^2}^*)$ state that vibronically couples with the ${}^1A_{2u}$ state along the Pt–ligand coordinate. The solvent effect on the **ISC** rate is assigned to the different stabilization energies of the ${}^3B_{2u}$ state; decreasing solvent polarity lowers the activation barrier by stabilizing the ${}^3B_{2u}$ state resulting in an increased **ISC** rate. This is exactly the opposite of what is observed in the present study. In addition, the population of the ${}^3B_{2u}$ state is spin-forbidden. For this model, we would therefore propose the ${}^3E_u(p_{x,y}(P) \rightarrow 6p_z(\text{Pt}))$ state as a possible thermally activated and **SO**-allowed pathway. This is the same state as proposed for the **SO**-vibronic mechanism described above. It is noted that this model is not in contradiction with the fact that we found a good fit of the data to a two-state relaxation model. If the 3E_u state relaxes to the ${}^3A_{2u}$ state on the time scale of hundreds of fs (or faster), the transient population of this state would be too low to experimentally detect. This model implies a strong perturbation of the potential along the distortion coordinate (depending on the nature of the 3E_u state). Such a perturbation is likely to influence the vibrational dynamics along the Pt–Pt coordinate via mode coupling and anharmonicity (manifested in a frequency chirp). This is clearly not the case here; the highly harmonic wave packet dynamics is a result of a largely unperturbed potential en-

ergy surface.

Other metal based systems of Pt(0) and Cu(I) show similar slow (3-15 ps) rates of ISC between singlet and triplet metal-to-ligand charge transfer (MLCT) states [294–296]. Just as in the case of PtPOP, the lowest singlet and triplet potential curves in these complexes are parallel (identical geometry) and direct SO interaction between them is forbidden. DFT calculations have shown that structural distortions in the singlet MLCT state cause large energy splitting between highest-occupied molecular orbital (HOMO) and HOMO-1, preventing a very fast ISC induced by strong spin-orbit interactions between these orbitals, which are mainly composed of metal d-orbitals. The relatively slow ISC is therefore induced by weak spin-orbit interactions with nearby triplet MLCT states with small d-orbital contribution. In PtPOP, among all low-lying triplet states, SO interaction is only allowed for the 3E_u LMCT state. This interaction is expected to be relatively weak due to the small Pt d-orbital contribution in the underlying molecular orbitals. However, DFT and quantum mechanical SO overlap calculations for the ES geometry need to be performed in order to quantify this.

6.4 Summary and conclusions

Femtosecond fluorescence up-conversion and femtosecond broadband TA measurements, combined with SVD and global fit analysis techniques, have allowed us to identify wave packet dynamics in the $^1A_{2u}$ state potential with a period of 224 fs and a coherence decay time of ~ 2 ps, concomitant with vibrational cooling within the $^1A_{2u}$ state potential in ~ 260 fs and 1-2 ps and ISC on the time scale of 10-30 ps. The latter two processes show a pronounced solvent dependence. The complete scenario of the excited state dynamics and relaxation is schematically presented in Figure 6.19.

By spectrally resolving the SE spectrum we mapped out the spatial distribution of the wave packet along the full Pt–Pt distortion coordinate ranging from 2.91 Å (ground state Pt–Pt bond length) to ~ 2.55 Å (at the ES far turning point), as determined by numerical calculations of the unrelaxed fluorescence based on dynamical FC overlap factors. The discrepancy between the Pt–Pt distortion as obtained here and by time-resolved X-ray absorption spectroscopy (see Section 8.3) might be due to the simplicity of either of the two distortion models employed. In particular, the involvement of the solvent at the open Pt coordination sites might affect the value of the derived distortions.

We conclude that the main vibrational energy dissipation channel likely involves direct

solute-solvent interaction along the axial coordination sites of the Pt atoms, possibly via Pt–H interaction. Due to the absence of vibrational modes with lower frequency than the Pt–Pt stretch, **IVR** is excluded in **PtPOP**. The P–O/P–O–H groups can play a distinct role in the formation of the hydrogen-bonded solute-solvent network and thus the overall intermolecular interaction. The highly harmonic wave packet dynamics independent of the excitation wavelength point to an exceptionally deep potential along the Pt–Pt coordinate. The vibrational depopulation time is as short as ~ 500 fs, nevertheless the vibrations remain coherent during the vibrational cooling time of ~ 2 ps. We thus observe the fascinating process that depopulation occurs without distorting the phases in the coherences; the standard relationship between phase and energy relaxation derived from the optical Bloch equations (Equations (3.1) and (3.2)) can not be used in this case. Coherence transfer between the vibronic levels in the harmonic ${}^1A_{2u}$ potential is thus very efficient. The large harmonicity, and the consequently long coherence decay time, are identified as being due to the constraining P–O–P bridging ligands that protect the Pt–Pt oscillator from random solvent fluctuations.

The low **ISC** rate compared to other metal complexes with smaller **SO** coupling constants is attributed to the facts that (i) direct **SO** coupling between two relevant states is symmetry forbidden and (ii) the singlet and triplet states lie far apart from each others and from the higher lying excited states of the molecule. The following two models, or a combination of both, are the most likely mechanisms of **ISC** in **PtPOP**: (1) a **SO**-vibronic mechanism involving mixing with a higher-lying ${}^3E_u(p_{x,y}(P) \rightarrow 6p_z(\text{Pt}))$ state and coupling via a non-totally symmetric mode of e_g symmetry; (2) symmetry breaking/lowering in the excited state, which can be either solvent-induced or manifested as a different conformation with a slightly higher energy. In general we can conclude that the large variability of values of the **ISC** rate among metal based molecular complexes can be rationalized by considering the structural and energetic constraints that affect the rate in spite of very large **SO** coupling constants in all cases. The present study shows that this can be generalized to intersystem crossing involving ligand-field and **LMCT** states.

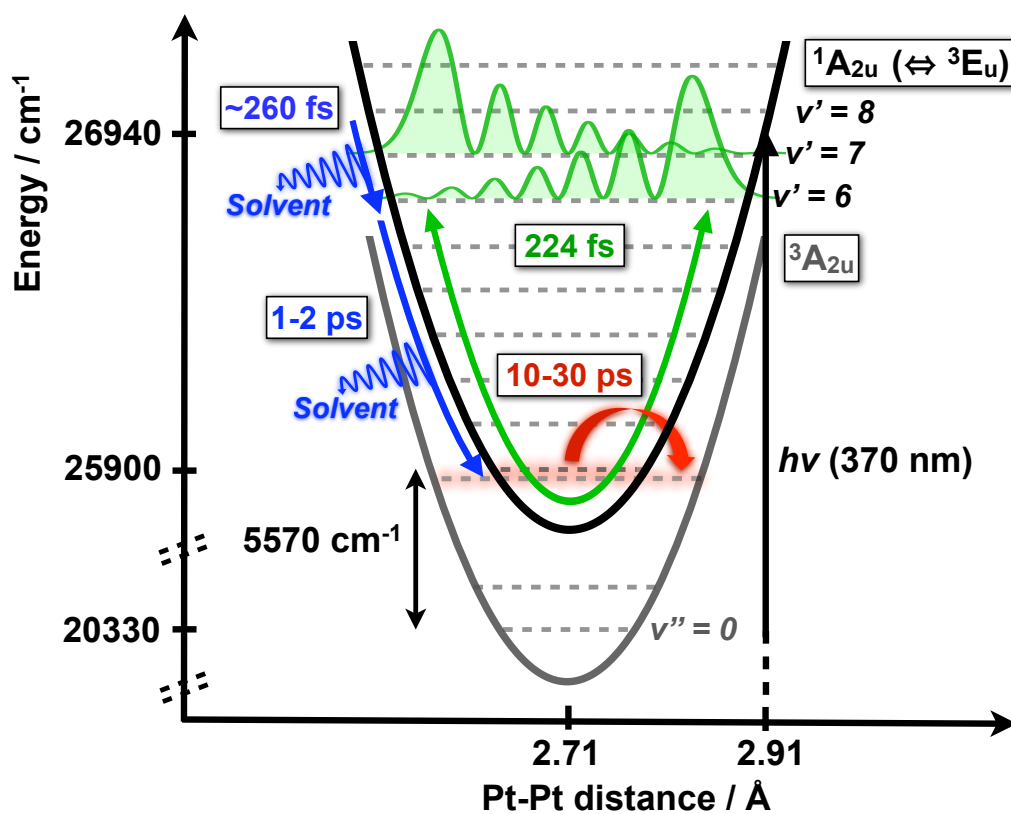


Figure 6.19: Potential energy level diagram summarizing the relative energies and the characteristic time scales of the various relaxation processes for PtPOP: wave packet oscillations (green), vibrational cooling and coherence decay with concomitant energy transfer to the solvent (blue) and ISC (red).

Chapter 7

Steady-state X-ray absorption spectroscopy

A key prerequisite for the analysis of the time-resolved **XAS** data of Chapter 8 is a thorough understanding of the ground-state **XAS** spectrum, which is the subject of this Chapter. First, we need to determine the molecular ground-state structure. For this the **EXAFS** spectrum is very useful as it can phenomenologically be described by a single equation allowing a simple parametrization of the structure. The **EXAFS** structural determination of **PtPOP** is described in Section 7.1. Second, we would like to assign the **XAFS** features to specific structural or electronic properties in the ground state, so that we can understand what happens if we see them changing in the time-resolved experiment. This is of particular importance for the **XANES** spectrum which contains both structural and electronic contributions. Interpretation of the ground-state **XANES** spectrum of **PtPOP** is given in Section 7.2. While a quantitative structural analysis of the **EXAFS** spectrum is possible, we will show that such an analysis of the **XANES** spectrum is impeded due to theoretical errors dominating the discrepancies with the experimental data.

A part of the results presented in Section 7.1 are published in reference [162]. The results presented in Section 7.2 are in part published in reference [164].

7.1 EXAFS structural analysis

The main goal of this Section is the structural determination and parametrization of the ground-state **PtPOP** molecule. The parametrization model developed in this Section, will also be applied in the excited-state **EXAFS** analysis in Section 8.3.

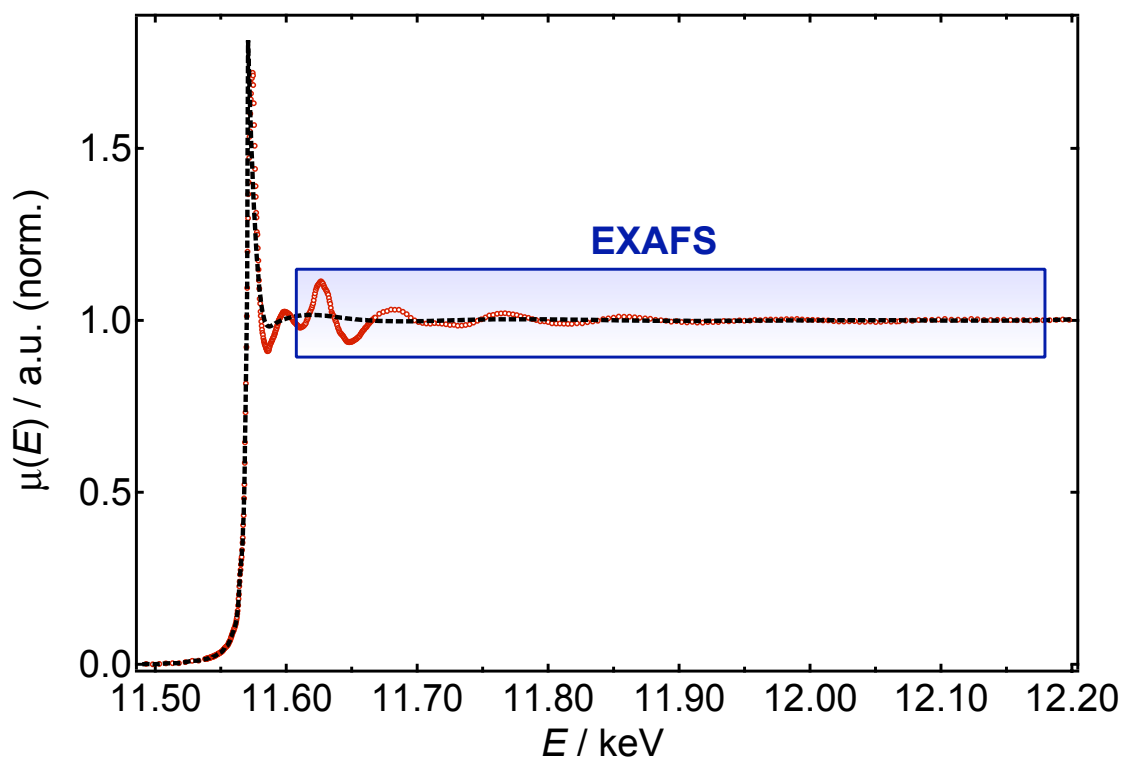


Figure 7.1: Normalized X-ray absorption spectrum of 18 mM $(\text{TBA})_4[\text{Pt}_2(\text{P}_2\text{O}_5\text{H}_2)_4]^{4-}$ in ethanol flown in a quartz capillary (energy axis calibrated). The dashed curve is the background function and the blue box denotes the range from which the EXAFS spectrum is extracted (see Figure 7.2).

7.1.1 Data reduction

Figure 7.1 shows the normalized X-ray absorption spectrum of PtPOP in ethanol (18 mM) around the Pt L_{III} edge at 11.564 keV (see Section 5.3 for a description of the experimental conditions). The energy axis is calibrated by comparing the edge position to the one of a Pt foil measured during the same experiment. Pre-edge subtraction and edge-jump normalization were performed as described in Section 4.3.1. In addition, a flattening correction was applied using the program ATHENA [226]. To display the flattened data, the difference in slope and quadrature between the pre- and post-edge lines is subtracted from the data, but only after E_0 . This has the effect of pushing the oscillatory part of the data up to the $\mu = 1$ line. Note that this is for display and has no impact on the extraction of $\chi(k)$ from the $\mu(E)$ spectrum. The dashed curve in Figure 7.1 represents the background function that is used to generate the normalized EXAFS $\chi(E)$. It was determined using the AUTOBK algorithm embedded in ATHENA [227]. It is noted that the background is not perfectly smooth. It exhibits slow oscillations which are expected to

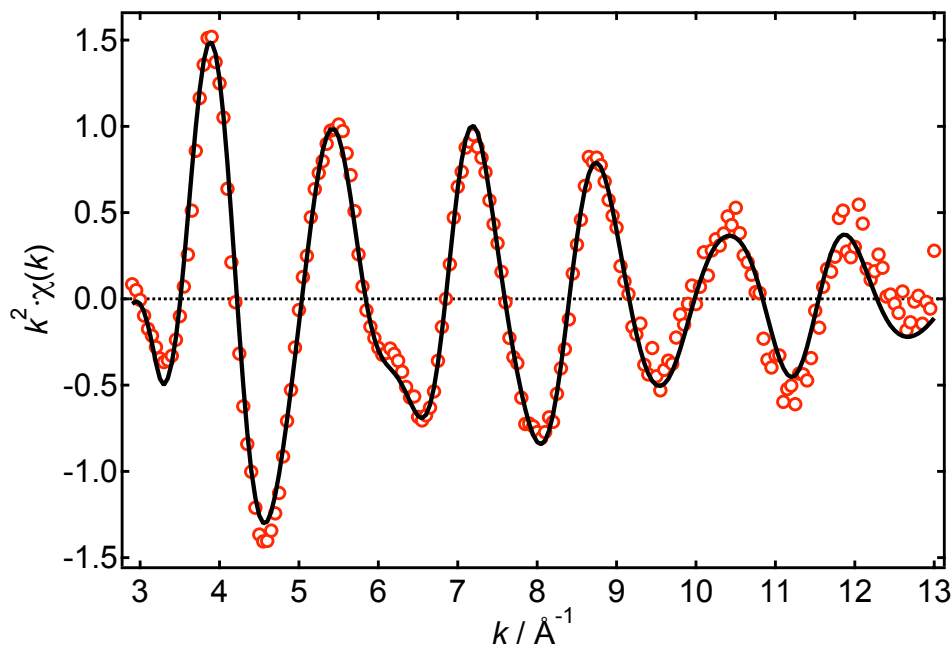


Figure 7.2: The EXAFS spectrum $\chi(k)$ weighted with k^2 (open circles) obtained from the data of Figure 7.1 after edge-jump normalization and background subtraction, together with the fit $\chi^{\text{fit}}(k)$ after back-FT (solid line).

contribute to the low- R region of the FT spectrum. Finally, the $\chi(E)$ data is converted to $\chi(k)$ by $E \rightarrow k$ coordinate transformation using Equation (4.9). The $\chi(k)$ spectrum weighted by k^2 is shown in Figure 7.2 in the range 2.9-13 \AA^{-1} .

7.1.2 Structural parametrization and fitting

The fitting analysis (Section 4.3.2) starts with the choice of a suitable model system as a starting point for the FEFF calculation. The structure of the model system is used to calculate the MT potentials, self-energy, and scattering amplitudes and phases which are necessary to generate the fine structure $\chi(k)$ according to Equation (4.10). The model system should be reasonably close to the structure of interest (to within $\sim 0.1 \text{\AA}$ of the real distances). In the case of PtPOP we can use the molecular structure determined by single-crystal XRD [297]. However, care should be taken, as the symmetry of the molecule can be reduced in the crystal due to Coulomb interactions between the ligands and positive counter ions which are absent in solution. In the potassium salt $\text{K}_4[\text{Pt}_2(\text{P}_2\text{O}_5\text{H}_2)_4]$ the K^+ ions coordinate to the phosphite O atoms producing deviations from exact fourfold symmetry [297], while such symmetry is expected in solution. In order to generate a suitable model system to fit the EXAFS data in Figure 7.2 we therefore modify the crystal structure such that the $\text{Pt}_2\text{P}_8\text{O}_4$ "cube" has D_{4h} symmetry, with the Pt atoms slightly out

No.	N_γ	R_γ	ampl.	fs	Pathway
1	4	2.308	100.0	-	Pt ₁ – P ₁ – Pt ₁
2	1	2.926	13.2	-	Pt ₁ – Pt ₂ – Pt ₁
3	4	3.241	33.7	-	Pt ₁ – O _t ² – Pt ₁
4	4	3.270	32.9	-	Pt ₁ – O _t ¹ – Pt ₁
5	4	3.293	32.3	-	Pt ₁ – O _b – Pt ₁
6	8	3.543	19.0	-	Pt ₁ – O _t ¹ – P ₁ – Pt ₁
7	8	3.555	17.8	-	Pt ₁ – O _t ² – P ₁ – Pt ₁
8	8	3.611	16.3	-	Pt ₁ – O _b – P ₁ – Pt ₁
9	4	3.747	24.5	-	Pt ₁ – P ₂ – Pt ₁
10	4	3.869	2.92	-	Pt ₁ – P ₁ – O _t ² – P ₁ Pt ₁
12	8	4.331	3.17	-	Pt ₁ – P ₂ – O _b – Pt ₁
16	8	4.490	2.85	-	Pt ₁ – P ₂ – Pt ₂ – Pt ₁
21	4	4.615	7.07	-	Pt ₁ – P ₁ – P ₁ – Pt ₁
22	4	4.615	19.15	1	Pt ₁ – P ₁ – Pt ₁ – P ₁ – Pt ₁
23	4	4.615	3.20	-	Pt ₁ – P ₁ – Pt ₁ – P ₁ – Pt ₁
25	4	4.778	3.51	-	Pt ₁ – O _t ¹ – P ₁ – O _t ¹ – Pt ₁

Table 7.1: Results from the FEFF6 calculation using the input file of Appendix A. Only paths with amplitudes $> 2.67\%$ relative to the strongest path (no. 1) are listed. N_γ = path degeneracy; R_γ = half-path distance (in Å); ampl. = amplitude (in %); fs = forward scattering event. In the last column, Pt₁ is the absorbing Pt atom, Pt₂ is the second Pt atom, P₁ are the nearest P atoms, P₂ are the far P atoms, O_b are the bridging O atoms, and O_t¹ and O_t² are the two sets of terminal O atoms. **SS** paths are colored blue; the collinear scattering path with forward scattering is colored red.

of the P₄ plane, with 4 equivalent bridging O atoms, and with 2 sets of terminal O atoms with P–O bond lengths for single and double P–O bonds, respectively. The atomic coordinates (see `feff.inp` file in Appendix A) were taken from the crystal structure data of K₄[Pt₂(P₂O₅H₂)₄] [297], except that the symmetry was increased as described above.

The ARTEMIS EXAFS fitting program (based on FEFF6) generates a list of single- and multiple scattering paths in sequence of their half-path distance R_γ^0 up to a maximum path length of R_γ^{\max} . For the case of PtPOP, the first 16 paths with amplitudes higher than 2.67% (relative to the strongest path) are listed in Table 7.1 ($R_\gamma^{\max} = 5.5$ Å). The structural parametrization model (Model 1) includes **SS** scattering paths to the nearest P atoms (path no. 1, Table 7.1), the second Pt atom (no. 2), the terminal O atoms (nos. 3 and 4), the bridging O atoms (no. 5), the far P atoms (no. 9), as well as a strong collinear **MS** path involving the absorbing Pt atom and two opposite P₁ atoms, with one forward scattering event at the absorbing Pt atom (no. 22). The relatively large amplitude of the latter path can be attributed to the focusing effect (Section 4.2.2). The scattering pathways are shown in Figure 7.3. In total 12 fitting parameters are used: S_0^2 , E_0 ,

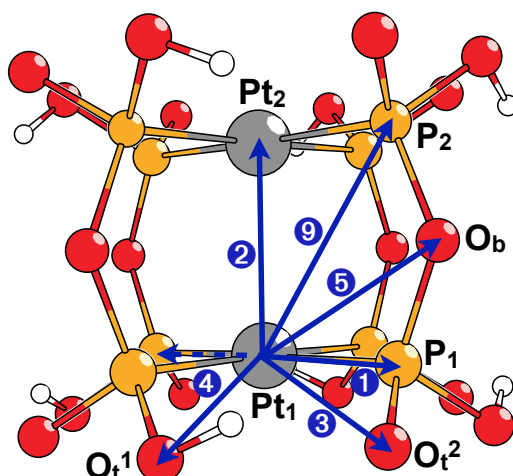


Figure 7.3: Structural parametrization model used for in the EXAFS analysis of PtPOP. The arrows denote the scattering pathways included in the model (Model 1). The numbers correspond to the pathway numbers in Table 7.1 (except for the forward MS pathway involving the absorbing Pt atoms and two opposite P atoms, which is not numbered). Of course, the choice of absorbing atom is arbitrary because the the two Pt atoms are equivalent by symmetry.

$\Delta R_{\text{Pt-P}_1}$, $\sigma_{\text{Pt-P}_1}^2$, $\Delta R_{\text{Pt-P}_2}$, $\sigma_{\text{Pt-P}_2}^2$, $\Delta R_{\text{Pt-O}_b}$, $\sigma_{\text{Pt-O}_b}^2$, $\Delta R_{\text{Pt-O}_t}$, $\sigma_{\text{Pt-O}_t}^2$, $\Delta R_{\text{Pt-Pt}}$ and $\sigma_{\text{Pt-Pt}}^2$. Only two parameters are used for both sets of terminal O atoms. The parameters for the MS path are expressed in terms of SS parameters: $\Delta R_{\text{MS}} = 2 \cdot \Delta R_{\text{Pt-P}_1}$, $\sigma_{\text{MS}}^2 = 2 \cdot \sigma_{\text{Pt-P}_1}^2$. In addition, in order to reduce the number of free fitting parameters, the squared DW factor for the Pt–Pt SS path is calculated independently by making use of Equation (4.11) and the Pt–Pt vibrational frequency of 118 cm^{-1} in solution (see Chapter 6). The reduced mass is that of two Pt atoms. In this way $\sigma_{\text{Pt-Pt}}^2 = 0.0053 \text{ \AA}^2$ is calculated, which is fixed to this value in the fit of the EXAFS data.

The data is fitted in R -space after FT using a Hanning window over the k -range $3.3 - 12.7 \text{ \AA}^{-1}$. The fit to the data is shown in Figure 7.4, and the fitted values, fit statistics and parameter correlations are given in Tables 7.2, 7.3 and 7.4, respectively. The fit region in R -space spans from 1.1 to 4.9 \AA (distances without phase correction). The FTs of the k -, k^2 - and k^3 -weighted data are fitted simultaneously in order to reduce the correlation between parameters with different k -dependences. The contributions of the various scattering paths are shown in the plot of Figure 7.4 as well (except for the Pt–O_t paths whose contributions were too small). The main peak around 1.9 \AA is due to SS to near P atoms. Three other distinct peaks around 2.7, 3.2 and 3.9 \AA are composed of scattering contributions from the bridging O atoms, the far P atoms and MS via the near P atoms, respectively. Important to note is that the collinear MS path involving the near P atoms and a forward scattering event is effectively the only path that contributes

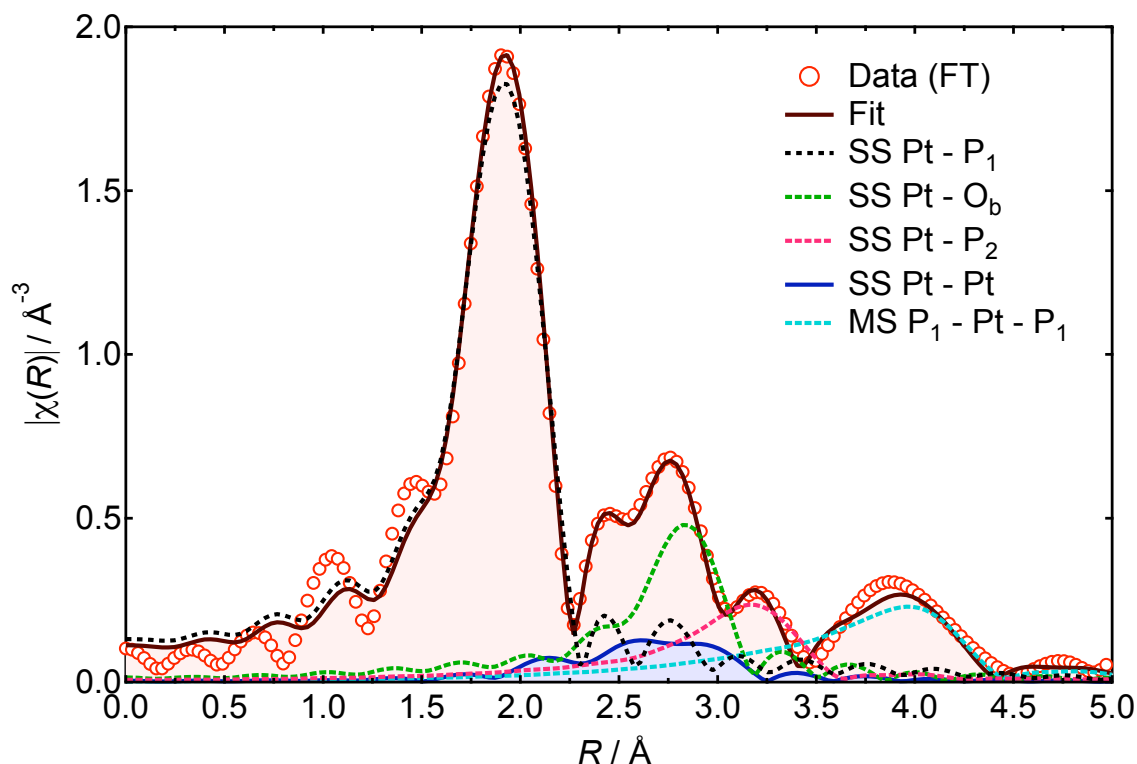


Figure 7.4: Magnitude of the FT of $\chi(k) \cdot k^2$ (open circles), the fit (solid line), and the contributions from different scattering paths (dashed lines). SS = single scattering path; MS = multiple scattering path; P_1 = near P atoms; P_2 = far P atoms; O_b = bridging O atoms. No phase correction is applied to the R -axis.

to the peak around 3.9 Å.

The Pt– O_t scattering contributions are very small due to the large DW factor for these paths. This is explained by the fact that the terminal O atoms are probably very flexible in solution, as they can be involved in hydrogen bonding with other P–O groups and with surrounding solvent molecules. Hydrogen bonding within the molecule delocalizes the charge over P and terminal O atoms so that the P–O bond length is ill-defined. Consequently, the DW factors (which include both thermal vibration and "static" disorder) are sufficiently large to make the contribution of these scattering paths almost negligible. As a result, the distortion $\Delta R_{\text{Pt}-O_t}$ is fitted to an unphysically large value (with a large standard deviation). The fitted values and statistics for the model without the terminal O atoms (Model 2) are also given in Tables 7.2 and 7.3. It is noted that the Pt– O_t paths were excluded from the fitting procedure described in reference [162] because inclusion of the SS paths to these O atoms does not improve the fit statistics (Table 7.3)*, while

*Although the χ^2 is lower for Model 1, χ^2_{ν} is higher, indicating that the fit is in fact not improved.

	S_0^2	E_0	$\Delta R_{\text{Pt-P}_1}$	$\sigma_{\text{Pt-P}_1}^2$	$\Delta R_{\text{Pt-P}_2}$	$\sigma_{\text{Pt-P}_2}^2$
Model 1	1.00(7)	8.2(9)	0.013(5)	0.0036(5)	-0.08(2)	0.011(3)
Model 2	0.98(4)	8.4(5)	0.013(4)	0.0034(4)	-0.08(2)	0.011(2)
	$\Delta R_{\text{Pt-O}_b}$	$\sigma_{\text{Pt-O}_b}^2$	$\Delta R_{\text{Pt-O}_t}$	$\sigma_{\text{Pt-O}_t}^2$	$\Delta R_{\text{Pt-Pt}}$	$\sigma_{\text{Pt-Pt}}^2$
Model 1	-0.03(1)	0.001(1)	-0.1(2)	0.07(6)	-0.05(3)	0.0053 (fixed)
Model 2	-0.03(1)	0.001(1)	-	-	-0.05(3)	0.0053 (fixed)

Table 7.2: Fitted values for the fit models with (Model 1) and without (Model 2) inclusion of the **SS** paths to the near terminal O atoms. Standard deviations are given in brackets. Units: E_0 in eV, ΔR in Å and σ^2 in Å².

	Model 1	Model 2
N_{indp}	22.4	22.4
N_{par}	11	9
χ^2	352	377
$\chi\nu^2$	31	28
\mathcal{R} -factor	0.0095	0.0098
ϵ (R -space)	0.002	0.002

Table 7.3: Fit statistics for the two models. Model 1: with inclusion of the near terminal O atoms; Model 2: without inclusion of these atoms. The meaning of the parameters are given in Section 4.3.2.

largely increasing the uncertainties of all other fitting parameters (Table 7.2). In the analysis of the excited-state **EXAFS** spectrum, however, the Pt – O_t paths were included in the parametrization model (see Section 8.3).

The triangular **MS** paths involving the near P and O atoms (nos. 6-8) are, despite their relatively large amplitudes (Table 7.1), not included in the fit. The reason for this is twofold: 1) the **DW** factors for these paths are expected to be rather large (resulting in small **FT** amplitudes); 2) including the paths would increase the number of fitting parameters by at least 4 (2 for terminal, 2 for bridging O atoms). The maximum number of fit parameters is limited by the information content of the data (see Section 4.3.2). In this case, the number of independent data points is $N_{\text{indp}} = 22$, calculated using Equation (4.13). The number of fitting parameters should therefore not exceed 14 (2/3 of N_{indp}).

After back-**FT** of the R -space fit in the range 1.1 – 4.9 Å, $\chi_{\text{fit}}(k)$ is obtained, which is shown together with the original data in Figure 7.2. The fit agrees very well with the experimental data. It should be noted that the wiggles below 1.5 Å in Figure 7.4 are caused by slow oscillations of the background function, as previously noted in Sec-

Model 1		Model 2	
$S_0^2 \leftrightarrow \sigma_{\text{Pt-P}_1}^2$	0.89	$E_0 \leftrightarrow \Delta R_{\text{Pt-P}_1}$	0.85
$E_0 \leftrightarrow \Delta R_{\text{Pt-P}_1}$	0.87	$S_0^2 \leftrightarrow \sigma_{\text{Pt-P}_1}^2$	0.81
$E_0 \leftrightarrow \sigma_{\text{Pt-O}_t}^2$	0.78	$\Delta R_{\text{Pt-O}_b} \leftrightarrow \Delta R_{\text{Pt-Pt}}$	0.71
$\Delta R_{\text{Pt-O}_b} \leftrightarrow \Delta R_{\text{Pt-Pt}}$	0.71	$E_0 \leftrightarrow \Delta R_{\text{Pt-O}_b}$	0.70
$\sigma_{\text{Pt-O}_b}^2 \leftrightarrow \Delta R_{\text{Pt-Pt}}$	0.64	$\sigma_{\text{Pt-O}_b}^2 \leftrightarrow \Delta R_{\text{Pt-Pt}}$	0.63
$S_0^2 \leftrightarrow \sigma_{\text{Pt-O}_t}^2$	-0.55	$\Delta R_{\text{Pt-P}_1} \leftrightarrow \Delta R_{\text{Pt-O}_b}$	0.60
$\Delta R_{\text{Pt-P}_1} \leftrightarrow \sigma_{\text{Pt-O}_t}^2$	0.53	$E_0 \leftrightarrow \Delta R_{\text{Pt-Pt}}$	0.59
$\Delta R_{\text{Pt-O}_b} \leftrightarrow \sigma_{\text{Pt-O}_b}^2$	0.48	$\Delta R_{\text{Pt-P}_1} \leftrightarrow \Delta R_{\text{Pt-Pt}}$	0.58
$\sigma_{\text{Pt-P}_1}^2 \leftrightarrow \sigma_{\text{Pt-O}_t}^2$	-0.44	$\Delta R_{\text{Pt-O}_b} \leftrightarrow \sigma_{\text{Pt-O}_b}^2$	0.49
$S_0^2 \leftrightarrow \Delta R_{\text{Pt-P}_2}$	-0.43	$E_0 \leftrightarrow \Delta R_{\text{Pt-O}_t}$	0.49

Table 7.4: List of the ten largest parameter correlations for the two different models. Model 1: with inclusion of the near terminal O atoms; Model 2: without inclusion of these atoms. A correlation of 1 means that two parameters are fully correlated.

tion 7.1.1. However, they do not significantly contribute to the FT above 1.5 Å. It is seen from Tables 7.2 and 7.3 that the uncertainties in and the correlations between different parameters, as determined by the fitting program, are fairly large. This is a common problem in cases where many scattering paths have similar distances and thus contribute to the same region in R -space. Here, Pt – O_b, Pt – O_t and Pt – Pt have very similar distances, as seen in Table 7.1. Unfortunately, this is unavoidable without including more external information such as temperature dependence of the DW factors. Nevertheless, the overall fit quality as given by the \mathcal{R} -factor (Section 4.3.2) is good; the data and theory agree to within less than a percent. As previously noted by Thiel *et al* [83], the contribution from Pt–Pt SS is small despite the heavy Pt atoms. This is mainly due to the fact that the Pt–Pt path has degeneracy 1 (compared to the degeneracy 4 of scattering to the bridging O atoms) and to the relatively large DW factor. In addition, due to the large overlap of scattering path contributions, the fitted $\Delta R_{\text{Pt-Pt}}$ value is therefore only indicative.

In Table 7.5, the absolute Pt – Pt and Pt – P₁ bond lengths inferred from the above ΔR fit parameters are compared with the distances from XRD measurements and DFT calculations. The bond lengths are in good agreement, although the Pt – Pt distance in solution, 2.88(3) Å, seems to be slightly smaller than that in the crystals, 2.913-2.942 Å. One possible explanation for the shorter Pt – Pt distance in solution would be the interaction between the filled highest molecular $\sigma^*d_{z^2}$ orbital and the slightly positively charged H atoms of the ethanol solvent (PtPOP is known to abstract hydrogen atoms from H atoms

	This work ^a	XRD ^b	XRD ^c	XRD ^d	DFT ^e
Pt – Pt	2.88(3)	2.925(1)	2.9126(2)	2.9419(3)	3.039
Pt – P ₁	2.32(4)	2.334(4)	2.3274(6)	2.3338(10)	2.393
Pt – P' ₁	-	2.307(4)	-	-	-

Table 7.5: Comparison between bond lengths in Å determined in this work and in previous studies. The molecule in the crystalline K-salt exhibits two sets of equivalent P₁ atoms because of Coulomb interactions in the crystal. Standard deviations are given in brackets.

^aPtPOP in ethanol

^bK₄[Pt₂(P₂O₅H₂)₄] · 2H₂O crystal [297]

^cTEA₂H₂[Pt₂(P₂O₅H₂)₄] crystal, TEA = tetraethylammonium [159]

^dTBA₄[Pt₂(P₂O₅H₂)₄] crystal, TBA = tetrabutylammonium [161]

^e[153]

donors [117]). Partial electron transfer from the anti-bonding $\sigma^*d_{z^2}$ orbital to the solvent causes a reduction of the Pt – Pt bond length. In fact, the time-resolved optical results of Chapter 6 also pointed to a potential (transient) axial coordination of solvent molecules. However, more measurements in different solvents would be necessary to strengthen this speculative explanation for the reduced Pt – Pt bond length. The question is whether the difference in Pt – Pt bond lengths is significant. As discussed above, due to overlapping contributions of different scattering paths, high correlations between the parameters and an independently derived DW factor for the Pt – Pt scattering path, our obtained Pt – Pt distance is only indicative.

In case solvent coordination occurs, one ideally detects the solvent molecules at the axial Pt sites directly. Doing this by means of EXAFS is complicated for several reasons. First, the coordination is likely to exhibit a large amount of disorder. The solute-solvent interaction is weak so that solvent molecules would move in and out of the axial Pt sites dynamically. This results in large DW factors and, consequently, small scattering contributions to the overall radial distribution function compared to the intramolecular first-shell atoms that are covalently bonded to the absorbing Pt atom. Second, the degeneracy of the Pt-solvent scattering paths is at most 2 (two solvent molecules coordinated at each side of the molecule). This compared to the degeneracies of 4 and 8 of some of the intramolecular paths (see Table 7.3). Third, if coordination takes place via H atoms from the solvent, the scattering will be very weak (usually H atoms are neglected in the scattering pathway calculations due to their weak scattering). However, closely coordinated H atoms might affect the potentials surrounding the absorbing Pt atom resulting in modified scattering phases and amplitudes for the latter (this effect is shown in Section 8.4.3 for the XANES spectrum). Fact is, in the present analysis, solvent coordination at the axial Pt sites can

not be derived due to many overlapping scattering paths for the range 3 – 3.5 Å, in which the Pt-solvent distance is also expected to occur. Adding Pt-solvent parameters would have a similar effect as the inclusion of the Pt – O_t parameters as discussed above: large DW factors, negligible scatter contributions and unphysical fit values, while the overall fit statistics is not improved.

7.2 L-edge XANES analysis

This Section provides a detailed description of the XANES spectrum of PtPOP. The SCF calculations in Section 7.2.1 show that the XANES spectrum (as calculated by FEFF) is sensitive to hybridization and charge transfer, two important chemical properties of molecular systems. In Section 7.2.2 we test different theoretical models of inelastic losses for the photoelectron. Using the best model from this analysis, in Section 7.2.3 we make an attempt at fitting the XANES spectrum for various electronic and structural parameters and we compare the results to the EXAFS analysis of the previous Section. Finally, in Section 7.2.4 we qualitatively interpret the XANES spectrum within a XAFS-like scattering theoretical framework and in terms of a final-state local LDOS. This interpretation will eventually allow us to relate transient XANES features to electronic and structural changes in the excited molecule.

For calculating the XANES spectra we make full use of the latest theoretical improvements by using version 9.02 of FEFF for all calculations [96].

7.2.1 Self-consistent field calculations

A XANES calculation typically starts with the computation of the scattering potentials. In FEFF, the SCF loop (see Section 7.2.1) computes the Coulomb potentials, the electron density, the Fermi energy E_F , occupation numbers as well as the charge transfer q_i between atoms. The latter accounts for the chemical properties of the different elements such as oxidation state and electron affinity and is especially important in coordination compounds for which metal-ligand bonding takes place through appreciable charge transfer (dative bonding).

The SCF (and FMS) calculations were performed on a cluster with a radius of 6 Å that contains all 30 atoms of the molecule (the H atoms are neglected). Five different potential labels were used for the absorbing Pt atom, the non-absorbing Pt atom, the P atoms, the bridging O atoms and the terminal O atoms (see input file in Appendix B). In the SCF loop, an angular momenta basis of s-, p-, d-, and f-scattering states ($l_{\max} = 3$) for the Pt atoms and s-, p-, d-scattering states ($l_{\max} = 2$) for the P and O atoms were used.

Element	6s	6p	5d	total (s, p, d)	q_i	Q [153]
Pt _{abs}	0.841 (0.872)	0.940 (0.990)	8.145 (8.822)	9.926 (10.684)	0.074 (0.317)	0.053
Pt	0.841 (0.850)	0.940 (0.961)	8.145 (8.155)	9.926 (9.966)	0.074 (0.033)	0.053
P	1.291 (1.290)	2.113 (2.105)	0.898 (0.894)	4.302 (4.289)	0.698 (0.710)	0.326
O _t	1.872 (1.873)	4.389 (4.402)	0.059 (0.061)	6.320 (6.336)	-0.320 (-0.336)	-0.379
O _b	1.815 (1.815)	4.284 (4.292)	0.055 (0.056)	6.154 (6.163)	-0.154 (-0.163)	-0.283

Table 7.6: The electron number counts for s-, p-, and d-electrons from the SCF calculation without core-hole and with core-hole (in brackets). The last two columns show the charge transfer q_i calculated by FEFF9 and the Hirshfeld charges Q from reference Novozhilova *et al* [153] (both calculations are done in the absence of a core-hole).

For the FMS calculation these l_{\max} values were increased by 1 to ensure convergence. After 9 iterations, self-consistency was reached for a Fermi energy of -7.416 eV (without core-hole). The calculation has been performed for a neutral molecule, as the total charge can not be specified in FEFF. The coordinates of the input structure are obtained from X-ray crystallography [297] and are in good agreement with the structure obtained from the EXAFS analysis of PtPOP (Section 7.1) [162].

The orbital occupation numbers for the various elements in PtPOP calculated with and without the presence of a core-hole (*i.e.* using ground-state potentials) are shown in Table 7.6.[†] The fractional charge counts among the s-, p- and d-orbitals are due to orbital hybridization, while the deviation of the total atomic charge counts from free-atom occupations[‡] can be assigned to charge transfer. It is seen that in the final-state calculation (with core-hole) the screening electrons mainly occupy the partially filled d-states at the absorbing Pt atom, which is later shown to result in reduced white-line intensities. The charge transfer calculated by FEFF shows good agreement with the calculated Hirshfeld charges from reference Novozhilova *et al* [153] (see Table 7.6). It is seen that the charge transfer is well correlated with the electronegativity of the various atoms (O>Pt>P [298]) and that the positive charge on the Pt atoms is in qualitative agreement with the formal oxidation state of +II. In addition, in agreement with the different chemical nature of the bridging and terminal P–O bonds, the terminal oxygen atoms are calculated to be more negatively charged than the bridging oxygen atoms.

As it is expected, Table 7.6 shows that the FEFF calculation with a core hole results in an increased charge transfer from the absorbing atom. The amount that is transferred additionally compared to the no-hole calculation is only +0.24 due to the effect of core-

[†]A calculation for an RPA-screened core-hole (*vide infra*) yielded identical occupation numbers as the no-hole calculation.

[‡]Pt: [Xe] 4f¹⁴ 5d⁹ 6s¹, P: [Ne] 3s² 3p³ and O: [He] 2s² 2p⁴

hole screening, *i.e.* the occupied valence states relax to screen the core hole which results in a redistribution of the valence electrons, in particular within the atom that contains the core hole. In this case the screening amounts to 76%, which is also seen from the fact that the total number of valence electrons at the absorbing atom in the presence of a core hole is increased by 0.76.

The above results show that the X-ray absorption spectrum based on the SCF scattering potentials contains information on chemical properties such as hybridization and charge transfer making it very sensitive to structural and electronic changes in the system.

7.2.2 *Ab initio* XANES calculations with improved many-body inelastic parameters

Figure 7.5 compares the calculated spectra with different models for the inelastic losses and core-hole screening (see Section 4.4.4) with the experimental Pt L_{III} -edge XANES spectrum. The energy axis is relative to the IP as calculated in the SCF loop and the

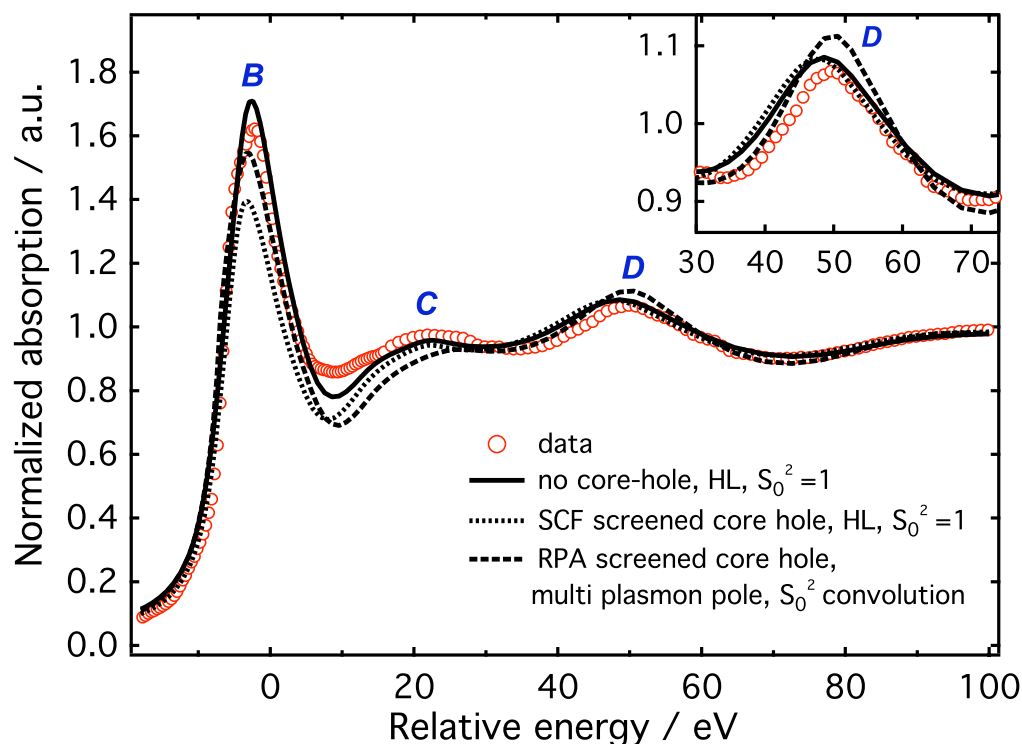


Figure 7.5: Experimental Pt L_{III} XANES spectrum of PtPOP in solution (open circles) and the results of XANES calculations with different models for the core-hole screening and inelastic losses (see text). The inset shows a zoom into feature D to illustrate its shift depending on the self-energy model that is used. The energy axis is relative to the IP.

experimental spectrum has been shifted horizontally in order to match the white-line position of the theoretical spectrum. Beside the Cartesian coordinates, the calculation does not require any input parameters. The three calculated spectra show reasonably good agreement with the experiment. All absorption features labeled *B*, *C* and *D* are reproduced by theory. Feature *D* is clearly red-shifted in the two spectra that use the HL single-plasmon-pole model for the self-energy, whereas its position is perfectly matched for the calculation with the multi-pole model, with a discrepancy in amplitude that is likely due to the overestimated self-energy near the plasmon resonance in the HL model.

The core-hole screening model mainly affects the white-line intensity. For the SCF screened core-hole calculation, the white-line intensity is reduced due to the screening valence electron density that occupies the empty final Pt 5d states and the attractive core-hole potential that shifts the spectrum to lower energies. Although many XAS calculations are based on the final-state rule, one-electron L_{II} - and L_{III} -calculations of d- and f- elements without a core-hole usually agree better with experiment [73]. This is also seen in the present case as the ground-state and RPA screened core-hole calculations show much better agreement for the white-line intensity.

As seen from the inset of Figure 7.5, the multi-pole model for the self-energy results in better agreement in peak positions, which is very important if one wants to extract quantitative structural information from the XANES region (the peak positions are directly correlated with the scattering path lengths and thus with the structure). We will therefore apply this model throughout the rest of this Chapter. With the multi-pole model, the overall best agreement with experiment was obtained by using an RPA-screened core-hole and a convolution of the spectrum with a many-body spectral function to include extrinsic losses [238]. This includes an *ab initio* calculation of the amplitude reduction factor S_0^2 starting from the dielectric response of the system (see Section 4.4.4).

7.2.3 Bayesian fitting of the ground-state XANES spectrum

A good agreement between the theoretical and experimental ground-state XANES spectra, which are also in line with the analysis from the EXAFS region (Section 7.1), is a prerequisite for obtaining quantitative structural information for the excited state. From Figure 7.5 it is obvious that, despite the improved *ab initio* calculation of many-body effects, theoretical errors still result in appreciable discrepancies between calculated and experimental spectra hampering a quantitative fitting analysis as is common practice for the EXAFS region (Sections 4.2 and 4.3).

Figure 7.6a shows the experimental data with the calculated spectrum $\mu(E)$ and the

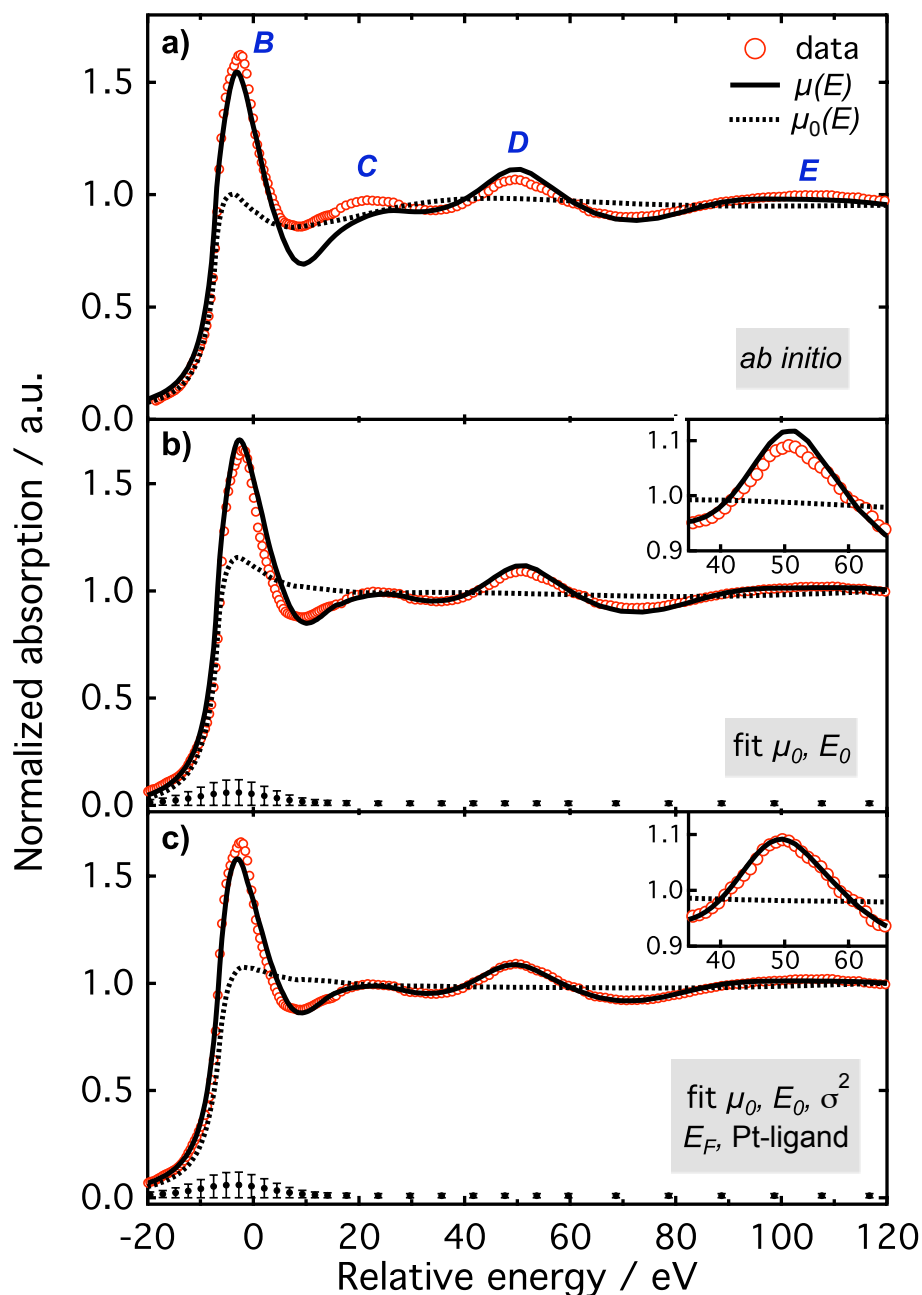


Figure 7.6: Experimental Pt L_{III} XANES spectrum of PtPOP (open circles) with the calculated and fitted absorption spectra $\mu(E)$ (solid lines) and embedded-atomic background spectra $\mu_0(E)$ (dotted lines). a) *ab initio* calculation without adjustable parameters; b) background-corrected spectrum using a five-point smoothing spline for μ_0 (the absolute energy shift E_0 was fitted simultaneously); c) fitted spectrum with the Fermi energy E_F , the DW factor σ^2 and the Pt-ligand distance as fitting parameters. The error bars in b) and c) denote the experimental error which is artificially increased by a factor of 6 in the white-line region in order to reduce its weight in the fit. The insets show a zoom into feature D .

embedded-atomic background spectrum $\mu_0(E)$ using the multi-pole self-energy, *ab initio* amplitude reduction factor and the RPA screened core-hole, as described in the previous section. It is seen that the missing intensity just after the white-line is related to a corresponding dip in the embedded-atomic background spectrum indicating that the theoretical errors causing this dip already occur on the level of the atomic scattering potentials. In fact, due to the low energy of the photoelectron, this region of the spectrum is expected to be particularly sensitive to full-potential effects, *i.e.* the lack of full potential corrections to the MT potentials, which are likely to play a role for such a small molecule as PtPOP. In addition, the molecule has an open cavity-like structure for which the spherical approximation inherent to the MT potentials might fail. The absorption features *B*, *C*, *D* and *E* are mainly contained in the MS fine structure χ via $\mu = \mu_0(1 + \chi)$, and the theoretical errors can be approximately corrected for by fitting the background spectrum with an empirical five-point smoothing spline [97], as described in Section 4.6. The result of the fitted spectrum and the corrected atomic background are shown in Figure 7.6b. Indeed, the background correction filled the dip after the white-line and the corrected μ_0 looks much smoother over the entire energy range. The fit also partially corrected the white-line intensity, although its width is still too large compared to experiment. Note that the five-point spline, with the support points placed on an exponential grid, is just sufficiently flexible to correct for the dip after the white-line, but is not flexible enough to shift any of the scattering features contained in χ .

A next step, which is a prerequisite for the excited-state analysis, is the verification that the ground-state structure, as obtained independently by XRD [297] and EXAFS spectroscopy (Section 7.1) [162], is consistent with the XANES experimental data and theoretical calculations. Using the Bayesian fitting program for FEFF [97] (Section 4.6), we therefore fitted the Pt-ligand distance (the P–O–P bridging ligand is moved as a whole, perpendicular to the Pt–Pt axis) and DW factor, which is not calculated from first principles, together with the overall energy shift E_0 , the Fermi energy E_F and the five-point background correction smoothing spline (similar to above) to the experimental data. The input file for this calculation is given in Appendix C. The results are shown in Figure 7.6c for a fitted Pt-ligand distance change value of $-0.015(2)$ Å, a DW factor of $\sigma^2 = 0.0052$ Å², an overall energy shift of $E_0 = 1.57(3)$ eV and a Fermi energy shift of $E_F = -1.55(6)$ eV. This result was found not to depend on the *a priori* estimates of the parameters and *a priori* uncertainties were chosen 5-10 times larger than the fitted values (to avoid constraining the fit). The corrected background remained almost unchanged while the width and intensities of all the fine-structure features show better agreement

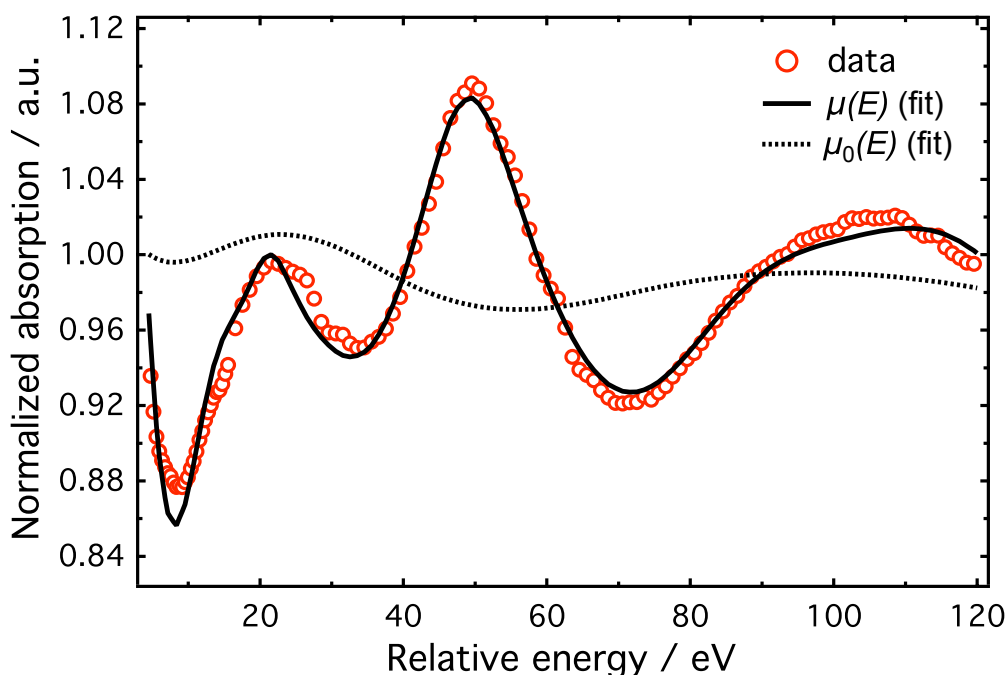


Figure 7.7: Experimental XANES (circles) and fit (solid curve) with the Pt–ligand and Pt–Pt distances as fitting parameters. The Pt–ligand distance change was fitted to -0.045 \AA and the Pt–Pt distance change to 0.17 \AA compared to the input crystal structure. A 5-parameter background spline and energy shift were also fitted to the data.

with the data. The resulting Pt–P bond distance as derived from the XANES fit is $2.301(2) \text{ \AA}$, compared to $2.321(4) \text{ \AA}$ obtained by fitting the EXAFS region of the spectrum (Section 7.1) [163], and $2.3183(13) \text{ \AA}$ and $2.307(4)/2.334(4) \text{ \AA}$ from X-ray diffraction on the TBA-salt [153] and K-salt [297] crystal structures, respectively (the molecule in the K-salt structure exhibits two sets of equivalent P atoms because of Coulomb interactions in the crystal). Although the XANES analysis delivers slightly smaller Pt–P bond distances, the agreement between the different measurements is satisfactory considering that the error for the XANES is expected to be larger than delivered by the program due to the fact that *a priori* theoretical errors are not taken into account in this procedure [97, 237]. It is noted that a fit of the Pt–ligand distance using the single-pole HL model for the self-energy (instead of the many-pole model as is used here) resulted in a significantly larger distortion of $-0.027(2) \text{ \AA}$ which is related to the mismatch in energy position of MS feature D (see Figure 7.5, Section 7.2.2). Next we include the Pt–Pt distance as a fitting parameter. Instead of increasing the error in the rise of the white line, we now exclude this part of the spectrum by starting the fit just after the white line. Again, a 5-parameter spline was fitted to the background spectrum simultaneously. The fit result is shown in Figure 7.7.

Adding the Pt–Pt fitting parameter did not change the χ_{Bayes}^2 (see Equation (4.20)) of the fit significantly. However, it is seen that the background function shows rather large oscillations, which were not present before fitting (Figure 7.6). The Pt–ligand distance change was fitted to $-0.045(3)$ Å and the Pt–Pt distance change to $-0.169(13)$ Å compared to the input crystal structure. Both distortions are unphysically large, also compared to the accurate results already obtained in the EXAFS analysis (Section 7.1) [163]. From this we conclude that it is difficult to extract accurate structural parameters from the XANES spectrum of PtPOP by means of fitting, because a) the theoretical errors due to non-MT and self-energy effects are too large in this region, and b) the XANES spectrum seems not very sensitive to the molecular structure (χ_{Bayes}^2 can not be improved by including more structural parameters). Nevertheless, we can conclude that the Pt L_{III} -edge XANES calculations for PtPOP are consistent with the ground-state structure obtained from the EXAFS analysis, which will be used as a starting point for the excited-state analysis (see Section 8.4).

7.2.4 Interpretation of the XANES spectrum

As discussed in Section 4.4, the real-space FMS Green’s function approach used in FEFF offers the possibility to interpret the XANES spectrum either within a XAFS-like scattering theoretical framework or in terms of a final-state local LDOS [237, 240]. In the following we present an interpretation of the various absorption features in the XANES spectrum of PtPOP. A cluster size dependence provides mainly structural assignments, while the analysis of the LDOS gives complementary electronic information about bound-bound transitions, orbital splitting and hybridization.

Cluster size analysis

A XANES analysis usually starts with a study of the dependence of the spectrum on the size of the FMS cluster in order to test the convergence with respect to the number of scattering paths. For small molecules, the optimum cluster size is usually the entire extent of the molecule, but a cluster size analysis is still useful to identify the dependence of XANES features on certain parts of the molecule and thus to assign the XANES spectrum to specific structural parameters.

The cluster size analysis for PtPOP is shown in Figure 7.8. The size was changed on a shell-by-shell basis, with the 1st shell given by the 4 P atoms surrounding the absorbing Pt atom ($R_{\text{FMS}} = 2.4$ Å), the 2nd shell contains the opposite Pt atom, the 4 bridging oxygen atoms and 8 terminal O atoms attached to the 1st shell P atoms ($R_{\text{FMS}} = 3.6$ Å), the 3rd

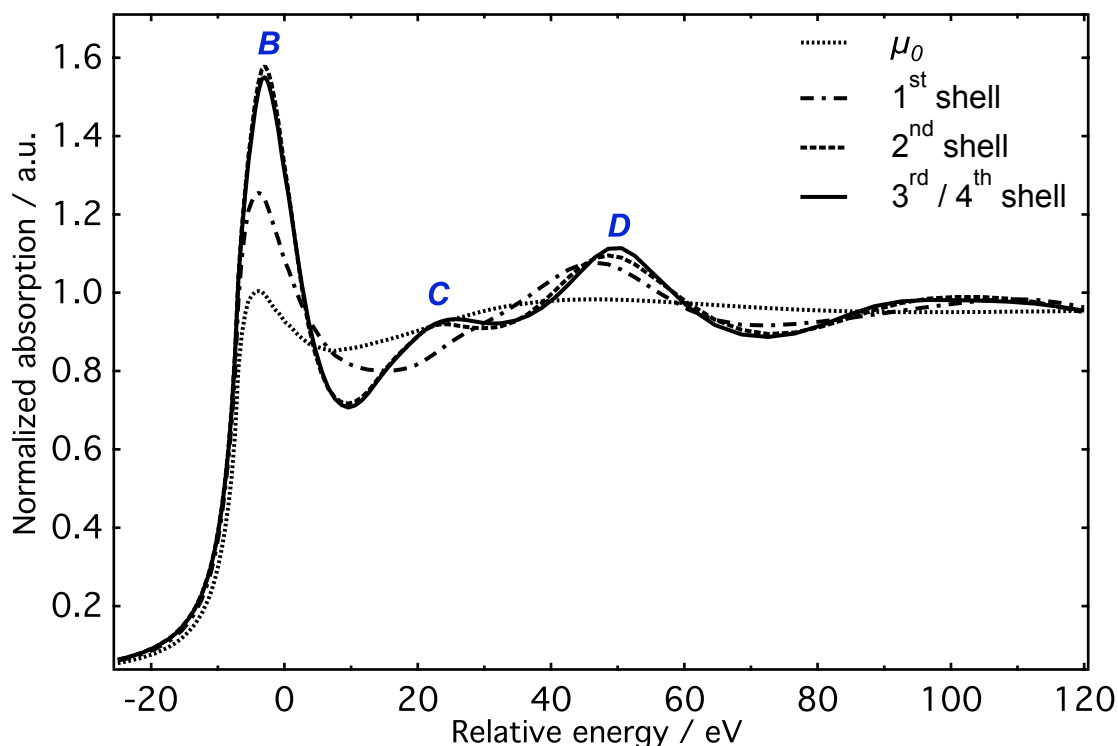


Figure 7.8: Cluster size analysis of the FMS calculation. μ_0 : embedded-atomic background; 1st shell: 4 P atoms; 2nd shell: opposite (with respect to the absorbing Pt atoms) Pt atom, 4 bridging O atoms and 8 terminal O atoms; 3rd shell: opposite P₄ plane; 4th shell: opposite terminal O atoms. The 3rd and 4th shell calculations are identical.

shell is the second P₄ plane ($R_{\text{FMS}} = 4.1 \text{ \AA}$), while the 4th shell includes the remaining terminal O atoms at the far side of the absorbing Pt atom ($R_{\text{FMS}} = 6.0 \text{ \AA}$). Note that all spectra were calculated with identical SCF potentials for the entire molecule. Any differences are therefore due to MS contributions only. It is clear from Figure 7.8 that the FMS has converged already after inclusion of the 2nd shell. Adding the 3rd shell only slightly affects the spectrum, while the 4th shell does not change the spectrum at all. The strong absorption feature D is already present in the 1st shell calculation suggesting that this is the first constructive interference feature of the single-scattering Pt–P paths as well as the strong in-plane collinear multiple scattering Pt–P–Pt–P–Pt paths and triangular Pt–P–P–Pt paths, which all have considerable amplitude as they exhibit symmetries that directly point towards the electron-rich ligands. Indeed, the kinetic energy of 50 eV corresponds to a photoelectron wavelength of 1.7 Å which is comparable to the 1st shell distance of $\sim 2.3 \text{ \AA}$.

Feature C only appears after inclusion of the 2nd shell, while it is hardly affected by adding the 3rd shell. This indicates that this feature originates from single and multiple

scattering involving the O atoms. The presence of the second Pt atom does not contribute to feature *C*, or in general to the XANES spectrum, as was tested by comparing the calculation with and without the Pt atom. Surprisingly, the 3rd and 4th shells do not change the XANES spectrum significantly despite the effective mean free path of 5.4 Å that samples the entire molecule (calculated from the 5.3 eV core-hole life time, see Table 4.1). This indicates that the multiple scattering pathways involving the second half of the molecule are unfavorable.

Electronic structure assignment

Figure 7.9 shows the Pt d-DOS together with the energy-integrated d-DOS multiplied by a factor of 2, *i.e.* the total d-electron count for a Pt₂ unit. The d-orbital ordering in square-planar complexes is often a matter of discussion, because it largely depends on the electronic and geometric properties of the ligands. In general, ligand field theory predicts a stabilization of the orbitals pointing in the out-of-plane direction (d_{z^2} and d_{xz} , d_{yz})

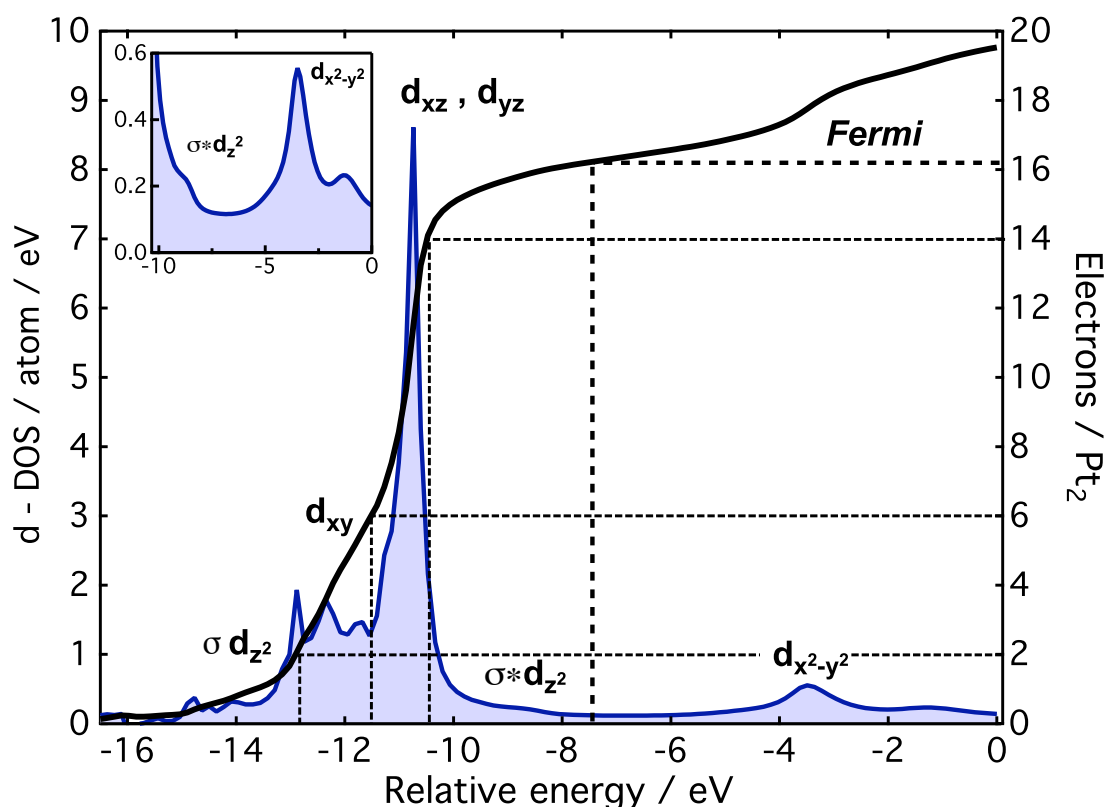


Figure 7.9: Electronic structure assignment of the d-levels in the Pt d-DOS of PtPOP (filled curve, left axis) by making use of the energy-integrated d-DOS (solid curve, right axis) per Pt₂ unit. The different levels are indicated by horizontal and vertical dashed lines. The inset in the upper left corner shows a zoom into the region close to the Fermi energy around -7.416 eV.

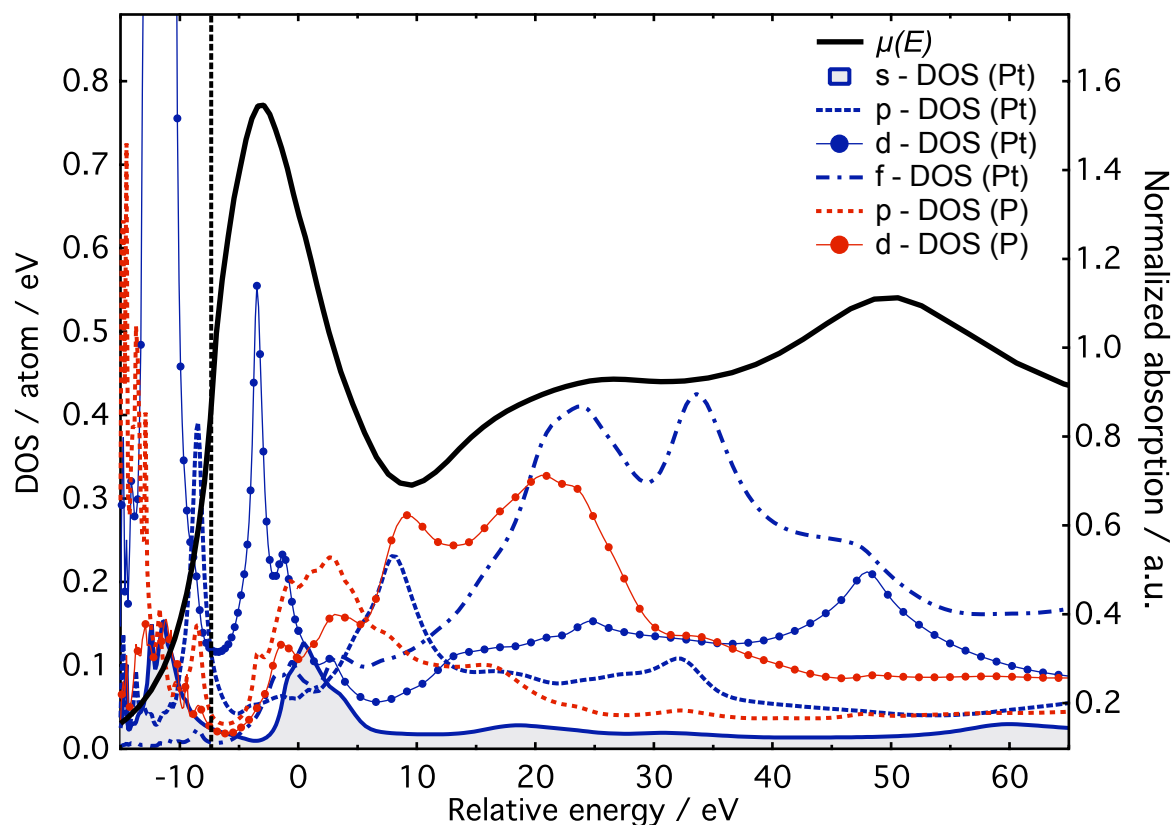


Figure 7.10: *s*-, *p*-, *d*-, and *f*-DOS of the absorbing Pt atom in PtPOP, *p*-DOS and *d*-DOS of the first-shell P-atoms (both left axis) and the calculated XANES spectrum $\mu(E)$ (solid curve, right axis). The Fermi level is indicated by a vertical dashed line at -7.416 eV.

and a destabilization of the orbitals that lie in the plane of the ligands ($d_{x^2-y^2}$ and d_{xy}). Similarly, we would expect the d_{z^2} and d_{xz} , d_{yz} orbitals to be raised in energy and split if two square-planar complexes approach each other along the z -axis, as is the case in PtPOP (see Figure 2.1). Based on these ligand-field considerations and using the steps in the energy-integrated *d*-DOS, we can assign the electronic structure of the *d*-levels in PtPOP, as shown in Figure 7.9. Note that the peaks around -9 eV and -13 eV are assigned to the σ -bonding and σ^* -anti-bonding molecular orbitals resulting from a linear combination of the atomic $5d_{z^2}$ -orbitals. The latter is the HOMO from which the optical excitation in the time-resolved XAS experiment occurs (see Chapter 8). The Fermi energy at -7.416 eV occurs for a total *d*-electron count of 16.3 electrons (see also Table 7.6) and it lies exactly in the gap between the HOMO $\sigma^*d_{z^2}$ orbital and the empty $d_{x^2-y^2}$ orbital, which gives rise to the strong dipole-allowed white-line in the XAS spectrum. As shown later, the shoulder to the right side of the $d_{x^2-y^2}$ peak is assigned to the resulting hybridization with Pt *s*- and P *p*-states. The ligand field splitting between the $\sigma^*d_{z^2}$ orbital and the

$d_{x^2-y^2}$ level is about 5 eV, slightly larger than the DFT calculated splitting of 3.74 eV from reference [153].

Most of the DOS in Figure 7.9 are bound occupied levels which are not directly accessible to the X-ray absorption process. Although the XAS features above the IP do not belong to bound states, they can still be interpreted in terms of the l -projected density of states [237, 240]. Figure 7.10 shows the s-, p-, d- and f-DOS at the absorbing Pt atom together with the p- and d-DOS of the surrounding P-atoms. The $2p \rightarrow \epsilon p$ and $2p \rightarrow \epsilon f$ transitions are dipole forbidden, leading to vanishingly small transition amplitudes. However, as expected from the dipole selection rules, it is seen that all the absorption features in the spectrum correlate with either the s- or d-density of states at the absorbing Pt atoms. In particular, features *B*, *C* and *D* can all be correlated with corresponding peaks in the d-DOS. The FWHM of the white-line of ~ 11 eV is much larger than expected from the L_{III} -edge life time broadening (5.3 eV, Table 4.1) only, which indicates that this peak is not pure $2p \rightarrow 5d_{x^2-y^2}$ but also contains contributions from other transitions. In fact, a strong peak in the s-DOS is seen just above the IP leading to a broadening of the white-line at its high-energy side. This s-DOS feature, together with close-by peaks in the p- and d-DOS at the Pt and P atoms, form a group of hybridized molecular orbitals involved in the formation of Pt-ligand coordination bonds.

The XANES spectrum of PtPOP qualitatively resembles the XANES spectra of other square-planar Pt complexes with ligands from the second or third row of the periodic table [70, 299]. Ankudinov *et al* assigned a post-edge XANES feature, similar to the *B*-feature in this case, as a so-called hybridization peak, *i.e.* a mixture between the photoelectron state and unoccupied 3d-states of the surrounding Cl atoms, mediated by multiple scattering [70]. Their evidence for this assignment was given by a strong peak in the d-DOS of the Cl atoms concurrent with the position of the post-edge feature. Such a peak in the d-DOS of the P atoms also occurs in the case of PtPOP, as seen in Figure 7.10. However, the cluster size analysis in Section 7.2.4 has shown that the *B*-feature only appears after inclusion of the second shell of O atoms, making the assignment of this feature as a pure 1st shell hybridization peak unlikely.

7.3 Summary and conclusions

The EXAFS spectrum of PtPOP is fitted to a simple parametrization model involving SS pathways to 1st, 2nd and 3rd shell atoms, as well as a strong collinear MS pathway in the PtP₄ plane. The fitted values are not too far from the input structure from XRD. The fitted Pt–Pt distance seems a bit smaller in solution than in the crystalline phase. However, due to several overlapping scattering paths within a small region in *R*-space, the uncertainties in and correlations between the parameters are rather large. For the same reason, no more scattering pathways, such as triangular MS pathways or Pt-solvent scattering, can be included in the fit model. The EXAFS fitting model presented in this Chapter is of importance for the upcoming excited-state analysis, as the choice of structural parametrization will determine which structural changes one is sensitive to in modeling the difference EXAFS spectrum.

The XANES theoretical investigation has allowed us to demonstrate the following: 1) The *ab initio* calculated Pt *L*_{III}-edge XANES spectrum for the ground state of PtPOP molecule shows good agreement with the experimental spectrum. The use of the multipole model to account for inelastic losses has proven to result in better agreement in the position of an above-continuum multiple-scattering resonance. 2) The above-continuum XANES spectrum can be interpreted in terms of multiple scattering resonances involving the in-plane P and second-shell O atoms. 3) The white-line region of the XANES spectrum of PtPOP is dominated by the 2p → 5d_{*x*²-*y*²} transition, but is broadened at its blue side due to the absorption into a group of hybridized orbitals involved in the formation of coordination bonds.

The XANES analysis presented in this Chapter shows that the Pt *L*_{III}-edge XANES spectrum can be used as a sensitive tool to probe distortions involving the ligands or, in the case of catalysis, the interaction of the metal d-orbitals with the valence orbitals of the reactants. In the following Chapter we will show how changes in the XANES spectrum of PtPOP reflect structural and electronic changes in its photocatalytically active excited state.

Chapter 8

Time-resolved X-ray absorption spectroscopy

This Chapter presents the results of the time-resolved **XAS** experiments performed at the microXAS beam line at the **Swiss Light Source (SLS)** (see Section 5.4 for experimental details). In Section 8.1 it is demonstrated how we obtain the transient **XAS** signal that is used for further analysis. In particular, it is shown that the signal at longer delay times is affected by photoproducts resulting from the highly reactive excited state of **PtPOP**. As a preparation for the transient **XAS** analysis, we performed laser-only pump-probe measurements to determine the fraction of excited molecules, which are described in Section 8.2. Finally, Sections 8.3 and 8.4 present the detailed transient **EXAFS** and **XANES** analyses, respectively. It will be shown that, while the **EXAFS** spectrum delivers precise structural information for the excited state, the changes in the **XANES** spectrum are due to a mixture of electronic and structural changes in the excited molecule. The semi-quantitative result for the Pt-Pt distortion obtained from the excited-state **XANES** spectrum is in good agreement with the result from the model-based transient **EXAFS** analysis.

The results and analysis presented in this Chapter were in part published in references [163] and [300] (both transient **EXAFS**), and [164] (time-resolved **XANES**).

8.1 Time-resolved XAS results

Figure 8.1 shows the steady-state Pt L_{III} -edge **XANES** spectrum of **PtPOP** (same data as in Chapter 7) together with the transient spectrum obtained by integrating all X-ray fluorescence difference (excited minus unexcited) spectra recorded up to 150 ns after excitation at 390 nm (~ 40 mW, 1 kHz). The latter includes data from three **multibunch (MB)** integration windows (Section 5.4.2) for the time delays 0-50 ns, 50-100 ns and 100-

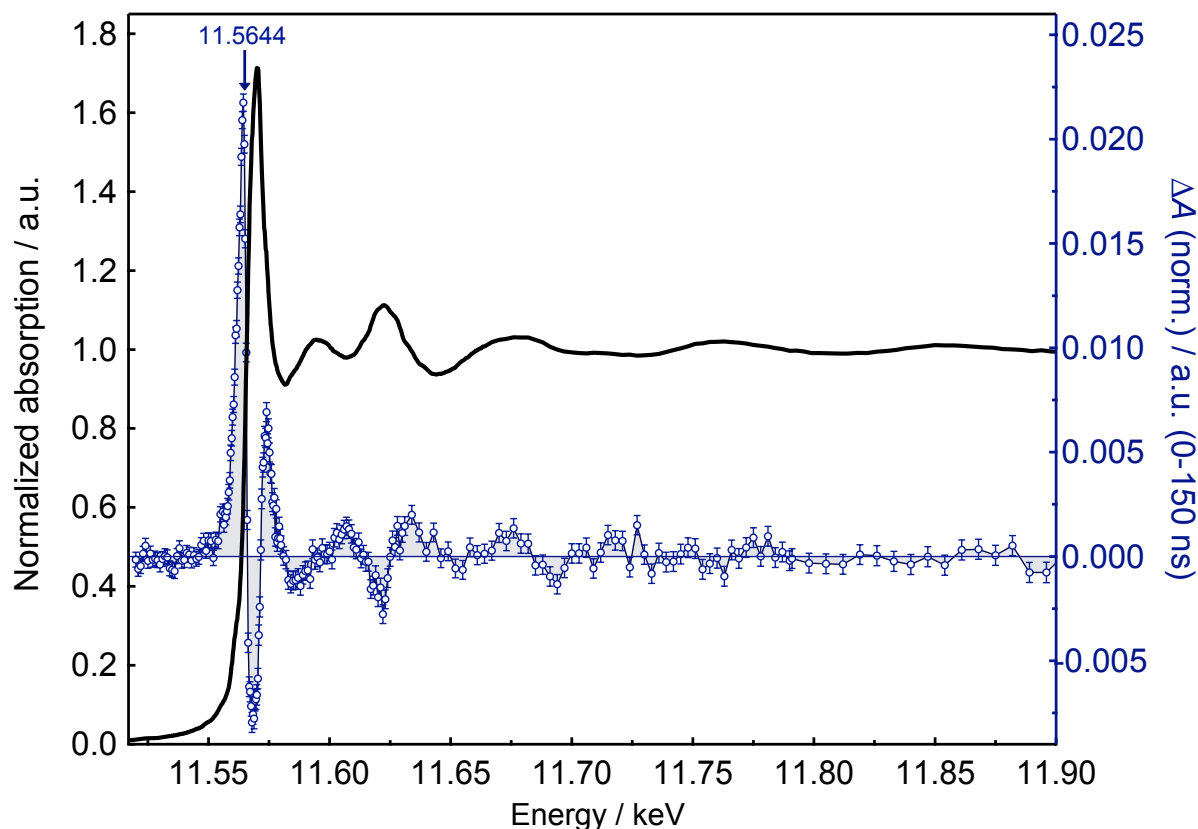


Figure 8.1: Steady-state XAS spectrum of 18 mM PtPOP in ethanol (black curve, left axis; pre-edge subtracted, edge-jump normalized and flattened) and transient (excited minus unexcited) XAS spectrum (blue circles, right axis; difference fluorescence detection, I_0 and edge-jump normalized) of ~ 10 mM PtPOP in ethanol for excitation at 390 nm (~ 40 mW, 1 kHz, see Section 5.4). The transient spectrum is the result of integrating data sets up to 150 ns time delay (see text). The arrow indicates the maximum of the transient signal at 11.5644 keV at which the time scans are performed (Figure 8.3). The energy axis is calibrated.

150 ns. It was verified that the transient XANES signal did not spectrally evolve for these time delays (see below, Figure 8.4b). The averaged fluorescence difference spectra obtained directly from the measurement were normalized to the energy-dependent incoming intensity and subsequently divided by the fluorescence edge jump magnitude according to Equation (5.14). The resulting normalized signal $\Delta A^{\text{norm}}(t, E)$ shown in Figure 8.1 represents the transient spectrum $\Delta\mu(E)$ scaled by the time-dependent excitation yield $f(t)$ and normalized to the edge jump $\Delta\mu_0(E_0)$, as described by Equation (5.12).

Zooms into the XANES and EXAFS regions are shown in Figures 8.2a and 8.2b, respectively. The transient XAS features directly reflect the electronic and structural changes of the molecule in the excited state. The maximum of the transient XANES spectrum amounts to $\sim 2\%$ of the edge jump, while changes in the EXAFS spectrum are

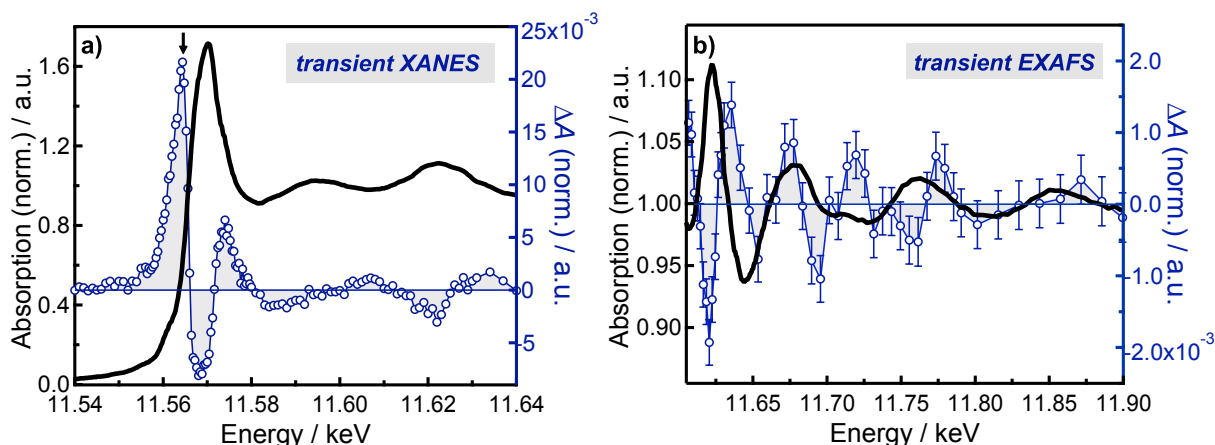


Figure 8.2: Steady-state (black) and transient (blue) **XANES** (a) and **EXAFS** (b) spectra of **PtPOP** in ethanol (same data as in Figure 8.1). In a), the error bars on the $\Delta A^{\text{norm}}(t)$ data are about the size of the data markers (not shown for clarity). All data are normalized to the edge jump magnitude and the energy axes are calibrated. The arrow in a) indicates the $\sigma^*5d_{z^2}$ resonance feature around 11.5644 keV at which the time scans of Figure 8.3 were performed. For clarity of presentation, the transient **EXAFS** data and the errors shown in b) were binned a factor of two.

smaller than 0.2%. It is shown in Appendix F that the transient signal magnitude could be doubled by exciting the sample at the center of the absorption band around 370 nm. Due to the factor 10 higher absorption cross-section at 370 nm compared to 390 nm, this caused appreciable aggregation at the inner wall of the flow capillary with a concomitant increase of the total X-ray fluorescence intensity. In order to ensure a more uniform laser penetration through the sample and therefore less aggregation, the experiment was performed with 390 nm excitation. In addition, the scans were taken at 4 different spots on the sample by vertically translating the holder after each scan.

8.1.1 Excited state decay monitored by transient XANES

In order to make sure that the transient spectrum belongs to the $^3A_{2u}$ state of **PtPOP**, we monitored the time dependence of the maximum transient **XAS** feature around 11.5644 keV and compared it to the decay of the optical phosphorescence around 520 nm measured *in situ* on the same sample. The decay curves are overlapped in Figure 8.3a together with a single exponential fit curve to the $\Delta A^{\text{norm}}(t)$ data that were measured using **camshaft (CS)** pulses ($\Delta t = 50$ ps). The second $\Delta A^{\text{norm}}(t)$ data set shown in Figure 8.3a corresponds to a 400 ns wide **MB** integration window that was measured simultaneously with the **CS** data. Although the data seem to include a second exponential component, the agreement between the decay curves is satisfactory. Interestingly, the **MB**

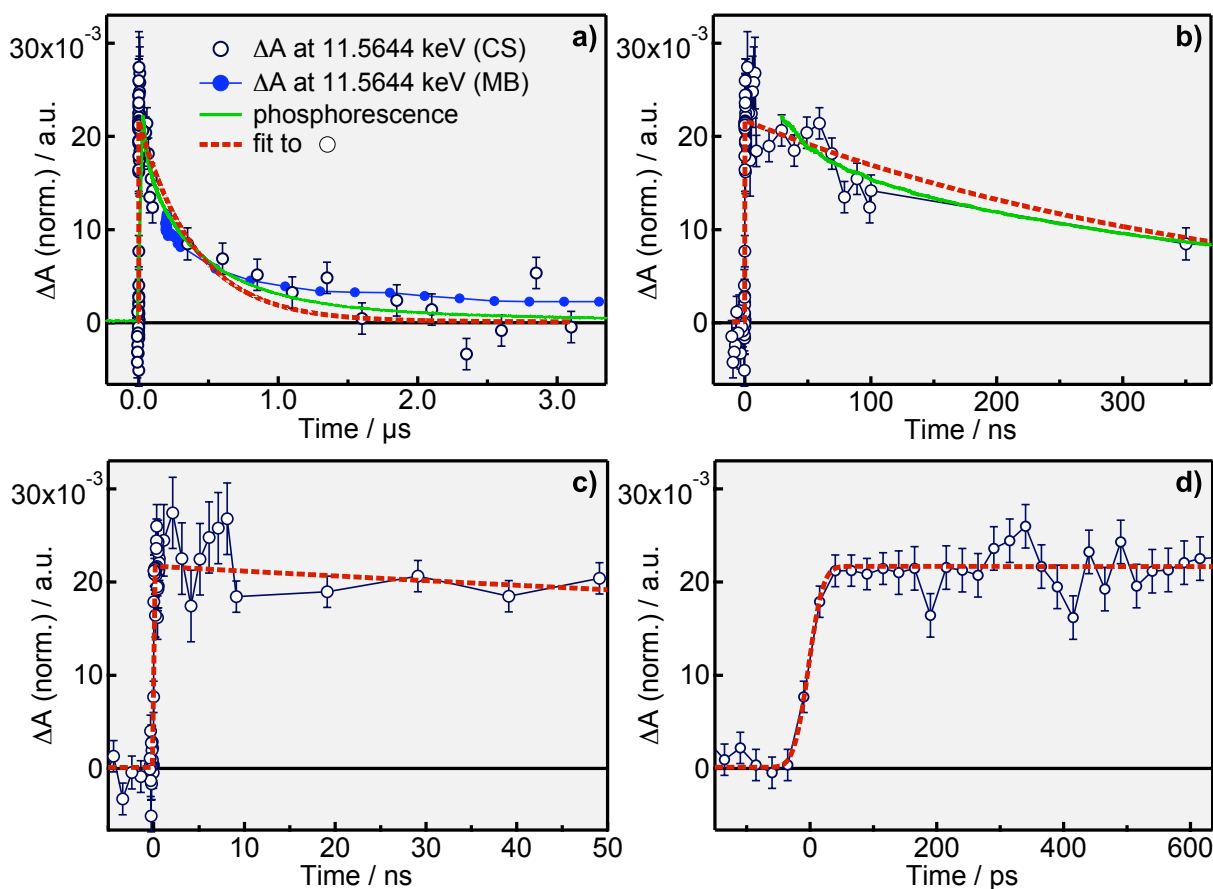


Figure 8.3: Time delay scans at 11.5644 keV (blue markers) and the exponential fit curve for a decay time of 440 ± 90 ns (dashed red). a) $\Delta A^{\text{norm}}(t)$ data from both the **CS** gate (open circles; $\Delta t = 65$ ps) and a **MB** gate (solid markers; $\Delta t = 400$ ns), together with the time-resolved optical phosphorescence around 520 nm (solid green). The latter was cut around the t_0 region because of excessive pump scatter saturating the diode; b-d) same data as in a), but shorter time windows. The magnitudes of the error bars vary in different parts of the scan due to different total integration times. Zero levels have been subtracted from the data.

$\Delta A^{\text{norm}}(t)$ signal does not decay to zero within $3 \mu\text{s}$, whereas the phosphorescence does. **MB** windows at even longer time delays up to $70 \mu\text{s}$ (not shown) still show a transient signal that can possibly be due to the excited ${}^3A_{2u}$ state. The energy transient of this long-lived signal is different from the early-time transient, as shown in Figure 8.4a. We therefore assign it to the formation of photoproducts, *e.g.* **PtPOP** molecules that have reacted with solvent and/or oxygen molecules. In Section 8.4.3 we will try to qualitatively simulate these changes in the transient **XANES** spectrum. At early times the decay curves of the phosphorescence and transient **XAS** match quite well, indicating that the transient for times < 300 ns indeed belongs to the ${}^3A_{2u}$ state. This is supported by Figure 8.4b, demonstrating that no spectral evolution takes place for time delays up to 150 ns. Within

the error bars, the transient spectra for the three different time windows (0-50 ns, 50-100 ns and 100-150 ns) are identical, which allows us to average these spectra together in order to increase the **signal-to-noise (S/N)** in the **EXAFS** region. The resulting average is shown in Figures 8.1 and 8.2, and will be the basis for all further analysis (Sections 8.3 and 8.4). Finally, the emergence of the A_{2u} state is established by the presence of a strong new absorption feature just below the white line around 11.5644 keV (see Figure 8.2a) appearing in the excited state, which results from a hole in the $\sigma^*5d_{z^2}$ orbital due to photoexcitation (recalling from Chapter 2 that the optical excitation into $^1,^3A_{2u}$ involves the transition $\sigma^*5d_{z^2} \rightarrow \sigma 6p_z$).

The exponential fit to the $\Delta A^{\text{norm}}(t)$ data yielded a decay time of 440 ± 90 ns. This is substantially shorter than the reported life time of $\sim 10 \mu\text{s}$ of the $^3A_{2u}$ state [129]. We attribute this discrepancy to oxygen and/or concentration quenching of the excited state. Despite degassing the solvent and flowing the sample in a closed loop without contact to air (see Section 5.2), a certain concentration of dissolved oxygen is unavoidable. The relation between the measured life time τ and the life time in the absence of quenching τ_0 is given by the *Stern-Volmer expression* [301]

$$\tau_0/\tau = 1 + k \tau_0 \cdot [\text{O}_2] \quad (8.1)$$

where $k = 2 \cdot 10^{10} \text{ M}^{-1}\text{s}^{-1}$ is the bimolecular diffusion-controlled quenching constant for O_2 in ethanol at room temperature [302] and $[\text{O}_2]$ is the concentration of O_2 in the solution (maximum solubility is $\sim 2.1 \cdot 10^{-3} \text{ M}^{-1}$ in ethanol [303]). Assuming we can reduce the O_2 concentration by a factor of 20 by degassing the solution with bubbling nitrogen for one hour, the measured life time according to Equation (8.1) would be $\tau = 480$ ns, *i.e.* reasonably close to the life time we inferred from the transient **XAS** decay. Furthermore, the triplet state might be quenched by the **PtPOP** molecules themselves (concentration quenching). Indeed, efficient quenching by oxygen (and other solutes) [135, 304–306] and concentration quenching for concentrations $> 10^{-4} \text{ M}^{-1}$ [297, 307] have been reported for **PtPOP** (the concentration in this experiment was ~ 10 mM).

Shorter time windows of the transient **XAS** delay scan are shown in Figures 8.3b-d, overlapped with the exponential fit curve. The data are corrected for drifts in the zero level.* For the fit in Figure 8.3d, the exponential fit function (multiplied by a step function) was convoluted with a Gaussian representing the **IRF** (cross-correlation between laser and X-ray pulses). The fitted Gaussian **FWHM** value of 43 ± 2 ps is slightly shorter

*Zero scans were performed every 5th delay scan. A zero scan is a dummy scan of 30 points (1 s integration) during which the X-rays are blocked. The averaged values of the various data channels are subtracted from the batch of data that is taken shortly before or after the zero scan.

than the X-ray CS pulse width (~ 65 ps, Section 5.1.1), but given the sparse data points in the rise of Figure 8.3d, the two values are considered to be in satisfactory agreement.

It is noted that one ideally measures the transient XAS spectrum at the shortest delay

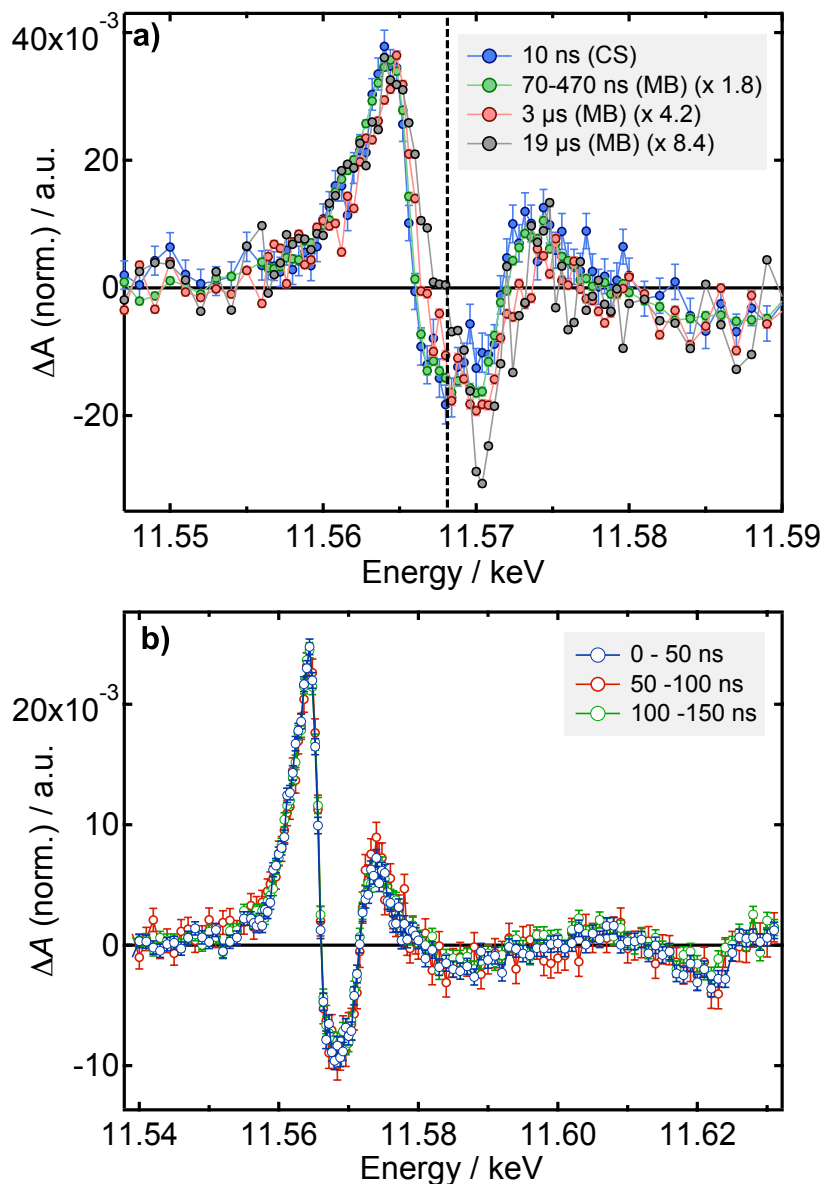


Figure 8.4: a) Transient XANES spectra at different time delays. The spectra are normalized to the maximum of the 10-ns transient (scaling factors in brackets in the legend). CS means that the CS pulse was used as a probe, MB means that an integration gate in the MB pulse train was used. The gate widths for the μ s delay times were approximately 400 ns. The vertical line indicates the position of the negative feature that evolves into a zero crossing at 19 μ s; b) Transient XANES spectra for three integration gates up to 150 ns. The spectra were scaled to make them overlap for comparison. These spectra were averaged together to generate the transient XAS spectrum of Figures 8.1 and 8.2.

possible (*i.e.* 65 ps) which would reduce the chances of photochemical reactions to occur. In the present case, however, the S/N of the 50-ps data was insufficient for a quantitative transient EXAFS analysis. Nevertheless, based on Figure 8.4b and the decay curves of Figure 8.3, we believe that the transient spectrum integrated from 0 to 150 ns is a good representation of the $^3A_{2u}$ state of PtPOP free of photochemical reaction products.

8.2 Estimation of the excitation yield from laser-only experiments

It was shown in Section 5.4.3 that the magnitude of the measured transient signal $\Delta A(t, E)$ is directly proportional to $\Delta\mu(E)$ and the excitation yield $f(t)$, *i.e.* the fraction of excited molecules at the time the sample is probed by the X-rays. The latter is not known *a priori*. Therefore, in modeling and fitting the transient and deriving structural parameters contained in $\Delta\mu(E)$, $f(t)$ needs to be determined as well. Ideally, in order to reduce the number of fitting parameters in the structural analysis, one determines $f(t)$ in a separate experiment and fixes the derived value in the transient XAS analysis. This was the aim of the laser-only broadband transient absorption (TA) measurements we performed in preparation of the pump-probe XAS measurements. The experimental technique that is used is identical to the optical measurements of Chapter 6, except that here, the conditions are such that they best match the conditions of the time-resolved XAS experiment, *i.e.* high excitation power, high sample concentrations and a 500 μm quartz capillary for flowing the sample.

Figure 8.5a shows an example of a transient absorption spectrum of a 1 mM solution, recorded 65 ps after excitation at 365 nm (65 ps corresponds to the X-ray pulse width, and therefore the earliest possible time delay in the pump-probe XAS experiment). As discussed in Chapter 6, the transient spectrum is characterized by two excited state absorption (ESA) bands around 340 nm and 473 nm and the ground state bleach (GSB) signal centered around 370 nm (overlapped with scatter from the excitation beam). Ideally, the excitation yield, in the linear regime of pump powers, is derived from the GSB signal in the optical transient absorption spectrum, using the known extinction coefficient of the ground state (GS) absorption spectrum (see Figure 2.2a). However, in the case of PtPOP, the excitation yield under the conditions of the time-resolved XAS experiment could not be determined very accurately by this method due to: a) overlapping contributions of the GSB and ESA signals; b) the high sample concentration of 10 mM causing saturation of the transient GSB signal ($\Delta\text{OD} > 1.5$); c) excessive pump scatter for high excitation power in the region around the excitation wavelength which overlaps with the

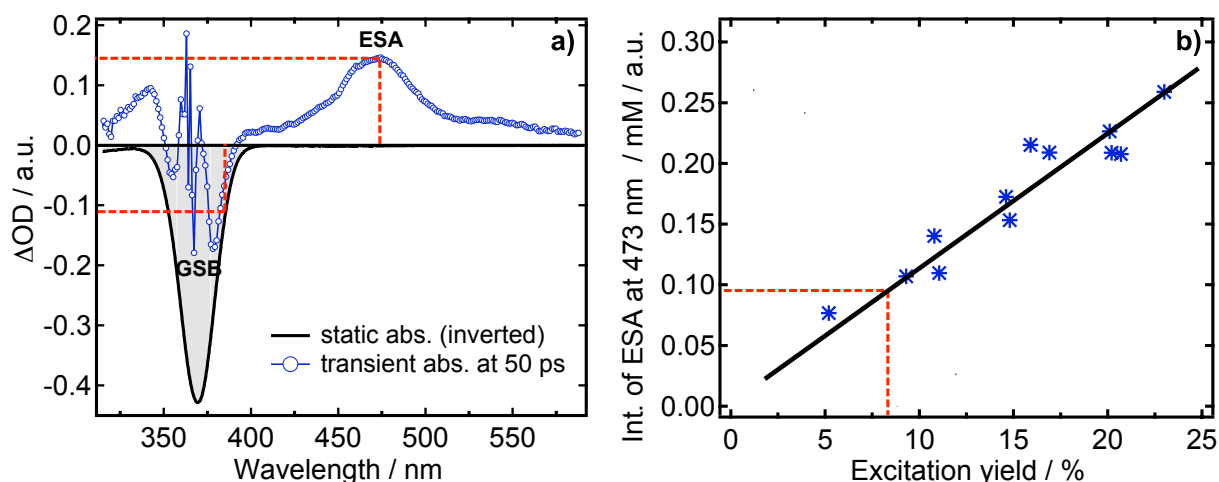


Figure 8.5: a) Broadband TA spectrum of PtPOP in ethanol in a 500 μm quartz capillary under low concentration (1 mM) / low excitation power conditions at 65 ps time delay, for excitation at 365 nm (blue circles) and the scaled, inverted GS spectrum (black trace). The spikes around 365 nm are caused by excessive laser scatter into the detection setup. The dashed lines are used to relate the GSB and the ESA values; b) Calibration curve for an estimate of the excitation yield. The blue data points represent a series of transient absorption measurements (65 ps) at low concentrations (0.5-2 mM) and low power (2-6 mW) with excitation wavelengths in the range 355-370 nm. The excitation yield was determined from the GSB at 385 nm (see left figure). The black line is a linear fit to the data points, the dotted lines show the derivation of the excitation yield from a transient absorption measurement under conditions of the X-ray experiment (10 mM, 40 mW).

narrow GSB feature.

We therefore estimated the excitation yield in an indirect way by: 1) performing a series of TA measurements at low excitation powers, low concentrations and excitation at the blue side of the main absorption to avoid pump scatter obscuring the red side of the GSB signal; 2) relating the magnitude of the GSB at 385 nm (after approximate compensation for the overlapping ESA of $\sim 0.015 \Delta\text{OD}$, extrapolated from 410 nm), to the excitation yield[†] and subsequently to the magnitude of a triplet-state ESA at 473 nm, which is not overlapping with the GSB, pump scatter or stimulated emission signals; 3) performing the measurements under realistic laser pump - X-ray probe conditions with high concentration and high excitation power and using the magnitude of the ESA to determine the excitation yield. From the low power (2-6 mW) / low concentration (0.5-2 mM) measurements, a calibration curve is determined for the ESA intensity at

[†]This is done by using Lambert-Beer law $\text{OD} = \epsilon cd$: the know extinction coefficient ϵ at 385 nm (see Figure 2.2a) is multiplied by the path length of $d = 500 \mu\text{m}$. The measured ΔOD at 385 nm is consequently divided by the above value ϵd , resulting in the excited state (ES) concentration c_{ES} . The excitation yield f is then c_{ES} divided by the initial sample concentration.

473 nm per concentration unit (mM) as a function of excitation yield, which shows a linear dependence (see Figure 8.5b). The magnitude of the **ESA** at 473 nm ($0.95 \Delta OD$) measured under the conditions of the X-ray experiment (10 mM, 40 mW), after dividing by the concentration, can now be directly used to derive the excitation yield using the calibration curve of Figure 8.5b. In this way an excitation yield of $\sim 8\%$ is derived at 65 ps time delay. From the scatter in the calibration curve and considering the systematic errors made in relating the **GSB** to the **ESA**, an uncertainty of $\pm 3\%$ is estimated for the derived excitation yield.

In the previous Section it is described that the transient **XAS** spectrum is integrated over the first 150 ns after excitation in order to improve the **S/N** of the transient **EXAFS** spectrum. A time scan at the maximum of the transient **XANES** feature showed a decay time of about 440 ns, which was confirmed to be the triplet state decay. The transient **XAS** signal at 150 ns has thus decayed to about 30% compared to the value at 65 ps. This results in an estimated excitation yield of, on average, $6 \pm 3\%$ for the 0-150 ns time window under the excitation conditions of the laser pump - X-ray probe experiment. Due to the rough approximations made in this estimation procedure, and the resulting large uncertainty in the value of f , we can not simply fix the excitation yield to this value in the time-resolved **XAS** analysis. However, in the next Section it will be shown that we can reliably derive the excitation yield from the transient **EXAFS** spectrum itself, yielding a value of f that is in good agreement with the above derived value of $6 \pm 3\%$.

8.3 Transient EXAFS analysis

In the following we will analyze the transient **EXAFS** spectrum of Figure 8.2b using a model-based fitting procedure in order to extract the structural distortions in the $^3A_{2u}$ excited state of **PtPOP**.

8.3.1 A novel data analysis approach for transient EXAFS spectra

Conventional methods for **EXAFS** analysis usually rely on fitting the (weighted) **Fourier transform (FT)** of the k -space **EXAFS** data, as was done for the structural analysis of the ground state **PtPOP** molecule described in Section 7.1. For the structural analysis of the excited state, we commonly extract a **XAS** (**XANES** and/or **EXAFS**) spectrum of the excited species using the difference spectra, the ground state spectrum and the excitation yield [94]. The latter is not always known with precision. In addition, the separate fitting of the ground state and of the excited state **EXAFS** spectrum may be flawed by systematic errors. Here we use as a quantitative structural analysis of the ex-

cited state, an approach based on fitting the recorded difference (excited minus unexcited) XAS spectrum directly in energy space, which has been shown to give superior accuracy of the derived structural changes compared to the above approach based on fitting full spectra [94]. It reduces the number of required fitting parameters by cancellation in the differences [94]. In addition, it allows to introduce the excitation yield as a fitting parameter, which is especially useful in cases where the excitation yield can not be accurately derived by optical pump-probe measurements. The second point in which this analysis differs from usual fitting procedures lies in that we calculate the EXAFS signal for each ES structure separately. In a usual EXAFS analysis, the *ab initio* FEFF [213] calculation is performed once for a structure that is thought to be close to the structure of the system under study, after which the structural parametrization and fitting are carried out (see Section 4.3). This approach requires a substantial amount of prior knowledge about the structure because only small ($\lesssim 0.1 \text{ \AA}$) deviations from the input structure are allowed, and the structural parametrization should respect the chemical integrity of the system, often resulting in complicated expressions for the structural parameters. Here, we allow the ES structure to change by large amounts in a chemically sensible way, in that we perform a FEFF calculation for every structure separately while no complicated structural parametrization is required. This method was successfully applied to an Fe(II) molecular complex in solution, for which subpicometer precision for the derived Fe-ligand bond elongation is achieved [94].

Optimizing the ground-state structure

The ES analysis is based on the parametrization model used for the steady-state (GS) EXAFS spectrum described in Section 7.1. It was found that the input structure from X-ray diffraction (XRD) was close but not identical to the fitted structure from EXAFS (Table 7.2). As a starting point for the ES distortions, we therefore need to determine the optimized GS structure, *i.e.* the structure that, if provided as input structure to the fitting program, would result in fitted ΔR_γ values close to zero. However, the tricky part here is, that the fitting model not necessarily parametrizes the structure in a chemically sensible way respecting the symmetry of the molecule. Changes in single scattering (SS) path distances distort the fitted structure radially originating in the absorbing atom, while multiple-scattering (MS) path length distances are composed of several such radial "through-space" distances and real bond distances. The fitted distortion of one scattering path is therefore not always structurally consistent with the distortion of an other path.

In the case of PtPOP, it is not immediately obvious from the fitted distortion parameters in Table 7.2 how to modify the structure so that the symmetry of the molecule is conserved and the structure is still chemically realistic. It is seen that almost all distances shorten, except the Pt-ligand coordination bond lengths which lengthen by ~ 0.01 Å. Maintaining the molecular D_{4h} symmetry, we have applied the following distortions to obtain the optimized GS structure: 1) decrease the Pt-Pt distance by 0.049 Å; 2) increase the Pt-ligand distance by 0.009 Å; 3) bring the P_4 planes (incl. the terminal O_t atoms) closer by 0.067 Å; 4) move the bridging O_b atoms inwards by 0.018 Å. The FEFF6 input file for the optimized GS structure is given in Appendix A. It was checked that, using the resulting optimized structure, all ΔR_γ values (except ΔR_{Pt-O_t}) are fitted to zero up to the third decimal point, while the energy shift E_0 , the amplitude reduction factor S_0^2 and the squared Debye-Waller (DW) factors σ^2 are fitted to the same values (within error bars) as for the initial input structure from XRD (Table 7.2). The fit qualities for both input structures are comparable. The drawback of the optimized structure as described above lies in the fact that the P– O_b bond lengths are slightly shorter (1.53 Å) than in the XRD structure (1.62 Å), and the Pt atoms lie at the opposite sides of the P_4 planes, *i.e.* inside for the XRD structure, at the outside for the optimized GS structure. Despite this, our approach of fitting the transient spectrum directly, allows to derive accurate *relative* changes between the ground state and excited state. Small systematic errors made in the "absolute" GS and ES structures (and spectra) are cancelled in the difference spectrum.

It is noted that a structural parametrization model that keeps the covalent intra-ligand P–O bonds fixed, would be more realistic. Although the implementation of such a model is, in principle, possible using common fitting programs, it requires complicated geometric relations between the scattering path distances and bond lengths. Alternatively, one could apply a similar approach as for the ES analysis which avoids parametrization in terms of ΔR_γ (see below), but it requires rerunning the calculation for every new structure and the parameter uncertainties and correlations need to be correctly taken into account. The new programming tools package DEMETER by Ravel *et al* [233] should be useful in such cases.

Statistical analysis

We recall from Chapter 4 that the absorption coefficient $\mu(E)$ is related to the fine structure $\chi(E)$ according to $\mu(E) = \Delta\mu_0(E_0) \cdot \chi(E) + \mu_0(E)$, where we have used the edge-jump normalization factor $\Delta\mu_0(E_0)$ instead of normalization to $\mu_0(E)$ in the definition of $\chi(E)$ (Equation (4.8)). Assuming that the background function $\mu_0(E)$ is identical for the ground

state and the excited state[‡], the change in absorption coefficient $\Delta\mu(E)$ between the two states can be expressed as

$$\Delta\mu(E) = \Delta\mu_0(E) \cdot [\chi_{\text{ES}}(E_0) - \chi_{\text{GS}}(E)] = \Delta\mu_0(E_0) \cdot \Delta\chi(E) \quad (8.2)$$

where $\chi_{\text{ES}}(E)$ and $\chi_{\text{GS}}(E)$ are the EXAFS functions of the ES and GS structures, respectively. Using Equation (5.12), we can then derive

$$\Delta A^{\text{norm}}(t, E) = f(t) \cdot \Delta\chi(E) \quad , \quad (8.3)$$

i.e. the normalized experimental transient XAS spectrum $\Delta A^{\text{norm}}(t, E)$ is directly proportional to the fine-structure difference $\Delta\chi(E)$. In the following we consider the difference XAS spectrum at a certain time-delay after time zero, which is justified for the case of a single intermediate ES with a life time that is long compared to the ~ 65 ps X-ray pulse. The procedure can be generalized for the case of evolving transient structures and superimposed intermediate states in a multi-step relaxation pathway [94].

EXAFS signals $\chi_{\text{ES}}^i(\Delta R_i, k)$ for a series of i possible ES structures are generated by using the FEFF6 code [213] included in the IFEFFIT software package [226] (the structural distortion compared to the optimized GS structure is denoted by ΔR_i). The $\chi_{\text{ES}}^i(\Delta R_i, k)$ signals are generated by using the same structural parametrization model as for the ground state (Model 1, Section 7.1.2), *i.e.* the same scattering paths, and the fitted values for S_0^2 , E_0 and σ^2 (Table 7.2) are used.[§] After conversion into energy space, the EXAFS fit $\chi_{\text{GS}}^{\text{fit}}(E)$ to the optimized GS structure is subtracted resulting in the theoretical differences

$$\Delta\chi^i(\Delta R_i, E') = \chi_{\text{ES}}^i(\Delta R_i, E') - \chi_{\text{GS}}^{\text{fit}}(E) \quad , \quad (8.4)$$

with $E' = E + \Delta E_0$, which are compared to the experimental difference signal $\Delta A^{\text{norm}}(E)$ in a non-linear least-squares fitting procedure for a series of excitation yields f and energy shifts ΔE_0 between ES and GS XAS spectra. ΔE_0 represents the chemical shift (Section 4.3.1) between the two states, which can be caused by a change in the ionization threshold as a result of the light-induced electronic and structural changes. The statistical

[‡]This is a valid assumption in cases where the changes in the excited state, *i.e.* coordination number changes, are not too large. For photodissociation reactions, however, this assumption should be revised.

[§]The transferability of these parameters from the ground state to the excited state is usually valid in cases where the ligand shell composition does not change, *i.e.* without photodissociation and/or ligand exchange reactions occurring.

figure that provides the quality of the fit is the normalized square residual

$$R^2(\Delta R_i, f, \Delta E_0) = \frac{1}{N-1} \sum_{j=1}^N \left(\frac{y_j/f - \Delta\chi^{i,j}(\Delta R_i, E')}{\sigma_j^y/f} \right)^2, \quad (8.5)$$

within the limited range of experimental data points j (total N data points), where σ_j^y represents the standard deviation of experimental data point y_j .

8.3.2 Model-based fitting of the transient EXAFS spectrum

The fitting procedure as described in the previous Section relies on additional knowledge about the possible structural changes that can occur upon excitation. The distortions need to be chemically reasonable respecting the nature of the optical excitation, while ample variation in their magnitude should be allowed. Ideally, this approach reduces the degrees of freedom considerably, and therefore it allows finding an unambiguous solution for the ES structure and extracting additional information, such as the chemical shift and excitation yield.

The antibonding-to-bonding $\sigma^*d_{z^2} \rightarrow \sigma p_z$ nature of the electronic transition led us to consider only structural distortions that involve a contraction along the Pt–Pt axis. As to whether and how the ligands are influenced by the excitation, four chemically reasonable deformation models are applied (Figure 8.6).

- **Model I:** In-/outwards movement of the Pt atoms along the Pt–Pt axis, while the ligands stay in place. The P–O_b–P angles do not change. This necessarily implies a small increase in the Pt–P bond lengths and a change in P–Pt–P bond angle.
- **Model II:** Contraction/expansion movement of the POP bridging ligands (incl. the terminal O_t atoms) along the Pt–P coordination bonds. The P–O_b–P angles do not change (thus the distance between both ligand planes is fixed).
- **Model III:** Contraction of the P₄ planes along the Pt–Pt axis while the P–O_b bonds within the ligands are kept fixed. This necessarily implies an outward movement of the bridging O_b atoms and a consequent change in P–O_b–P angle.
- **Model IV:** The Pt atoms stay in the plane of the P atoms as the molecule contracts along the Pt–Pt axis. Again, the P–O_b bonds are kept fixed and the P–O_b–P angle decreases, while the Pt–P bond lengths do not change. This model was suggested as a mode of distortion in references [83, 129].

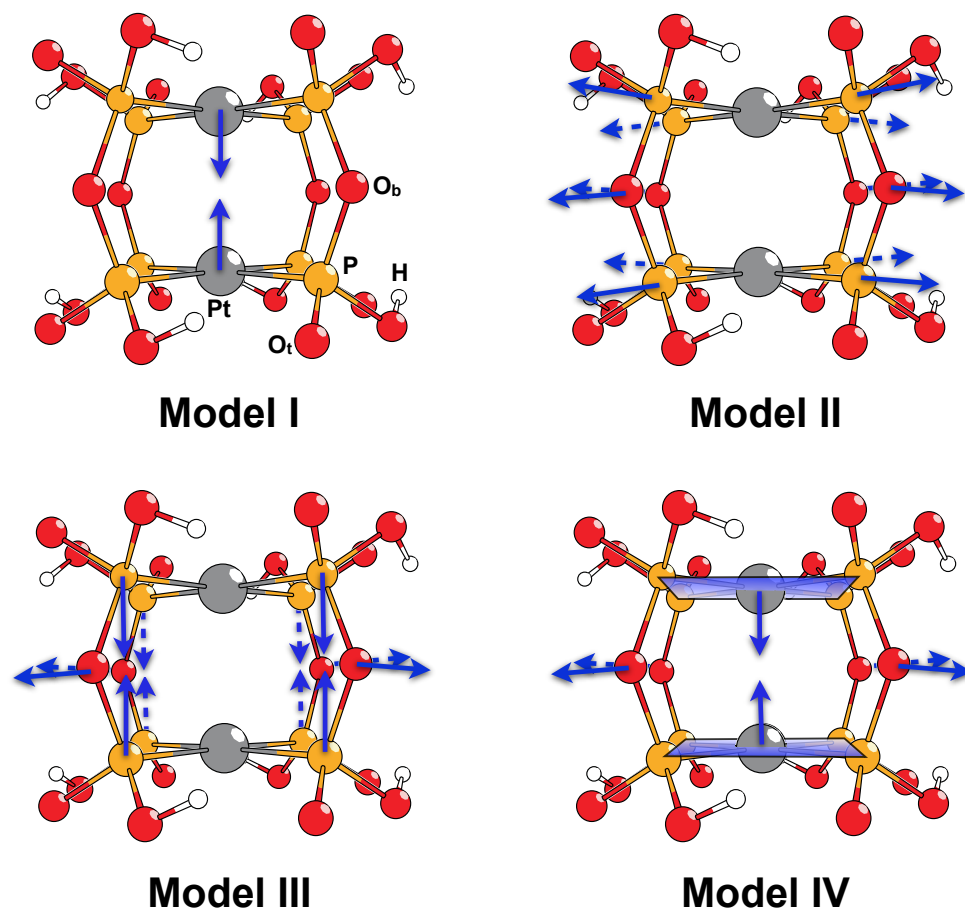


Figure 8.6: Schematic representation of the structural distortion models I-IV considered in the statistical analysis (distortion indicated by arrows). The bridging $\text{P}-\text{O}_b$ bond lengths are fixed for the distortions of models III and IV.

The assumption that the $\text{P}-\text{O}_b$ bond length does not change is based on the large amount of energy that would be required to change such a covalent bond. Because the electronic transition does not involve charge transfer to the ligands, the electron density on the ligands does not change, ruling out a modification of covalent bond lengths. However, the change in $\text{P}-\text{O}_b-\text{P}$ angle requires substantially less energy and this distortion is considered in Models III and IV. It is noted that these models do not include any scattering to the surrounding solvent molecules (see Discussion, Section 8.3.3).

For clarity of presentation, the transient EXAFS data and the errors shown in the plots were binned a factor of two. The non-linear least-square fitting according to Equation (8.4), however, was done with the raw, unbinned data.

Models I and II

The first two distortion models are tested in an iterative way: (1) Model I is applied to the **GS** structure in steps of 0.01 Å which results in an absolute minimum of $R^2 = 1.67$ at 0.31 Å Pt–Pt contraction, 8% excitation yield and a -1 eV energy shift; (2) the POP-ligand contraction/expansion movement according to Model II is then applied in steps of 0.002 Å while the Pt–Pt contraction is kept at 0.31 Å, from which a new minimum of $R^2 = 1.39$ at 0.010 Å distortion, 7% excitation yield and zero energy shift was obtained; (3) an optimization of the Pt–Pt contraction was again performed, but now with the POP-ligand expansion fixed to 0.010 Å. This last step yields an $R^2 = 1.39$ minimum for a Pt–Pt contraction of 0.31 Å, a 7% excitation yield and zero energy shift, confirming the results of step (2), so that no new iteration of the POP-ligand contraction/expansion movement was necessary. The R^2 dependencies according to Equation (8.5) for the combined distortions of Models I and II are shown in Figure 8.7 (after convergence of the fit). The errors of the structural distortions belonging to the minima are obtained by taking a R^2 significance level of 5%, as is indicated by the dotted lines in Figure 8.7. A structural distortion is considered to be statistically significant if the R^2 value of the undistorted structure lies outside the 5% significance level of the R^2 minimum belonging to the distorted structure. R^2 values were also calculated for energy shifts between -5 to 5 eV, but they resulted in significantly higher values over the whole distortion range.

Figure 8.8 compares the fit quality with and without the inclusion of the POP expansion of Model II. It is clearly seen that several oscillatory features are better fit both in amplitude and position if the POP expansion of 0.01 Å is included. Especially the negative feature around 11.695 keV is reproduced much better by including the ligand expansion. The $\chi(E)$ data and best-fits are shown in Figure 8.9, together with their Fourier transforms. The main effect from Model I on the scattering in the first coordination shell (near- P_1 atoms within the original Pt- P_4 plane), is given by the reduced amplitude of the strong collinear multiple scattering path along P–Pt–P. The additional Pt–P elongation due to Model II mainly affects the frequency in the difference spectrum, which, because of parameter correlation, leads to the anticipated zero energy shift.

The 7% excitation yield obtained from the fit is in good agreement with the one estimated ($6 \pm 3\%$) from independent optical pump-probe measurements (Section 8.2). Furthermore, the fitted zero energy shift may be expected for a metal-centered transition without change of oxidation state of the absorbing metal.

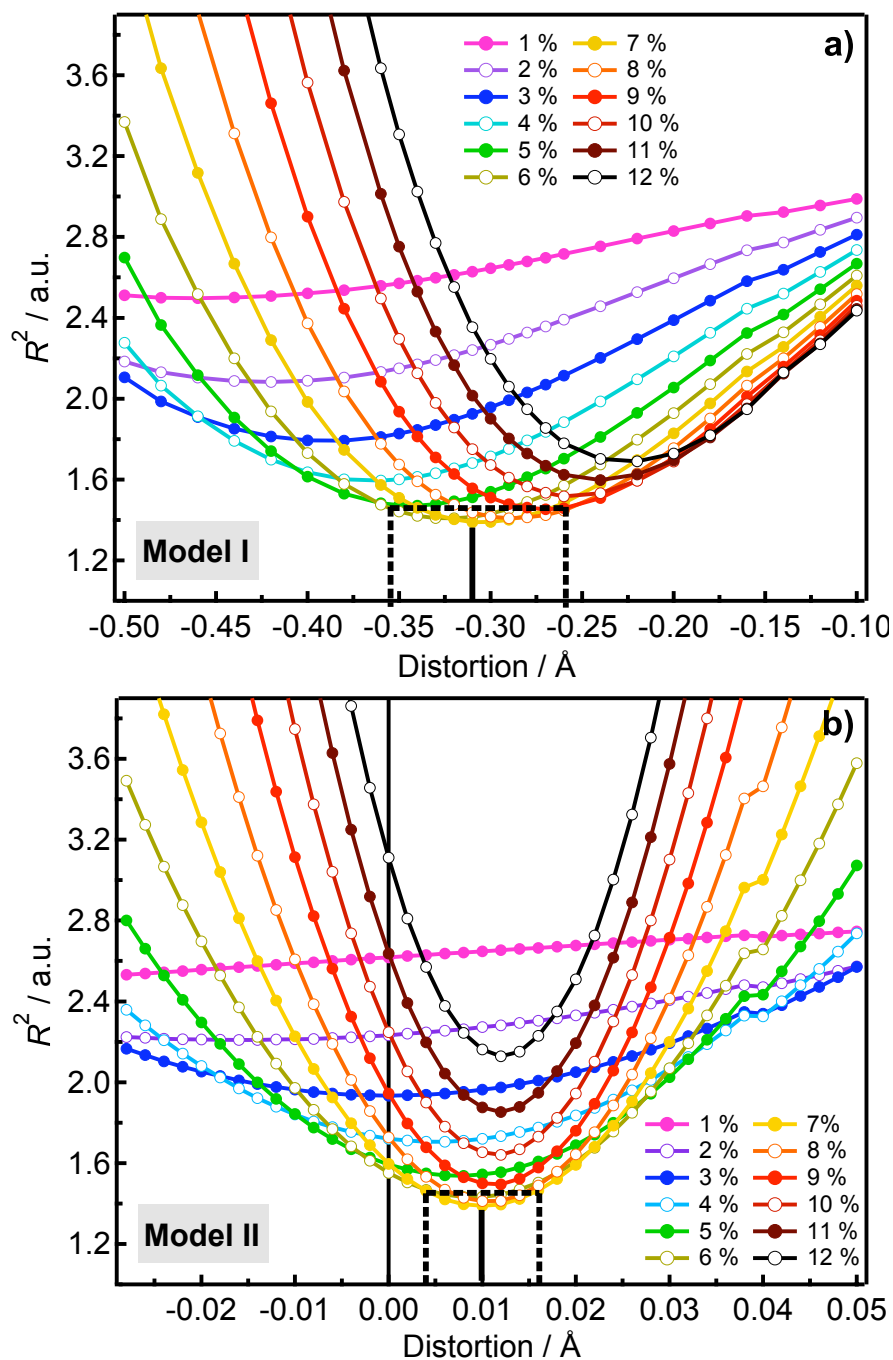


Figure 8.7: R^2 dependencies according to Equation (8.5) as a function of distortion and excitation yield after iterative optimization of the fit by changing the structure according to Models I and II; a) R^2 dependence as a function of Model I (negative distortion = reduced Pt–Pt distance) for a series of excitation yields and a fixed POP expansion of $0.010(6)$ Å ($\Delta E_0 = 0$); b) R^2 dependence as a function of Model II (positive distortion = increased Pt–P distance) for a series of excitation yields and a fixed Pt contraction of $0.31(5)$ Å ($\Delta E_0 = 0$). The solid vertical lines denote the absolute minima in the 4-parameter space ($\Delta\text{Pt–Pt}$, $\Delta\text{Pt–P}$, ΔE_0 , f), while the dashed lines show the significance level of 5%.

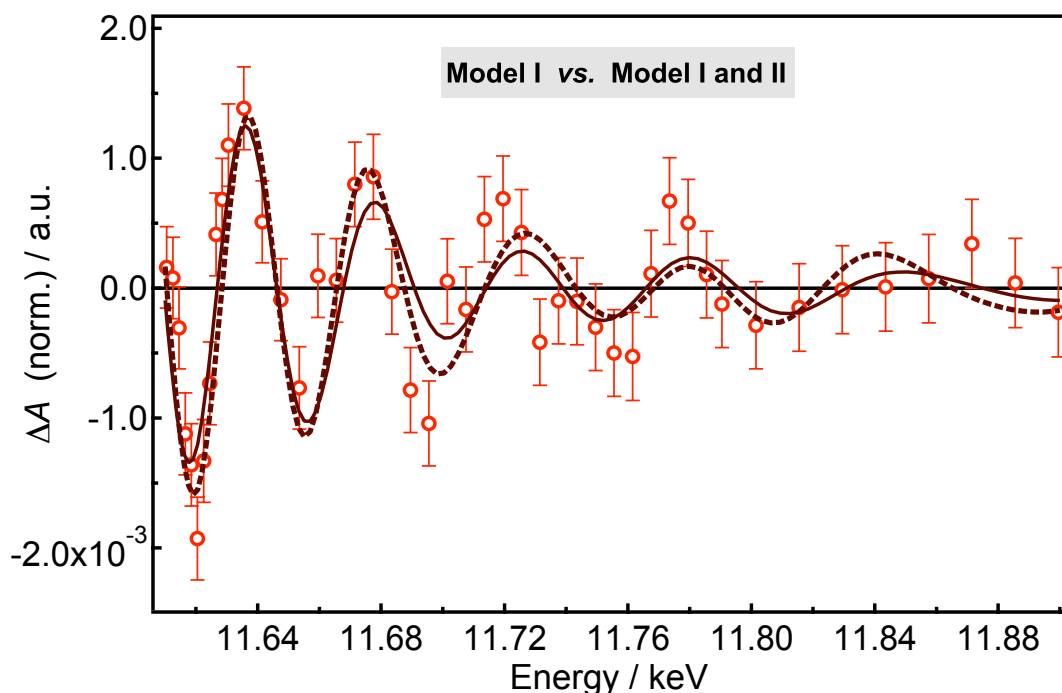


Figure 8.8: Comparison between the fit with (Model I and II; dotted trace) and without (Model I; solid trace) the Pt–POP expansion of $0.010(6)$ Å for a Pt–Pt contraction of $0.31(5)$ Å, zero energy shift and 7% and 6% excitation yields, respectively.

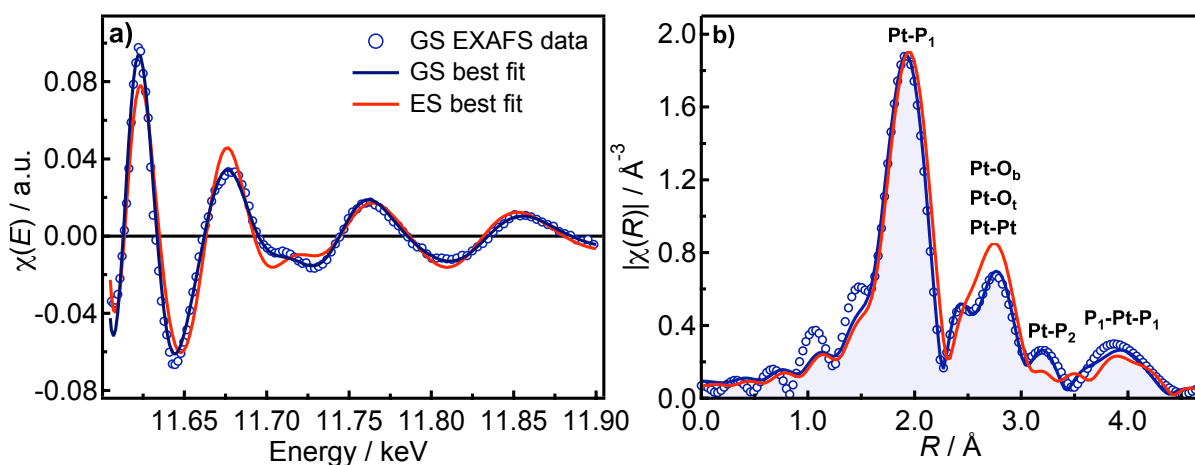


Figure 8.9: a) Ground state EXAFS data $\chi_{\text{GS}}(E)$ with best fit (blue circles and line) and best-fit ES EXAFS signal $\chi_{\text{ES}}(E)$; b) Fourier transform of the data in a) with the assignment of scattering pathways (same color assignment, P_1 is the P shell closest to the absorbing Pt atom, P_2 are the third-shell atoms).

Model III

In order to test whether the POP bridging ligands bend due to the contraction of the Pt atoms, we also implemented Model III. A similar iteration procedure as the one described above was performed for the motions of Models I and III and the combined motions of Models I, II and III. The resulting R^2 plot for Model III with the Pt–Pt contraction fixed to 0.31 Å and the POP expansion fixed to 0.010 Å is given in Figure 8.10. The shape of the R^2 plot looks basically the same if Model II is left out, but all curves are vertically shifted by ~ 0.3 a.u. corresponding to the same difference in R^2 as was found for just the combined motions of Model I and II. This demonstrates the stability of the fit with respect to the different motions, *i.e.* their combination and their order of application did not affect the fitted parameter values.

A very shallow minimum is obtained, located around -0.02 Å contraction of the P_4 planes and 8% excitation yield, but the improvement of the fit at the minimum is not statistically significant ($R^2 = 1.35$ compared to $R^2 = 1.39$ for the excited state structure belonging to a combination of Models I and II). As is seen in Figure 8.10, the R^2 value

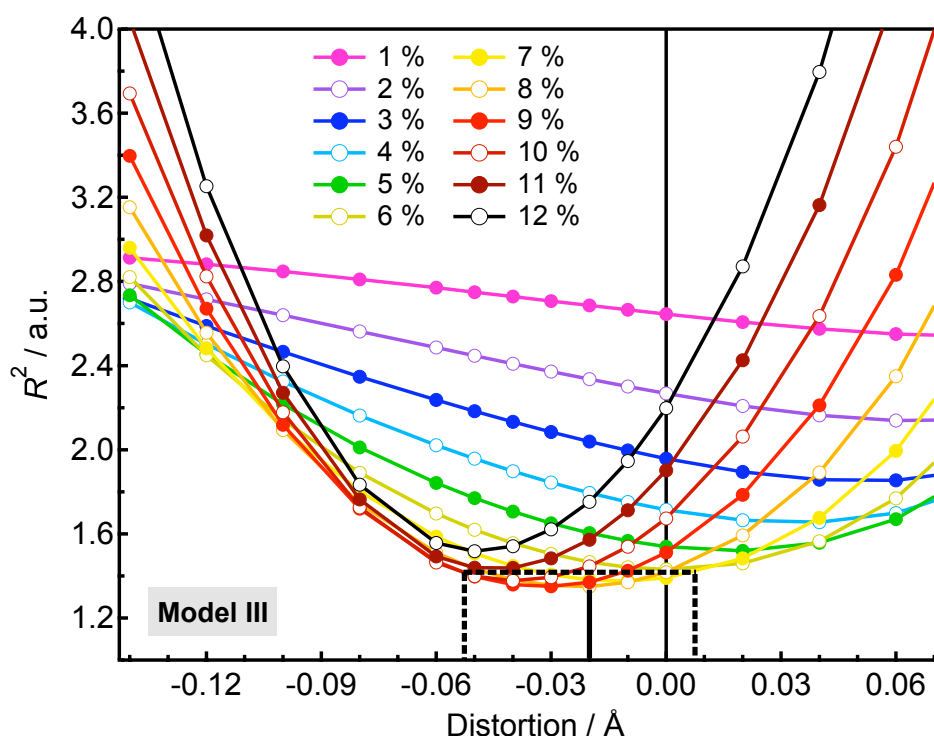


Figure 8.10: R^2 dependence as a function of Model III (negative distortion = P_4 planes contract) for a series of excitation yields ($\Delta E_0 = 0$). The Pt–Pt contraction was fixed to 0.31 Å and the POP expansion was fixed to 0.010 Å. The solid vertical line denotes the minimum, while the dashed vertical lines show the significance level of 5%.

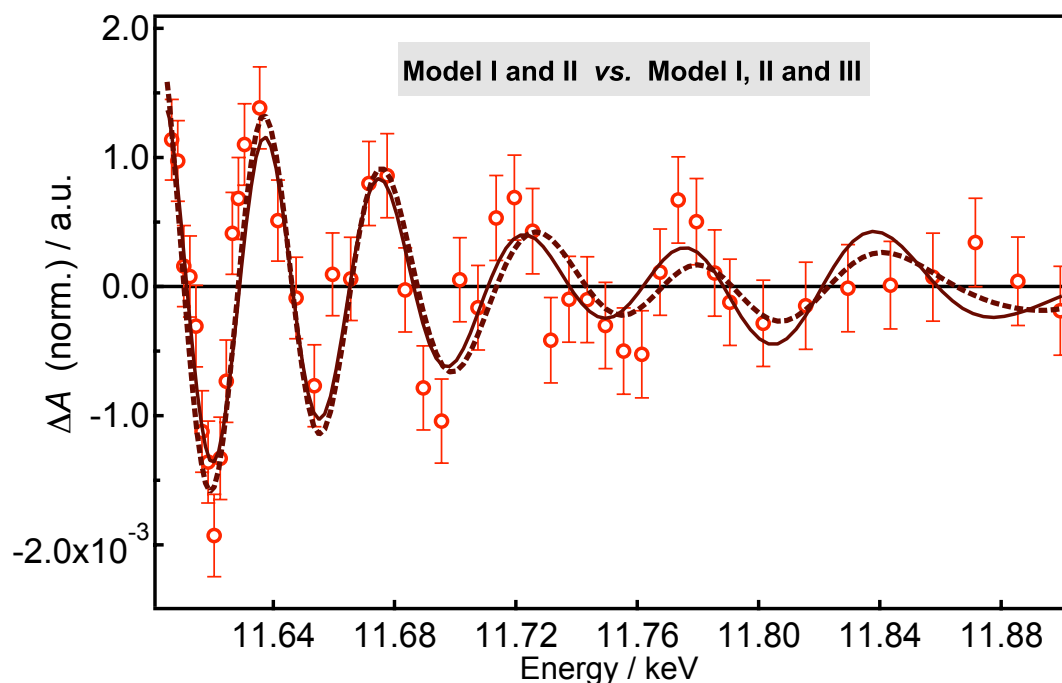


Figure 8.11: Comparison between the fit with (Model III; solid trace) and without (Model I and II; dotted trace) the $P_4 - P_4$ contraction of -0.02 \AA , for a Pt–Pt contraction of $0.31(5) \text{ \AA}$, a Pt–POP elongation of $0.010(6) \text{ \AA}$, zero energy shift and 7% excitation yield

for the structure without the Model III distortion (vertical axis at 0 \AA) lies inside the 5% significance interval. The fits to the transient EXAFS spectrum with and without the -0.02 \AA $P_4 - P_4$ contraction of Model III are compared in Figure 8.11. In the low-energy region, the two curves are identical within the uncertainty of the data, while at higher energy the fit of Model III exhibits larger oscillatory features (but that do not heavily contribute to the R^2 value due to the low signal-to-noise ratio in this region). From these results, we can neither validate nor exclude a contraction of the P_4 planes up to values of -0.05 \AA based on the R^2 statistics of Figure 8.10. However, we can put an upper limit to this distortion because, for contractions that are larger than -0.05 \AA , the fitting statistics gets significantly worse (*i.e.* lies outside the 5% significance interval). From the fact that the contraction of the P_4 planes (max. 0.05 \AA) is small compared to the Pt–Pt contraction ($0.31(5) \text{ \AA}$), it can be concluded that the POP bridges are very constraining.

Model IV

We also tested Model IV that was proposed by Thiel *et al* [83] and in reference [129]. In Model IV, the P atoms are fully adapting to the motion of the Pt atoms, implying flexible, non-constraining POP bridging ligands. A series of R^2 vs. distortion plots is

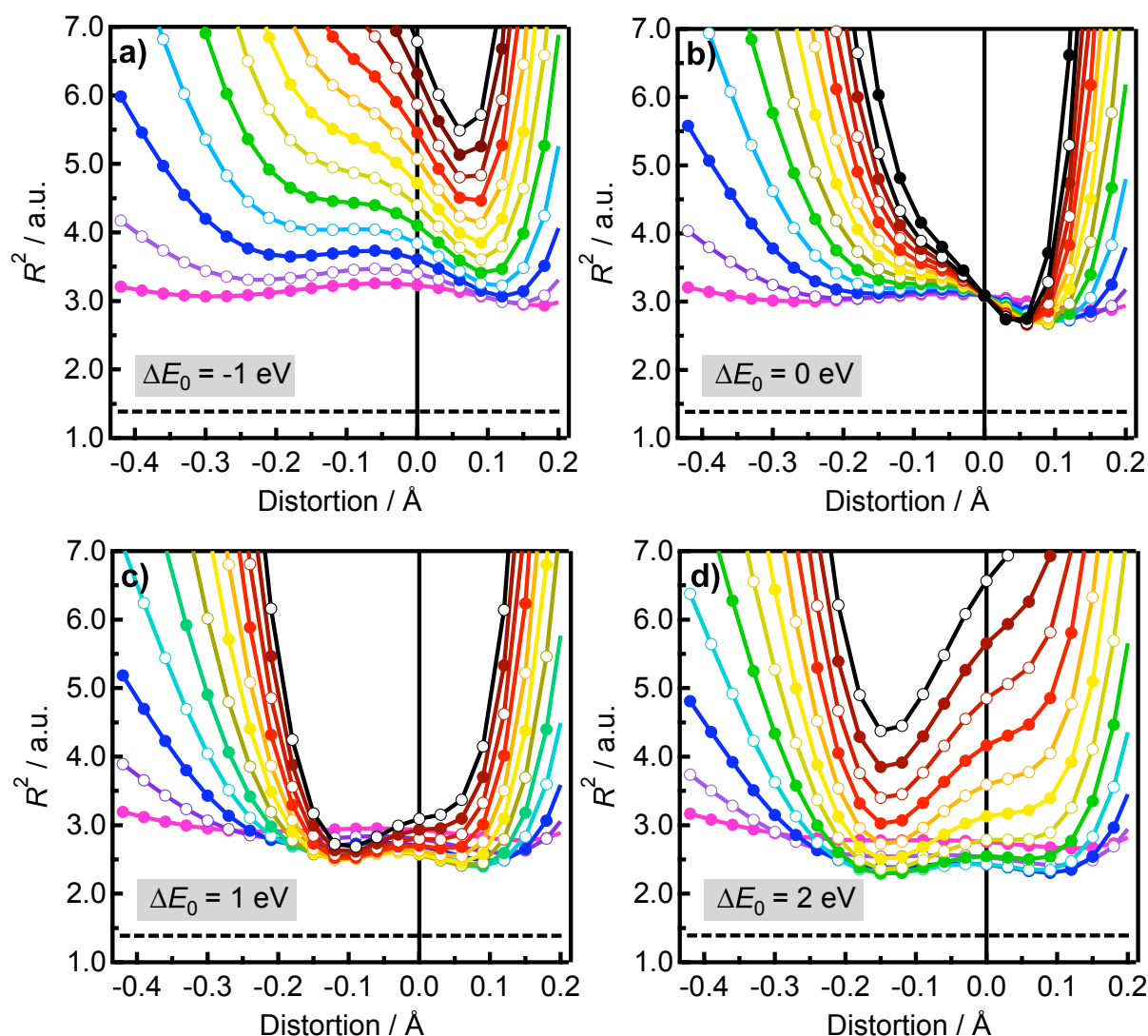


Figure 8.12: R^2 dependencies for Model IV (negative distortion = contraction of the PtP_4 planes). The colors represent different excitation yields from 1% (magenta) to 12% (black) in steps of 1% (the black dotted curve in b) represents $f = 14\%$). The energy shifts are shown in the respective graphs. The point at which the curves cross in Figure b) represents the R^2 value of a flat line (no distortion, no energy shift). The horizontal dashed lines at $R^2 = 1.39$ denote the absolute minimum obtained for Models I and II (Figure 8.7).

shown in Figure 8.12 for different energy shifts. It is seen that the R^2 values at the minima are much larger than the best fit R^2 value of Model I ($R^2 = 1.39$). The minimum R^2 value decreases as the energy shift is increased while the excitation yield that contains the minimum decreases. This continues for even larger energy shifts up to 10 eV for which the absolute minimum of $R^2 = 1.7$, an excitation yield of 1% and no distortion is obtained. It is clear that the Model IV results in unrealistic energy shifts and excitation yields. In fact the absolute minimum in R^2 is obtained for no distortion of the P–O–P

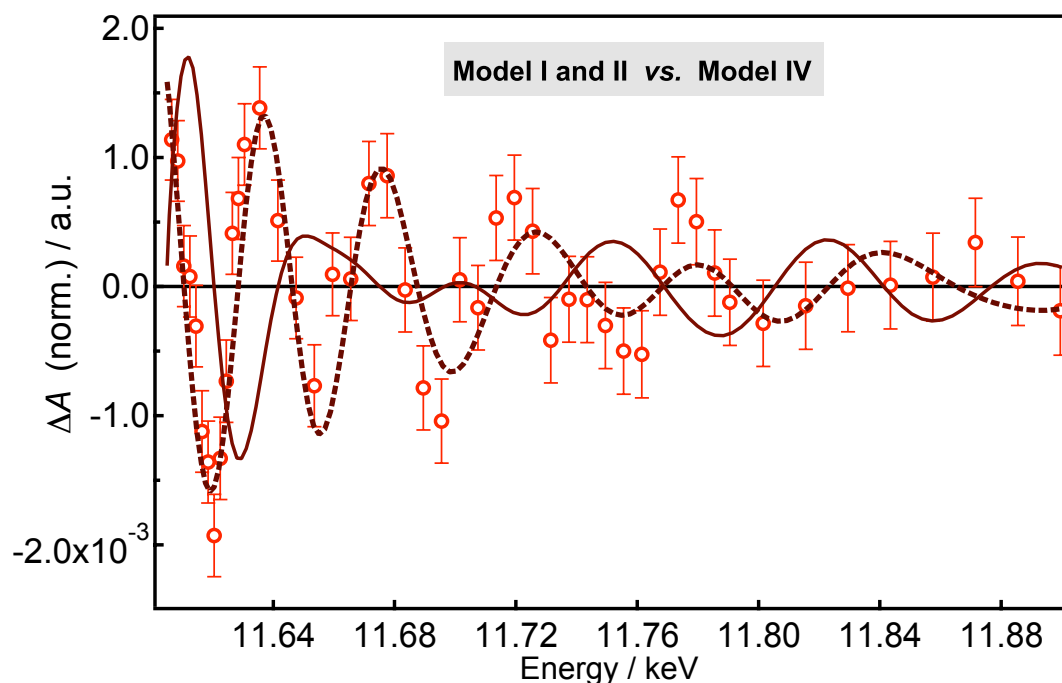


Figure 8.13: Comparison between the best fit of Model II (0.31(5) Å Pt–Pt contraction, 0.10(6) Å POP expansion, 7% excitation yield and zero energy shift; dotted trace) and a fit belonging to a local minimum in R^2 of Model IV (0.15 Å contraction, 5% excitation yield and 2 eV energy shift; solid trace).

angle at all. To illustrate the misfit of this model, Figure 8.13 compares the fit belonging to a local R^2 minimum at 0.15 Å contraction, 5% excitation yield and 2 eV energy shift (see Figure 8.12d) with the best fit obtained from Model II. It is obvious that Model IV can be excluded as a possible mode of distortion in the excited state.

8.3.3 Discussion and conclusions

The result of iteratively applying Models I and II is unique in the sense that the structural distortions, 0.31(5) Å Pt–Pt contraction and 0.010(6) Å ligand dilation, both lead to a unique combination of distance changes. These in turn influence the phases and amplitudes of the scattering paths and their mutual interference in an unambiguous way, leading to the good agreement with the experimental data. There is, however, a resulting discrepancy between the fit and the data, which we assign to the simplified structural parametrization model (see below).

The present study shows for the first time an elongation of the Pt–P coordination bonds by 0.013(6) Å, which is significantly larger than just the elongation based on the geometric considerations for Model I (0.003 Å). The additional increase in the Pt–P dis-

tance confirms the predictions of **density functional theory (DFT)** calculations [153]. The high sensitivity of our transient **EXAFS** measurement to the dominant Pt–P scattering path, together with our novel structural analysis based on fitting transient **EXAFS** spectra directly in energy space, allow us to detect this small Pt–ligand elongation. We believe it is due to a weakening of the coordination bonds upon formation of the Pt–Pt bond in the excited state, which reduces the overlap of the coordinating ligand orbitals with the Pt $5d_{x^2-y^2}$ orbitals, as confirmed by **XANES** calculations in the next Section. The herein derived Pt–Pt contraction of $0.31(5)$ Å is close to the value determined by time-resolved X-ray diffraction ($0.28(9)$ Å) [159] and X-ray scattering ($0.24(6)$ Å) [43], and within the range of values from **DFT** calculations [153]. However, it is larger than the distortions obtained from the wave packet calculations of Chapter 6 (~ 0.2 Å) and previous optical studies (0.15 – 0.25 Å [129, 137, 146, 149]). This discrepancy between the Pt–Pt values obtained from optical and X-ray measurements has been pointed out in Section 6.3.2. In the present case, we believe it is partially due to the limited structural parametrization model that is used in the calculation of the **EXAFS** signals. The number of parameters was limited due to the large overlap of scattering paths narrowing down the information content of the data. Ideally, we would include more scattering pathways in the fitting model, such as intramolecular **MS** paths and solute-solvent scattering. Neglecting these contributions might result in an overestimated value for the Pt–Pt distortion.

The present analysis reliably excludes the **ES** distortion model (Model IV, Figures 8.12 and 8.13), in which the Pt atoms remain in the plane of the P atoms. The P atoms follow the Pt atoms up to only $0.02(3)$ Å in the contraction along the Pt–Pt axis (Model III, Figure 8.10), which is very small compared to the large contraction of the Pt atoms themselves pointing to the exceptional rigidity of the POP bridging ligands.

8.4 Time-resolved *L*-edge XANES analysis

In this Section we analyze the excited-state *L*-edge XANES spectrum of **PtPOP** with the aim of gaining insight into the changes in Pt d-electron density, ligand field splitting and orbital hybridization upon excitation of the photocatalytic **PtPOP** anion. Similar to the interpretation of the **GS XANES** spectrum (Section 7.2), we will separate the analysis of the photo-induced spectral changes into 1) **XAFS**-like **MS** contributions in the above-continuum **XANES** region, and 2) changes in the molecular d-levels which are analyzed by looking at the Pt d-**density of states (DOS)** in the white-line region. The theoretical details given in Section 7.2 for the **GS** calculations do also apply for the **ES** calculations of this Section, unless otherwise noted.

The comparison between the *ab initio* calculated and experimental XANES spectra for the GS molecule (Figure 7.5) has shown that theoretical errors cause appreciable discrepancies. Although the Bayesian background-correction fitting procedure seems to be adequate to empirically correct for these errors, we prefer to adopt a semi-quantitative approach instead of fitting in the analysis of the excited state. The reason for this is twofold: first, it is presently not possible to account for the theoretical errors in the statistical analysis (beside the fact that theoretical errors are difficult to estimate) and, second, the photo-induced changes in electron occupancy of the valence orbitals, in particular of the d-orbitals, can not be specified in FEFF, as pointed out in Section 4.7. The d-state electron density removed by the laser can therefore only be simulated by downshifting the Fermi energy, which does not necessarily give the right transition intensities. In the analysis that follows, we rely on the results obtained from the time-resolved EXAFS analysis described in the previous Section, which has shown that the Pt atoms contract by as much as 0.31(6) Å in the excited state concomitant with a Pt–ligand elongation of

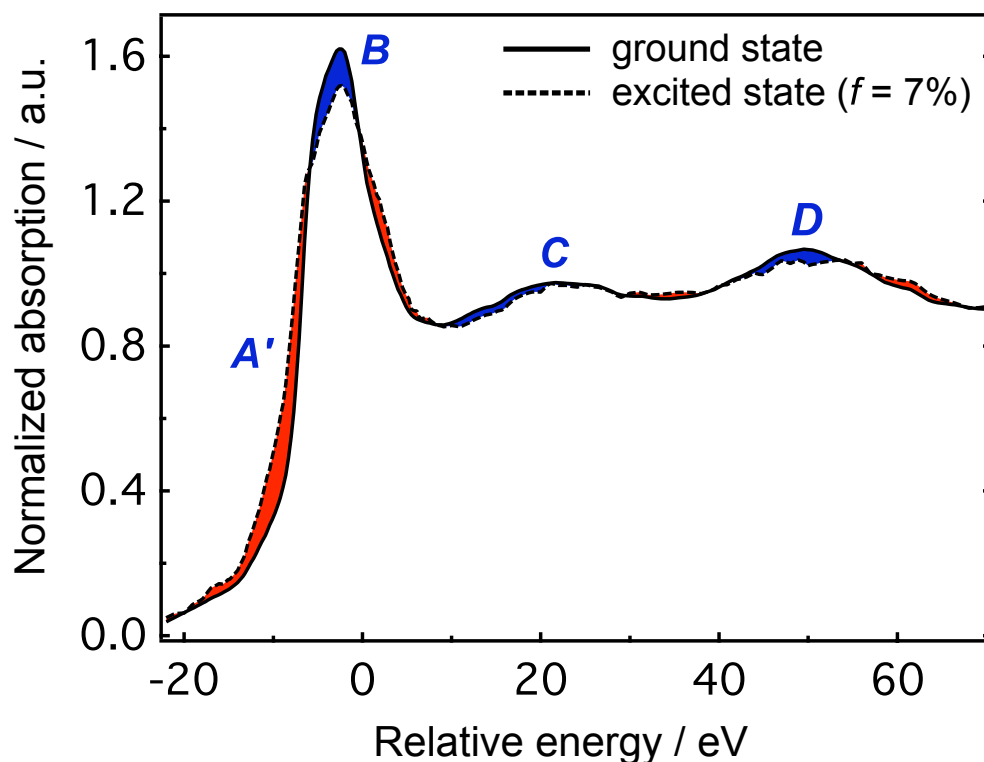


Figure 8.14: Experimental GS Pt L_{III} XANES spectrum (solid curve) and the ES XANES spectrum 150 ns after excitation for an excitation yield of $f = 7\%$ (dashed curve). Note that a new absorption (A') appears in the ES spectrum. Red indicates an increase in absorption, blue indicates a decrease in absorption compared to the ground state.

0.010(5) Å. By using *ab initio* FEFF9 calculations for different distorted geometries, we will show that the **ES XANES** spectrum is in excellent agreement with these results.

Figure 8.14 shows the experimental **GS XANES** spectrum and the **ES XANES** spectrum 0-150 ns after excitation. The latter is generated by dividing the normalized transient **XANES** spectrum (Figure 8.2a) by the excitation yield $f = 0.07$ (as determined in Section 8.3) and adding the normalized **GS XANES** spectrum, according to Equations (5.9) and (5.12). A new absorption, labeled A' , appears in the pre-edge region before the white-line, which we identify as the dipole-allowed transition from the 2p into the $\sigma^*d_{z^2}$ orbital that is opened-up by the laser excitation (see Figure 2.1). The white-line intensity itself is appreciably reduced while broadened at its blue side. In addition, the **ES** spectrum shows less pronounced modulations of **MS** features C and D compared to the **GS** spectrum.

8.4.1 Multiple scattering and above-continuum XANES

Figure 8.15 shows a zoom into the spectral region of features C and D for different values of the Pt–Pt contraction. It is seen that the distortion tends to reduce the spectral modulations of both features. In Figure 8.16, the calculated **GS** spectrum and simulated **ES** spectrum for a contraction of -0.3 Å and a small energy shift of 0.5 eV with respect to

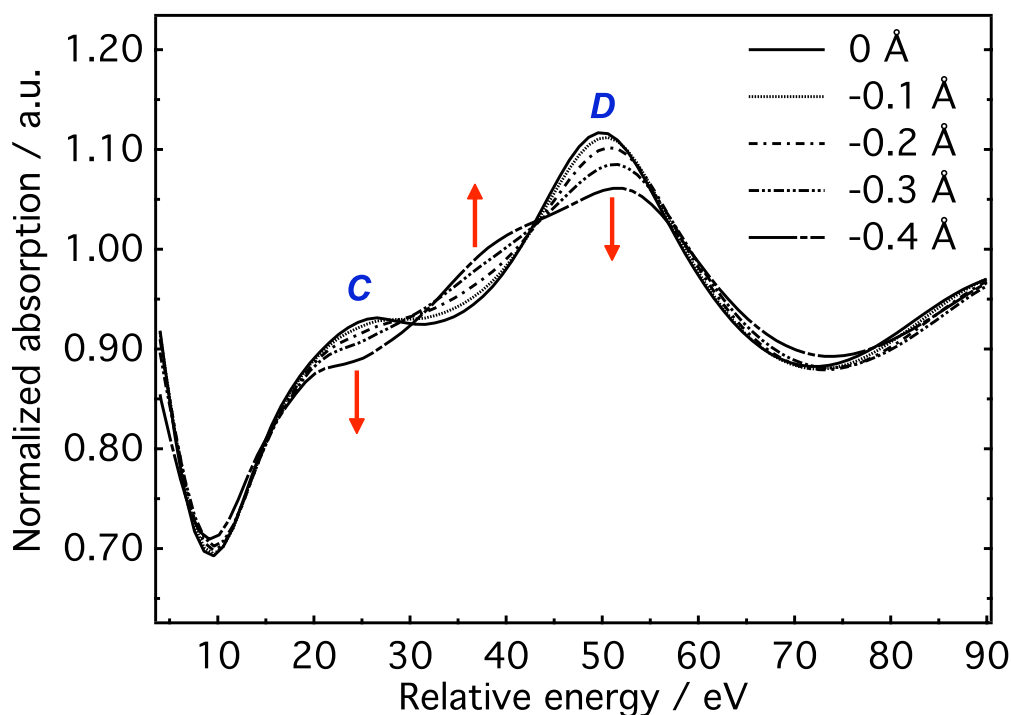


Figure 8.15: Effect of the Pt–Pt distortion on the calculated **XANES** spectrum above the **IP** (features C and D). A negative value means a contraction of the Pt–Pt bond. The arrows indicate the intensity changes as a function of the Pt–Pt contraction.

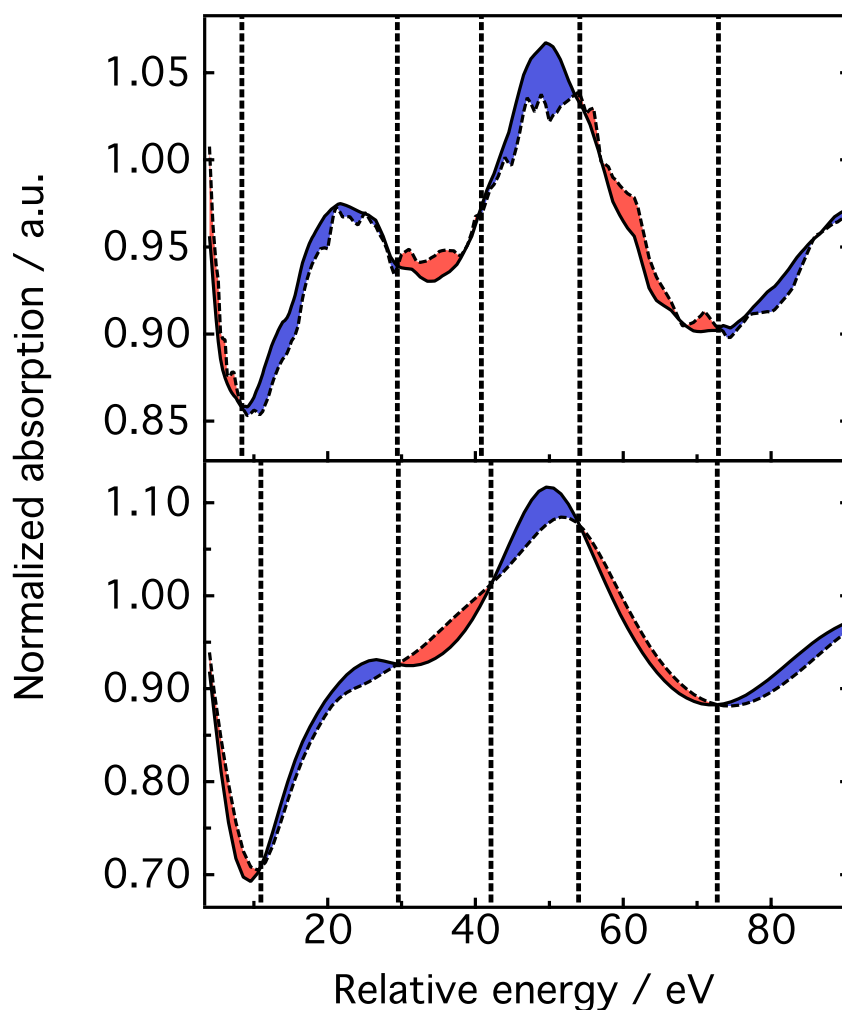


Figure 8.16: Comparison between a) experimental and b) *ab initio* theoretical XANES spectra of the ground state (GS) and excited state (ES) of PtPOP (GS: solid curves; ES: dashed curves). The excited state simulation has been performed for a Pt–Pt contraction of 0.3 Å and an edge shift of 0.5 eV. The vertical dashed guidelines locate the ES–GS crossing positions. Red indicates an increase in absorption, blue indicates a decrease in absorption compared to the ground state.

the ground state are compared to the experimental ES and GS spectra. The similarity of the crossing positions and the amplitude changes between the simulated and experimental spectra is striking. By comparing the experimental spectra in Figure 8.16a with the calculations for different Pt–Pt contractions in Figure 8.15, one sees that the distortion of -0.3 Å shows the best semi-quantitative correspondence both in terms of the difference area (colored) and the positions of the intersections, confirming the results from the time-resolved EXAFS analysis of Section 8.3. The 0.5 eV edge shift of the simulated ES spectrum with respect to the GS spectrum gave slightly better agreement for the

amplitude change of the *C* feature (although, within the accuracy of the analysis, the shift was not indispensable). As discussed later, the 0.5 eV shift also results in a better qualitative agreement in the white-line region.

Based on the cluster-size analysis of the **GS XANES** spectrum (Section 7.2.4), we can interpret the changes in the above-continuum region of the **XANES** spectrum as being due to reduced **MS** amplitudes in the PtP₄ plane (reduction of feature *D*) and between Pt–P–O (reduction of feature *C*). The rather strong in-plane multiple scattering is less favorable in the contracted excited state where the Pt atoms lie outside the P₄ planes by as much as 0.15 Å. The effect of the Pt-ligand distance on the **XANES** spectrum is only small. It is therefore beyond the accuracy of these **XANES** calculations to compare different Pt-ligand distortions.

8.4.2 d-DOS and the white-line region

Up to now we have interpreted the photo-induced changes in the **XANES** spectrum above the **IP** level based on structural **MS** arguments. The spectrum between the Fermi level and the **IP** energy however, is characterized by bound-bound transitions and can best be interpreted in terms of the local *l*-projected density of states (**LDOS**).

A zoom into the white-line region of the experimental **GS** and **ES XANES** spectra is shown in Figure 8.17a. As noted before, the optical excitation creates a single-electron hole in the **highest-occupied molecular orbital (HOMO)** $\sigma^*d_{z^2}$ orbital which appears as a new strong (dipole-allowed) absorption *A'* in the **ES** pre-edge region. The white-line intensity itself is largely reduced while the peak broadens to higher energies in the excited state. Figure 8.17b shows a simulation of the **ES** white-line for the same Pt–Pt distortion (-0.3 Å) and edge shift (0.5 eV) as in the previous section, but in this case with an additional shift of the Fermi energy of -2 eV in order to simulate the hole in the $\sigma^*d_{z^2}$ orbital. It is seen from the **d-DOS** in Figure 8.17 that the -2 eV shift puts the Fermi level just below the peak which we assigned to the $\sigma^*d_{z^2}$ orbital from which laser excitation occurs (Section 7.2.4). Qualitatively all the spectral changes are reproduced, although theory seems to underestimate the magnitude of the changes. This might partially be due to the fact that the Fermi energy shift does not adequately account for the changed electron density in the $\sigma^*d_{z^2}$ orbital resulting in incorrect intensities. The edge shift of 0.5 eV gave slightly better results for the intensity reduction and broadening of the white-line than the calculation without this shift, but due to the theoretical uncertainties that encompass this region, the shift might not be physically meaningful. In fact, the time-resolved **EXAFS** analysis (Section 8.3) has not shown the necessity of such a shift. It is

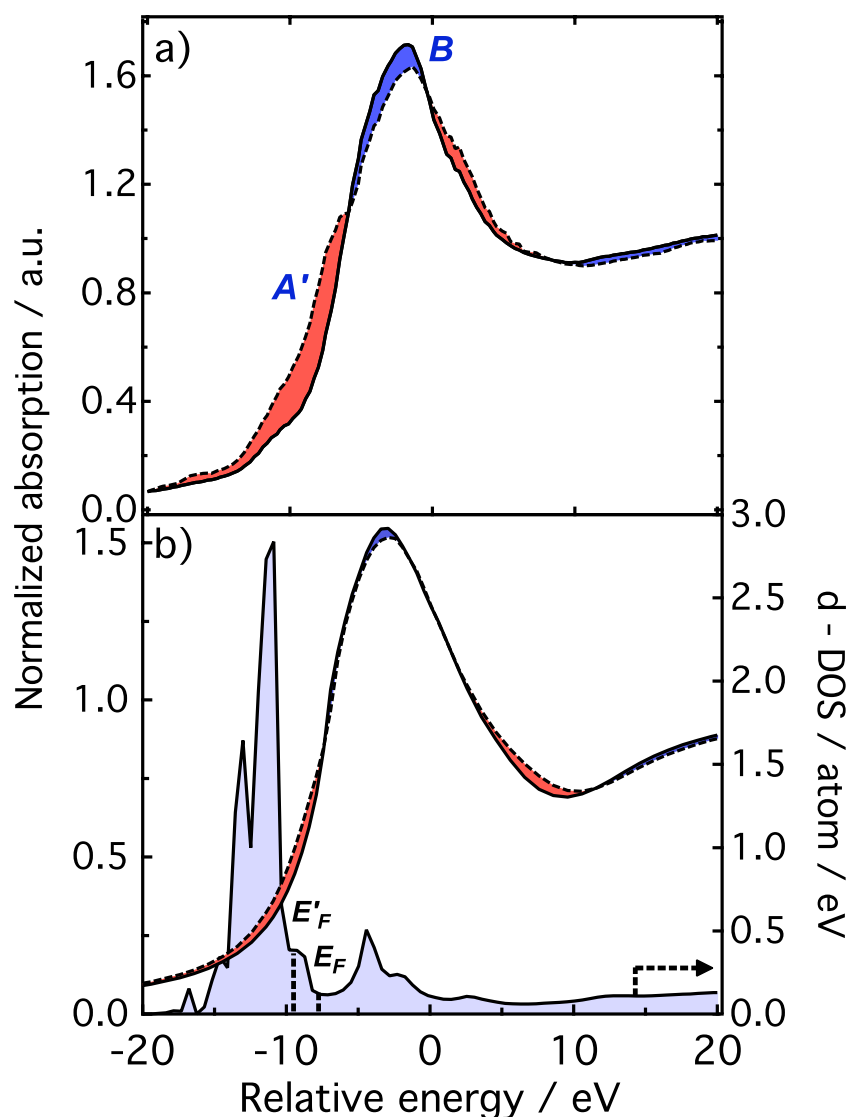


Figure 8.17: Comparison between a) experimental ($f = 7\%$) and b) *ab initio* theoretical pre-edge XANES spectra of the ground and excited states of PtPOP (GS: solid curves; ES: dashed curves; both left axis). The excited state has been calculated for a Pt–Pt contraction of -0.3 \AA , a shift of the Fermi level E_F by -2 eV in order to simulate the hole in the $\sigma^*d_{z^2}$ orbital (see d-DOS, greyed-out area, right axis) and an edge shift of 0.5 eV . Red indicates an increase in absorption, blue indicates a decrease in absorption compared to the ground state.

however remarkable that the photo-induced spectral changes that occur so close to the IP are reproduced by theory, if one recalls that this part of the spectrum is especially sensitive to the fine details of the potentials which are, of course, changed by the optical excitation.

The white-line is primarily due to absorption into the empty $5d_{x^2-y^2}$ orbitals. In order to understand the above two effects of intensity reduction and broadening, we take

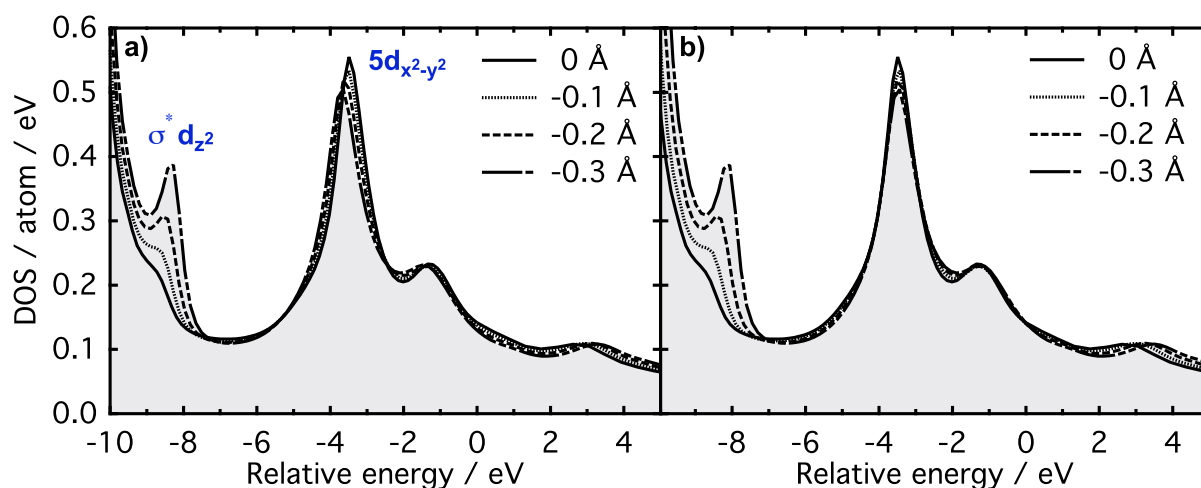


Figure 8.18: a) Pt d-DOS as a function of Pt–Pt distance (negative value = Pt–Pt contraction). The $\sigma^*5d_{z^2}$ is destabilized and the ligand field splitting decreases as the Pt atoms move closer; b) same as a), but the peaks are aligned at the maximum of the $5d_{x^2-y^2}$ peak in order to show its broadening.

a close look at the d-DOS around the IP level as a function of the Pt–Pt distortion. In Figure 8.18a one sees that the ligand field splitting between the filled d-orbitals and the empty $5d_{x^2-y^2}$ orbital decreases as the Pt–Pt distance decreases. This indicates a reduction of the ligand field strength as the Pt atoms move out of the plane of the P atoms. The $5d_{x^2-y^2}$ level is stabilized by ~ 0.4 eV, which is in good agreement with the ~ 0.5 eV stabilization energy from DFT calculations [153]. The reduced ligand field strength supports the results from the time-resolved EXAFS analysis (Section 8.3), which have shown that 1), the Pt atoms contract in the excited state while the ligands remain largely undistorted (the overlap of the Pt $5d_{x^2-y^2}$ orbitals and the ligand p orbitals is thus reduced resulting in a weaker ligand field), 2) the Pt–ligand coordination bonds slightly elongate in the excited state as a result of this. At the same time, the $\sigma^*d_{z^2}$ orbital is destabilized as the Pt atoms come closer, confirming the Pt–Pt σ^* anti-bonding nature of this orbital.

In order to analyze the line shape of the $5d_{x^2-y^2}$ peaks independent of the ligand field changes, the spectra are aligned to their maximum peak intensities around -3.5 eV, shown in Figure 8.18b. Small changes as a function of Pt–Pt bond length are visible. In particular, the amplitude is reduced while the area underneath the $5d_{x^2-y^2}$ peak stays approximately constant, *i.e.* the peak broadens. We assign this to an increased splitting of the $5d_{x^2-y^2}$ orbitals in the contracted excited state due to an increased in-plane π interaction, while the number of d-“holes” stays constant (thus the area remains constant [71, 308]). Indeed, a small 0.2 eV splitting of these orbitals in the excited state has

been calculated by Novozhilova *et al* [153]. The broadening of the $5d_{x^2-y^2}$ peak in the d-DOS can be directly correlated to the experimentally observed white-line amplitude reduction and the growth of the shoulder to higher energies in the ES XAS spectrum as seen in Figure 8.17. These effects demonstrate the particular sensitivity of this bound-bound transition to changes of purely structural origin.

8.4.3 XANES signatures of photoproduct formation

The PtPOP molecule is highly reactive in its excited state [116, 117, 130, 131] resulting from the radical character of the partially filled $\sigma^*d_{z^2}$ orbital which is localized at the axial positions of the Pt atoms. The PtPOP molecule is thus coordinatively unsaturated and it can readily abstract atoms from surrounding molecules (with concomitant electronic relaxation and oxidation) [309]. We now try to simulate the spectral evolution at long time delays, shown in Figure 8.4, by performing XANES and d-DOS calculations for a PtPOP molecule with two H atoms (from the solvent) at 1.86 Å distance from the two Pt atoms [71]. The Pt atoms are contracted by 0.3 Å in order to simulate the oxidized structure.

The simulations are shown in Figure 8.19. The main effect is an increase of the $5d_{x^2-y^2}$ peak intensity at the red side compared to the excited state structure, but a decrease at the blue side. The overall effect is thus an apparent blue shift of the negative difference feature, with the zero-crossing occurring at higher energies. This is also seen in the experimental spectra in Figure 8.4a. The white line of the H-coordinated molecule is broadened at its red-side due absorption into anti-bonding σ^* states that result from hybridization of H 1s orbitals with the Pt $\sigma^*d_{z^2}$ orbital [71], as seen from the d-DOS in Figure 8.19a. This could give rise to the remaining positive, and slightly blue-shifted, absorption in the transient spectrum around 11.575 keV.

The picture presented here provides only a suggestive explanation of the observed spectral evolution in the transient XANES spectrum of PtPOP. A better understanding of the photochemistry of the excited molecule and the reactants would require more systematic experimental investigations in different solvents. First, it is not sure that coordination, if occurring at all, takes place through the H-atoms of the solvent or via other atoms (*e.g.* O atoms of either the solvent or molecular oxygen). In fact, there is no experimental evidence of "static" coordination in the excited state [124]. Our ultrafast optical measurements of Chapter 6 have indicated that there might be a solute-solvent interaction playing a role in funneling vibrational energy, but at the time scales of the time-resolved XAS experiment this process does not play a role anymore. Second, we do not know whether

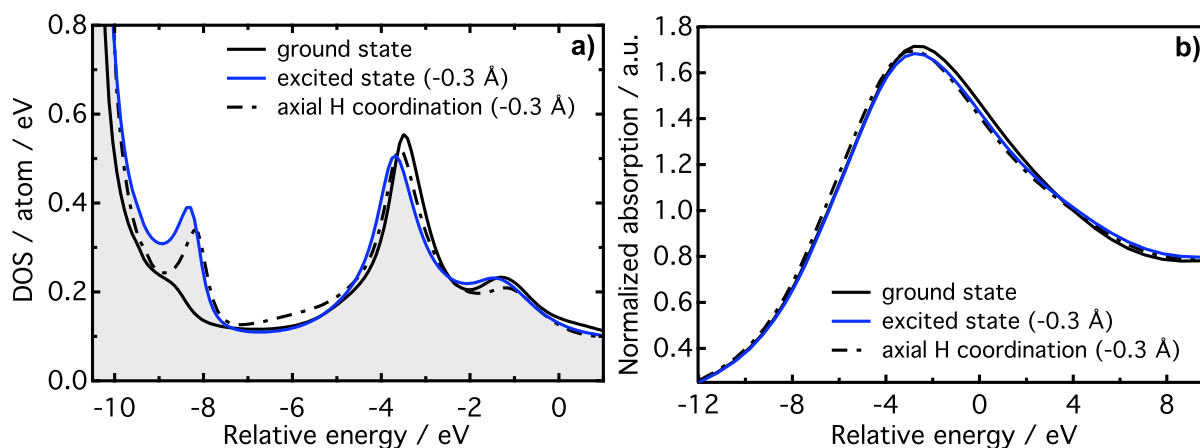


Figure 8.19: a) Pt d-DOS for the GS structure, the excited state structure (-0.3 Å) and the excited state structure with two H atoms coordinated at the axial positions; b) The white line absorption for the three structures of a).

the PtPOP molecule returns to the ground state immediately when coordination occurs or whether an exciplex is formed, that slowly decays to a ground state complex.

In any case, our results demonstrate the formation of photochemical products resulting from the reaction of the triplet-excited molecule with other molecules in the solution. Pt *L*-edge XANES spectroscopy can thus be sensitively used to probe the chemistry and dynamics at active sites of homogeneous photocatalysts.

8.5 Summary and conclusions

The present study demonstrates that accurate structural changes in photoexcited molecules can be determined by fitting the transient EXAFS spectrum directly in energy space and that additional non-structural information, such as the excitation yield and chemical shift, can be extracted from the fit due to the largely reduced parameter space in a model-based analysis as is shown here. There are no limitations on the magnitude of the distortions and no complicated parameterization of the scattering paths is necessary, because the EXAFS signal of every (chemically reasonable) excited-state structure is calculated separately. The analysis has been applied to the transient Pt *L*_{III}-edge EXAFS data of the photoexcited PtPOP. A rigorous statistical comparison of several different ES structures according to distortion models that involve a contraction along the Pt–Pt axis resulted in a best-fit distortion involving mainly the heavy Pt atoms (contraction by 0.31(5) Å) and a small Pt-ligand elongation of 0.010(6) Å. Remarkably, the

bridging POP ligands hardly follow the heavy Pt atoms in their contraction, which indicates weak(ened) Pt-ligand coordination bonds and rigid bridging ligands. The Pt–Pt contraction of 0.31(5) Å is slightly higher compared to the values obtained by optical measurements, which could be caused by the limited structural parametrization that is used for modeling the **ES** and **GS EXAFS** signals, or the presence of solute-solvent scattering that is not taken into account in the excited-state models.

The photo-induced changes in the white-line region of the **XANES** spectrum are assigned to the appearance of a new dipole-allowed transition into the molecular $\sigma^*d_{z^2}$ orbital opened-up by the laser and a splitting of the $5d_{x^2-y^2}$ -level resulting from increased π -interaction between the Pt orbitals in the ~ 0.3 Å contracted excited state. The above-continuum **XANES** spectrum can be interpreted in terms of multiple scattering resonances involving the in-plane P and second-shell O atoms. The modulation of these scattering features is reduced in the excited state owing to the out-of-plane movement of the Pt atoms. The present study shows that a semi-quantitative **XANES** analysis of the excited state is in good agreement with results from the transient **EXAFS** spectrum.

Chapter 9

Conclusions and outlook

The ability to visualize molecular structure in the course of a chemical reaction or a biological function has been the aspiration of scientists for decades. **X-ray absorption spectroscopy (XAS)** is ideal in this respect because it is chemically selective and can be implemented in any type of medium. Furthermore, using **X-ray absorption near-edge structure (XANES)** and **X-ray absorption fine structure (EXAFS)** in laser pump/X-ray probe experiments allows the retrieval of not only the local geometric structure of the system under study, but also the underlying electronic structure changes that drive the structural dynamics. A time resolution of 50-100 ps is reached at present synchrotron X-ray sources, but time-resolved **XAS** is not limited by the time scale. In reaching the femtosecond scale (*e.g.* with the fs slicing scheme or X-ray free electron lasers), we will be able to directly observe dynamical processes including coherent nuclear wave packet motion and ephemeral transition states of complex chemical and biological systems. Ultrafast laser spectroscopy routinely accesses the time scale of these ultrafast processes, but it is mainly sensitive to the electronic properties of the system. Only in favorable cases, atomic-scale spatial resolution is achieved by exploiting nuclear coherence in the optical excitation process.

In this thesis we applied the ultrafast X-ray and optical spectroscopy techniques to a diplatinum molecular complex, $[\text{Pt}_2(\text{P}_2\text{O}_5\text{H}_2)_4]^{4-}$ (**PtPOP**), which is one of the most extensively studied members in the class of binuclear d^8 - d^8 compounds. These complexes exhibit unique photophysical and photochemical properties related to intermetallic bonding and the nature of the bridging ligands, making them good candidates for potential photocatalytic applications.

Femtosecond optical spectroscopy

We performed femtosecond fluorescence up-conversion and femtosecond broadband **transient absorption (TA)** measurements to address the ultrafast (100 fs - 50 ps) structural and electronic relaxation processes upon excitation into the ${}^1A_{2u}$ ($\sigma^*d_{z^2} \rightarrow \sigma p_z$) excited state of the **PtPOP** anion. We identified and quantified the processes of wave packet dynamics of the metal-metal stretch (224 fs), coherence decay (~ 2 ps), vibrational cooling (1-2 ps) and intersystem crossing (10-30 ps) for various solvent environments and excitation wavelengths. We extracted from the broadband **TA** measurements the spectral distribution of the wave packet at given time delays, which reflects the distribution of Pt-Pt bond distances as a function of time, *i.e.* the structural dynamics of the system. The **PtPOP** molecule thus represents the unique case of a polyatomic molecule for which the structural dynamics can be retrieved from optical time-resolved spectra. This is possible due to the presence of only a single, highly harmonic Franck-Condon active mode in combination with our broadband detection scheme.

Despite its size and complexity, the **PtPOP** molecule provides an ideal opportunity to evaluate the microscopic details of solute-solvent interactions on vibrational relaxation. Excitation into the ${}^1A_{2u}$ ($\sigma^*d_{z^2} \rightarrow \sigma p_z$) state represents the limiting case of exciting an isolated vibrational mode with no **intramolecular vibrational energy redistribution (IVR)** to lower-frequency modes. The only mechanism for energy relaxation is by transferring it directly to the solvent. From our data in four different solvents we conclude that an axial Pt-solvent energy dissipation channel, likely involving Pt-H interactions, accounts for the vibrational cooling in the singlet state. The depopulation time of the ${}^1A_{2u}$ -state vibronic levels (~ 500 fs) is much shorter than the coherence decay time of ~ 2 ps. We thus observe the fascinating process that depopulation occurs without phase distortion, which is in contrast to the common optical Bloch description of energy and phase relaxation (Section 3.1.1). This points to an unconventional coherence decay mechanism in **PtPOP** which could be related to the exceptional harmonicity of the ${}^1A_{2u}$ potential, assuring vibronic energy matching and efficient coherence transfer between levels. In addition, the cage-like structure of **PtPOP** protects the metal-metal oscillator from the stochastically fluctuating surrounding solvent.

Intersystem crossing (ISC) from the ${}^1A_{2u}$ to the ${}^3A_{2u}$ state takes place through spin-vibronic coupling with a higher-lying triplet state and/or (transient) symmetry breaking in the ${}^1A_{2u}$ excited state. In spite of the very large spin-orbit coupling strength of the Pt atoms, it was found that the relatively slow rate of **ISC** in **PtPOP** is governed by energetic, structural and symmetry constraints. These factors seem generally to be responsible for

the large variability of the values of the **ISC** rate among metal based molecular complexes [279, 290, 294, 295].

We believe that the wave packet dynamics observed in **PtPOP** is a general phenomenon for binuclear d^8-d^8 complexes excited to the $^1A_{2u}$ state. However, besides the solvent effect, changes in the metal atoms and/or ligands are expected to have a large impact on ultrafast relaxation steps, such as the wave packet oscillation frequency and the rates of vibrational cooling and **ISC** and the accompanying structural distortions. The structural and energetic tunability of these processes make d^8-d^8 complexes particularly interesting for photochemical applications. It is therefore of primary future interest to investigate the ultrafast dynamics of these compounds with femtosecond X-ray methods in order to relate the changing electronic and structural properties to photochemical reactivity and selectivity, and to understand the influence of the solvent in affecting them.

Ultrafast X-ray absorption spectroscopy

The steady-state and nanosecond-resolved **XAS** results in this thesis establish the electronic and geometric structures of the singlet ground and excited triplet states of the **PtPOP** complex in solution. Our results represent the necessary preparative step for future femtosecond **XAS** measurements on this compound.

A rigorous model-based analysis of the transient **EXAFS** spectrum allowed us to determine the structural changes in the lowest triplet excited state resulting from the metal-centered $\sigma^*d_{z^2} \rightarrow \sigma p_z$ transition (aligned along the Pt-Pt axis). We found that the Pt-Pt distance decreases by 0.31(5) Å due to the formation of a new intermetallic bond, while the Pt-ligand bonds were found to elongate by 0.010(5) Å. The latter dilation of the coordination bonds was predicted by theory, but this represents the first experimental confirmation, owing to the exceptional sensitivity of the **XAS** spectrum to changes in radial distances aligned along specific scattering pathways (such as along Pt-ligand).

The time-resolved **EXAFS** study in this thesis demonstrates that precise structural changes in photoexcited molecules can be determined by fitting the transient **EXAFS** spectrum directly in energy space (instead of in Fourier space) and that additional non-structural information, such as the excitation yield and chemical shift, can be extracted from the fit due to the largely reduced parameters space in a model-based analysis. This novel approach has also been successfully applied to an other transition metal complex [94], yielding, in favorable cases, fitted values for structural distortions with picometer precision. However, the outcome of the transient **EXAFS** fitting analysis can depend on the parameterization model that is already applied for the ground-state **EXAFS** spec-

trum. The number of fitting parameters is limited by the information content of the data, and a good choice of scattering pathways and parameters is indispensable to guarantee a realistic sensitivity of the simulated excited-state EXAFS spectra to the various structural distortions. This becomes of particular importance in cases where many scattering pathways have similar distances (which is partially the case in PtPOP). Whereas a certain (limited) choice of fitting parameters might suffice to satisfactorily fit the ground-state spectrum, this is not necessarily the case for the excited-state structure. In these cases, it is needed to limit the number of free fitting parameters as much as possible by, for example, geometric parameterization of multiple scattering pathways and including prior knowledge about structure, Debye-Waller factors and electronic parameters.

Both the herein derived values for the Pt-Pt distortion from time-resolved optical (~ 0.2 Å) and X-ray ($\sim 0.31(5)$ Å) spectra are in good agreement with previous steady-state optical (0.175-0.225 Å [129, 137, 146, 149]) and X-ray scattering / diffraction (0.24(6) Å [43] and 0.28(9) Å [159]) studies, respectively, but there seems to be a systematic discrepancy between the values derived by optical and X-ray methods. Given the rather large uncertainties in the values, this discrepancy might not be statistically significant. On the other hand, the simplicity of the models underlying the various analyses could be responsible for the differences. In the case of the optical analyses, the models assume only a single Franck-Condon active mode. The role of the bridging ligands is not included in these studies. The X-ray studies might be affected by the influence of the (solvent) environment. In the present time-resolved XAS study, the neglected solute-solvent scattering, as well as the above mentioned difficulties with the structural parameterization model could be responsible for the slightly high value for the derived Pt-Pt distortion.

It should be noted that, despite the immense technological improvements in ultrafast XAS during the last several years, the measurement of good-quality transient EXAFS spectra is still not routine. The photoinduced changes in EXAFS are often of the order of only 0.1%, both due to the inherently small magnitude of the absorption fine-structure and the small fraction of laser-excited molecules (typically 5-20%). The recent implementation of ultrafast XAS at MHz repetition rates is promising in this respect [310]; it allows to obtain statistically better transient EXAFS data for concentrated (>10 mM) samples without constraints on the molecular structure. Furthermore, it opens the venue for ultrafast XAS on dilute biological samples, which has recently been demonstrated for the photoinduced ligand dissociation and recombination dynamics of Myoglobin [311].

$L_{II,III}$ -edge XANES essentially probes the empty density of d- and s-states via dipole al-

lowed 2p-to- ϵ (d,s) transitions, making it, extended into the ultrafast time domain, the ideal tool to gain insight into the changes in Pt d-electron density, ligand-field splitting and orbital hybridization upon excitation of the photocatalytic PtPOP anion. We have applied state-of-the art XAS theory (implemented in the *ab initio* FEFF9 code) to simulate and interpret the Pt L_{III} -edge XANES spectrum of PtPOP and the photoinduced changes that occur therein. An excellent qualitative agreement between theoretical and experimental ground-state XANES spectra was achieved, and we were able to relate all photoinduced changes in the spectra to either structural or electronic changes in the excited molecule. However, despite the improved calculation of many-body effects with the FEFF9 code, a quantitative fitting analysis of the transient XANES spectrum was impeded due to appreciable discrepancies between the *ab initio* calculated and experimental spectra, occurring already for the ground state. These discrepancies are likely caused by the theoretical approximations made in the representation of the scattering potentials. They can be approximately "ad hoc" corrected for by using a novel Bayesian fitting procedure for FEFF [97], which also allows fitting structural and electronic parameters to the data. In the present case, however, the theoretical errors were too large to obtain meaningful physical parameters from such a fit. The incorporation of full-potential effects would be the logical next step to improve the *ab initio* agreement between calculated and measured XAS spectra of PtPOP [95, 312]. As soon as the accuracy of the *ab initio* theory approximates that of the experiment, the Bayesian fitting procedure will be very useful for its application to fitting transient XANES spectra directly in energy space.

Despite the aforementioned difficulties, we were able to derive a semi-quantitative value for the Pt-Pt contraction (~ 0.3 Å) by comparing the calculated above-continuum multiple scattering resonances for different excited state distortions to the experimental excited-state XANES spectrum. This value is in excellent agreement with the results from the transient EXAFS spectrum. Besides the multiple scattering features, we have shown that theoretical XAS codes qualitatively reproduced the photoinduced changes in bound-bound transitions, which have been related to reduced ligand-field strength and orbitals splitting in the excited state. Yet, a quantitative match is hampered due to the changed valence d-electron density caused by the optical excitation. At present, there is no appropriate way to specify the electron occupancies of the valence orbitals in the multiple-scattering XANES codes (*e.g.* FEFF).

Ultrafast XAS is a growing field of research with many promising applications in chemistry, biology and materials science [45, 47, 49]. Thanks to technical advances during the last

decade, it has now become almost routine to measure ps-resolved transient **XAS** spectra at synchrotron X-ray sources. Very recent and ongoing technical efforts extend the application of time-resolved X-ray spectroscopies to the soft X-ray regime [313, 314], MHz repetition rate detection [310], energy-dispersed X-ray emission detection [269], **ultra-violet (UV)** and X-ray photoelectron spectroscopy [315], as well as to fs time scales using slicing sources at synchrotrons [61]. The forthcoming use of very intense X-ray free electron lasers in the field of ultrafast X-ray spectroscopies and scattering on (bio)chemical systems, offers the exciting perspective of routinely accessing the ultimate time scale of molecular motion; the "femtosecond era" of X-ray science is now beginning! The **PtPOP** molecule represents an ideal model system for such studies. Hand in hand with technical breakthroughs, future advances on the theory and data analysis side are indispensable to optimally exploit the wealth of chemical information contained in ultrafast **XAS** spectra.

Appendix A

Input files for FEFF6 EXAFS calculations of PtPOP

Input structure from X-ray crystallography [297]

```
* file name: feff.inp (* = comment)
TITLE PtPOP FEFF6 EXAFS calculations
HOLE 4 1.0 * Pt L3 edge (11564.0 eV), second
number is S02
* mphase,mpath,mfeff,mchi
CONTROL 1 1 1 1
PRINT 1 0 0 0
RMAX 5.5
NLEG 4
POTENTIALS
* ipot Z element
0 78 Pt
1 78 Pt
2 15 P
3 8 0
ATOMS
0.00000 0.00000 0.00000 0
2.30745 0.00000 -0.02636 2
-2.30745 0.00000 -0.02636 2
0.00000 2.30745 -0.02636 2
0.00000 -2.30745 -0.02636 2
1.10068 -2.96851 3.74286 3
-1.10068 2.96851 3.74286 3
-2.96851 -1.10068 3.74286 3
2.96851 1.10068 3.74286 3
0.00000 0.00000 2.92557 1
2.30745 0.00000 2.95194 2
-2.30745 0.00000 2.95194 2
0.00000 2.30745 2.95194 2
0.00000 -2.30745 2.95194 2
-1.17535 -2.89221 3.79652 3
1.17535 2.89221 3.79652 3
-2.89221 1.17535 3.79652 3
2.89221 -1.17535 3.79652 3
2.95000 0.00000 1.46279 3
0.00000 2.95000 1.46279 3
-2.95000 0.00000 1.46279 3
0.00000 -2.95000 1.46279 3
2.96851 1.10068 -0.81728 3
1.10068 -2.96851 -0.81728 3
-1.10068 2.96851 -0.81728 3
-2.96851 -1.10068 -0.81728 3
2.89221 -1.17535 -0.87094 3
-2.89221 1.17535 -0.87094 3
-1.17535 -2.89221 -0.87094 3
1.17535 2.89221 -0.87094 3
END
```

Optimized ground-state structure as input

```
* file name: feff.inp (* = comment)
TITLE PtPOP FEFF6 EXAFS calculations
HOLE 4 1.0 * Pt L3 edge (11564.0 eV), second
number is S02
* mphase,mpath,mfeff,mchi
CONTROL 1 1 1 1
PRINT 1 0 0 0
RMAX 5.5
NLEG 4
POTENTIALS
* ipot Z element
0 78 Pt
1 78 Pt
2 15 P
3 8 O
END
```

	ATOMS			
	0.00000	0.00000	0.00000	0
	2.3162	0.00000	0.04080	2
	-2.3162	0.00000	0.04080	2
	0.00000	2.3162	0.04080	2
	0.00000	-2.3162	0.04080	2
	1.10068	-2.98181	3.62602	3
	-1.10068	2.98181	3.62602	3
	-2.98181	-1.10068	3.62602	3
	2.98181	1.10068	3.62602	3
	0.00000	0.00000	2.87590	1
	2.3162	0.00000	2.83510	2
	-2.3162	0.00000	2.83510	2
	0.00000	2.3162	2.83510	2
	0.00000	-2.3162	2.83510	2
	-1.17535	-2.90551	3.67968	3
	1.17535	2.90551	3.67968	3
	-2.90551	1.17535	3.67968	3
	2.90551	-1.17535	3.67968	3
	2.9316	0.00000	1.43795	3
	0.00000	2.9316	1.43795	3
	-2.9316	0.00000	1.43795	3
	0.00000	-2.9316	1.43795	3
	2.98181	1.10068	-0.75012	3
	1.10068	-2.98181	-0.75012	3
	-1.10068	2.98181	-0.75012	3
	-2.98181	-1.10068	-0.75012	3
	2.90551	-1.17535	-0.80378	3
	-2.90551	1.17535	-0.80378	3
	-1.17535	-2.90551	-0.80378	3
	1.17535	2.90551	-0.80378	3

Appendix B

Input file for FEFF9 XANES calculations of PtPOP

```
* file name: feff.inp (* = comment)
TITLE PtPOP FEFF9 XANES calculations

* Pt L3 edge energy = 11564.0 eV
EDGE L3
SO2 1.0
EGRID 2 grid.inp

CONTROL 1 1 1 1 1 1
PRINT 1 0 0 0 0 0

EXCHANGE 0 0.0 0.0 2

NOHOLE 2
PLASMON 4
SO2CONV

SCF 6 1 30 0.2 1

LDOS -20 60 0.02

XANES 9 0.05 0.0

FMS 6 1

POTENTIALS
0 78 Pt 3 4
1 78 Pt 3 4
2 15 P 2 3
3 8 0 2 3
4 8 0 2 3

ATOMS
0.00000 0.00000 0.00000 0
0.00000 2.3162 -0.04000 2
2.3162 0.00000 -0.04000 2
0.00000 -2.3162 -0.04000 2
-2.3162 0.00000 -0.04000 2
1.09920 3.02160 -0.76310 3
-1.35850 2.98090 -0.44090 3
2.87080 1.31350 -0.94890 3
3.10740 -1.09050 -0.42210 3
1.52280 -2.92920 -0.37440 3
-0.85930 -3.07030 -0.95020 3
-0.21900 -2.89590 1.42890 4
-2.89560 -1.32280 -0.82240 3
-3.12920 1.12380 -0.27390 3
-2.82410 -0.61540 1.53010 4
0.00000 0.00000 2.95460 1
0.00000 -2.3162 2.99460 2
-2.3162 0.00000 2.99460 2
0.00000 2.3162 2.99460 2
2.3162 0.00000 2.99460 2
-1.09930 -3.02160 3.71770 3
1.35850 -2.98090 3.39550 3
-2.87080 -1.31350 3.90360 3
-3.10750 1.09050 3.37680 3
-1.52280 2.92920 3.32900 3
0.85930 3.07030 3.90480 3
0.21890 2.89600 1.52570 4
2.89560 1.32280 3.77700 3
3.12920 -1.12380 3.22850 3
2.82410 0.61540 1.42450 4
END
```


Appendix C

Input file for the Bayesian fitting program applied to PtPOP

```
* file name: feffit.inp (* = comment)
*** command to run FEFF9
fffcmd feff90

*** read-in experimental XANES spectrum
data XANES exp.dat
*** experimental errors
eps 0.005 exp
*** increase error in white-line region
*** (center, max, width)
gausserr 11570.6 19 5

*** feff input file
fffinp feff.inp
*** do not pre-align theo. and exp.
*** spectra
noalign

*** background spline fit function
bkg 5 1.5 * (no. knots, a priori error)
*** spline knots placed on an
*** exponential grid
bkgpos exp

*** def. overall energy shift
*** fit parameter
e0 deltae
guess deltae 0.0 * a priori guess value
*** def. Fermi energy and DW factor
*** fit parameters
vr vr1 * Fermi energy
guess vr1 -1.4 2.0 * (value, error)
ss2 sig2 * DW factor
guess sig2 0.0052 0.01

*** def. struct. Pt-ligand
*** fit parameter
guess dx 0.0 0.05
set dy = dx
*** list of atoms
xdist1 -dx
ydist2 -dy
ydist3 dy
xdist4 dx
xdist6 dx
ydist7 -dy
xdist8 -dx
ydist9 dy
xdist10 -dx
xdist11 dx
ydist12 dy
ydist13 dy
xdist14 dx
ydist15 -dy
ydist16 -dy
xdist17 -dx
xdist18 -dx
ydist19 -dy
ydist20 dy
xdist21 dx
xdist22 dx
ydist23 dy
xdist24 -dx
ydist25 -dy
ydist26 -dy
xdist27 dx
xdist28 -dx
ydist29 dy
end
```


Appendix D

Singular value decomposition, global fit and global analysis

Two alternative approaches for the quantitative analysis of multivariable data sets have emerged [316, 317]: (i) **singular value decomposition (SVD)** in combination with a **global fit (GF)** target analysis and (ii) **global analysis (GA)**. The broadband **TA** data sets recorded in these experiments are a typical example of 2-variable (λ, t) measurements, where the independently measured variables are the wavelengths and the time delay between pump and probe pulses. The **SVD-GF** and **GA** techniques allow for simultaneous analysis of the dynamical information across the entire spectral and temporal range by fitting the data with just one model scenario.

SVD is essentially a data reduction and noise suppression method which allows to determine a lower limit of the number of spectrally distinguishable molecular species (or excited states of the same molecule) given the uncertainty of the data and is independent of any kinetics analysis [317]. The result of the **SVD** on a $m \times n$ **TA** data matrix $\Delta\mathbf{A}$ is a set of several transient basis spectra and an associated set of time-dependent amplitude vectors, which constitute together a reduced representation of the original data, according to [316]

$$\Delta\mathbf{A} = \mathbf{U}\mathbf{S}\mathbf{V}^T \quad (\text{D.1})$$

where \mathbf{U} is an $m \times k$ matrix having the property that $\mathbf{U}^T\mathbf{U} = \mathbf{I}_m$, where \mathbf{I}_m is the $m \times m$ identity matrix, \mathbf{V}^T is an $k \times n$ matrix such that $\mathbf{V}^T\mathbf{V} = \mathbf{I}_k$, and \mathbf{S} is a diagonal $k \times k$ matrix of nonnegative elements. For (λ, t) -data matrices, the columns of \mathbf{U} are a set of orthonormal basis spectra, and the columns of \mathbf{V} represent an orthonormal set of kinetic basis vectors. The diagonal elements of \mathbf{S} are called the singular values s of $\Delta\mathbf{A}$. **SVD** on a real data matrix usually gives several components with large s -values besides a large number of components that have s -values near zero which represent the statistical noise in the data. Only the components with s -values that significantly differ from this noise

background are taken into consideration for the **GF** of the kinetic basis vectors according to a specific physical model that describes the kinetics of the system. The advantage of **SVD** compared to a **GA** of the unreduced $\Delta\mathbf{A}$ data matrix is the fact that the number of components that have to be fit is significantly reduced. A second important property of the **SVD** is that the first set of n largest components provides the best n -component approximation to the data in the least-squares sense. In our case, the **TA** absorption kinetics are modeled as a sum of N exponential functions convoluted with the Gaussian **instrumental response function (IRF)**, according to [316]

$$f_{\text{kin}}(t) = \sum_{i=1}^N A_i \text{ExpErf}[B, t_0, \tau_i, t] \quad (\text{D.2})$$

with $\text{ExpErf}[B, t_0, \tau_i, t]$ defined by

$$\begin{aligned} \text{ExpErf}[B, t_0, \tau_i, t] \equiv & \text{Exp} \left[\left(\frac{B}{2 \cdot 1.66511 \cdot \tau_i} \right)^2 - \frac{t - t_0}{\tau_i} \right] \dots \\ & \cdot \frac{1}{2} \left(\text{Erf} \left[\frac{t - t_0}{B} \cdot 1.66511 - \frac{B}{2 \cdot 1.66511 \cdot \tau_i} \right] + 1 \right), \end{aligned} \quad (\text{D.3})$$

where Exp is an exponential and Erf is an error function (the ExpErf function results from convoluting an exponential with a Gaussian). B in Equation (D.2) is the **full-width-half-maximum (FWHM)** of the Gaussian **IRF**, t_0 is the wavelength dependent time zero and τ_i is the time constant of the i th one-exponential decay (time in which the signal decays to $1/e$ of its initial value). The **GF** consists of simultaneous fitting of all significant \mathbf{V}_k traces weighted by their singular values s_k with a sum of $A_{i,k} \text{ExpErf}[B, t_0, \tau_i, t]$ functions, where the amplitudes $A_{i,k}$ are fitted on a local basis (*i.e.* for each \mathbf{V}_k trace individually), and the B , t_0 and τ_i parameters are fitted globally (*i.e.* one set for all \mathbf{V}_k traces).

The coefficients $A_{i,k}$ obtained in the fit can be used to calculate the corresponding decay associated difference spectra (**DADS**) of the involved kinetics by using the set of M properly weighted \mathbf{U}_k spectral **SVD** components via [316]:

$$\text{DADS}_i = \sum_{k=1}^M A_{i,k} s_k \mathbf{U}_k \quad . \quad (\text{D.4})$$

The obtained DADS_i contain the contribution of corresponding lifetime decays τ_i in the spectral evolution of the system.

Strictly spoken, the **SVD** method in combination with a **GF** of the kinetic amplitude vectors is only applicable on time-resolved spectra in which no spectral shift takes place, because the method assumes that the (transient) spectrum at any time can be represented

by a linear combination of spectra that belong to independent molecular species [316]. In the present case this is certainly not fulfilled as the coherent dynamics inherently imply shifting bands due to the wavepacket motion on the excited state potential and vibrational cooling is reflected by narrowing of the spectral features. However, **SVD** is still useful in order to quantify the time scales of the various relaxation processes, and in particular, in order to separate the population kinetics from the wavepacket modulations.

GA, on the other hand, involves the global fitting of a large number of time traces from the unreduced data matrix according to a single fit function as in Equation (D.2). The number of amplitude parameters that must be varied in carrying out this fit scales with the number of time traces that are included.

Appendix E

Character and product tables

	E	$2C_4(z)$	C_2	$2C'_2$	$2C''_2$	i	$2S_4$	σ_h	$2\sigma_v$	$2\sigma_d$	linears, rotations	quadratic		
A_{1g}	1	1	1	1	1	1	1	1	1	1	R _z	$x^2 + y^2, z^2$		
A_{2g}	1	1	1	-1	-1	1	1	1	-1	-1		(R _x , R _y)	$x^2 - y^2$	
B_{1g}	1	-1	1	1	-1	1	-1	1	1	-1			z	xy
B_{2g}	1	-1	1	-1	1	1	-1	1	-1	1				(x, y)
E_g	2	0	-2	0	0	2	0	-2	0	0				
A_{1u}	1	1	1	1	1	-1	-1	-1	-1	-1				
A_{2u}	1	1	1	-1	-1	-1	-1	-1	1	1				
B_{1u}	1	-1	1	1	-1	-1	1	-1	-1	1				
B_{2u}	1	-1	1	-1	1	-1	1	-1	1	-1				
E_u	2	0	-2	0	0	-2	0	2	0	0				

Table E.1: Character table of the D_{4h} point group [293].

	A_{1g}	A_{2g}	B_{1g}	B_{2g}	E_g	A_{1u}	A_{2u}	B_{1u}	B_{2u}	E_u
A_{1g}	A_{1g}	A_{2g}	B_{1g}	B_{2g}	E_g	A_{1u}	A_{2u}	B_{1u}	A_{2u}	E_u
A_{2g}	A_{2g}	A_{1g}	B_{2g}	B_{1g}	E_g	A_{2u}	A_{1u}	B_{2u}	B_{1u}	E_u
B_{1g}	B_{1g}	B_{2g}	A_{1g}	A_{2g}	E_g	B_{1u}	B_{2u}	A_{1u}	A_{2u}	E_u
B_{2g}	B_{2g}	B_{1g}	A_{2g}	A_{1g}	E_g	B_{2u}	B_{1u}	A_{2u}	A_{1u}	E_u
E_g	E_g	E_g	E_g	E_g	$A_{1g}+A_{2g}+B_{1g}+B_{2g}$	E_u	E_u	E_u	E_u	$A_{1u}+A_{2u}+B_{1u}+B_{2u}$
A_{1u}	A_{1u}	A_{2u}	B_{1u}	B_{2u}	E_u	A_{1g}	A_{2g}	B_{1g}	B_{2g}	E_g
A_{2u}	A_{2u}	A_{1u}	B_{2u}	B_{1u}	E_u	A_{2g}	A_{1g}	B_{2g}	B_{1g}	E_g
B_{1u}	B_{1u}	B_{2u}	A_{1u}	A_{2u}	E_u	B_{1g}	B_{2g}	A_{1g}	A_{2g}	E_g
B_{2u}	B_{2u}	B_{1u}	A_{2u}	A_{1u}	E_u	B_{2g}	B_{1g}	A_{2g}	A_{1g}	E_g
E_u	E_u	E_u	E_g	E_g	$A_{1u}+A_{2u}+B_{1u}+B_{2u}$	E_g	E_g	E_g	E_g	$A_{1g}+A_{2g}+B_{1g}+B_{2g}$

Table E.2: Product table of the D_{4h} point group [293].

Appendix F

Transient XAS excitation wavelength dependence

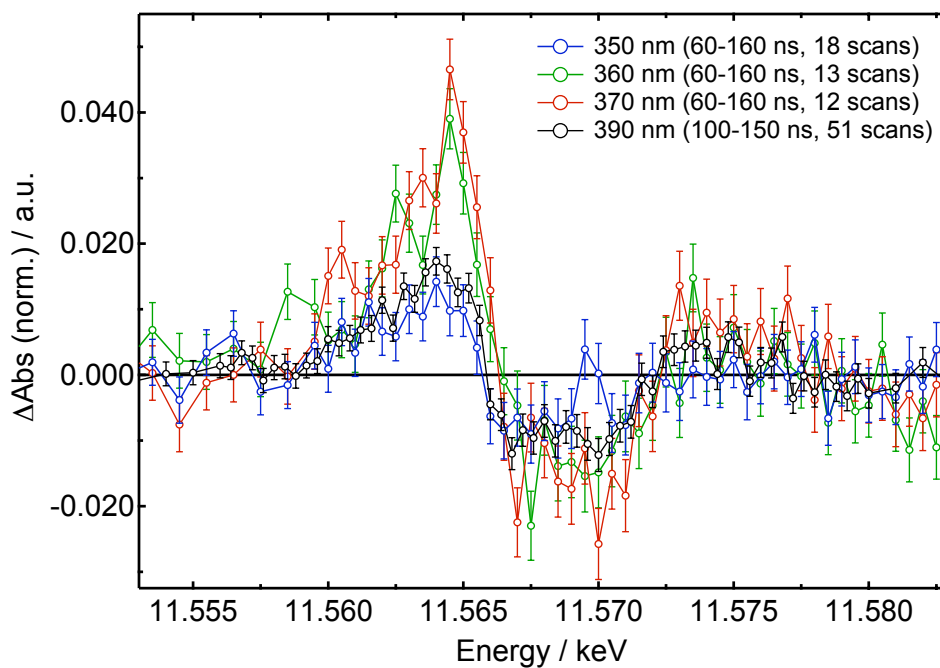


Figure F.1: Transient XANES for different excitation wavelengths. The laser power was kept the same for all data sets. The energy axis is calibrated.

Physical constants

Avogadro constant	N_A	$6.022 \times 10^{23} \text{ mol}^{-1}$
Boltzmann constant	k_B	$1.381 \times 10^{-23} \text{ JK}^{-1}$
Electron mass	m_e	$9.10938188 \times 10^{-31} \text{ kg}$
Planck's constant	h	$6.626 \times 10^{-34} \text{ Js}$
Speed of light	c	$2.998 \times 10^8 \text{ ms}^{-1}$
Elementary charge	e	$1.60217646 \times 10^{-19} \text{ C}$

Abbreviations

2D	two-dimensional
3D	three-dimensional
APD	avalanche photodiode
BBO	β -BaB ₂ O ₄
BO	Born-Oppenheimer
BPF	band-pass filter
BS	beam splitter
CCD	charge-coupled device
CPM	cross-phase modulation
CS	camshaft
CW	continuous-wave
DA	diode array
DADS	decay associated difference spectrum
DCM	4-(Dicyanomethylene)-2-methyl-6-(4-dimethylaminostyryl)-4 <i>H</i> -pyran
DFT	density functional theory
DMF	dimethylformamide
DOS	density of states
DW	Debye-Waller
ES	excited state
ESA	excited state absorption
EVR	external vibrational relaxation
EXAFS	X-ray absorption fine structure
FC	Franck-Condon
FMS	full multiple-scattering
FT	Fourier transform

FU	fluorescence up-conversion
FWHM	full-width-half-maximum
GA	global analysis
GF	global fit
GS	ground state
GSB	ground state bleach
GVD	group velocity dispersion
HL	Hedin-Lundqvist
HOMO	highest-occupied molecular orbital
IC	internal conversion
IP	ionization potential
IR	infrared
IRF	instrumental response function
ISC	intersystem crossing
IVR	intramolecular vibrational energy redistribution
KB	Kirkpatrick-Baez
LDOS	<i>l</i> -projected density of states
LMCT	ligand-to-metal charge transfer
LUMO	lowest-unoccupied molecular orbital
MB	multibunch
MC	metal-centered
MLCT	metal-to-ligand charge transfer
MS	multiple-scattering
MT	muffin-tin
OD	optical density
PD	photo-diode
PL	polarizer
PtPOP	tetrakis μ -pyrophosphitodiplatinate(II), $[\text{Pt}_2(\text{P}_2\text{O}_5\text{H}_2)_4]^{4-}$
RF	radiofrequency
RISRS	resonant impulsive stimulated Raman scattering
RPA	random-phase approximation

List of symbols

S/N	signal-to-noise
SCF	self-consistent field
SE	stimulated emission
SFG	sum-frequency generation
SHG	single-harmonic generation
SLS	Swiss Light Source
SO	spin-orbit
SS	single scattering
SVD	singular value decomposition
TA	transient absorption
TBA	tetrabutyl ammonium
TOPAS	traveling-wave optical parametric amplifier of superfluorescence
UV	ultra-violet
VP	vibrating plate
WLC	white-light continuum
WP	wave plate
XAFS	X-ray absorption fine structure
XANES	X-ray absorption near-edge structure
XAS	X-ray absorption spectroscopy
XRD	X-ray diffraction

List of Symbols

A_i	amplitude of component i
A_m	atomic mass number
B	FWHM of the Gaussian instrumental response function
χ	X-ray absorption fine structure
χ_m^{ES}	vibrational wavefunction in the $^1A_{2u}$ state
χ_m^{GS}	vibrational wavefunction in the ground state
c_{mol}	molar sample concentration
d	distortion along the Pt-Pt coordinate
$\Delta\nu_{\text{abs}}$	inhomogeneous line broadening in the $^1A_{2u}$ absorption spectrum
E_0	absolute energy necessary to expel the electron from its core level (edge position in XAS)
E	X-ray photon energy
E_{el}	kinetic energy of the photoelectron
E_F	Fermi energy
ϵ_f	X-ray fluorescence yield
ϕ	phase of the wave packet oscillation
I_0	incoming X-ray intensity
I_F	X-ray fluorescence intensity
I_T	transmitted X-ray intensity
j	total angular momentum quantum number
λ	photoelectron mean free path
l	orbital angular momentum quantum number
λ_{el}	wavelength of the photoelectron

m	magnetic quantum number
μ_{vib}	reduced mass of the Pt-Pt stretch vibration
μ_0	embedded-atom X-ray absorption background function
μ	linear X-ray absorption coefficient
n	principal quantum number
N_{indp}	number of independent data points
ν_{00}	frequency of the 0-0 (zero-phonon) transition
ν_{ave}	average vibrational energy of the wavepacket superposition state (relative to the $v = 0$ level of the ${}^1A_{2u}$ state)
ν_{ES}	vibrational Pt-Pt stretch frequency in the excited ${}^1A_{2u}$ state
ν_{GS}	vibrational Pt-Pt stretch frequency in the ground state
Ω	solid angle of detection
ρ_m	mass density
S	Huang-Rhys factor
s	spin quantum number
S_0^2	amplitude reduction factor
$\Sigma(E)$	complex photoelectron self-energy
σ	Debye-Waller factor
σ_a	atomic absorption cross section
s_k	singular value of the k^{th} component resulting from SVD
T	temperature in Kelvin
t_0	time delay zero (time at which pump and probe pulses overlap)
t	time delay
τ_1	time constant of vibrational cooling in the ${}^1A_{2u}$ state (1/e value)
τ_2	time constant of vibrational cooling in the ${}^1A_{2u}$ state (1/e value)
τ_3	intersystem crossing time constant (1/e value)
τ_4	life time of the ${}^3A_{2u}$ state (1/e value)

List of symbols

τ_C	coherent decay time of the wave packet in the ${}^1A_{2u}$ state ($1/e$ value)
T_{ES}	period of the vibrational wave packet oscillation in the ${}^1A_{2u}$ state
T_{GS}	period of the vibrational wave packet oscillation in the ground state
τ_i	exponential decay time of component i ($1/e$ value)
v	vibrational quantum number
\mathbf{V}_k	k^{th} kinetic basis vector resulting from SVD
Z	atomic number

References

- [1] AH Zewail. *J. Phys. Chem. A*, 104(24):5660–5694, 2000.
- [2] M Chergui. *Femtochemistry: Physics and Chemistry of Ultrafast Processes in Molecular Systems*. World Scientific, Singapore, 1996.
- [3] RGW Norrish and G Porter. *Nature*, 164(4172):658–658, 1949.
- [4] KJ Kaufmann and PM Rentzepis. *Acc. Chem. Res.*, 8(12):407–412, 1975.
- [5] SH Lin. *Radiationless transitions*. Academic Press, New York, 1980.
- [6] A Laubereau and W Kaiser. *Rev. Mod. Phys.*, 50(3):607–665, 1978.
- [7] NF Scherer, JL Knee, DD Smith, and AH Zewail. *J. Phys. Chem.*, 89(24):5141–5143, 1985.
- [8] M Dantus, MJ Rosker, and AH Zewail. *J. Chem. Phys.*, 87(4):2395–2397, 1987.
- [9] MJ Rosker, M Dantus, and AH Zewail. *Science*, 241(4870):1200–1202, 1988.
- [10] L Dhar, JA Rogers, and KA Nelson. *Chem. Rev.*, 94(1):157–193, 1994.
- [11] DM Jonas, SE Bradforth, SA Passino, and GR Fleming. *J. Phys. Chem.*, 99(9):2594–2608, 1995.
- [12] AH Zewail. *Laser Phys.*, 5(3):417–442, 1995.
- [13] AH Zewail. *Angew. Chem. Int. Edit.*, 40(23):4371, 2001.
- [14] RM Bowman, M Dantus, and AH Zewail. *Chem. Phys. Lett.*, 161(4-5):297–302, 1989.
- [15] M Gruebele, G Roberts, M Dantus, RM Bowman, and AH Zewail. *Chem. Phys. Lett.*, 1990.
- [16] TS Rose, MJ Rosker, and AH Zewail. *J. Chem. Phys.*, 91(12):7415–7436, 1989.
- [17] T Baumert, M Grosser, R Thalweiser, and G Gerber. *Phys. Rev. Lett.*, 67(27):3753–3756, 1991.
- [18] T Baumert, V Engel, C Rottgermann, WT Strunz, and G Gerber. *Chem. Phys. Lett.*, 191(6):639–644, 1992.
- [19] TJ Dunn, JN Sweetser, IA Walmsley, and C Radzewicz. *Phys. Rev. Lett.*, 70(22):3388–3391, 1993.
- [20] M Dantus, MJ Rosker, and AH Zewail. *J. Chem. Phys.*, 89(10):6128–6140, 1988.
- [21] TS Rose, MJ Rosker, and AH Zewail. *J. Chem. Phys.*, 88(10):6672–6673, 1988.
- [22] M Dantus, RM Bowman, M Gruebele, and AH Zewail. *J. Chem. Phys.*, 91(12):7437–7450, 1989.
- [23] M Chergui and AH Zewail. *Chem. Phys. Chem.*, 10(1):28–43, 2009.

-
- [24] BJ Siwick, JR Dwyer, RE Jordan, and RJD Miller. *Science*, 302(5649):1382–1385, 2003.
- [25] AH Zewail. *Annu. Rev. Phys. Chem.*, 57:65–103, 2006.
- [26] JR Dwyer, CT Hebeisen, R Ernstorfer, M Harb, VB Deyirmenjian, RE Jordan, and RJD Miller. *Philos. T. R. Soc. A*, 364(1840):741–778, 2006.
- [27] P Baum, D-S Yang, and AH Zewail. *Science*, 318(5851):788–792, 2007.
- [28] B Barwick, HS Park, O-H Kwon, JS Baskin, and AH Zewail. *Science*, 322(5905):1227–1231, 2008.
- [29] F Carbone, O-H Kwon, and AH Zewail. *Science*, 325(5937):181–184, 2009.
- [30] AH Zewail and JM Thomas. *4D Electron Microscopy: Imaging in Space and Time*. Imperial College Press, 2010.
- [31] P Coppens. *Chem. Comm.*, 12:1317–1320, 2003.
- [32] P Coppens. *Angew. Chem. Int. Edit.*, 48(24):4280–4281, 2009.
- [33] K Moffat. *Chem. Rev.*, 101(6):1569–1581, 2001.
- [34] C Rischel, A Rousse, I Uschmann, PA Albouy, JP Geindre, P Audebert, JC Gauthier, E Forster, JL Martin, and A Antonetti. *Nature*, 390(6659):490–492, 1997.
- [35] R Neutze, R Wouts, S Techert, J Davidsson, M Kocsis, A Kirrander, F Schotte, and M Wulff. *Phys. Rev. Lett.*, 87(19):195508–195508, 2001.
- [36] S Techert, F Schotte, and M Wulff. *Phys. Rev. Lett.*, 86:2030, 2001.
- [37] E Collet, MH Lemeé-Cailleau, M Buron-Le Cointe, H Cailleau, M Wulff, T Luty, SY Koshihara, M Meyer, L Toupet, P Rabiller, and S Techert. *Science*, 300(5619):612–615, 2003.
- [38] C Von Korff Schmising, M Bargheer, M Kiel, N Zhavoronkov, M Woerner, T Elsaesser, I Vrejoiu, D Hesse, and M Alexe. *Phys. Rev. Lett.*, 98(25):257601, 2007.
- [39] M Woerner, F Zamponi, Z Ansari, J Dreyer, B Freyer, M Premont-Schwarz, and T Elsaesser. *J. Chem. Phys.*, 133(6):064509, 2010.
- [40] M Cammarata, M Levantino, F Schotte, PA Anfinrud, F Ewald, J Choi, A Cupane, M Wulff, and H Ihee. *Nat. Methods*, 5(10):881–886, 2008.
- [41] H Ihee, M Wulff, J Kim, and S Adachi. *Int. Rev. Phys. Chem.*, 29(3):453–520, 2010.
- [42] K Haldrup, M Christensen, M Cammarata, Q Kong, M Wulff, SO Mariager, K Bechgaard, R Feidenhans'l, N Harrit, and MM Nielsen. *Angew. Chem. Int. Edit.*, 48(23):4180–4184, 2009.
- [43] M Christensen, K Haldrup, K Bechgaard, R Feidenhans'l, Q Kong, M Cammarata, M Lo Russo, M Wulff, N Harrit, and MM Nielsen. *J. Am. Chem. Soc.*, 131(2):502–508, 2009.
- [44] M Christensen, K Haldrup, KS Kjaer, M Cammarata, M Wulff, K Bechgaard, H Weihe, NH Harrit, and MM Nielsen. *Phys. Chem. Chem. Phys.*, 12(26):6921–6923, 2010.
- [45] C Bressler and M Chergui. *Chem. Rev.*, 104(24):1781–1812, 2004.
- [46] LX Chen. *Angew. Chem. Int. Ed.*, 43(22):2886–2905, 2004.
- [47] M Chergui. *Acta Crystallogr. A*, 66:229–239, 2010.

- [48] C Bressler, R Abela, and M Chergui. *Z. Kristallogr.*, 223(4-5/2008):307–321, 2008.
- [49] C Bressler and M Chergui. *Annu. Rev. Phys. Chem.*, 61:263–282, 2010.
- [50] BJ Siwick, JR Dwyer, RE Jordan, and RJD Miller. *J. Appl. Phys.*, 92(3):1643–1648, 2002.
- [51] A Yurtsever and AH Zewail. *Science*, 326(5953):708–712, 2009.
- [52] P Baum and AH Zewail. *Chem. Phys.*, 366(1-3):2–8, 2009.
- [53] M Bargheer, N Zhavoronkov, Y Gritsai, JC Woo, DS Kim, M Woerner, and T Elsaesser. *Science*, 306(5702):1771–1773, 2004.
- [54] M Bargheer, N Zhavoronkov, M Woerner, and T Elsaesser. *Chem. Phys. Chem.*, 7(4):783–792, 2006.
- [55] T Elsaesser and M Woerner. *Acta Cryst. Sec, A*, 66:168–178, 2010.
- [56] P Beaud, S. L Johnson, A Streun, R Abela, D Abramsohn, D Grolimund, F Krasniqi, T Schmidt, V Schlott, and G Ingold. *Phys. Rev. Lett.*, 99(17):174801, 2007.
- [57] SL Johnson, P Beaud, E Vorobeva, CJ Milne, ED Murray, S Fahy, and G Ingold. *Phys. Rev. Lett.*, 102(17):175503, 2009.
- [58] P Beaud, SL Johnson, E Vorobeva, U Staub, RA De Souza, CJ Milne, QX Jia, and G Ingold. *Phys. Rev. Lett.*, 103(15):155702, 2009.
- [59] SL Johnson, E Vorobeva, P Beaud, CJ Milne, and G Ingold. *Phys. Rev. Lett.*, 103(20):205501, 2009.
- [60] M Herzog, W Leitenberger, R Shayduk, RM van der Veen, CJ Milne, SL Johnson, I Vrejoiu, M Alexe, D Hesse, and M Bargheer. *Appl. Phys. Lett.*, 96(16):161906, 2010.
- [61] Ch Bressler, C Milne, V-T Pham, A ElNahas, RM van der Veen, W Gawelda, S Johnson, P Beaud, D Grolimund, M Kaiser, CN Borca, G Ingold, R Abela, and M Chergui. *Science*, 323(5913):489–492, 2009.
- [62] R Neutze, R Wouts, D van der Spoel, E Weckert, and J Hajdu. *Nature*, 406(6797):752–757, 2000.
- [63] T Tschentscher. *Chem. Phys.*, 299(2-3):271–276, 2004.
- [64] AP Mancuso, A Schropp, B Reime, L-M Stadler, and A Singer et al. *Phys. Rev. Lett.*, 102(3):035502, 2009.
- [65] BD Patterson and R Abela. *Phys. Chem. Chem. Phys.*, 12(21):5647–5652, 2010.
- [66] CM Kewish, P Thibault, O Bunk, and F Pfeiffer. *New J. Phys.*, 12:035005, 2010.
- [67] L Young, EP Kanter, B Kraessig, Y Li, and AM March et al. *Nature*, 466(7302):56–U66, 2010.
- [68] DC Koningsberger and R Prins. *X-ray absorption: principles, applications, techniques of EXAFS, SEXAFS, and XANES*. Wiley-Interscience, 1988.
- [69] BC Gates, H Knoezinger, and F Jentoft. *Advances in Catalysis*. Elsevier, 2009.
- [70] AL Ankudinov, JJ Rehr, and SR Bare. *Chem. Phys. Lett.*, 316(5-6):495–500, 2000.
- [71] AL Ankudinov, JJ Rehr, J Low, and SR Bare. *Phys. Rev. Lett.*, 86(8):1642–1645, 2001.
- [72] AL Ankudinov, JJ Rehr, JJ Low, and SR Bare. *J. Synchrotron Radiat.*, 8(2):0495,

- 2001.
- [73] AL Ankudinov, JJ Rehr, JJ Low, and SR Bare. *J. Chem. Phys.*, 116(5):1911–1919, 2002.
- [74] DC Koningsberger, MK Oudenhuijzen, J de Graaf, JA van Bokhoven, and DE Ramaker. *J. Catal.*, 216(1-2):178–191, 2003.
- [75] J Singh, M Tromp, OV Safonova, P Glatzel, and JA van Bokhoven. *Catal. Today*, 145(3-4):300–306, 2009.
- [76] J Stöhr. *NEXAFS spectroscopy*. Springer Series in Surface Sciences, 1992.
- [77] VM Parmon, A Vorontsov, D Kozlov, and P Smirniotis. *Photocatalysis: Catalysts, Kinetics and Reactors*. Wiley-VCH, 2010.
- [78] M Tromp. *Development of time-resolved XAFS spectroscopy techniques: applications in homogeneous catalysis*. University of Utrecht, Debye Institute (PhD thesis), 2004.
- [79] J Singh, EMC Alayon, M Tromp, OV Safonova, P Glatzel, M Nachtegaal, R Frahm, and JA van Bokhoven. *Angew. Chem. Int. Edit.*, 47(48):9260–9264, 2008.
- [80] T Ressler. *Catal. Today*, 145(3-4):258–266, 2009.
- [81] LX Chen. *Annu. Rev. Phys. Chem.*, 56(1):221–254, 2005.
- [82] DM Mills, A Lewis, A Harootunian, J Huang, and B Smith. *Science*, 223(4638):811–813, 1984.
- [83] DJ Thiel, P Livijn, EA Stern, and A Lewis. *Nature*, 362(6415):40, 1993.
- [84] LX Chen, PL Lee, D Gosztola, WA Svec, PA Montano, and MR Wasielewski. *J. Phys. Chem. B*, 103(16):3270–3274, 1999.
- [85] LX Chen, WJH Jager, G Jennings, DJ Gosztola, A Munkholm, and JP Hessler. *Science*, 292(5515):262–264, 2001.
- [86] LX Chen, G Jennings, T Liu, DJ Gosztola, JP Hessler, DV Scaltrito, and GJ Meyer. *J. Am. Chem. Soc.*, 124(36):10861–10867, 2002.
- [87] M Saes, C Bressler, R Abela, D Grolimund, SL Johnson, PA Heimann, and M Chergui. *Phys. Rev. Lett.*, 90(4):047403, 2003.
- [88] M Khalil, MA Marcus, AL Smeigh, JK McCusker, HHW Chong, and RW Schoenlein. *J. Phys. Chem. A*, 110(1):38–44, 2006.
- [89] S Nozawa, T Sato, M Chollet, K Ichiyanagi, A Tomita, H Fujii, S Adachi, and S Koshihara. *J. Am. Chem. Soc.*, 132(1):61, 2010.
- [90] W Gawelda, M Johnson, FMF de Groot, R Abela, C Bressler, and M Chergui. *J. Am. Chem. Soc.*, 128(15):5001–5009, 2006.
- [91] W Gawelda, V-T Pham, M Benfatto, Y Zaushitsyn, M Kaiser, D Grolimund, SL Johnson, R Abela, A Hauser, C Bressler, and M Chergui. *Phys. Rev. Lett.*, 98(5):057401, 2007.
- [92] A El Nahas. *Time-Resolved Optical and X-ray Spectroscopy Of Rhenium Based Molecular Complexes*. EPFL (PhD thesis), 2010.
- [93] A Juris, V Balzani, F Barigelletti, S Campagna, P Belser, and A Vonzelwesky. *Coord. Chem. Rev.*, 84:85–277, 1988.
- [94] W Gawelda, V-T Pham, RM van der Veen, D Grolimund, R Abela, M Chergui, and

- C Bressler. *J. Chem. Phys.*, 130(12):124520, 2009.
- [95] JJ Rehr, JJ Kas, MP Prange, AP Sorini, Y Takimoto, and F Vila. *C. R. Phys.*, 10(6):548–559, 2009.
- [96] JJ Rehr, JJ Kas, FD Vila, and K Jorissen. *Phys. Chem. Chem. Phys.*, 12:5503, 2009.
- [97] JJ Rehr, J Kozdon, J Kas, HJ Krappe, and HH Rossner. *J. Synchrotron Radiat.*, 12:70–74, 2005.
- [98] M Benfatto, A Congiu-Castellano, A Daniele, and S Della Longa. *J. Synchrotron Radiat.*, 8(2):0495, 2001.
- [99] G Smolentsev and AV Soldatov. *Comp. Mat. Science*, 39(3):569–574, 2007.
- [100] A Vlček. *Coord. Chem. Rev.*, 200:933–977, 2000.
- [101] M Bixon and J Jortner. *J. Chem. Phys.*, 48(2):715, 1968.
- [102] DP Chock, J Jortner, and SA Rice. *J. Chem. Phys.*, 49(2):610, 1968.
- [103] R Englman and J Jortner. *Mol. Phys.*, 18(2):145, 1970.
- [104] SH Lin. *J. Chem. Phys.*, 44:3759, 1966.
- [105] S Dym and RM Hochstrasser. *J. Chem. Phys.*, 51(6):2458, 1969.
- [106] PM Felker and AH Zewail. *J. Chem. Phys.*, 82(7):2961–2974, 1985.
- [107] MA El-Sayed. *Accounts Chem. Res.*, 1(1):8, 1968.
- [108] M Klessinger and J Michl. *Excited States and Photo-Chemistry of Organic Molecules*. Wiley-VCH, 1995.
- [109] EA Juban and JK McCusker. *J. Am. Chem. Soc.*, 127(18):6857–6865, 2005.
- [110] A El Nahhas, A Cannizzo, F van Mourik, AM Blanco-Rodriguez, S Zalis, A Vlček, and M Chergui. *J. Phys. Chem. A*, 114(22):6361–6369, 2010.
- [111] V Balzani and V Carassiti. *Photochemistry of coordination compounds*. Academic Press, London, 1970.
- [112] DC Smith and HB Gray. *Coord. Chem. Rev.*, 100:169–181, 1990.
- [113] JL Marshall, AE Stiegman, and HB Gray. *Acc. Sym. Ser.*, 307:166–176, 1986.
- [114] S Rice, S Milder, and HB Gray. *Coord. Chem. Rev.*, 43:349–354, 1982.
- [115] PD Harvey. *Coord. Chem. Rev.*, 219:17–52, 2001.
- [116] AP Zipp. *Coord. Chem. Rev.*, 84:47–83, 1988.
- [117] D Roundhill, H Gray, and C Che. *Acc. Chem. Res.*, 22:55–61, 1989.
- [118] P Coppens, O Gerlits, II Vorontsov, AY Kovalevsky, YS Chen, T Graber, M Gem-bicky, and IV Novozhilova. *Chem. Comm.*, 2004(19):2144–2145, 2004.
- [119] IV Novozhilova, AV Volkov, and P Coppens. *Inorg. Chem.*, 43(7):2299–2307, 2004.
- [120] V Miskowski, S Rice, H Gray, and R Dallinger. *Inorg. Chem.*, 33:2799–2807, 1994.
- [121] JR Winkler, JL Marshall, TL Netzel, and HB Gray. *J. Am. Chem. Soc.*, 108(9):2263–2266, 1986.
- [122] VM Miskowski, TP Smith, TM Loehr, and HB Gray. *J. Am. Chem. Soc.*, 107(26):7925–7934, 1985.
- [123] SF Rice. *Optical spectroscopic studies of square planar d8 dimers*. Caltech (PhD

- thesis), 1982.
- [124] A Stiegman, S Rice, H Gray, and V Miskowski. *Inorg. Chem.*, 26:1112–1116, 1987.
- [125] SF Rice, VM Miskowski, and HB Gray. *Inorg. Chem.*, 27(26):4704–4708, 1988.
- [126] VM Miskowski, SF Rice, HB Gray, and SJ Milder. *J. Phys. Chem.*, 97(17):4277–4283, 1993.
- [127] SJ Milder and DS Kliger. *J. Phys. Chem.*, 89(20):4170–4171, 1985.
- [128] RJ Sweeney, EL Harvey, and HB Gray. *Coord. Chem. Rev.*, 105:23–34, 1990.
- [129] W Fordyce, J Brummer, and G Crosby. *J. Am. Chem. Soc.*, 103:7061–7064, 1981.
- [130] DM Roundhill. *J. Am. Chem. Soc.*, 107(14):4354–4356, 1985.
- [131] A Vlček Jr and H Gray. *Inorg. Chem.*, 26:1997, 1987.
- [132] A Vlček and HB Gray. *J. Am. Chem. Soc.*, 109(1):286–287, 1987.
- [133] E Harvey, A Stiegman, A Vlček Jr, and H Gray. *J. Am. Chem. Soc.*, 109:5233, 1987.
- [134] H Iguchi, S Takaishi, H Miyasaka, M Yamashita, H Matsuzaki, H Okamoto, H Tanaka, and S Kuroda. *Angew. Chem. Int. Edit.*, 49(3):552–555, 2010.
- [135] C Che, L Butler, and H Gray. *J. Am. Chem. Soc.*, 103:7796, 1981.
- [136] P Stein, M Dickson, and D Roundhill. *J. Am. Chem. Soc.*, 105:3489–3494, 1983.
- [137] S Rice and H Gray. *J. Am. Chem. Soc.*, 105:4571–4575, 1983.
- [138] C Che, L Butler, H Gray, R Crooks, and W Woodruff. *J. Am. Chem. Soc.*, 105:5492, 1983.
- [139] J Markert, D Clements, M Corson, and J Nagle. *Chem. Phys. Lett.*, 97:175, 1983.
- [140] L Bär and G Gliemann. *Chem. Phys. Lett.*, 108(1):14, 1984.
- [141] J Brummer and G Crosby. *Chem. Phys. Lett.*, 112:15, 1984.
- [142] CM Che, LG Butler, PJ Grunthaner, and HB Gray. *Inorg. Chem.*, 24(26):4662–4665, 1985.
- [143] H Isci and W Mason. *Inorg. Chem.*, 24:1761, 1985.
- [144] Y Shimizu, Y Tanaka, and T Azumi. *J. Phys. Chem.*, 89:1372, 1985.
- [145] Y Tanaka and T Azumi. *Inorg. Chem.*, 25(3):247–248, 1986.
- [146] T Ikeyama, S Yamamoto, and T Azumi. *J. Phys. Chem.*, 92:6899, 1988.
- [147] T Uchida, N Kitamura, H Kim, S Tazuke, and T Yagi. *J. Am. Chem. Soc.*, 111:7466, 1989.
- [148] S Milder and B Brunshwig. *J. Phys. Chem.*, 96:2189–2196, 1992.
- [149] KH Leung, DL Phillips, CM Che, and VM Miskowski. *J. Raman Spectrosc.*, 30(11):987–993, 1999.
- [150] Y Shimizu, Y Tanaka, and T Azumi. *J. Phys. Chem.*, 88:2423–2425, 1984.
- [151] EA Boudreaux, SP Doussa, and M Klobukowski. *Int. J. Quantum Chem.*, 30, 1986.
- [152] G Gellene and D Roundhill. *J. Phys. Chem. A*, 106:7617–7620, 2002.
- [153] IV Novozhilova, AV Volkov, and P Coppens. *J. Am. Chem. Soc.*, 125:1079–1087, 2003.
- [154] SR Stoyanov, JM Villegas, and DP Rillema. *J. Phys. Chem. B*, 108(32):12175–12180, 2004.

- [155] RE Marsh and FH Herbstein. *Structural Science*, 39(2):7681, 1983.
- [156] C Che, F Herbstein, W Schaefer, and R Marsch. *J. Am. Chem. Soc.*, 105:4604, 1983.
- [157] R Clark, M Kurmoo, H Dawes, and M Hursthouse. *Inorg. Chem*, 25:409, 1986.
- [158] N Yasuda, M Kanazawa, H Uekusa, and Y Ohashi. *Chem. Lett.*, 31(11):1132–1133, 2002.
- [159] CD Kim, S Pillet, G Wu, WK Fullagar, and P Coppens. *Acta Crystallogr. A*, A58:133–137, 2002.
- [160] Y Ozawa, M Terashima, M Mitsumi, K Toriumi, N Yasuda, H Uekusa, and Y Ohashi. *Chem. Lett.*, 32(1):62–63, 2003.
- [161] N Yasuda, H Uekusa, and Y Ohashi. *Bull. Chem. Soc. Jpn.*, 77(5):933–944, 2004.
- [162] RM van der Veen, CJ Milne, V-T Pham, A El Nahhas, JA Weinstein, J Best, CN Borca, C Bressler, and M Chergui. *Chimia*, 62(4):287–290, 2008.
- [163] RM van der Veen, CJ Milne, A El Nahhas, FA Lima, V-T Pham, J Best, JA Weinstein, CN Borca, R Abela, C Bressler, and M Chergui. *Angew. Chem. Int. Edit.*, 48(15):2711–2714, 2009.
- [164] RM van der Veen, JJ Kas, CJ Milne, V-T Pham, A El Nahhas, FA Lima, D Amarasinge, JJ Rehr, R Abela, and M Chergui. *Phys. Chem. Chem. Phys.*, 12:5551–5561, 2010.
- [165] AH Zewail. *Science*, 242(4886):1645–1653, 1988.
- [166] AH Zewail, FC de Schryver, S de Feyter, and G Schweitzer. *Femtochemistry: with the Nobel lecture of A. Zewail*. Wiley-VCH, 2001.
- [167] J Yeazell and T Uzer. *The physics and chemistry of wave packets*. Wiley, 2000.
- [168] E Schrodinger. *Naturwissenschaften*, 14:664–666, 1926.
- [169] V Engel, H Metiu, R Almeida, RA Marcus, and AH Zewail. *Chem. Phys. Lett.*, 152(1):1–7, 1988.
- [170] N Pugliano, DK Palit, AZ Szarka, and RM Hochstrasser. *J. Chem. Phys.*, 99(9):7273–7276, 1993.
- [171] A Assion, M Geisler, J Helbing, V Seyfried, and T Baumert. *Phys. Rev. A*, 54(6):605–608, 1996.
- [172] M Schmitt, G Knopp, A Materny, and W Kiefer. *Chem. Phys. Lett.*, 270(1-2):9–15, 1997.
- [173] A Vierheilig, T Chen, P Waltner, W Kiefer, A Materny, and AH Zewail. *Chem. Phys. Lett.*, 312(5-6):349–356, 1999.
- [174] MH Vos, F Rappaport, JC Lambry, J Breton, and JL Martin. *Nature*, 363(6427):320–325, 1993.
- [175] RW Schoenlein, LA Peteanu, Q Wang, RA Mathies, and CV Shank. *J. Phys. Chem.*, 97(46):12087–12092, 1993.
- [176] AH Zewail. *J. Phys. Chem.*, 100(31):12701–12724, 1996.
- [177] QL Liu, JK Wang, and AH Zewail. *Nature*, 364(6436):427–430, 1993.
- [178] F Vigliotti, L Bonacina, and M Chergui. *Phys. Rev. B*, 67(11):115118, 2003.

-
- [179] AH Zewail. *J. Phys. Chem. A*, 104(24):5660–5694, 2000.
- [180] B Kohler, VV Yakovlev, JW Che, JL Krause, M Messina, KR Wilson, N Schwentner, RM Whitnell, and YJ Yan. *Phys. Rev. Lett.*, 74(17):3360–3363, 1995.
- [181] M Guehr, M Bargheer, M Fushitani, T Kiljunen, and N Schwentner. *Phys. Chem. Chem. Phys.*, 9(7):779–801, 2007.
- [182] VA Apkarian and N Schwentner. *Chem. Rev.*, 99(6):1481–1514, 1999.
- [183] E Condon. *Phys. Rev.*, 28(6):1182–1201, 1926.
- [184] W Heisenberg and C Eckart. *The physical principles of the quantum theory*. The University of Chicago Press, 1930.
- [185] WT Pollard, SY Lee, and RA Mathies. *J. Chem. Phys.*, 92:4012, 1990.
- [186] J Janszky and AV Vinogradov. *Phys. Rev. Lett.*, 64(23):2771–2774, 1990.
- [187] J Janszky, P Adam, AV Vinogradov, and T Kobayashi. *Spectrochim. Acta A*, 48(1): 31–39, 1992.
- [188] R Zadoyan, Z Li, CC Martens, and VA Apkarian. *J. Chem. Phys.*, 101(8):6648–6657, 1994.
- [189] A Ozawa, K Takimiya, T Otsubo, and T Kobayashi. *Chem. Phys. Lett.*, 409(4-6): 224–229, 2005.
- [190] RM Stratt and M Maroncelli. *J. Phys. Chem.*, 100(31):12981–12996, 1996.
- [191] JC Owrrutsky, D Raftery, and RM Hochstrasser. *Annu. Rev. Phys. Chem.*, 45: 519–555, 1994.
- [192] AL Harris, JK Brown, and CB Harris. *Annu. Rev. Phys. Chem.*, 39(1):341–366, 1988.
- [193] M Li, J Owrrutsky, M Sarisky, JP Culver, A Yodh, and RM Hochstrasser. *J. Chem. Phys.*, 98(7):5499–5507, 1993.
- [194] DAV Kliner, JC Alfano, and PF Barbara. *J. Chem. Phys.*, 98(7):5375–5389, 1993.
- [195] JM Jean and GR Fleming. *J. Chem. Phys.*, 103(6):2092–2101, 1995.
- [196] AG Redfield. *IBM J. Res. Dev.*, 1(1):19–31, 1957.
- [197] D Kohen and DJ Tannor. *J. Chem. Phys.*, 107(13):5141–5153, 1997.
- [198] *Mathematica Edition: Version 7.0*, Wolfram Research, Inc. Wolfram Research, Inc., 2008.
- [199] WW Parson. *Modern optical spectroscopy: with examples from biophysics and biochemistry*. Springer, 2007.
- [200] CJ Ballhausen. *Molecular electronic structures of transition metal complexes*. McGraw-Hill, 1979.
- [201] II Guseinov, BA Mamedov, and AS Ekenoglu. *Comput. Phys. Commun.*, 175(3): 226–231, 2006.
- [202] K Huang and A Rhys. *Proc. R. Soc. Lon. Ser-A*, 204(1078):406–423, 1950.
- [203] A Stanton. *Nature*, 53:274 – 276, 1896.
- [204] J Als-Nielsen and D McMorow. *Elements of modern X-ray physics*. John Wiley & Sons, Ltd, 2001.

- [205] A Einstein. *Ann. Phys-Berlin*, 17(6):132–148, 1905.
- [206] BK Teo. *EXAFS: basic principles and data analysis*. Springer, 1986.
- [207] A Beer. *Ann. Phys-Berlin*, 162(5):78–88, 1852.
- [208] M Sanchez del Rio and RJ Dejus. *X-ray oriented programs (XOP 2.1)*. 2003.
- [209] A Messiah. *Quantum mechanics, Volume 1*. John Wiley & Sons., 1966.
- [210] MO Krause. *J. Phys. Chem. Ref. Data*, 8(2):307–327, 1979.
- [211] MO Krause and JH Oliver. *J. Phys. Chem. Ref. Data*, 8:329–338, 1979.
- [212] K Hamalainen, DP Siddons, JB Hastings, and LE Berman. *Phys. Rev. Lett.*, 67(20):2850–2853, 1991.
- [213] JJ Rehr and RC Albers. *Rev. Mod. Phys.*, 72(3):621–654, 2000.
- [214] AC Thompson, D Vaughan, and Center for X-ray optics. *X-ray data booklet*. Center for X-ray Optics, 2001.
- [215] R Kronig. *Z. Phys. A-Hadron Nucl.*, 70(5):317–323, 1931.
- [216] R Kronig. *Z. Phys. A-Hadron Nucl.*, 75:191, 1932.
- [217] DE Sayers, EA Stern, and FW Lytle. *Phys. Rev. Lett.*, 27(18):1204–1207, 1971.
- [218] FW Lytle, DE Sayers, and EA Stern. *Phys. Rev. B*, 11:4825, 1974.
- [219] EA Stern, DE Sayers, and FW Lytle. *Phys. Rev. B*, 11(12):4836–4846, 1975.
- [220] DR Hartree, R del Kronig, and H Petersen. *Physica*, 1:895–924, 1934.
- [221] SJ Cyrin. *Molecular vibrations and mean square amplitudes*. Elsevier, Amsterdam, 1968.
- [222] PA Lee and JB Pendry. *Phys. Rev. B*, 11(8):2795–2811, 1975.
- [223] JJ Rehr and RC Albers. *Phys. Rev. B*, 41(12):8139–8149, 1990.
- [224] SK Zabinsky, JJ Rehr, A Ankudinov, RC Albers, and MJ Eller. *Phys. Rev. B*, 52(4):2995–3009, 1995.
- [225] L Hedin and S Lundqvist. *J. Phys. Part C Solid*, 4(14):2064, 1971.
- [226] B Ravel and M Newville. *J. Synchrotron Radiat.*, 12:537–541, 2005.
- [227] M Newville, P Livins, Y Yacoby, J Rehr, and E Stern. *Phys. Rev. B*, 47(21):14126–14131, 1993.
- [228] M Newville, B Ravel, D Haskel, JJ Rehr, EA Stern, and Y Yacoby. *Physica B*, 208:154–156, 1995.
- [229] M Newville. *J. Synchrotron Radiat.*, 8:322–324, 2001.
- [230] A Di Cicco. *Physica B*, 208(1-4):125–128, 1995.
- [231] T Ressler. *J. Synchrotron Radiat.*, 5:118–122, 1998.
- [232] N Binsted. *EXCURV98: CCLRC Daresbury Laboratory computer program*. 1998.
- [233] B Ravel. *Demeter: Perl programming tools for creating Iffffit applications*. 2010.
- [234] M Newville. *FEFFIT - Using FEFF to model XAFS data*. 1998.
- [235] L Brillouin. *Science and information theory*. Dover Phoenix Editions, 2004.
- [236] HJ Krappe and HH Rossner. *J. Synchrotron Radiat.*, 6:302–303, 1999.
- [237] AL Ankudinov, B Ravel, JJ Rehr, and SD Conradson. *Phys. Rev. B*, 58(12):7565–

- 7576, 1998.
- [238] JJ Kas, AP Sorini, MP Prange, LW Cambell, JA Soininen, and JJ Rehr. *Phys. Rev. B*, 76(19):195116, 2007.
- [239] PAM Dirac. *P. R. Soc. Lond A-Conta*, 114(767):243–265, 1927.
- [240] B Ravel. *J. Alloy Compd.*, 401(1-2):118–126, 2005.
- [241] JL Beeby. *Proc. R. Soc. Lon. Ser-A*, 279(1376):82, 1964.
- [242] WL Schaich. *Phys. Rev. B*, 8(8):4028–4032, 1973.
- [243] CA Ashley and S Doniach. *Phys. Rev. B*, 11(4):1279–1288, 1975.
- [244] AL Ankudinov and JJ Rehr. *Phys. Rev. B*, 56(4):R1712–R1715, 1997.
- [245] D Lu and JJ Rehr. *Phys. Rev. B*, 37(11):6126–6133, 1988.
- [246] CR Natoli, M Benfatto, and S Doniach. *Phys. Rev. A*, 34(6):4682–4694, 1986.
- [247] EL Shirley, JA Soininen, and JJ Rehr. *Phys. Scripta*, T115:31–34, 2005.
- [248] JJ Rehr. *FEFF*. <http://leonardo.phys.washington.edu/feff/>, 2009.
- [249] P D’Angelo, A Lapi, V Migliorati, A Arcovito, M Benfatto, OM Roscioni, W Meyer-Klaucke, and S Della-Longa. *Inorg. Chem.*, 47(21):9905–9918, 2008.
- [250] HJ Krappe and HH Rossner. *Phys. Rev. B*, 66(18):184303, 2002.
- [251] AL Ankudinov, CE Bouldin, JJ Rehr, J Sims, and H Hung. *Phys. Rev. B*, 65(10):104107, 2002.
- [252] HJ Krappe and HH Rossner. *Phys. Rev. B*, 70(10):104102, 2004.
- [253] KV Klementev. *J. Phys. D Appl. Phys.*, 34(2):209–217, 2001.
- [254] JJ Rehr and AL Ankudinov. *J. Synchrotron Radiat.*, 8:61–65, 2001.
- [255] *The microXAS/FEMTO beam line*. <http://sls.web.psi.ch/view.php/beamlines/mxas/>, 2000.
- [256] *Swiss Light Source*. <http://sls.web.psi.ch>, 2000.
- [257] *The SLS handbook*. 2010.
- [258] EJM Wilson. *An introduction to particle accelerators*. Oxford University Press, USA, 2001.
- [259] RW Schoenlein, S Chattopadhyay, HHW Chong, TE Glover, PA Heimann, CV Shank, AA Zholents, and MS Zolotarev. *Science*, 287(5461):2237, 2000.
- [260] P Beaud, SL Johnson, A Streun, R Abela, D Abramsohn, D Grolimund, F Krasniqi, T Schmidt, V Schlott, and G Ingold. *Phys. Rev. Lett.*, 99:174801, 2003.
- [261] SL Johnson, P Beaud, CJ Milne, FS Krasniqi, ES Zijlstra, ME Garcia, M Kaiser, D Grolimund, R Abela, and G Ingold. *Phys. Rev. Lett.*, 100(15):155501, 2008.
- [262] E Hecht. *Optics*. Addison Wesley, 2002.
- [263] CT Chantler, CQ Tran, D Paterson, Barnea, and DJ Cookson. *X-Ray Spectrom.*, 29:449–458, 2000.
- [264] G Bunker. *Estimating photon flux from ion chamber currents*. BioCAT: Basic Techniques for EXAFS, 1988.
- [265] *Center for X-ray Optics*. http://henke.lbl.gov/optical_constants/, 2000.
- [266] Newville. *Fundamentals of XAFS*. Number 1.7. <http://xafs.org/>, 2004.

- [267] E Kleimenov, A Bergamaschi, JA van Bokhoven, M Janousch, B Schmitt, and M Nachtegaal. *J. Phys.: Conf. Ser.*, 190:012035, 2009.
- [268] P Glatzel, M Sikora, G Smolentsev, and M Fernandez-Garcia. *Catal. Today*, 145(3-4):294–299, 2009.
- [269] G Vanko, P Glatzel, V-T Pham, R Abela, D Grolimund, CN Borca, SL Johnson, CJ Milne, and C Bressler. *Angew. Chem. Int. Edit.*, 49(34):5910–5912, 2010.
- [270] A Meents, B Reime, M Kaiser, X-Y Wang, R Abela, E Weckert, and C Schulze-Briese. *J. Appl. Crystallogr.*, 42:901–905, 2009.
- [271] S Pommeret, T Gustavsson, R Naskrecki, G Baldacchino, and JC Mialocq. *J. Mol. Liq.*, 64(1-2):101–112, 1995.
- [272] K Ekvall, P van der Meulen, C Dhollande, LE Berg, S Pommeret, R Naskrecki, and JC Mialocq. *J. Appl. Phys.*, 87(5):2340–2352, 2000.
- [273] G Zgrablic. *solvent effects on the ultrafast dynamics of the retinal chromophore of bacteriorhodopsin*. EPFL (PhD Thesis), 2006.
- [274] E Baranoff. *personal communication*. EPFL, 2009.
- [275] RM van der Veen, A Cannizzo, F van Mourik, A Vlček Jr, and M Chergui. *J. Am. Chem. Soc.*, accepted, 2010.
- [276] DM Jonas, SE Bradforth, SA Passino, and GR Fleming. *J. Phys. Chem.*, 99(9):2594–2608, 1995.
- [277] Z Bihary, R Zadoyan, M Karavitis, and VA Apkarian. *J. Chem. Phys.*, 120(16):7576–7589, 2004.
- [278] W Gawelda, A Cannizzo, VT Pham, F van Mourik, C Bressler, and M Chergui. *J. Am. Chem. Soc.*, 129(26):8199–8206, 2007.
- [279] A Cannizzo, F van Mourik, W Gawelda, G Zgrablic, C Bressler, and M Chergui. *Angew. Chem. Int. Ed.*, 45(19):3174–3176, 2006.
- [280] A Mokhtari, J Chesnoy, and A Laubereau. *Chem. Phys. Lett.*, 155(6):593–598, 1989.
- [281] G Giraud and K Wynne. *J. Chem. Phys.*, 119(22):11753–11764, 2003.
- [282] Y Lei, HR Li, HH Pan, and SJ Han. *J. Phys. Chem. A*, 107(10):1574–1583, 2003.
- [283] KA Connors. *Chemical kinetics: the study of reaction rates in solution*. Wiley-VCH, 1990.
- [284] M Guhr and N Schwentner. *J. Chem. Phys.*, 123(24):244506, 2005.
- [285] GM Hasselman, DF Watson, JR Stromberg, DF Bocian, D Holten, JS Lindsey, and GJ Meyer. *J. Phys. Chem. B*, 110(50):25430–25440, 2006.
- [286] SB Piepho, PN Schatz, and AJ McCaffer. *J. Am. Chem. Soc.*, 91(22):5994, 1969.
- [287] JK McCusker, KN Walda, RC Dunn, JD Simon, D Magde, and DN Hendrickson. *J. Am. Chem. Soc.*, 115(1):298–307, 1993.
- [288] D Kuciauskas, JE Monat, R Villahermosa, HB Gray, NS LEWIS, and JK McCusker. *J. Phys. Chem. B*, 106(36):9347–9358, 2002.
- [289] JK McCusker. *Accounts Chem. Res.*, 36(12):876–887, 2003.
- [290] A Cannizzo, AM Blanco-Rodriguez, A El Nahhas, J Sebera, S Zalis, A Vlček, and M Chergui. *J. Am. Chem. Soc.*, 130(28):8967–8974, 2008.

- [291] JN Harvey. *Faraday Discuss.*, 127:165–177, 2004.
- [292] G Ramakrishna, T Goodson, JE Rogers-Haley, TM Cooper, DG McLean, and A Urbas. *J. Phys. Chem. C*, 113(3):1060–1066, 2009.
- [293] PR Bunker and P Jensen. *Fundamentals of molecular symmetry*. Taylor & Francis, 2005.
- [294] ZA Siddique, Y Yamamoto, T Ohno, and K Nozaki. *Inorg. Chem.*, 42(20):6366–6378, 2003.
- [295] Z Abedin-Siddique, T Ohno, and K Nozaki. *Inorg. Chem.*, 43(2):663–673, 2004.
- [296] GB Shaw, CD Grant, H Shirota, EW Castner, GJ Meyer, and LX Chen. *J. Am. Chem. Soc.*, 129(7):2147–2160, 2007.
- [297] S Neidle, M Sanderson, A Subbiah, and R Kuroda. *J. Chem. Soc.*, pages 13–15, 1980.
- [298] L Pauling. *J. Am. Chem. Soc.*, 54:3570–3582, 1932.
- [299] C Battocchio, F D’acapito, G Smolentsev, AV Soldatov, I Fratoddi, G Contini, I Davoli, G Polzonetti, and S Mobilio. *Chem. Phys.*, 325(2-3):422–428, 2006.
- [300] RM van der Veen, C Bressler, CJ Milne, V-T Pham, A El Nahhas, FA Lima, W Gawelda, CN Borca, R Abela, and M Chergui. *J. Phys.: Conf. Ser.*, 190:012054, 2009.
- [301] O Stern and M Volmer. *Phys. Z.*, 20:183–188, 1919.
- [302] JR Lakowicz. *Principles of fluorescence spectroscopy*. Springer, 2006.
- [303] Battino. *Solubility data series. Volume 7: Oxygen and Ozone*. 1981.
- [304] JK Nagle and BA Brennan. *J. Am. Chem. Soc.*, 110(17):5931–5932, 1988.
- [305] D Roundhill, Z Shen, C King, and S Atherton. *J. Phys. Chem*, 92:4088–4094, 1988.
- [306] WB Heuer, MD Totten, GS Rodman, EJ Hebert, HJ Tracy, and JK Nagle. *J. Am. Chem. Soc.*, 106:1163–1164, 1984.
- [307] J Peterson and K Kalyanasundaram. *J. Phys. Chem.*, 1985.
- [308] AL Ankudinov, AI Nesvizhskii, and JJ Rehr. *J. Synchrotron. Rad.*, 8:92–95, 2001.
- [309] DM Roundhill, SJ Atherton, and ZP Shen. *J. Am. Chem. Soc.*, 109(20):6076–6079, 1987.
- [310] CJ Milne, FA Lima, DA Vithanage, RM van der Veen, M Reinhard, HM Rittmann-Frank, CN Borca, SL Johnson, F van Mourik, R Abela, and M Chergui. *in preparation*, 2010.
- [311] FA Lima, CJ Milne, M Reinhard, HM Rittmann-Frank, V-T Pham, RM van der Veen, CN Borca, and M Chergui. *in preparation*, 2010.
- [312] Y Joly. *Phys. Rev. B*, 63(12):125120, 2001.
- [313] N Huse, TK Kim, L Jamula, JK McCusker, FMF de Groot, and RW Schoenlein. *J. Am. Chem. Soc.*, 132(19):6809–6816, 2010.
- [314] N Huse, H Wen, D Nordlund, E Szilagy, D Daranciang, TA Miller, A Nilsson, RW Schoenlein, and AM Lindenberg. *Phys. Chem. Chem. Phys.*, 11(20):3951–3957, 2009.
- [315] O Link, E Lugovoy, K Siefertmann, Y Liu, M Faubel, and B Abel. *Appl. Phys. A*,

References

- 96(1):117–135, 2009.
- [316] IHM van Stokkum, DS Larsen, and R van Grondelle. *BBA-Bioenergetics*, 1657(2-3): 82–104, 2004.
- [317] ER Henry and J Hofrichter. *Methods in enzymol.*, 210:129–192, 1992.

Curriculum Vitae

Villigen, December 13, 2010

PERSONAL DETAILS

Renske Marjan van der Veen

Schartenstrasse 117

CH-5430 Wettingen

Switzerland

Phone (home): +41 56 511 2144

Phone (work): +41 56 310 5362

E-mail: renske.van_der_veen@alumni.ethz.ch

Date of birth: 12th of June, 1984

Nationality: The Netherlands

Civil status: Single

EDUCATION

2006–2010 PhD at the *École Polytechnique Fédérale de Lausanne* (EPFL) and the Swiss Light Source (SLS), Paul Scherrer Institute (PSI) under the supervision of Prof. M. Chergui

2005–2006 Master in Chemistry at the ETH in Zürich, Switzerland (*with distinction*); Specialization: Physical Chemistry

2002–2005 Bachelor in Chemistry at the ETH in Zürich, Switzerland

1996–2002 Gymnasium, Bussum, The Netherlands

ACADEMIC VISITS

- April 2010** *"Time-resolved X-ray powder diffraction experiments on molecular crystals"*
Hosting Professor: Prof. T. Elsässer
Institution: Max Born Institut für Nichtlineare Optik und Kurzzeitspektroskopie, Berlin, Germany
- Oct./Nov. 2009** *"Time-resolved X-ray diffraction experiments on molecular crystals"*
Hosting Professor: Prof. P. Coppens
Institution: Department of Chemistry, The State University of New York at Buffalo, Buffalo NY, United States
- Nov. 2008** *"Bayesian approach to fitting transient XANES spectra by using the new ab initio FEFF9 code"*
Hosting Professor: Prof. J.J. Rehr
Institution: Department of Physics, The State University of Washington, Seattle WA, United States

AWARDS AND GRANTS

- Apr. 2009** Young scientist travel grant awarded by the Società di Chimica Italiana to attend the 14th International Conference on X-ray Absorption Fine Structure, July 14-21, Camerino, Italy
- Sept. 2007** ESF Short visit grant in the field of "Ultrafast Structural Dynamics in Physics, Chemistry, Biology and Material Science" to visit the group of J.A. Weinstein, Department of Chemistry, University of Sheffield, United Kingdom
- Sept. 2007** Swiss Chemical Society prize for the best poster talk/presentation in Physical Chemistry, SCS Fall Meeting, 12 September 2007, Lausanne
- Nov. 2006** One-year fellowship awarded by the École Doctorale en Photonique, EPFL

ORAL PRESENTATIONS

1. *Ultrafast X-ray and optical spectroscopy of metal complexes in solution*, Photonics Day, EPFL, Lausanne, Switzerland, November 2010 (invited)
2. *Ultrafast dynamics in molecular complexes studied by time-resolved X-ray and optical spectroscopies*, SLS Symposium in electron dynamics, Villigen, Switzerland, September 2010

3. *Femtosecond wavepacket dynamics in dimetal complexes*, Max-Born-Institut für Nicht-lineare Optik und Kurzzeitspektroskopie, Berlin, Germany, November 2009
4. *Retrieving photochemically active structures by ultrafast optical and X-ray spectroscopies*, Swiss Chemical Society Fall Meeting, Lausanne, September 2009 (contributed)
5. *Retrieving photochemically active structures using time-resolved EXAFS spectroscopy*, XAFS XIV conference, Camerino, Italy, July 2009 (contributed)
6. *Ultrafast X-ray Absorption Spectroscopy on Metal Complexes in Solution - Structural determination of the triplet excited state of PtPOP*, time-resolved crystallography group of Prof. P. Coppens, SUNY Buffalo, United States, October 2008 (invited)
7. *Ultrafast Structural Dynamics in Coordination Compounds Studied by Time-Resolved Optical and X-Ray Spectroscopies*, Department of Chemistry, The University of Sheffield, United Kingdom, October 2007
8. *Pump-probe Chemistry Studied by Ultrafast X-Ray Techniques*, SLS Symposium, PSI Villigen, October 2007
9. *Ultrafast Structural Dynamics in Organometallic Platinum Complexes*, Swiss Chemical Society Fall Meeting, EPFL, September 2007 (contributed)

POSTER PRESENTATIONS

1. *Retrieving photochemically active structures by time-resolved EXAFS and XANES spectroscopy*, 1st International Conference on Ultrafast Structural Dynamics, EPFL, Lausanne, June 2010
2. *Photoinduced chemical processes in solution studied by ultrafast X-ray absorption spectroscopy*, EU-XFEL 3rd User Meeting, DESY, Hamburg, February 2009
3. *Time-resolved EXAFS spectroscopy of the photo-excited $Pt_2(P_2O_5H_2)_4^{4-}$ anion in solution*, XAS Workshop, Paul Scherrer Institute, Swiss Light Source, 2008
4. *Observation of Photogenerated Nascent Iodine Radicals via Picosecond X-Ray Absorption Spectroscopy*, DESY Research School, Hamburg, March 2007
5. *Picosecond Optical Pump / X-Ray Probe Studies of Photoionized Aqueous Halides*, Photonics Day, EPFL, September 2006

ATTENDED COURSES

1. *Elements of microscopy*, ETH, Zürich, SS 2010
2. *Ultrafast X-Ray Summer School*, PULSE Stanford, June 2007
3. *Introduction to Particle Accelerators*, EPFL, WS 2006/2007
4. *DESY Research School on New X-Ray Sources*, Hamburg, March 2007
5. *Ultrafast Phenomena*, EPFL, WS 2006/2007

SS: summer semester, WS: winter semester

TEACHING EXPERIENCE

- Science outreach and demonstrations in the visitor's center (PSI Forum) and student lab (iLab) of the Paul Scherrer Institute, Villigen, since January 2007
- Supervision of practical student courses at the Swiss Light Source, 2010

LANGUAGES

Dutch: fluent (mother tongue)
English: fluent
German: fluent
French: moderate (European A2 level)

SOCIAL ACTIVITIES / INTERESTS

- Music: playing the cello
- Sports: field hockey at international level (7 European Cup tournaments), running

PUBLICATIONS

1. "Vibrational relaxation and intersystem crossing in binuclear metal complexes in solution",
R.M. van der Veen, A. Cannizzo, F. van Mourik, A. Vlček Jr. and M. Chergui,
J. Am. Chem. Soc., accepted (November 2010)
2. "Femtosecond X-ray Absorption Spectroscopy of a Light-Driven Spin-Crossover Process",
C.J. Milne, V.-T. Pham, W. Gawelda, A. El Nahhas, R.M. van der Veen, S.L. Johnson, P. Beaud, G. Ingold, C.N. Borca, D. Grolimund, R. Abela, M. Chergui and C. Bressler
Acta Phys. Pol. A **117**, 391
3. "Ultrafast manipulation of hard X-rays by efficient Bragg switches",
M. Herzog, R. Shayduk, W. Leitenberger, R.M. van der Veen, S. Johnson, Ch. Milne, I. Vrejoiu, M. Alexe, D. Hesse and M. Bargheer,
Appl. Phys. Lett. **96**, 161906 (2010)
4. "L-edge XANES analysis of photoexcited metal complexes in solution",
R.M. van der Veen, J.J. Kas, C.J. Milne, V.-T. Pham, A. El Nahhas, F.A. Lima, D.A. Vithanage, J.J. Rehr, R. Abela and M. Chergui,
Phys. Chem. Chem. Phys. **12**, 5551 (2010) (invited article)
5. "The solvent shell structure of aqueous iodide: X-ray absorption spectroscopy and classical, hybrid QM/MM and full quantum molecular dynamics simulations",
V. T. Pham, I. Tavernelli, C.J. Milne, R.M. van der Veen, P. D'Angelo, Ch. Bressler and M. Chergui,
Chem. Phys. **371**, 24 (2010)
6. "Retrieving photochemically active structures by time-resolved EXAFS spectroscopy",
R.M. van der Veen, C. Bressler, C.J. Milne, V.-T. Pham, A. El Nahhas, F.A. Lima, W. Gawelda, C.N. Borca, R. Abela and M. Chergui,
J. Phys. Conf. Ser. **190** 012054 (2009)
7. "Time-resolved x-ray absorption spectroscopy: Watching atoms dance",
C.J. Milne, V.-T. Pham, W. Gawelda, R.M. van der Veen, A. El Nahhas, S.L. Johnson, P. Beaud, G. Ingold, F. Lima, D.A. Vithanage, M. Chergui, et al
J. Phys. Conf. Ser. **190** 012052 (2009)
8. "Structural determination of a photochemically reactive diplatinum molecule by time-resolved EXAFS spectroscopy",
R.M. van der Veen, C.J. Milne, V.-T. Pham, A. El Nahhas, J. Best, J.A. Weinstein, C.N. Borca, R. Abela, C. Bressler and M. Chergui,
Angew. Chem. Int. Ed. **48** (15), 2711-2714 (2009)

9. "Structural analysis of ultrafast EXAFS with sub-picometer spatial resolution: application to solvated spin cross-over complexes",
W. Gawelda, V.-T. Pham, R.M. van der Veen, D. Grolimund, R. Abela, M. Chergui and C. Bressler,
J. Chem. Phys. **130** (12), 124520 (2009)
10. "Femtosecond XANES of the photocycle of Iron(II) Molecular complexes",
C. Bressler, C.J. Milne, V.-T. Pham, A. El Nahhas, R.M. van der Veen, S.L. Johnson, P. Beaud, A. Hauser, D. Grolimund and M. Chergui,
Science **323**, 489 (2009)
11. "EXAFS structural determination of the $\text{Pt}_2(\text{P}_2\text{O}_5\text{H}_2)_4^{4-}$ anion",
R.M. van der Veen, C.J. Milne, V.-T. Pham, A. El Nahhas, J.A. Weinstein, J. Best, C.N. Borca, C. Bressler and M. Chergui,
Chimia **62**(4) (2008) (invited article)
12. "Light-induced spin crossover probed by ultrafast optical and X-ray spectroscopies",
W. Gawelda, A. Cannizzo, V.-T. Pham, A. El Nahhas, C.J. Milne, R. van der Veen, C. Bressler and M. Chergui,
Chimia **61**(4), 179 (2007) (invited article)
13. "Jahn-Teller effect in the methane cation: rovibronic structure and the geometric phase",
H.-J. Wörner, R. van der Veen and F. Merkt,
Phys. Rev. Lett. **97**, 173003 (2006)